A Refined Numerical Modelling Technique for Shot Peening

by

Kovthaman Murugaratnam

A thesis submitted for the degree of
Doctor of Philosophy

Department of Engineering Science

University of Oxford

Exeter College

Michaelmas Term 2014

ABSTRACT

A REFINED NUMERICAL MODELLING TECHNIQUE FOR SHOT PEENING

A thesis submitted for the degree of Doctor of Philosophy

Kovthaman Murugaratnam
Exeter College, University of Oxford
Michaelmas Term, 2014

Compressive residual stresses (CRS) are beneficial for enhancing the fatigue life of metal components. Shot Peening (SP) is an industrial cold working process that is applied to induce a field of CRS and modify the mechanical properties of the metal component. The SP process involves impacting a surface with tiny shots with forces sufficient to create plastic deformation. The process is governed by a number of important parameters such as the shot size, angle of attack, initial velocity, mass flow rate and the distance from the shot nozzle to the surface being peened. The relationship between the optimal peening outcome, particularly the residual stress distribution of the treated surface, and the peening parameters is still unknown and needs to be investigated further. Manufacturers are interested in producing a uniform peening process for complex geometries which optimises the SP parameters. Modelling the process is complex as it involves the interaction of a metallic surface with a large number of shots of very small diameter. Conventionally, such problems are solved using finite element software to predict stresses and strains of a single shot impact then applying superposition. At the moment there are no Finite Element Method (FEM) modelling

solutions involving more than tens of shots. The number of shots and elements required for such a modelling process made the approach unfeasible prior to the work described herein.

The objective of this work is to develop an appropriate numerical modelling approach that can better simulate the real SP process. The model will be provided by combining Discrete Element Method (DEM) with FEM. The DEM is employed to get a distribution of impact velocities over space and time which are then implemented into a FEM analysis. A discrete element model with randomly distributed steel shots bombarding a steel component at various velocities has been developed as benchmark example. With this model the SP shot - shot interaction, the shot - target interaction, the surface coverage, angle of impingement, shot size, impact velocity and the overall shot flow can be parametrically studied in details and with little computational effort. The novel approach also proposes a new method to dynamically change the coefficient of restitution for repeated impacts during the simulation and predicts the CRS more effectively. The effects of SP on different materials of relevance to gas turbine engine components will be investigated in order to improve the understanding of the interaction between the shots and the targeted material. Initially, an uncoupled analysis was peforned, in order to assess the capabilities of the two modelling systems, DEM and FEM, to delivery an improved solutuion when combining two commercially available codes. This parametric analysis is performed using the state-of-the-art Discrete Element (DE) application EDEM. In the subsequent part of this work, a dynamic Finite Element (FE) application Abaqus will be used to investigate single shot impacts and to obtain the residual stress distribution. This gives us a prescribed residual stress distribution and peening coverage.

A Combined DEM/FEM tool (DEST) is proposed that eliminates any manual pre-processing required for linking/coupling, eliminating the use of two different applications and provide an integrated solution for the simulation of the Shot Peening process. In the

subsequent chapter, the implementation of essential tools for the enchanced modelling of Shot Peening process functionalities, such as the nozzle, bounding box, coverage and intensity is described.

A number of computational improvements are also implemented to reduce the computation time. The existing binary search is enhanced to self-balancing search tree and further improved to allow insertion and deletion of elements. A bounding box feature which removes shots that move out of the domain during the course of the simulation is also implemented. Experiments featuring single shot impacts are performed to gain better understanding the deformation process in the target material subjected to impact conditions to those occurring in the production peening. The single shot impacts are experimentally examined using SEM and EBSD.

During final chapter, case studies are performed to compare the results of the simulations with large-scale experimental work. The coverage of peening of single and multiple nozzles with different angle of impingements are assessed. Finally, possible directions for further research concerning the accurate quantification of material responses to SP are identified in the report.

ACKNOWLEDGEMENTS

I am heartily thankful to Prof. Nik Petrinic and Dr. Stefano Utili for supervising me during this study, allowing me to discuss my ideas and offering me the chance to gain valuable knowledge in the field of Shot Peening and having the faith in me. They had been invaluable in overcoming the obstacles and difficulties that I had encountered throughout this dissertation.

To all in the Impact Engineering team, including those who have now moved on, thank you for your interest and frequent, often challenging, discussions of my research and yours. Having been part of the Impact Engineering team in Oxford was a challenging and enriching experience. I would like to thank all of my colleagues who contributed with their own research to the content of this thesis, including Ben Cousins for the discussion on the material model, Francesco de Cola and Mattia Montanari for the discussion on contact algorithms.

My thanks to my fellow colleagues in Room 11 and 12 who have been inspirational, and to my friends here in Oxford who have been supportive including the DEM research group at Oxford University: Dr Chiara Modenese, Dr Chia Weng Boon, Dr Tao Zhao and Giulia Macaro, for the rewarding discussions concerning the discrete element method and for sharing their knowledge on numerical algorithms and software. Many aspects of my work could not have been addressed as professionally without this great team of young and motivated people around me.

My special thanks go to the workshop team, in particular Stuart Carter, who has always accommodated my unexpected pleas to machine more specimens at short notice and Dr. Hamid Reza Abolvand and Dr. Rajesh Korla from the Materials Department for helping me to characterise the specimens, and especially to perform the SEM, EBSD and micro indentation analysis.

The generous support of Rolls Royce Plc. and DEM Solutions is gratefully acknowledged.

Finally, and most importantly, I would like to thank my family. Nilani, who has supported me in every decision I have made, and has encouraged me to follow my dreams and aspirations. My sister who taught me that I can achieve whatever I set my mind to. My father who has aspired me to pursue knowledge and my mother who throughout my life has been willing to sacrifice anything to help me to achieve my dreams and has been a constant source of strength and support.

Contents

List of Figures

List of Tables

List of Algorithms

Notation and conventions

Explanations of the Symbols used throughout the text are given in the correspondence of their first mention in text. Nevertheless, some symbols and acronyms of widespread use are given below.

A_h	Almen strip height
C(t)	Percentage of coverage at particular time *t*
E*	Effective contact modulus
G*	Shear modulus
δ	Overlap of contacting entities
e	Coefficient of restitution
R	Sphere radius
m	Mass
t	Peening time
d_{shot}	Shot diameter
d	Peening distance
α	Angle of incidence
σ	Effective stress
ν	Poisson's ratio
μ	Coefficient of friction
u	Displacement vector field
θ	Peening angle
r	Radius of the circle in the contact plane
V	Velocity
F	Force
p	Mass density
b, h ,l	width, thickness and length of the strip
I_m	Reference distance for measuring the Almen intensity
η	Damping coefficient
M_x	Bending moment
r_m	Flow rate
k	Stiffness
d_n	Nozzle diameter

n_s	Number of shot peening sources
H^1	Linear strain hardening parameter
d_{bz}	Buffer zone
d_{cz}	Contact zone
R_a	Arithmetic average roughness
R_{RMS}	Root Mean Square of a surface
R_T	Peak-to-valley roughness parameter
R_P	Maximum peek roughness parameter
R_V	Minimum valley roughness parameter
A	Section area of the target component
PV	Surface roughness Peek and Valley
BST	Binary space tree
BSP	Binary space partitioning
RS	Residual stress
DE	Discrete element
FE	Finite element
CRS	Compressive residual stress
MRS	Maximum compressive residual stress
SRS	Surface residual stress
DMRS	Depth of maximum compressive residual stress
SEM	Scanning electron microscope
EBSD	Electron Backscatter Diffraction

Equations, figures and tables and are numbered according to the chapter number. Cross-referencing to equations is given in brackets, e.g. (Eq. 6.2), and to reference titles in brackets, e.g. (König G. 2002). Figures and tables and are referenced using their caption names together with their numbers, for example Figure 2.1 and Table 6.1. Bibliographic references are listed in alphabetic order.

CHAPTER 1 INTRODUCTION

This chapter includes background information about Shot Peening processes, the motivation for research and objectives set to achieve the results presented in this thesis.

1.1 Background information on Shot Peening processes

It has been known for a long time that pre-stressing or work-hardening can make metals harder and more durable. Shot Peening (SP) was used in the forging process as early as the Bronze-Age to strengthen armour, swords and tools. Gun barrels were peened to increase the hardness of Damascus steels, and as early as 1922 the fillets of crankshafts in early European race cars were hand peened with special hammers (Kloos and Macherauch, 1987). Today, major failures of many aircraft engine components are often the results of metal fatigue due to mechanical and thermal cyclic loads (König G., 2002).

SP is a cold working process in which the surface of a component is bombarded with a large number of small spherical particles called shots. Each single shot striking the material surface acts as a tiny peening hammer, imparting a small indentation to the surface. As a result, the material directly under the surface is subjected to high compressive forces from the deformation and tries to restore the outer surface to its initial shape. A uniform compressive layer at the surface of the material is then created by the overlapping indentations created from shot impacts. Grains structures are subjected to compressive confinement because of the presence of compressive stresses and this significantly delays the initiation of fatigue cracking, thereby increasing the fatigue life of the part. Figure 1.1 shows the process of Shot Peening.

Most surfaces are thought to contain tiny cracks that are not visible to the naked eye. Such free surfaces are weaker than the bulk material and when subjected to machine and handling defects, cracks are more likely to occur. For this reason, to improve fatigue life

considerable attention is devoted to ensuring that no tensile residual stresses are present. Typically, fatigue failure can be described in three different stages. In the first stage, the crack is initiated at the surface of the body. Subsequently, the crack grows from the free surface into the body in a direction perpendicular to the direction of the applied stress, for example, in Mode I fracture. The crack then continues to grow into the body, however under the action of shear stresses the crack path can change direction. In the second stage, the crack grows further, under tensile or shear stresses defining the crack growth direction. In the third stage the crack propagates until the material is no longer able to carry the load and fast fracture occurs.

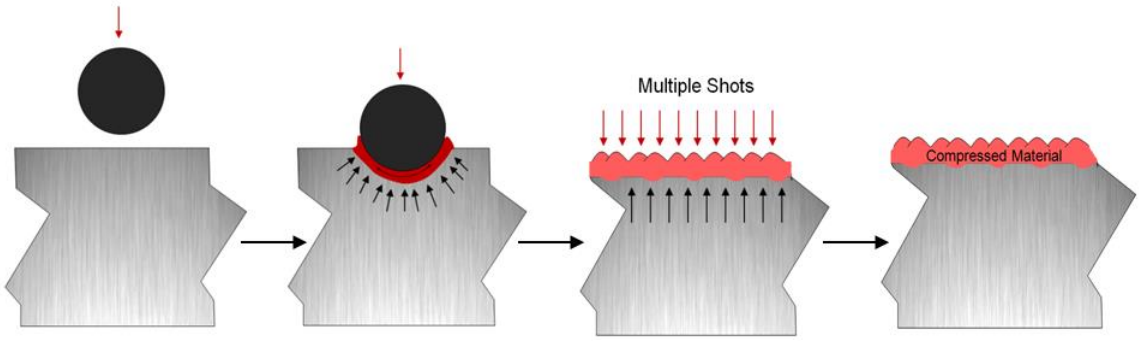

Figure 1.1: The process of Shot Peening.

It is known that crack initiation, in its early propagation stages can be delayed and the fatigue life of the components can be extended. Since cracks will not propagate in the compressed area of a work piece, it is possible to induce Compressive Residual Stresses (CRS) onto the surface layer to compensate for tensile loading stresses (Almen and Black, 1963).

The application of SP has several advantages. Firstly, shot peened components are generally smaller and lighter and have higher load capability for the same design as other components. Secondly, SP can mitigate problems due to stress corrosion and porosity in metals. In addition, the surface texture created by SP can provide a benefit in lubrication due to oil retention (Higounenc, 2005). SP is also applied to relieve tensile stress in welded materials to improve fatigue life. When fatigue failures occur in areas of tension, SP the part

can enhance the fatigue strength anywhere from 70 % to 100 % (Lieurade, H.P. 2005; Peyrac and Flavenot 2005). It has been reported that fatigue resistance in the inner material of shot peened work pieces is nearly one-third higher than that of the component surface (Peige et al., 1996). The maximum CRS produced at the surface of the component part is at least as great as half the yield strength of the material being peened. Shot peened parts leave a uniformly textured and finished surface that can immediately be painted or coated without pre-processing the component.

In industry, manufacturers spend several hundred thousand pounds on optimising their SP process every year. Optimising the SP process of turbine blades involves the peening of many components before obtaining the desired peening effects. The SP process is controlled by a number of peening parameters that have a direct effect on the CRS. Hence, choosing the right peening parameters and controlling the peening process for new components is very important. Moreover, the SP method is particularly popular because of its versatility, high productivity rates, a notably modest equipment cost and low energy consumption (Tatton R.J.D., 1987).

1.2 Motivation

A numerical Shot Peening model can help study the effect of process parameters on the peening quality. Experimental knowledge and statistical analyses can reveal the relationship between the process parameters and peening quality. Peening quality can be analysed without the need of destructive methods. A numerical model using DEM and FEM can provide information about the optimal SP parameters to be used for the peening process. DEM can be used to study the effect of shot interaction and energy transfer. FEM analysis can help to understand the CRS profile resulting from the energy transfer. A combined model can help to maximise the energy transfer per unit time, reducing the production time, improving the quality control and more importantly increasing the confidence in the process.

1.3 Objectives and strategy

The objective of this work is to develop an appropriate numerical model that can better simulate the real SP process. A 3D discrete element model with numerous randomly distributed steel shots bombarding a steel component at various velocities has been developed. With this model, the SP shot - shot interaction and shot - target interaction, surface coverage, angle of impingement, shot size, impact velocity and the overall shot flow can be studied in detail. The DE model will provide a good indication of the impact energy over time for given peening parameter and component geometry.

A method to change the coefficient of restitution for repeated impacts is implemented to take into account the effect of material hardening. A parametric study is performed using FEM to analyse single shot impacts on a flat surface to investigate the development of residual stress for different shot diameters, impact velocity and angle of impingement. The effect of repeated impact is also investigated and a method is presented to link DEM and FEM to retrieve the CRS for multiple shots.

A combined DEM/FEM tool (DEST) is proposed that eliminates any manual pre-processing required for the linking/coupling, thus eliminating the use of two different applications and provides a one-off solution for Shot Peening simulations. The subsequent sections focus on the implementation of the essential tools in DEST required for the proper modelling of the Shot Peening process, such as the nozzle, coverage, intensity and surface roughness. A number of computational improvements are implemented to reduce the computation time. The existing binary search is enhanced to create a self-balancing search tree and further improvements to allow insertion and deletion of elements. A bounding box feature to remove shots that move out of the domain during the course of the simulation has been implemented.

In chapter 6, single shot impacts are performed to gain a better understanding of what

happens to the material under impact conditions similar to those used in production peening. The single shot impacts are experimentally examined using SEM and EBSD. Large-scale analysis of the peening on Ti-6Al-4V Almen strip like test blocks with single and multiple nozzles at different angles are conducted to compare simulations with experimentally measured coverage, intensity and residual stresses.

1.4 Thesis structure

The literature review on relevant published work is presented in the next chapter, in order to justify the above proposed objectives and the strategy for achieving them, a numerical model for Shot Peening optimisation is presented in Chapter 3. The results of the parametric study performed in DEM and FEM is presented in Chapter 4. Chapter 5 describes the numerical implementation of the Shot Peening features, algorithms and aspect of the computational improvements. Chapter 6 describes the single shot impacts performed using Ti-6Al-4V and peening media for various conditions. Large scale simulation of Shot Peening of Ti-6Al-4V test blocks with single and multiple nozzles is presented in Chapter 7. Chapter 8 presents the overall conclusions of the thesis and future work is proposed in Chapter 9.

CHAPTER 2 LITERATURE REVIEW

This chapter includes background about SP, the principles and the equipment used in the peening process. Previous experimental and finite element (FE) modelling work is also reviewed and discussed. This chapter also lists the gaps in knowledge and related capabilities which have been addressed in the research presented in this thesis.

2.1 Shot Peening

SP is an industrial cold working process that is applied to induce a layer of CRS on the component's surface. In the process, the treatment surface is bombarded by a large amount of spherical metal 'shots' at high velocities. Each shot acts as a tiny peen hammer, causing the surface to yield in plastic deformation and leaving a concave depression on the surface of the target component. The stress field of the depressions are similar to a flat bar being bent, with a maximm compressive stress on the concave surface, zero stress at the centre of the bar and maximum tensile stress on the convex surface. Figure 2.1 shows the typical residual stress profile created by Shot Peening.

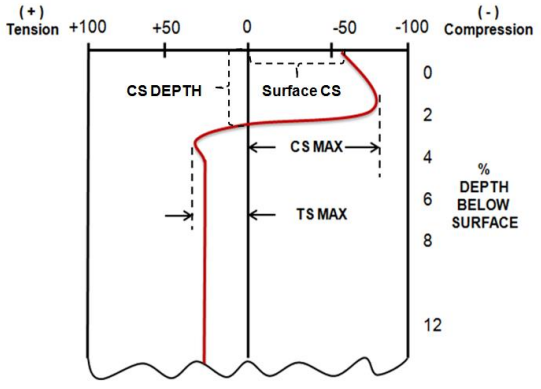

Figure 2.1: Example of residual stress profile created by Shot Peening.

In SP, the maximum compressive stress resides at the component surface due to the impact deformation on the surface. At the transition zone that yields by plastic deformation and the material below, the stresses tend to approach zero. Further below the transition zone the

undeformed subsurface is in tension, trying to pull back the compressed surface to its initial shape. Usually, the thickness of the material is greater than the depth of the deformed surface, therefore there is a larger area to distribute the tensile stresses beneath the surface. The tensile stress below the component surface is of lower magnitude than the compressive stress on the component surface. When compressive stresses from SP are added, fatigue strength increases proportionately to increased strength. However, if the surface temperature exceeds the normalized temperature of the metal, the CRS will be relieved and the SP benefits will be lost.

The most important aspects of SP are the SP parameters used in the process. The SP parameters have direct influence on the CRS. Figure 2.2 shows the peening parameters affecting the peening quality. The peening parameters must be controlled to improve the quality of the peening (Deslaef et al., 2000; Meguid et al., 1999; Guagliano, 2001). If the peening is too intensive, the depth of the shot peened surface will be excessive, creating a high tensile stress below the surface and leading to cracks being initiated below the surface at stress levels lower than those at which cracks would have been initiated without peening. Similarly, if peening intensity is very low, the CRS will be insufficient and no improvement in fatigue stress will occur.

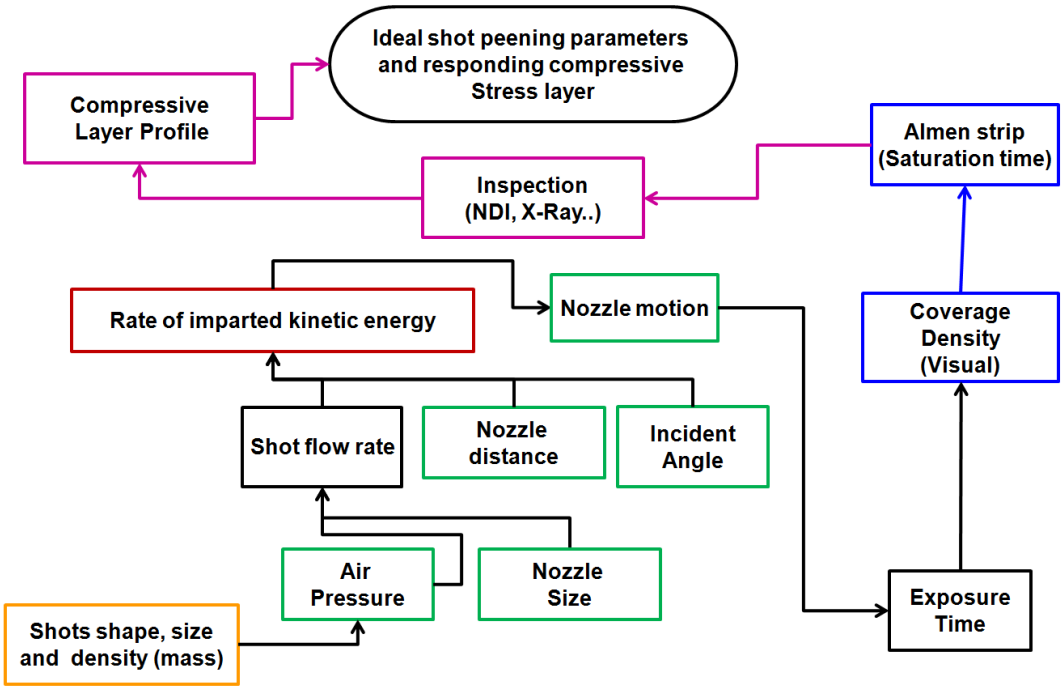

Figure 2.2: Parameters affecting the peening process.

2.1.1 Shot Peening systems

Before mechanised methods for SP were applied, a manual technique using some custom-made hand held equipment such as special hammers were used. Advances in SP took place primarily in the automotive industry where high volumes of production could not be achieved with manual peening techniques. Mechanised techniques use multi-nozzle systems to treat high volume components. A SP machine must be able to accurately control the delivery of media and ensure repeatability of the peening process. Other requirements for an effective SP machine include: directional control enabling mechanized variation of the shot flow direction and work piece motion, a means of media return which include systems for grading, cleaning and classifying shot, cycle control and computer control. Different component types may be more or less suited to specific peening systems. The common media delivery systems include centrifugal wheel, pressure fed systems, gravity fed systems and vacuum/suction fed systems. In the aircraft industry, centrifugal wheels are preferred due to better energy efficiencies, velocities, higher coverage and flow rates compared to air nozzle systems (Baughman, 1981).

To maintain the quality of the peening, various types of separating systems such as sieves and multi-step air separating systems can be implemented. Centrifugal wheels are generally used for large peening processes because of their economic benefits. Air pressured peening systems are preferred where flexibility is required as they are capable of peening different types of parts using one machine. A wheel can throw about 45 kg to 250 kg of shots per minute. A single air nozzle can shoot about one tenth of that amount although it can concentrate the flow onto smaller target areas. Furthermore, multiple nozzles can therefore be used to reduce peening time.

2.1.2 Media

The media material employed to shoot a surface must be at least as hard as the peened material. It has been reported that in the 1930s chilled iron grit was used for blast cleaning to improve car valve springs. However, it was discovered that iron shots shattered too quickly and in the 1950s, cast steel was introduced. Today cast steel shots are probably the most common peening material. In the 1960s cut steel wire and glass shots were introduced. Glass shots are considerably smaller on average than steel shots making it possible to peen thin pieces. Cut wire shots are used as a blasting material to achieve cutting without wearing out the equipment. Cut wire shot changes shape from cylinders to oblongs to spherical shapes during peening and produce a more consistent depth than steel shots. In the early 1980s, the most common media used for SP was cast steel and cut wire because they can be employed for several hundred thousand cycles whereas glass shots or beads could be used for only a few cycles. Later, ceramic shots were introduced to achieve higher intensities. The variation of shot size, shape and hardness can have an important impact on the cold working process and the consequent CRS development.

2.1.3 Shot Peening metrics

In the practical Shot Peening application, the process is characterised in terms of Almen intensity, saturation time and coverage.

Intensity

To evaluate the performance of the peening process and the variety of peening parameters, J.O Almen, an engineer at the General Motors Corporation, introduced a method in the 1940's to measure the peening intensity called the 'Almen peening intensity'. SP intensity is quantified by means of the Almen-scale which measures the residual arc height of the Almen Strip. The strip is made of a specific material and size (Almen and Black 1963). In the measurement procedure, a flat metal strip (SAE1070) is clamped to a test block and blasted with shots. After peening the strips is removed and its deflection is measured using an Almen gauge. The Almen arc height A_h of each strip is plotted as a function of its exposure time t to obtain the saturation curve. Figure 2.3 shows the measurement procedure.

There are three different types of Almen Strips. They are all 3.0" (76.2mm) long and 0.75" (19.05mm) wide but vary in thickness.

- Type 'N' - 0.031" (0.7874 mm) - for low intensity;
- Type 'A' - 0.051" (1.2954 mm) - for average intensity
- Type 'C' - 0.0938" (2.3825 mm) - for high intensity.

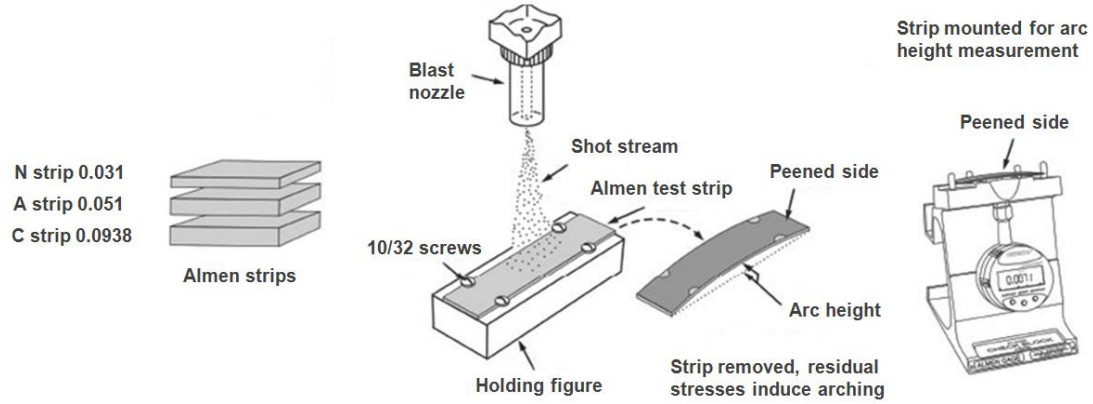

Figure 2.3: The Almen Strip standard. (1) Peening the Almen Strip, (2) removing the Almen Strip and measuring the arc height with a gauge (3) after (Gillespie K. 2009).

SP saturation is defined as the point at which doubling the Almen Strip exposure time results in 10 % or less increase in curvature arc height. It is assumed that the curvature of the Almen Strip will indicate the rate of compressive stress that leads to a resistance to fatigue failure.

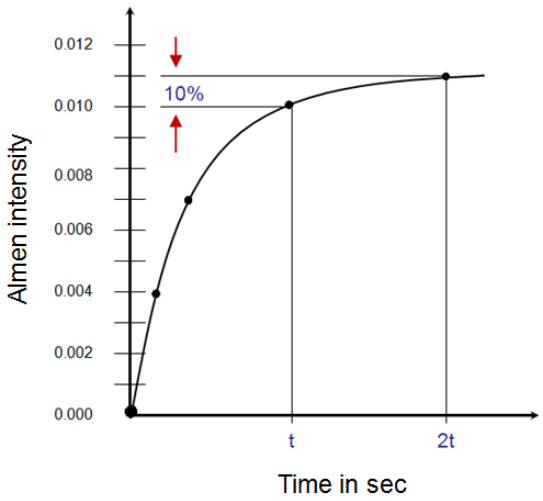

Figure 2.4: Shows the Almen saturation curve as a function of exposure time.

Cao et al. (1995) proposed an approximate model able to relate Almen intensity to shot velocity, however the relationship with the residual stresses in a mechanical part was not dealt with. Many approaches recorded in published research deal with the prediction of residual stresses due to SP but do not relate them with Almen intensity and are therefore of limited practical interest (Watanabe and Hasegawa 1995; Al-Hassani S.T.S. 1981). In contrast, Guagliano (2001) has used the FEM to predict the residual stresses induced by SP in a metal part and related these stresses to Almen intensity. The FE analysis simulates the impact of one or more shots on a plate and makes it possible to determine the residual stress profile of a metal part on the basis of the shot material and diameter (Guagliano, 2001).

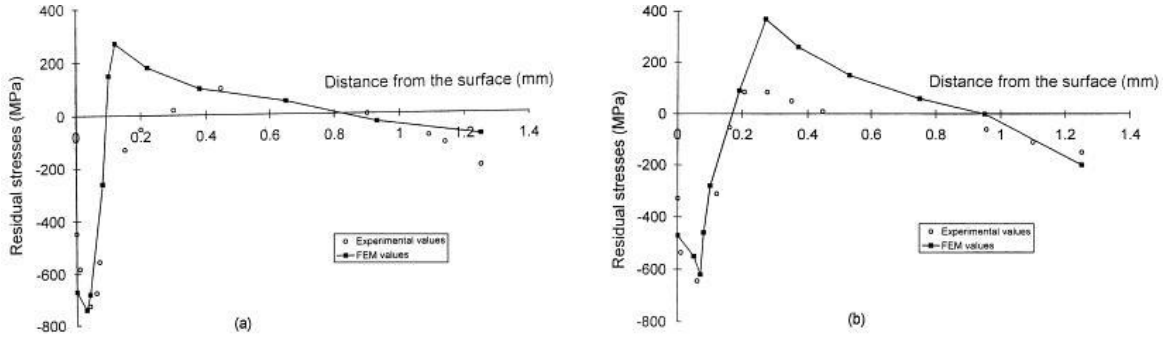

Figure 2.5: Experimental and numerical longitudinal residual stress trends obtained on the Almen Strip: (a) Almen intensity 0.3 mm A, shot diameter 0.3 mm, (b) Almen intensity 0.3 mm A, shot diameter 0.6 mm after (Guagliano, 2001).

In Figure 2.5 the correlation is good for the compressed part of the strip but when the residual stresses change sign and become tensile the numerical values exceed the experimental values. For the measurements below the surface, it is necessary to remove much of the thickness of the strip.

Alternatively, Miao et al. (2010) introduced an analytical model to predict Almen intensity for any combination of peening parameters (shot size, velocity, and peening angle) for steel and ceramic shots. The geometric characteristics of the plastic indentation are calculated assuming a rigid shot impinging upon a rigid perfectly plastic target.

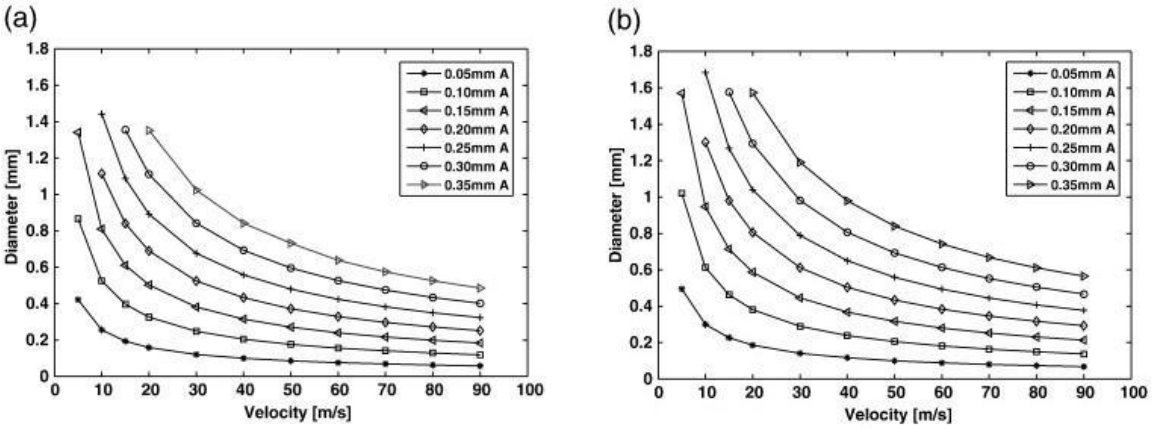

Figure 2.6: Relationship between diameter and velocity for seven different Almen intensities (Almen Type A strip): (a) Steel shot, (b) Ceramic shot after (Miao et al., 2010).

Results from Figure 2.5 were used to establish a relationship between peening parameters and Almen intensity. The trend of the Almen intensity is described by the following equation for steel shots: Eq. 2.1

$$A_{h(steel)}(d_{shot}, V) = 0.06735\, d_{shot} + 0.01184\, d_{shot}V - 0.00002824\, d_{shot}V^2 - 0.00004991\, d_{shot}{}^2V$$

The Coefficient of determination being to $R^2 = 0.998$,

d_{shot} is expressed in mm and V is expressed in m/s.

This equation is only valid for the range of shot diameters and shot velocities represented in Figure 2.6 and should not be used outside this range of validity as it may lead to unrealistic results, especially for small shot diameters.

Residual stress profiles in Almen Strips from normal impacts of steel shots involving three different combinations of shot size and velocity were considered by Guagliano (2001). This revealed that each combination resulted in the same Almen intensity.

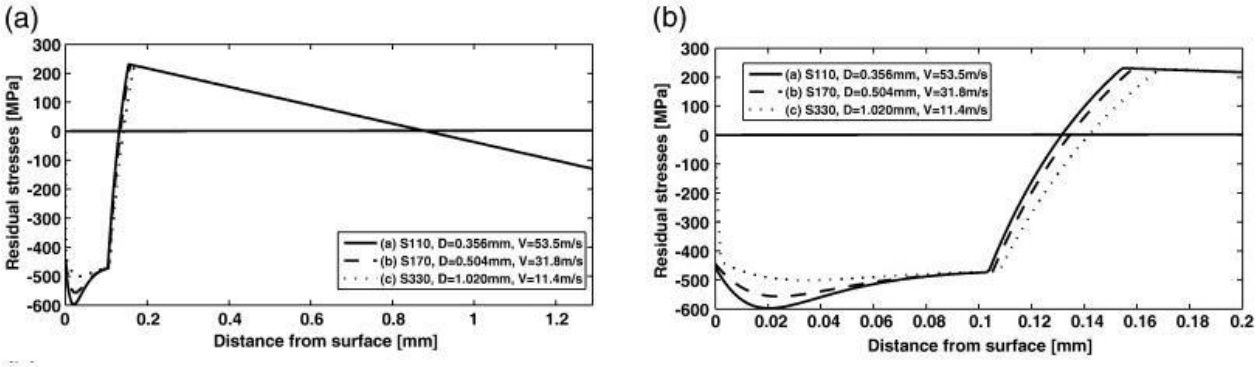

Figure 2.7: Calculated residual stresses for different combinations of peening parameters, with identical Almen intensity (0.2 mm A). (a) Residual stress profiles for three cases following the whole depth (1.29 mm). (b) Residual stress profiles for three cases for three cases on the top surface (0 to 0.2mm) after (Guagliano, 2001).

Figure 2.7 shows that no unique correspondence exists between Almen intensity and residual stress profile. Although the predicted results in the study correlated well with the published experimental results, each residual stress profile corresponds to a different Almen intensity. In contrast, a given Almen intensity can relate to many different residual stress profiles.

A relationship between Almen intensity and residual stress was found in both studies (Guagliano, 2001; Miao et al., 2010) but both studies also concluded that simultaneous change of multiple parameters such as shot diameter and shot velocity may produce the same Almen intensity. In SP, Almen intensity is one of the important control parameters to ensure the repeatability of the SP process. Each combination of shot diameter and shot velocity yields a unique residual stress profile.

Coverage

Coverage is defined as the percentage of a given surface that is deformed by dents or dimples. The coverage is determined by observing the surface using a 10 times magnifying glass or the PEENSCAN process. In the PEENSCAN process fluorescent tracer liquid is applied onto the peening component surface. Once the liquid has dried the peening is performed and the rate of removal of the fluorescent elastic coating is observed. The removal is proportional to the percentage of peening coverage. Finally, a UV light is used to examine the surface coverage and show as light on a dark background the regions where the peening coverage is not sufficient.

Coverage $c(t)$ at exposure time t is determined by dividing the area covered by impact dimples by the total area of the specimen and is generally expressed as a percentage (SAE Standard J2277, 2009). Firgure 2.8 shows the definition of coverage. Coverage beyond 100 % is referred to as full coverage or multiples of time to achieve 100 % coverage. Thus, 200 % coverage requires twice the time to achieve the full coverage. In practice, full coverage is slightly less (98 %) than 100 %. The reason for this is that coverage percentages are difficult to be distinguished as 100 % coverage is approached. The time to achieve the desired coverage percentage depends on shot media size, peening intensity and media flow rate. The peening intensity is influenced by the shot size and velocity. Media hardness will only have a minor effect on the overall coverage. This is because the media hardness relative to the

component material hardness, for a given velocity, determines how much energy is transferred into making the dimple and how much energy is transferred into deforming the shot media. The media flow determines the rate of media coming out of the nozzle and directly relates to the rate at which coverage is achieved. The percentage of area, C, which has been covered by the impressions can be calculated very simply using the Avrami equation (Kirk and Abyaneh 1993):

Eq. 2.2

$$C(t) = 100\left\{1 - \exp\left(-\frac{3r^2\dot{m}t}{4A\bar{r}^3p}\right)\right\}$$

$C(t)$ is the coverage at any particular time
$\dot{m}$ is the mass flow rate of shots
r is the average radius of the indentations
p is the density of the shot
A is the area of shot spread
t is the time during which the indentations were being created
$\bar{r}$ is the average radius of the shots

This equation makes the assumption that each shot generates the same size dimple and that the shot particles arrive at the surface in a random manner, but at a rate which is uniform over a significant period of time. However, in practice, it is known that the size of impressions will vary due to limited shot size variation, shot velocity, impact angle and peened material properties and is not suited for measuring coverage.

Holdgate (1993) extended the existing model to describe the development of coverage from a general peening system involving multiple peen sources. The proposed model describes the overall coverage $C(t)$ for reference area A and peening time t.

Thus the overall coverage after the interval δt is approximately given by:

Eq. 2.3

$$C(t+\delta t) = 1 - [1 - C(t)]\prod_{j=1}^{n_s}\left[1 - \frac{a_j}{A}\right]^{\delta N_i}$$

n_s is the number of peen sources, a_j is the total surface area of indentation caused by the shots from the jth peen source at time δt. δN_i is the number of peens from the jth peen source to impact the reference area in an interval of time δt.

The application of the Holdgate model requires the determination of the coverage ratio after an initial interval of the Shot Peening. This ratio is obtained from experimental measurements. Results show that the coverage predictions by the Holdgate model are accurate (Holdgate, 1993).

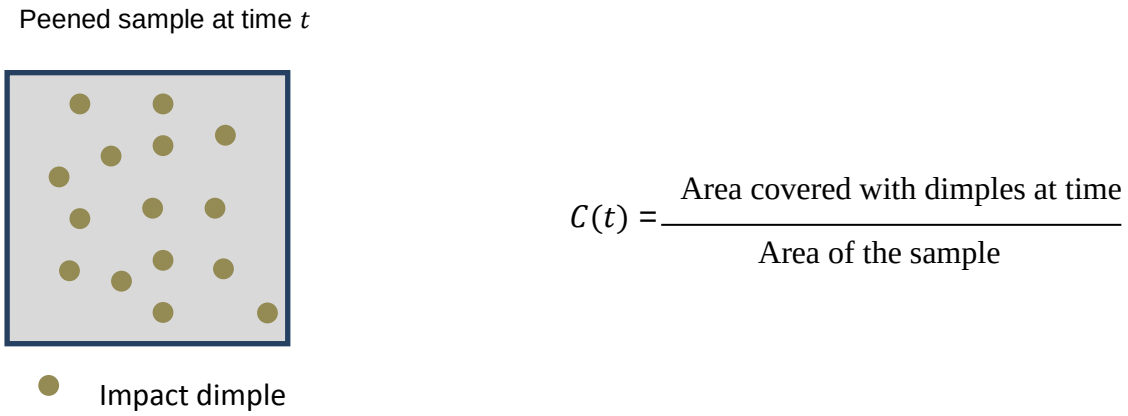

Figure 2.8: Definition of coverage.

Practitioners have used alternative methods such as circular disks to monitor the peening intensity interactively. The Almen Round was developed in 1994 by Rudolf Bosshard in Switzerland (Sharma et al., 2002). The Almen Round is a circular cutting (diameter of 18.7 mm) from an original Almen Strip of material SAE1070. It can either be of type "A", "C" or "N" and in various quality grades. When the Almen Round is shot peened, it bends in the direction of peening and a processing unit converts the linear transformation into an electric signal. The advantage of the Almen Round is that it is designed for the direct exposure and enables to monitor the Almen standard arc high during the peening process (Kirk 2012). Since the Almen Round is a simple shape and small in size, it is more suitable for automated processing and some complex geometries.

However, one difficulty of the spring/disk approach is that the Almen Strip material is different, often substantially, from the work piece materials. Therefore, the dimpling behaviour of the work piece will be significantly different from the behaviour of the Almen Strip as a result of differences in material properties. It is conceivable that in some materials, the plastic zone will be substantially smaller. This leads to the question: How can one determine whether saturation in a work piece is achieved without making an Almen Strip out of the same work piece material?

2.1.4 Peen forming

Peen forming is a process derived from Shot Peening and is a method that is widely used in the aeronautic industry. Popular applications are the production of thin components such as wing skins that involve complex shapes and double curvatures. Shot peen forming is very cost-effective compared to conventional forming techniques, as it does not require a set of dies for each target shape. In addition, the application is more flexible as it allows manufacturers to achieve various contours by altering the treatment parameters and the application region. The application of peen forming is explained as illustrated in Figure 2.10. The stress factor of a peening component that is fully restrained during the peening process such that it cannot move or bend during the SP process is defined as induced stress $\sigma^{induced}$. The forces F_{con} and moments M_{con} from the induced stress can be obtained from the induced stress profile and are defined as:

Eq. 2.4

$$M_{con} = \int_0^h \sigma^{induced}(z)\left(z - \frac{h}{2}\right) dz$$

Eq. 2.5

$$F_{con} = \int_0^h \sigma^{induced}(z)\, dz$$

F_{con} and M_{con} are calculated per unit width of the strip, where h is the thickness (Guagliano and Vergani 2001). During the peening process the generation of induced stress results in the component being modified plastically, however the response of the component following the release of the constraints is usually elastic (Homer and VanLuchene 1991). This allows one to use the superposition principle to calculate the stress profiles $\sigma_{axial}(z)$ and $\sigma_{bend}(z)$ associated with elongation and bending of the component, respectively (Guagliano and Vergani 2001):

Eq. 2.6

$$\sigma_{axial}(z) = -\frac{F_{con}}{h}$$

Eq. 2.7

$$\sigma_{bend}(z) = -\frac{12M_{con}\left(z-\frac{h}{2}\right)}{h^3}$$

and the residual stress $\sigma^{residual}(z)$ is determined as:

Eq. 2.8

$$\sigma^{residual}(z) = \sigma^{induced}(z) + \sigma_{axial}(z) + \sigma_{bend}(z)$$

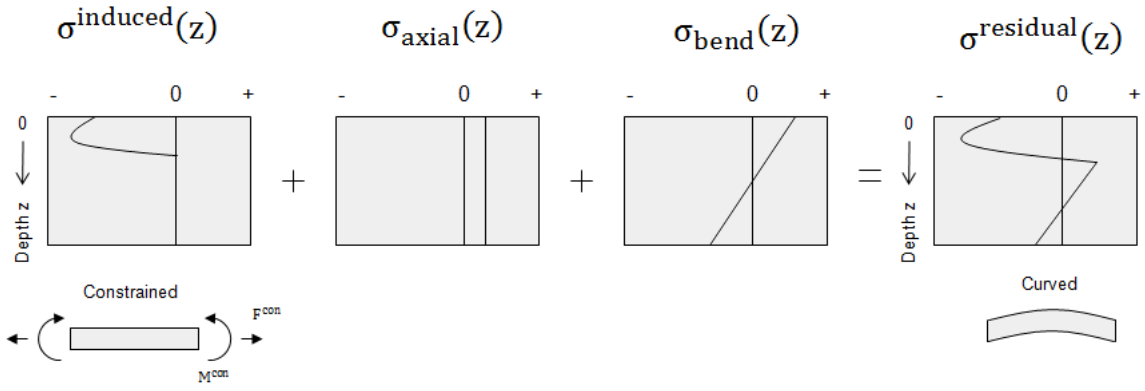

Figure 2.9: Relationship between induced stress $\boldsymbol{\sigma^{induced}}$ and residual stress $\boldsymbol{\sigma^{residual}}$ profiles.

If we assume that defections after the peening process remains small and assuming that the Shot Peening is isotropic, the component material introduces an equibiaxial stress field, a

curvature $\frac{1}{R}$ of the component, where R is the radius of curvature, and in-plane elongation ε_e. $\frac{1}{R}$ and ε_e can be calculated as:

Eq. 2.9

$$\frac{1}{R} = -\frac{12(1-v)M_{con}}{Eh^3}$$

Eq. 2.10

$$\varepsilon_e = -\frac{(1-v)F_{con}}{Eh}$$

where v is the Poisson's ratio and E is the Young's elastic modulus.

When Shot Peen forming is performed at very high intensities, the plastic strains are presented in the whole cross-section and are more intense towards at the surface opposite to the impacted side (Kopp and Schulz 2002). This results in a concave forming such that the component bends away from the shot stream. Concave forming results in larger elongations than convex peen forming.

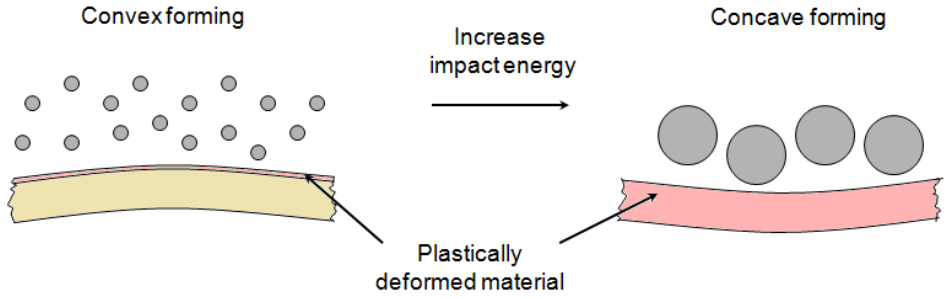

Figure 2.10: Difference between convex and concave forming.

2.1.5 Other peening methods

There are other types of surface treatments that produce comparable residual stress states to that observed by Shot Peening. Some include Laser Shock Peening, Deep Rolling, Ultrasonic Impact Treatment and Low Plasticity Burnishing. These are briefly described in the following sections.

Laser shock peening

Laser Peening, or Laser Shock Peening (LSP), is a metalworking process in which pulses from a powerful laser are directed onto the surface of the metal component surface to enhance its mechanical properties. The magnitude of the residual compressive stress arising from LSP can be four times higher than that achievable from conventional Shot Peening treatments. Prior to treatment, the component is prepared by applying two overlays, one opaque to the laser and one transparent to the laser. The laser is then passed through the transparent overlay, striking the second opaque layer. At this point, the engery vaporises and becomes trapped between the transparent overlay and the surface of the component. The pressure increases and causes a shock wave to propagate into the material. The beam is then repositioned and repeated, often as many as four times, until the desired compression level is reached. An average compressive layer as deep as 1 - 2 mm may be produced. Figure 2.11 illustrates the laser shock peening treatment.

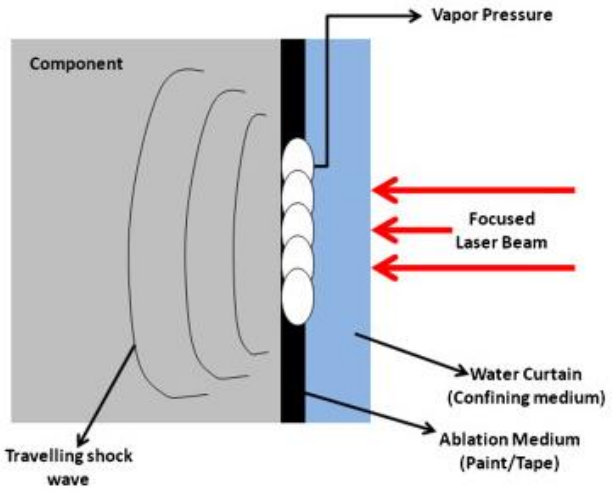

Figure 2.11: Illustration of the Laser Shock Peening treatment after (Zhao et al., 2010).

Deep Rolling

Deep Rolling is a method whereby the surface of the component material is plastically deformed by a spherical rolling element under controlled pressure (Altenberger et al., 1999). This technique is relatively inexpensive compared to other alternative methods and produces

a very smooth component surface finish. However, the application is restricted to certain component geometries.

Ultrasonic Impact Treatment

Ultrasonic Impact Treatment (UIT) is a technique, in which ultrasonic energy is applied to metal component through the contact of specially designed steel pins to control residual compressive stress, grain refinement and grain size reduction. When the ultrasonic transducer, pins and other components come into contact with the component it acoustically couples with the work piece creating mechanical impulses imparting compressive residual stresses and improving the grain structure. These frequencies range between 25 and 55 kHz (Fisher et al., 2001), with the displacement amplitude of the resonant body of between 22 and 50 μm (0.00087 and 0.0020 in).

Low Plasticity Burnishing

Low Plasticity Burnishing (LPB) is a very similar treatment to deep rolling, except that it has been optimised to minimise the plastic work generated in the material during the process. The cold work produced from LPB is typically minimal and much less than that of Shot Peening, Laser Shock Peening, or Deep Rolling. The residual stress state is induced by the deformation caused by the burnishing of the surface by a hydraulically floated ball, which is pressed and rolled freely along the surface, plastically deforming the surface material. The stress distribution created is more similar to that of LSP than Shot Peening. Figure 2.12 illustrates the LPB process.

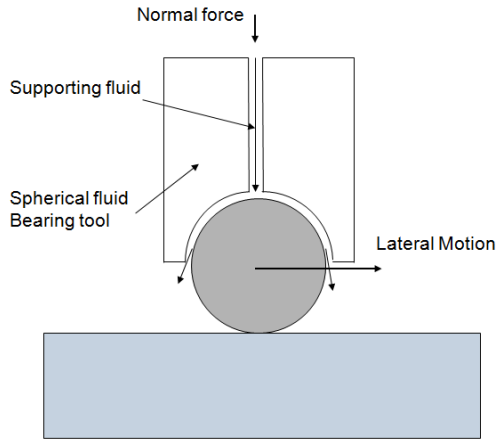

Figure 2.12: Process of Low Plasticity Burnishing (LPB).

2.1.6 Residual stress measurement techniques

Residual stresses remain within the material after manufacturing and material processing and can be defined as either macro or micro stresses and can be classified into three different types.

Type I: Macro residual stresses are on a scale larger than the grain size of the material and are assumed to be continuous from grain to grain. Type I stresses are defined as macro stresses σ^{I}.

Type II: Micro residual stresses are discontinuous between neighbouring grains and vary on the scale of an individual grain. Type II stresses are defined as micro stresses σ^{II}.

Type III: Micro residual stresses exist within a single grain and are inhomogeneous across the grain. These can vary due to sub-grain formation and crystal defects such as dislocations and vacancies, and are also of a shorter length scale than the grain size. Type III stresses are defined as micro stresses σ^{III}.

Various techniques for measuring different types of residual stresses in components have been developed. They can be classified in three categories, destructive, semi-destructive or non-destructive as shown in Figure 2.13.

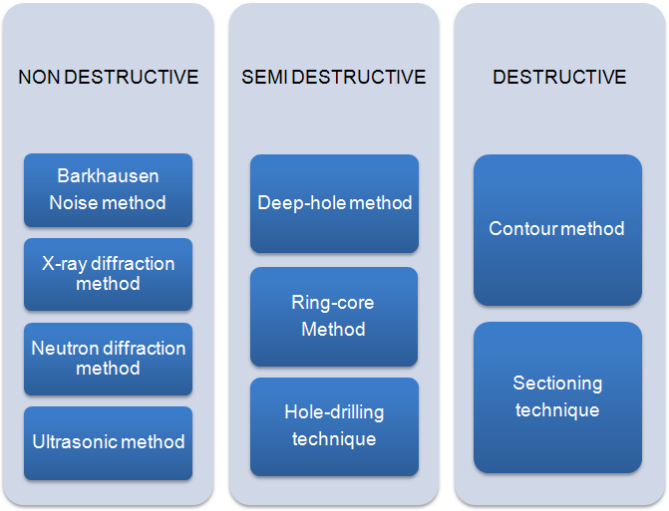

Figure 2.13: Methods to measure residual stresses.

The non-destructive residual stress measurements preserve the specimen and are useful for production quality control in valuable components. However, most of these methods require detailed calibration of the specimen material data. Compared to non-destructive method, the destructive and semi-destructive residual stress measurement methods only measure basic quantities such as displacements or strains and do not require much calibration, therefore these are applicable to a wide range of applications. Barkhausen noise and Ultrasonic are fast, and low cost methods but only provide a low resolution. X-ray diffraction techniques can be used to assess both macro and micro residual stresses, but are lab based methods and can be applied to small components only.

Neutron diffraction has an optimal resolution over the all the non-destructive measurement techniques but it requires expensive equipment. Hole and deep hole drilling methods are semi destructive methods but are easy and fast and can be applied to wide range of materials. However these are limited in strain resolution capabilities.

Hole-drilling method

The hole-drilling method is one of the most popular semi destructive methods to evaluate residual stresses. It is widely accepted as a standardised method with convenient pratical

application. The method involves the drilling of a small hole that is about 1.8 mm in diameter at the component surface location where residual stresses are to be measured. Strain gauges are attached around the hole, which measure the strain of the surface that is relieved during the drilling of the hole. The residual stresses are then calculated from the strains measured around the hole. Usually, the damage caused to the component is localized to the small hole and is often acceptable or repairable allowing the component to be used for further processing.

The ring-core method is a variation of the hole-drilling method and is an inside-out method where an annular shot is cut into the material and the deformation of the central area is measured (Milbradt, 1951; Kiel, 1992). Similar to the hole-drilling method, it has straightforward procedures to evaluate in-plane stresses (Kiel, 1992), and provides much larger surface strains (Ajovalasit et al., 1996). The disadvantages of the method is that it creates much larger specimen damage and is less convenient to apply in practice and is therefore less frequently used.

In general the hole-drilling method is applicable to all groups of materials. However, to effectively measure the residual stresses, the analysed materials should be machineable, i.e. the drilling of the hole should not alter the measured strain. Furthermore the materials should be isotropic and the elastic parameters of the material should be known.

As with many other measurement methods, the local resolution and quality of the method is thoroughly dependent on the measurement equipment used. A comparison of the most common residual stress measurement techniques including their advantages, disadvantages and limitation can be found in Table 2.1.

Table 2.1: Comparison of residual stress measurement techniques after (Rossini et al., 2012).

Technique	Advantage	Disadvantage
X-ray diffraction	Generally available Wide range of materials Hand-held systems Macro and Micro RS	Lab-based systems Small components Only basic measurements
Hole Drilling	Fast Easy use Generally available Hand-held Wide range of materials	Interpretation of data Semi destructive Limited strain sensitivity and resolution
Neutron Diffraction	Macro &Micro RS Optimal penetration & resolution 3D maps	Only specialist facility Lab-based system
Barkhausen Noise	Very quick Wide sensitive to Microstructure effects especially in welds Hand-held	Only ferromagnetic materials Need to divide the microstructure signal from that due to stress
Ultrasonic	Wide range of material Economy & speed Hand-held	Destructive Interpretation of data Limited strain resolution
Sectioning	Wide range of material Economy & speed Hand-held	Destructive Interpretation of data Limited strain resolution
Contour	Deep interior stresses measurement Thick section components Wide range of material	Interpretation of data Semi destructive Limited strain sensitivity and resolution
Synchrotron	Improved penetration & resolution of X-rays Depth profiling Fast Macro and micro RS	Only specialist facility Lab-based systems

2.1.7 Causes of the effect of Shot Peening

Shot Peening produces changes in the microstructure, residual stresses and topography of the work piece material. Some of these changes are beneficial, whereas others are potentially detrimental and could diminish the fatigue life of the work piece. The lack of a clear definition for Shot Peening intensity makes it difficult to isolate the critical factors and contributing factors of the process. Although, this thesis focuses on numerical modelling for Shot Peening process optimisation, it does not go far enough to study the effect of fatigue life of peened components; some potentially critical factors are listed in the sections below.

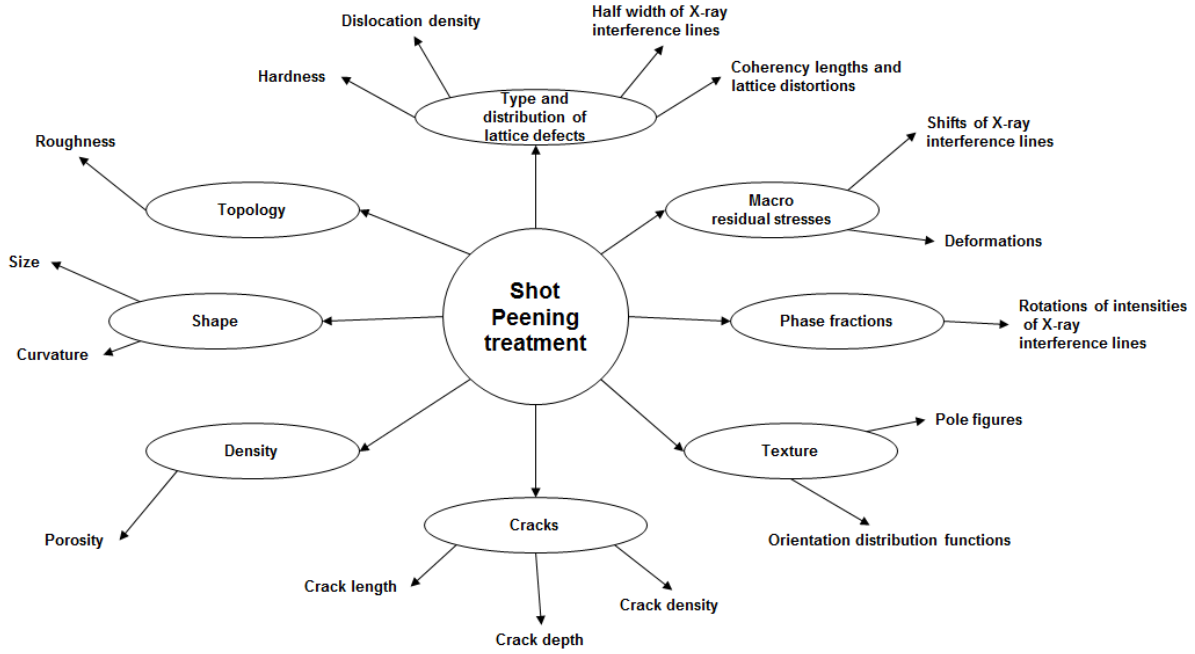

Figure 2.14: Causes of the effect of Shot Peening after (Schulze, 2002).

Fatigue and propagation of cracks

The fatigue process can be separated into four phases.

1. Work hardening or work softening
2. Crack nucleation
3. Crack propagation
4. Failure

Shot Peening plastically deforms the surface layer. Although the grade of saturation depends on peening intensity and coverage, the plastic deformation involves generation of dislocations. Cyclic plastic deformation generates features such as persistent slip bands, which are favourable crack nucleation sites. Other favourable crack initiations are grain boundaries and inclusions (Lukáš˘, 1996).

The failure of metal components can be the result of repeated cyclic plastic (or micro-plastic) deformations and the mechanisms of plastic deformation during cyclic loading correlates with the microstructures, thereby shaping the mechanisms of failure (Christ and Mughrabi. 1992). The propagation of fatigue crack occurs whenever work hardening in the

surface layer reaches a critical value. Komotori and Shimizu (1992) observe that the fatigue life in the extremely low cycle fatigue regime is primarily controlled by the mechanisms of work hardening and increase of internal micro-voids. In the study, all specimens were peened to Almen saturation condition. However, some specimens were allowed additional peening time: these showed improved fatigue strength over those peened to saturation, which they speculated was due to a more uniform stress distribution. Like Wagner and Luetjering (1981), they also noted that excessive peening can cause the fatigue strengths of some materials to decrease. The Shot Peening process induces changes in the surface layer of the work piece material. These can be generally grouped into three categories - microstructure, residual stresses and topology.

Micro structural plastic deformation and slip band development

The effect of Shot Peening varies depending on the microstructure of the material. The microstructure is changed during the peening process. Altenberger et al. (2001) studied the crack formation of polished and of surface treated (shot peened a deep rolled) samples of austenitic stainless steel AISI 304. They discovered a distinct difference in damage mechanism depending on the surface state. Polished surface states exhibited crack formation preferentially at sites of extensive multiple planar slip, and cracks in mechanically surface treated states were mostly formed in a brittle manner without observable surface slip. They also concluded that in shot peened specimens, regions not covered by the Shot Peening process exhibited slip line formation similar to non-peened polished specimen. These locations were preferential locations for crack stress fields and in early crack propagation.

Several Authors Al-Hassani (1982), Burck et al. (1970), Timothy and Hutchings (1981), have characterized plastic deformation developed by repeated impacts using etching to reveal slip band formation.

Timothy and Hutchings (1981) conducted ballistic studies using small particles ranging from 0.25 inches to 0.0313 inches (medium ccw31 shot size) and velocities ranging from 1,970 to 13,400 in/s. At these conditions, they observed permanent indentations, however optical metallography showed that plastic deformation beneath the craters was not homogeneous at high velocities. Adiabatic shear bands were formed for impact conditions corresponding to shot diameter ratios of about 0.57 to 0.65. They concluded that this occurs due to some critical value of strain and ruled out impact velocity, impact kinetic energy and strain rate as alternative criteria.

Sub-grain size changes.

Ru et al. (1996) investigated the residual stresses, microstructure and density of HIP René 95 powder superalloy due to Shot Peening. They reported that sub-grain sizes decrease in René 95 due to Shot Peening, from 7.0 μin (0.179 μm) to 0.6 μin (0.015 μm. Furthermore, they did not grow substantially with heating to 1200 °F (650 °C). Tange and Okada (2002) carried out experiments using SUS631 and SUS304 steel. They adjusted the grain diameter by changing the bright annealing temperature after cold working and concluded that fatigue strength increases in proportion with decreasing grain diameter.

Topography and surface roughness effects

Shot Peening changes the surface finish and the surface topology. Schulze (2002) has shown that Shot Peening causes multiple changes in the state of the material close to the surface of components. Holzapfel et al. (1998) demonstrated that increasing size and hardness of the shot also cause higher values of surface roughness. Even when the values of shot hardness were lower than that of the work piece, distinct effects on topography were found. They found that at high mass flow rates and peening pressures, especially at ductile materials states, the roughness may decrease due to effects of mutual impacts of shots in the nozzle.

The impact of shots at high velocity produces indentations on the surface of the treated material, which results in an increased surface roughness. A higher surface roughness presents more irregularities, acting as a stress concentration and can reduce the fatigue life of the component (Sharp et al., 1994). In practice, surface roughness parameters are assessed with electronic contact (stylus) instrument. The measurement results depend strongly on the selections of the scanning length and the limit wavelength (Clausen and Stangenberg 1999).

Erosion

Several Authors (Jain et al. 2002; Iain et al. 1967; Misra and Finnie 1981) studied the effect of erosion caused by Shot Peening. They agree that the erosion of ductile materials depends strongly on the plastic deformation of the target caused by the impact of the particles. Jain et al. (2002) observed the positive effect of Shot Peening on erosion resistance of the magnesium alloy AZ80. Experiments were performed on an erosion testing machine: on average, a 33 to 45 % reduction in erosion was found in shot peened as compared to non-peened specimens.

Hutchings et al. (1976) performed experimental studies to study the factors controlling an important erosion situation arising from the removal of surface material by spherical projectiles. They projected steel spheres obliquely onto mild steel target and studied the energy balance in the impact process using high-speed photography. They proposed a model that predicts the indentation formation, volume of material displaced and the energy lost by a single impacting sphere. They concluded that the target metal becomes detached along a band of intense subsurface shear and illustrated that this could be due to the production of local high temperatures.

Erosion studies by Finnie et al. (1992) showed that for ductile materials, erosion was minimized for incidence angles approaching 90°, and maximized at acute incidence angles

around 10 to 30 degrees. A change in erosion behaviour corresponding to particle size has been observed for brittle materials, and the maximum erosion was observed to occur at 90°. Misra and Finnie (1981) investigated the wear process in erosion and both two- and three-body abrasion of ductile metals. They observed that the wear process becomes less efficient as the eroding or abrading particle sizes decrease below about 100 μm and concluded that the higher yield strength of shallow surface layers was responsible for the reduction in erosion.

Component life behaviour

Empirical observations of component life behaviour have been observed for shot peened specimens compared with unpeened specimens. Jain et al. (2002) investigated the fatigue of magnesium alloy AZ80. The improvement in fatigue life of AZ80 was found to be more than 70 times due to Shot Peening with 1 mm cast steel at an intensity of 0.28 mm at 200 % coverage.

Hammond and Meguid (1990) investigated effects of peening and re-peening upon the fatigue fracture behaviour of metallic components in the presence of Shot Peening residual stresses. They performed rotating bending fatigue tests for both the steel and aluminium specimens. The specimen were first peened and then partially fatigued to a "known" proportion of their anticipated fatigue life. A number of these specimens were then re-peened and tested to ultimate fracture. The test revealed that fatigue life improvement for both the steel and aluminium specimens over unpeened specimens. However, when specimens were re-peened, after being partially fatigued, only the steel specimens showed further life enhancement. Koster et al. (1981) showed that many machining processes degrade the fatigue life capability, and that Shot Peening is often used to restore lost fatigue capability.

2.2 Shot Peening modelling

2.2.1 Single and multiple shot impact

Modelling the SP process is very complex and involves the dynamic analysis of very fast moving shots bombarding geometrically complex metallic surfaces. SP parameters need to be controlled in order to produce the optimal CRS profile in the peening component. The peening parameters are categorized into three groups that are associated with peening media properties, the target properties and the process.

1. Media: size, shape, density, hardness.
2. Target: geometry, material properties such as initial yield stress, work hardening characteristics, hardness, strain-rate.
3. Process parameters: nozzle diameter, mass flow rate, air pressure, angle of attack, distance between nozzle and target surface, peening time.

A quantitative relationship between the peening parameters and residual stress characteristics need to be established in order to control the residual stress distribution more effectively. Modelling the complete SP process and measuring the residual stress profile within the peening component is very time consuming and expensive. Moreover, it does not allow the dynamic examination of the effect of the parameters.

The FEM is primarily used for the evaluation of the CRS and can accommodate features such as strain rate variations, impact friction and complex material properties. The first FEM analyses of SP were undertaken by Edberg et al. (1995). However, they only simulated a single shot impacting visco-plastic and elasto-plastic materials. Subsequently, Al-Hassani et al. (1999) studied single and multiple shot impacts on a target and examined single shots impacting with an incident angle but provided very limited results. Deslaef et al. (2000) presented a FE simulation of single and multiple shots impacting a target and examined the effect of rigid and deformable shots. The numerical results were compared with

experimental measurements obtained for multiple shots impacts and showed significant differences. Meguid et al. (1999) conducted a dynamic FE analysis of single and multiple shot impacts, but did not model the shot stream and shot - shot interaction and are therefore of limited interest.

SP in industrial applications involves more than 10^6 shots and the FEM cannot model the stream of that many shots impacting on the target component and the shot - shot interaction of rebounding shots. Most FEM studies (Al-Hassani et al. 1999; Guagliano and Vergani 2001; Rouquette and Rouhaud 2005; Meguid et al. 1999) do not include multiple shot impacts and do not simulate the stream of discrete shots impacting on the target and, as such, are of limited use. In these cases, the numbers of shots used in the simulations were very low and, rather than predicting the pattern of shots impacting the surface, they specified the pattern of shots impact and did not consider the incoming and rebounding shots. The shot - shot interaction has an effect on the overall peening quality. Experimental studies have used specific targets and, as a result, it is not easy to relate the effect of each parameter to the resulting residual stress distribution. A few attempts have been made to simulate large numbers of impacts using FEM. An explicit dynamic algorithm for modelling up to 1000 impacts was described by Wang et al. (2006) who demonstrated that the FEM is able to investigate the macroscopic effects (e.g. curvature) of SP as well as the microscopic effects (e.g. local plasticity and residual stresses). The study, however, did not include any shot - shot interaction. Kim et al.(2012) averaged the computed results over the representative area that the CRS are experimentally measured. They created three-dimensional finite volumes with symmetry boundary conditions which were impacted by 4 spherical shots each placed at the corner of the target volume. They repeated the impact sequence for 3 cycles and computed the RS after each cycle. Comparison with experimental results was very promising and validated the importance of averaging the computed RS over the representative area.

Klemenz et al. (2005) simulated the impact of 121 rigid shots onto a steel target material. The main focus was on the surface topography and surface RS after a single and two shot impacts. The results correlated well. In the study, shots were assigned the same velocity and no shot - shot interaction was considered.

H Y. Miao et al. (2009) simulated the impact of rigid shots onto an aluminium target plate using LS-Dyna. 6, 12, 24, 48 and 96 shots were randomly generated within an area of 1.5 by 1.5 mm. The computed RS was then averaged over a reference area of 1 mm^2. Only normal impact and impact at 60° angle were considered in the study. (Gariépy, 2012) simulated the peening of an Almen-sized AA-2024 aluminium strip in an Almen holder using two different shot velocities in Abaqus. High-speed images were taken to determine the actual shot stream definition. This would imply that experimental trials must be carried out priorto modelling the SP process. In this study only 48 impacts were simulated, but comparison with experimental saturation results showed promising agreement for three sets of peening parameters. The authors also proposed a new shell-based finite element model to investigate sequence-sensitive aspects of the forming process. A numerical method that handles numerous particle interactions needs to be applied to solve the shot stream problem.

The effect of Shot Peening parameters with FE analysis

Since the performance of any SP process depends on many controlling parameters, it is very difficult to identify the effect of each individual parameter when combined together. Deslaef et al. (2000) were one of the first to investigate multiple parameters using the commercial ABAQUS FEM software. They concluded that increasing the diameter of the shot would only increase the depth of the CRS and that increasing the velocity results in a larger magnitude of CRS. This finding was confirmed by Guagliano and Vergani (2001). However, with increasing shot velocity the surface residual stress $\sigma^{surface}$ decreases. Deslaef et al. (2000) studied various SP parameters, including the shot size and velocity both theoretically and

empirically. Their results showed that the residual stress field reached a saturated state after a limited number of impacts. For the case of normal Shot Peening, the process reaches saturation and full coverage after approximately 48 impacts. Peening was performed on a target area 2 mm × 2 mm × 1 mm with shot size d_{shot} = 0.5 mm and shot velocity V_i= 50 m/s. However, their model did not include the shot interaction. Majzoobi et al. (2005) studied the effect of velocity and peening coverage on CRS profiles and concluded that the residual stress distribution was highly dependent on impact velocity. Additionally, Rouquette and Rouhaud (2005) developed a thermo-elastic-plastic model to calculate the temperature during the peening process. In all these studies, the CRS provides an average rate of the multiple shots since all shots are not modelled as individual shots.

FEM analysis may also be dependent on the choice of the element type and the mesh size. In particular, it has been shown that linear elements can produce inaccurate results and cubic elements can increase the simulation time to a large degree. To reduce the simulation time, assumptions are made during the mesh generation and symmetry is used to simplify calculations.

FEM / DEM combined analysis

The discrete element method (DEM) was developed by Cundall and Strack (1979) and is an explicit numerical method used to model the dynamic behaviour of distinct objects. It uses Newton's laws to predict the position, velocity and acceleration of the objects. Various contact laws have been developed to effectively predict forces and simulate objects. Lately, combined DEM - FEM methods have been implemented. In this approach, the surface geometry metrics were exported to DEM where the contact forces or pressure distribution is obtained and applied onto FEM mesh to get the CRS. According to the records, Han et al. (2000a) were one of the first ones publish a study of combined finite and discrete element methods to simulate the SP process. Using two-dimensional analyses, they modelled the

sphere as a rigid circle and studied different interaction laws for the shot - target interactions. They investigated the linear, Hertz, Winkler and power laws including damping. Later, they extended the model to three dimensions (Han et al., 2000). In this 3D study, they simulated multiple shots using a few shots where the target was repeatedly impacted by a set of regular aligned shots and no stream of shots was modelled. However, like other studies, Han et al. (2000) did not consider incoming and rebounding shots.

Hong et al.(2005) used the DEM to determine the effect of mass flow rate, shot initial velocity and angle of incidence of the energy loss of the target surface. In this approach the coefficient of restitution (CoR) for shot - shot and shot - target was evaluated using ABAQUS Explicit software. As the target material is strain - hardening, subsequent impacts at the same location are likely to hit a harder surface than the previous ones. In terms of shot - target interaction, the CoR varies substantially depending on whether the treatment surface has been previously hit. Hong et al. (2005) did not include this feature in their simulation.

In a recent study, Bhuvaraghan et al. (2008) modelled a combined DEM - FEM simulation that used FEM analysis to get the residual stresses from contact pressures, calculated from the contact forces obtained from DEM. Their DEM simulation incorporated the simulation of the shot stream and the shot - shot and rebounding shot interactions. Bhuvaraghan et al. (2008) concluded that to have 100% coverage when the shots are delivered from the nozzle on a random basis it is necessary to have 3 - 4 times the number of shots that will be required when they are positioned in an orderly manner. On average each point of the surface is likely to be hit 3-4 times. To take account of strain hardening in the calculations, a FEM analysis with multiple impacts at the same location was performed and the average CoR was evaluated. The average CoR was found to be 0.57 and used throughout the simulation for the shot - target interaction. The rebounding angle was based on the un-deformed target surface and the effect of surface variation due to previous impacts was

ignored in this study.

2.3 Summary

From the literature review it can be concluded that there are number of limitations within the exiting studies;

1. In many of existing FE models, the SP sequence and location were defined a priori according to a pattern.
2. Most investigations relating to intensity and coverage are based on theory, with limited experimental validation and cannot be applied on a larger scale.
3. The Almen intensity is defined by Almen Strips made of steel which may be different from the peening component. It is impossible to establish a direct relationship between the development of the coverage on Almen Strips and any given material.
4. Many SP models are based on single shot analysis and pseudo-multi impacts and do not include the shot stream and shot interaction. The shot - shot interaction has an influence on the overall peening quality. For a true multi-impact environment more advanced techniques have to be used in order to better simulate a real SP process.
5. Existing studies investigated the peening of flat surfaces. None of the reviewed articles investigated complex geometries such as geometries with curvature and edges.
6. Most peening systems have dynamic nozzles that will be in motion during the peening process. The shot stream of a static nozzle will be significantly different from that of a dynamic nozzle that is in motion. This will have an effect on the intensity, coverage and the overall peening quality.
7. To the best of the author’s knowledge, at the time of writing there is no one complete numerical solution for SP optimisation.

CHAPTER 3 THE NUMERICAL MODEL

This chapter describes the proposed numerical modelling in DEM and FEM. It attempts to demonstrate the capabiltites of existing commercially available tools to improve the understanding of the Shot Peening process and improve modelling capabilities, as well as outline the limitations of such an approach.

3.1 Discrete element modelling of shot stream

3.1.1 Discrete Element Method

The DEM is a numerical method capable of describing the mechanical behaviour of assemblies of rigid elements.The method records the motion of each single particle and its interaction with other particles and surfaces using Newton's laws of motion. The state of the system is updated incrementally. In every cycle or time step particle accelerations, velocities and positions are calculated. Contact mechanics laws relate the inter-particle elastic force with the particle deformation through the physical and geometrical properties of the particles. An extra force, called the damping force, is added to the contact force in order to take account for the loss of kinetic energy observed experimentally when a particle collides against another particle or a target. Once all the forces in the system are calculated a new cycle of calculations starts and the whole process is repeated. Figure 3.1 shows the Discrete Element Method cycle.

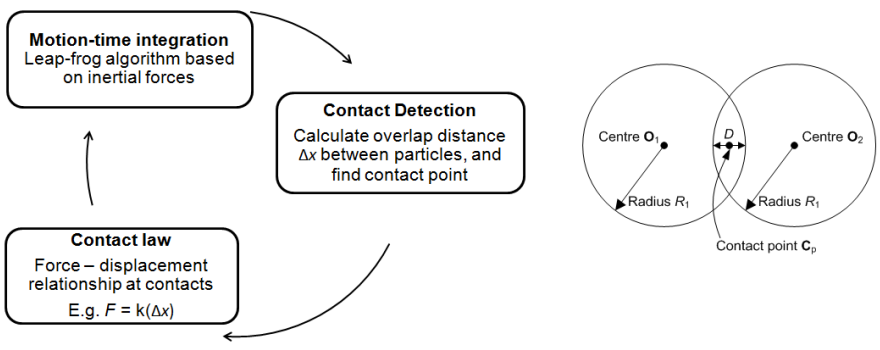

Figure 3.1: The Discrete Element Method cycle.

3.1.2 Contact law

The Hertz-Mindlin contact law will be used to model the shot to shot interaction and the shot to treatment surface interaction. The model is based on the work of (Mindlin, 1949).

Normal direction of impact

In the normal direction, if shots and the treatment surface are assumed to be elastic, the exact analytical solution for the pressure and therefore the force upon the contact is given by the Hertz law (Johnson, 1985). According to this law the normal force-displacement (N - δ) relationship is non-linear. Considering a collision between 2 particles with elastic modulus E, Poisson's ratio ν and radii *R1* and *R2*

Eq. 3.1

$$F_n = \frac{4}{3} E^* \sqrt{R^*} \delta_n^{\frac{3}{2}}$$

where the equivalent Young's Modulus E^*, the equivalent radius R^* are defined as

Eq. 3.2

$$\frac{1}{E^*} = \frac{(1 - v_i^2)}{E_i} + \frac{(1 - v_j^2)}{E_j}$$

Eq. 3.3

$$\frac{1}{R^*} = \frac{1}{R_i} + \frac{1}{R_j}$$

With $E_{i,} v_i, R_i$ and $E_{j,} v_j, R_j$ being the Young's Modulus, Poisson ratio and radius of each sphere in contact. Additionally there is a damping force, F_n^d, given by

Eq. 3.4

$$F_n^d = -2\sqrt{\frac{5}{6}} \beta \sqrt{K_n m^*} V_n^{\overrightarrow{rel}}$$

where $m^* = \left(\frac{1}{m_i} + \frac{1}{m_j}\right)^{-1}$ is the equivalent mass, $V_n^{\overrightarrow{rel}}$ is the normal component of the relative velocity and β and K_n (the normal stiffness) are given by

Eq. 3.5

$$\beta = \frac{ln\, e}{\sqrt{ln^2 e + \pi^2}}$$

Eq. 3.6

$$K_n = 2E^* \sqrt{R^* \delta_n}$$

with e the coefficient of restitution.

Coefficient of restitution

Metal spheres do not behave elastically but undergo permanent deformations during collisions at high speed. This means that the particle kinetic energy is dissipated by the occurrence of plastic strains and elastic wave propagation. According to the literature the latter phenomenon is negligible in comparison with the energy dissipated by plastic deformations (Wu et al., 2009). Therefore, we aim to model only the former phenomenon in our DEM simulations. To use a contact law characterised by an elasto-plastic model such as those that are typical of continuum mechanics would be overly complex and time consuming from a computational point of view. As a result, the approach to be followed is based on the coefficient of restitution (CoR). This is a coefficient that expresses the total amount of energy dissipated during an impact without giving any information on the deformations undergone by the surfaces coming into contact. It is defined as:

Eq. 3.7

$$e = \frac{V_r}{V_i}$$

with V_r and V_i the rebound and impact velocities respectively. At this point it is important to note that the CoR in the normal direction, e_n, can be significantly different from the one in the tangential direction. This is typically due to lack of data leading to the assumption that $e_t = e_n$. Unfortunately in many publications this fact is taken for granted and the reader

might come to the conclusion that this is always the case. However, experimental evidence proves the contrary, demonstrating that $e_t = e_n$ is only a reasonable assumption if there is lack of experimental data, otherwise a suitable value of e_t should be used.

The CoR is likely to play an important role in defining the final results and therefore it should be determined as accurately as possible for the different types of interactions. In this regard, input is expected from Rolls Royce. The CoR depends on both the impact velocity, and the impact angle, θ_i. Therefore, values of e_n and e_t should be experimentally determined for a set of values of V_i intial velocity and θ_i the angle of impingement. The CoR for the shot - surface interaction will substantially vary depending on the previous hits and plastic deformation of the component. Experimental data is used to apply the change of CoR for subsequent hits at the same location from Table 3.1. The change of CoR for repeated impacts can be taken into account by keeping track of the location and the number of impacts per location. In this way, the CoR used in the numerical simulation would be assigned dynamically as a function that takes into account the number of previous impacts for a given location. However, if this approach has a negligible effect on the overall results, an average value for the CoR for the number of collisions can be applied throughout the analysis.

Table 3.1: CoR for shot interaction after (Bhuvaraghan et al., 2008).

Impact No	Input velocity m/sec	Rebound velocity m/sec	CoR
1	100	40.27	0.402
2	100	54.04	0.540
3	100	58.28	0.583
4	100	76.31	0.763

The CoR for sphere - sphere interaction, e_{s-s} is different from the sphere - flat plate interaction e_{s-p}. In the absence of experimental data, e_{s-p} = 0.4 for both normal and tangential direction independent of the angle of impact and the relative velocity between colliding shots will be assumed for the time being (Hong et al., 2008). This study negates the

deformation of shots given that the deformation of shots will increase the computation time tremendously, making it unfeasible.

The CoR cannot be assigned directly to the contact law since the collision has a finite duration during which contact forces vary over time. Therefore, it is necessary to assign a damping force, F_d, to the spherical shot during impact such that an appropriate value for the coefficient of restitution is obtained. In the contact law, the damping force is opposed to the relative velocity, *V*, between two particles at the contact:

Eq. 3.8

$$F_d = -\eta V$$

with η being the damping coefficient. In most of DEM analyses, this coefficient is chosen on the basis of an empirical approach. However, if η is chosen empirically, then the restitution coefficient can no longer be controlled. In other words, the final velocity obtained at the end of the impact would no longer satisfy Eq.3.8. However, a relationship between the desired CoR and the damping coefficient has been found by Tsuji et al. (1992) so that if η is taken as:

Eq. 3.9

$$\eta = \alpha\sqrt{mK_H}\delta^{\frac{1}{4}} \qquad \text{with} \quad \alpha = \sqrt{\frac{5}{4}}\frac{2ln(e)}{\sqrt{((ln(e))^2+\pi^2)}}$$

the damping coefficient during impact can be assigned in order to achieve any desired CoR. However, the CoR approach is limited by the fact tha the interaction of different bodies would be affected by their respectives materials, surfaces, geometries properties and relative velocities.

Tangential direction of impact

The tangential force,F_t , depends on the tangential overlap δ_t and the tangential stiffness K_t.

Eq. 3.10

$$F_t = -K_t\delta_t$$

with

$$K_t = 8G^* \sqrt{R^* \delta_n} \quad \text{Eq. 3.11}$$

Here G^* is the equivalent shear modulus.

$$\frac{1}{G^*} = \frac{(1 - v_i^2)}{G_i} + \frac{(1 - v_j^2)}{G_j} \quad \text{Eq. 3.12}$$

Additionally, tangential damping is given by:

$$F_t^d = -2\sqrt{\frac{5}{6}}\beta\sqrt{K_t m^*}V_t^{\overrightarrow{rel}} \quad \text{Eq. 3.13}$$

where $V_t^{\overrightarrow{rel}}$ is the relative tangential velocity.

As in the normal direction, we assume that the plastic dissipation can be expressed by a CoR. However, it is important to note that dissipation can also occur due to friction. Therefore, unlike the normal case, the contact law is made by a linear spring, a dashpot and a slider. In the first instance, if experimental data from Rolls Royce are not available, the CoR will be assumed equal to the normal case: $e_t = e_n$. In the same way the tangential damping force will be calculated according to Eq. 3.7 and Eq. 3.8.

In the second tier of the approach, if necessary a much more complex law taking into account the reality of partial slip could be used. This is a very complex phenomenon which requires a long description that can be found in Johnson (1985) and Mindlin (1949). Alternative formula can be found in Thornton and Yin (1991) but, it is expected that the Thornton approach could make the simulation runtime significantly longer. Moreover, the relationship between damping coefficient and CoR would become less evident so that it would become more difficult to impose a prescribed CoR for each impact.

Drag force

The drag equation calculates the force that is experienced by an object moving through a fluid at relatively large velocity (high Reynolds number, R_e >~1000). The force on a moving object due to fluid is:

$$F_D = -\frac{1}{2} pAC_d(V \cdot V)\frac{V}{||V||} \quad \text{Eq. 3.14}$$

where

F_D is the force vector of drag

p is the density of fluid, here density of air 1.1839 kg/m^3

V is the velocity of the object relative to the fluid

A is the reference area, here for sphere πr^2

C_d is the drag coefficient, a dimensional parameter for sphere is 0.47

The drag force can be implemented using the commercial application Fluent, coupled with EDEM.

Time step

The time step is the amount of time between interactions in the Simulator. It is fixed and remains constant throughout the simulation. The Rayleigh time step is the time taken for a shear wave to propagate through a solid particle. When using the simulation with a range of particle sizes, the Rayleigh time step is calculated based on the smallest particle size. The time step for the DEM simulations will be taken as the minimum between 20 % of the Rayleigh time step and 10 % of the average collision duration.

3.1.3 Model setup

The three-dimensional DE Model was developed using the commercial discrete element code EDEM (EDEM, 2013). As shown in Figure 3.2 (right), shots were delivered from a circular nozzle, impacting onto the flat target surface. The nozzle was modelled using an inner

diameter d_n and the distance between nozzle and target surface d with an angle of attack to the horizontal surface θ. The shots were modelled as spherical particles and in the initial simulation all particles are identical. However, EDEM allows for a variation of shot sizes using a standard deviation. The shot stream was generated at the nozzle cross section using the Particle Factory function in EDEM. EDEM can generate particles randomly or statistically. For the SP simulation, random particle generation was chosen. The number of shots delivered from the nozzle in a time period depends on the mass flow rate used in the peening process. The initial velocity of the shots, V_i, depends on the air pressure of the peening system. In this simulation a variation of 5 % around the initial velocity is applied. The drag and other fluid effects were not included in the present model but can be added at a later stage using DEM - CFD coupling in EDEM with the commercial Computational Fluid Dynamics (CFD) application FLUENT. The Hertz-Mindlin contact law discussed in section 3.1.2 is used to compute the shot - shot and shot - target interactions. The energy dissipation is described using the coefficients of restitution outlined in the previous section. The algorithm that changes the CoR for repeated impacts is explained in section 3.1.4. SP quality is determined by the CRS pattern within the target component derived by the energy transfer and plastic deformation. The impact energy can be easily extracted from the DE simulation. One way to evaluate the impact energy is to determine the velocity of the shot just before impact. In the DEM simulation, the shots impacting on the target were continuously monitored and recorded along with the time of impact, impact position and the components of this velocity along three coordinates are V_{ox}, V_{oy} and V_{oz} respectively. The total kinetic energy of shots delivered from the nozzle E_o can be evaluated from the initial velocity and the actual number of shots delivered from the nozzle. It should be noted that this kinetic energy is not the same energy that is impacted on the target surface E_{imp}. E_{imp} relates to the number of shots impacting on the target surface and the velocity of the shots just before

impact V_{imp}. The impact velocities along the normal and tangential direction to the surface are referred to as the normal impact velocity V_n .The tangential impact velocity V_t and their kinetic energies are denoted by E_n and E_t.

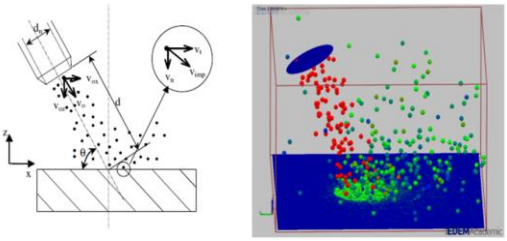

Figure 3.2: Three-dimensional DE modelling of SP (left) after (Hong et al., 2005) and snapshot of DE simulation animation (right).

3.1.4 Coefficient of restitution for repeated impacts

Algorithm and implementation

An algorithm to change the CoR for repeated impacts for the same location was implemented using the User Defined Library (UDL) in EDEM. The EDEM application triggers the UDL module for every shot - shot and shot - target collision. Once a shot - target collision is detected, the contact location of the target surface is retrieved and for every new contact the impact number of geometry face lets within the predefined impact diameter is incremented. The corresponding CoR data for the impact number is then retrieved from Table 2.1 and applied to compute the contact forces. Figure 3.3 shows the process flow diagram. The results depend on the mesh size, the number of impacts per geometry face let and the values of the CoR data.

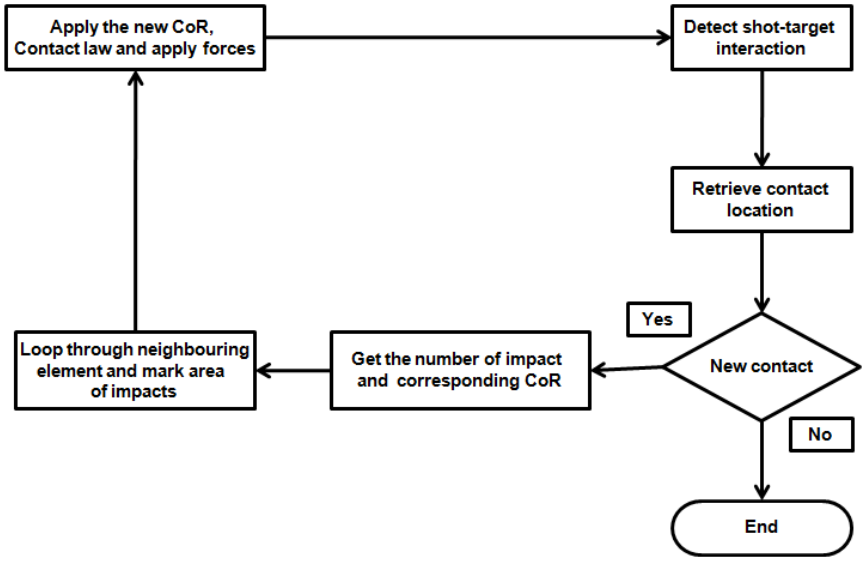

Figure 3.3: Shows the process for changing the CoR for subsequent impacts.

3.1.5 DEM - FEM linking

The DEM has been used to model the SP process and examine the individual peening parameters. However, the current DE method cannot model plastic deformation and residual stresses. The FEM tool is used to post-process the DE results to determine the CRS in the peened component. A UDL is created within the EDEM program to extract the forces and location. This information is then used to create the Abaqus input file. The mesh used in DEM is different to the mesh used in the FEM application Abaqus. Hence, there is a need to match the location and the mesh during the coupling process. Figure 3.4 shows the process flow diagram between the commercial DEM application EDEM and the FEM application Abaqus.

The Steps outlining the coupling;

1. The *.stl geometry is loaded into Abaqus and the material properties are selected. The input file is created and separated into dynamic and static parts; parts that need to be populated and parts that will remain unchanged regardless of the number of impacts, location etc. Respectively, the main input file is divided into four separate files. Dynamic parts are deleted and the static parts are saved to be used in step 6.

2. The *.stl is loading into the commercial EDEM program along with a file containing the geometry surface data from FEM.
3. The SP model is set up with the individual peening parameters.
4. The DEM SP simulation is run, applying the CoR for repeated impacts. For each new shot - target contact the highest force is recorded along with the impact location.
5. When the simulation ends, two separate files are created containing the *Nset, *Step and Loads parts of the Abaqus file. Impacts that are far away from each other have been grouped together to reduce the computation time and output file size.
6. The two output files created from the EDEM simulation is merged together with the two files from step one to generate the Abaqus input file.
7. The input file is then loaded into Abaqus to obtain the residual compressive stresses.

Depending on target geometry size, complexity and number of impacts, the input file can become very large and sorting or populating the file can be very difficult. Nonetheless, this approach is more efficient and less time consuming than running a set of programs to translate the DE output file to a computable FE input file because the sorting and populating steps are performed within the DE simulation.

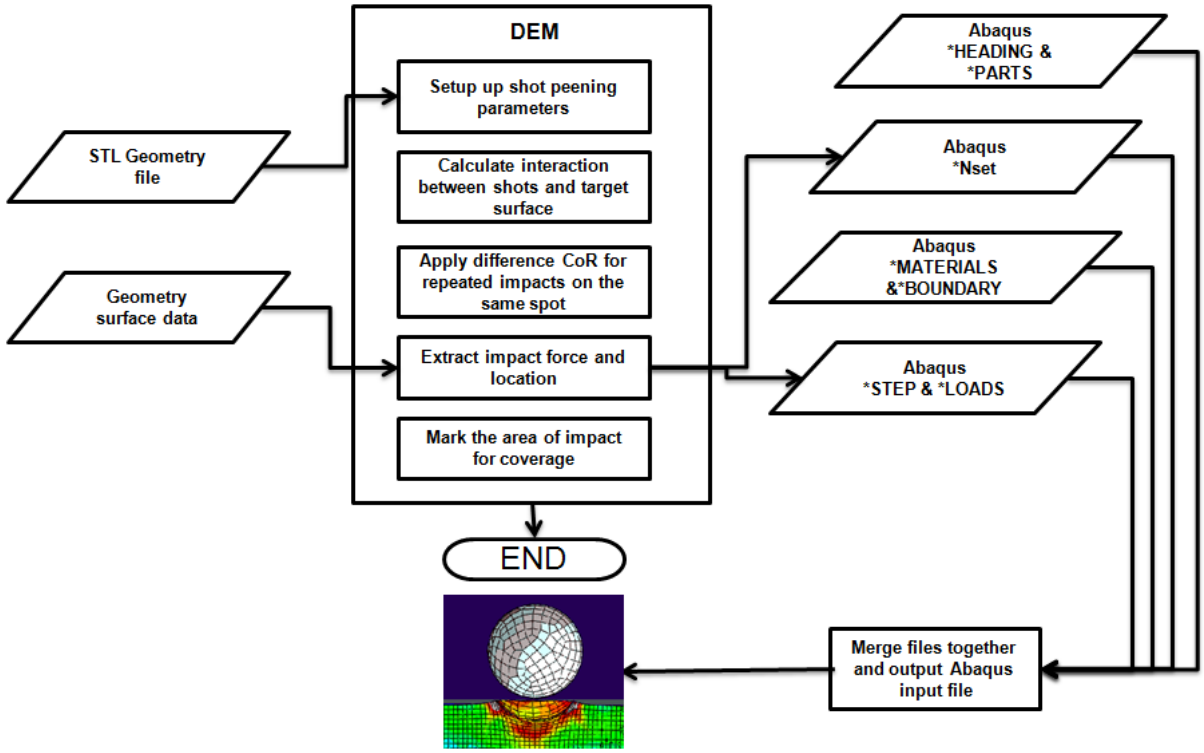

Figure 3.4: The diagram shows the DEM - FEM coupling process.

3.1.6 DEM speedup

The DEM simulations were run on a single computer with an Intel i7 870 processor (4 cores) with 8 MB cache and 16 GB of memory running Linux CentOS. The CPU speed scaling is almost linear in the application EDEM. The simulation time was further reduced by increasing the data save interval (data points) and choosing the selective save option. The selective save option allows an operator to save partial data such as contacts, collisions, particle data, geometry data or interaction data and discarding all other information. The computation time was also affected by the overall simulation time and the chosen fixed time step. A small speedup was further achieved by excluding the visual output and running the simulation in the command line terminal.

CHAPTER 4 PARAMETRIC ANALYSIS USING DEM AND FEM

This chapter reports the results obtained using the DEM model, FEM model and DEM - FEM coupling described in Chapter 3. A parametric analysis of the shot stream was performed using the DEM model and single shot analyses were performed using the FEM application Abaqus. Finally, a number of combined DEM - FEM simulations with 1000 shots impacting on a flat surface were performed to improve the understanding of coverage, CRS and saturation.

4.1 Discrete element simulation

Analysing the peening parameters

A parametric analysis was performed to investigate the effect of process parameters including initial velocity, angle of attack, shot size, mass flow rate and distance between nozzle and target. This section provides an understanding of the effect of the key parameters relating to SP. The parameters used in this study were adapted from the values commonly used in the industrial process (Hong et al., 2005). Shots were modelled as spheres with diameter d_{shot} = 0.58 mm, density ρ = 7800 kg/m^3, elastic modulus E = 200 GPa and Poisson's ratio v = 0.3. The nozzle was modelled as a single circle with inner diameter d_n = 8 mm. EDEM factory generates and places the particles in such a way that particles midpoints are placesd on the plane of the factory geometry. Therefore when the diameter d_n = 8 mm, the realistic diameter is 8 mm + 0.5 times the shot size. As a result, the input value in EDEM for the nozzle is 7.71 mm. The target is made of a steel cube with the dimensions 30 mm x 30 mm x 30 mm. The material properties were taken as having an elastic modulus E = 200 GPa, Poisson's ratio v = 0.3 and density ρ = 7800 kg/m^3 respectively. 10, 000 particles were used in all simulations. A large number of simulations were run to cover a wide range of parameter values for initial

velocity, angle of attack, and distance between nozzle and target. Initial velocity V_i= 50, 75, 100 m/s; Mass flow rate r_m = 5.5, 9.25, 13 kg/min; angle of attack θ = 35°, 45°, 62.5°, 67.5°, 90°;and distance between the nozzle and target surface = 10, 20, 40, 60, 80 mm. The coefficient of restitution for shot - shot e_{s-s} = 0.5 and shot - target e_{s-t} was dynamically chosen, depending on the number of previous impacts at the same location. The friction contact was considered for the interactions by using a friction coefficient μ = 0.20 in all simulations. Gravity of -9.81 m/s^2 is applied throughout the simulations. The effect of the distance d on peening quality was found not to be significant as long as d is greater than 20 mm if the diameter of shot is less than 2 mm. The results presented were obtained using a distance between the nozzle and target surface of d = 20 mm.

4.1.1 Effect of impact number

First, the number of impacts after which the system reaches a steady sate was investigated. Impact velocities just before the shot - target collision were recorded and analysed. Figure 4.1 shows the distribution of normalised impact velocities for the reference case (mass flow rate r_m= 9.25 m/s, initial velocity V_i = 75 m/s, angle of attack $\theta = 67.5°$, distance d = 20 mm and shot diameter $d_{shot} = 0.58$ mm. It emerges that in the first 50 impacts about 64 % of shots hit the target surface with the initial velocity (V_i =$0.9v_o \sim 1.0v_o$). This indicates that these shots had no interaction with other shots before hitting the target surface. The remaining 36 % of shots (18 shots) had energy dissipation due to interaction with others shots. Steady state is reached after an initial period of 4000 impacts, with 33.65 % of impacts hitting the surface with the initial velocity. The most unstable state is obtained with the highest mass flow rate and lowest initial velocity and angle of attack θ = 90° and distance d = 20 mm. An impact number of 10, 000 impacts can be taken as the steady state for all combination of parameters used in this study.

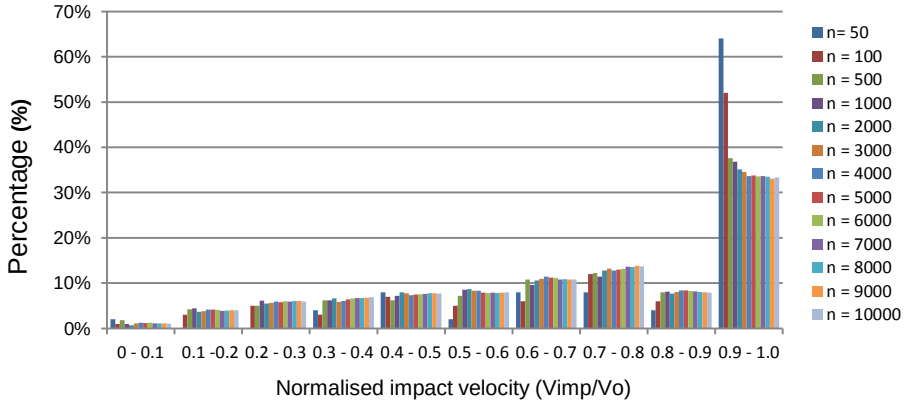

Figure 4.1: Illustrates the percentage of shots retaining their initial velocity at impact for the reference case (mass flow rate r_m= 9.25 m/s, initial velocity V_i = 75 m/s, angle of attack $\theta = 62.5°$, distance d = 20 mm and shot diameter $d_{shot} = 0.58$ mm).

4.1.2 Effect of nozzle distance

Next, the effect of the distance between the nozzle and target surface was investigated. Distances ranking from 5 mm to 30 mm were investigated. Figure 4.2 shows the number of shot - target interactions for different distances d. The effect of distance on the peening quality was not found to be significant when d greater than 20 mm was and shot diameter is 0.58 mm.

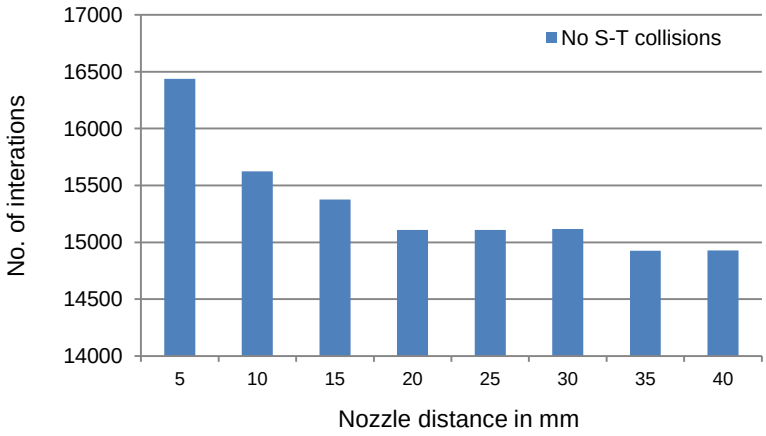

Figure 4.2: Shot - target collisions for different Nozzle distance d for the reference case.

4.1.3 Effect of mass flow and initial velocity

A set of simulations covering various mass flow rates and initial velocities was carried out next. Table 4.1 shows the different parameters for different mass flow rates. For simplicity a parameter ε is introduced and defined as $\frac{r_m}{v_o}$.

Figure 4.3 shows the number of shot - shot and shot - target interactions for the different initial velocities. It can be concluded that the number of shot - shot and shot target interactiosn increase with lower initial velocities. Compared to the shot - target collisions, the shot - shot interactions nearly doubles from 75 m/s to 200 m/s.

Table 4.1: Different parameter values for different mass flow rates and velocities and their corresponding γ.

No	1	2	3	4	5	6	7	8	9
γ g/m	4.333	3.083	2.889	2.167	2.056	1.833	1.542	1.222	0.917
$r_m$kg/min	13	9.25	13	13	9.25	5.5	9.25	5.5	5.5
V_im/s	50	50	75	100	75	50	100	75	100

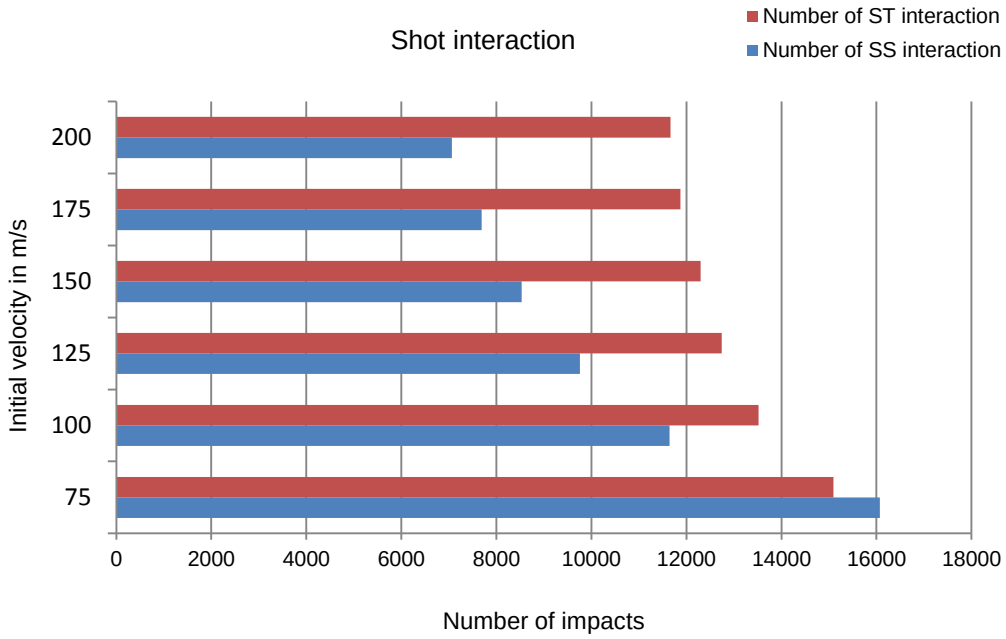

Figure 4.3: Shows the number of shot - shot and shot - target interactions at different initial velocities.

Table 4.2 and Table 4.3 show the effect of mass flow rate and initial velocity on the distribution of normalised impact velocity for $\theta = 90°$ and $\theta = 62.5°$. It can be seen that the parameter ε is significant. For a lower γ value, more shots hit the surface with initial velocity than in the simulation with a higher value. The key parameters r_m = 5.5, $\theta = 62.5°$ and V_i = 100 m/s corresponds to the lowest value of ε = 0.917 where at which point about 56 % of impacts maintain their initial velocity at impact (V_{imp} =0.9 $V_i \sim 1.0\ V_i$). This indicates that the shots had little or no energy dissipation from the nozzle to the surface. The lowest percentage of normalised impact velocity was encountered with the highest value γ = 4.333 with the mass flow rate r_m= 13, $\theta = 90°$ and V_i = 50 m/s where only 3.89 % of shots maintained their initial velocity. In can be concluded that with a higher mass flow rate r_m the energy dissipation increases due to the large number of shot - shot interactions. A lower mass is therefore more suitable for the peening process with smaller shot - shot interactions associated with lower energy dissipation. With a lower initial velocity the shots do not move quickly enough and the likelihood of interactions with rebounding shots increases. With a much higher initial velocity the shots move quicker and the probability of interactions between the shots decreases. Looking at results from $\theta = 90°$ and $\theta = 62.5°$ it can be concluded that the angle of attack has a significant influence on the outcome. Hence, the angle of attack needs to be investigated next.

Table 4.2: Effect of mass flow rate and initial velocity ($\theta = 90°$)

Normalised impact velocity	1	2	3	4	5	6	7	8	9
> 0.9	3.89%	13.79%	14.74%	22.64%	25.25%	28.35%	31.96%	37.56%	42.18%
> 0.8	5.20%	16.70%	18.09%	26.75%	29.81%	32.26%	36.69%	41.95%	46.91%
> 0.7	7.89%	21.24%	23.37%	32.46%	35.20%	37.24%	42.46%	46.96%	52.19%
> 0.6	12.45%	28.33%	30.60%	39.74%	42.35%	44.31%	49.22%	53.75%	57.97%
> 0.5	18.78%	37.09%	39.18%	48.44%	50.88%	53.53%	57.00%	62.22%	65.27%
> 0.4	27.02%	47.72%	49.24%	58.10%	60.50%	63.20%	66.35%	70.88%	73.30%
> 0.3	39.04%	59.49%	60.62%	68.79%	70.47%	73.99%	75.88%	79.51%	81.51%
> 0.2	54.94%	72.88%	73.89%	79.74%	81.15%	84.06%	84.96%	87.98%	89.27%
> 0.1	75.47%	87.29%	87.81%	91.10%	91.93%	93.56%	93.63%	95.23%	95.71%
> 0.0	100.00%	100.00%	100.00%	100.00%	100.00%	100.00%	100.00%	100.00%	100.00%

Table 4.3: Effect of mass flow rate and initial velocity ($\theta = 62.5°$)

Normalised impact velocity	1	2	3	4	5	6	7	8	9
> 0.9	13.25%	23.34%	25.05%	32.71%	33.80%	40.22%	43.11%	50.58%	56.03%
> 0.8	15.94%	26.89%	28.45%	36.45%	37.63%	43.72%	47.10%	54.30%	59.62%
> 0.7	19.59%	31.07%	32.73%	40.37%	41.91%	47.68%	51.22%	57.93%	62.72%
> 0.6	25.55%	37.05%	38.78%	45.94%	47.36%	53.27%	55.68%	62.07%	66.11%
> 0.5	33.76%	45.10%	46.77%	53.16%	54.48%	60.46%	62.20%	68.00%	70.96%
> 0.4	42.89%	54.49%	55.86%	61.55%	63.21%	68.63%	69.84%	75.14%	77.70%
> 0.3	54.09%	64.50%	65.83%	70.84%	72.59%	76.76%	77.48%	81.74%	83.52%
> 0.2	67.26%	76.06%	76.81%	80.63%	82.05%	85.18%	85.33%	88.49%	89.34%
> 0.1	83.54%	88.52%	88.71%	90.73%	91.78%	93.42%	93.21%	94.87%	95.29%
> 0.0	100.00%	100.00%	100.00%	100.00%	100.00%	100.00%	100.00%	100.00%	100.00%

4.1.4 Effect of angle of attack

The effect of angle of attack was investigated with the following parameters; mass flow rate $r_m = 9.25$ m/s, initial velocity V_i = 100 m/s, distance $d = 20$ mm and shot diameter $d_{shot} =$ 0.58 mm. Figure 4.4 shows the percentage of shots retaining their initial velocity for different angles of attack. Analysing the velocity at impact, for $\theta = 35°$, about 74 % of shot retained their initial velocity and had fewer interactions between shots. Shot - shot interactions increased significantly when $\theta = 90°$ and only 50 % of shots retained their initial velocity. This is explained by the large number of rebounding shots coinciding with incoming shots.

The percentage of shots retaining their initial velocity decreases with the angle of attack increasing.

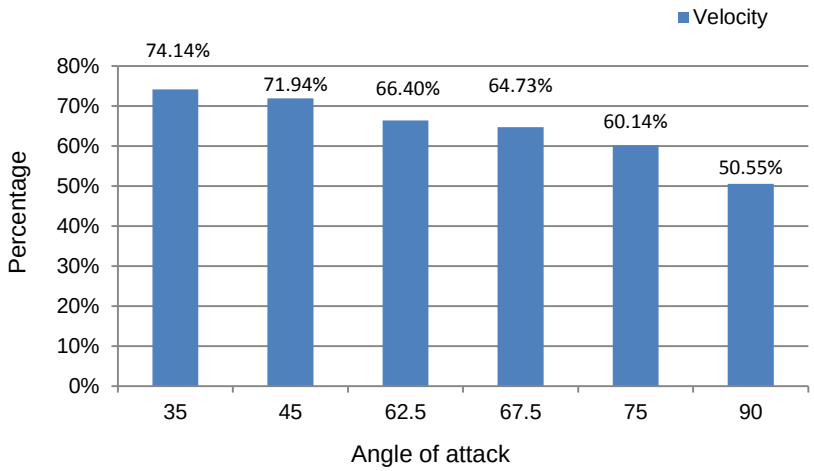

Figure 4.4: Effect of angle of attack on the percentage of particles maintaining their initial velocity at impact.

To measure CRS, the normal impact velocity is more significant than the tangential component. Figure 4.5 shows the effect of angle of attack on the percentage of particles retraining their normal impact velocity (V_i = 100 m/s). Looking at the normal impact velocity it can be shown that $\theta = 62.5°$ provides the highest percentage of shots retaining initial velocity at impact (62.83 %).

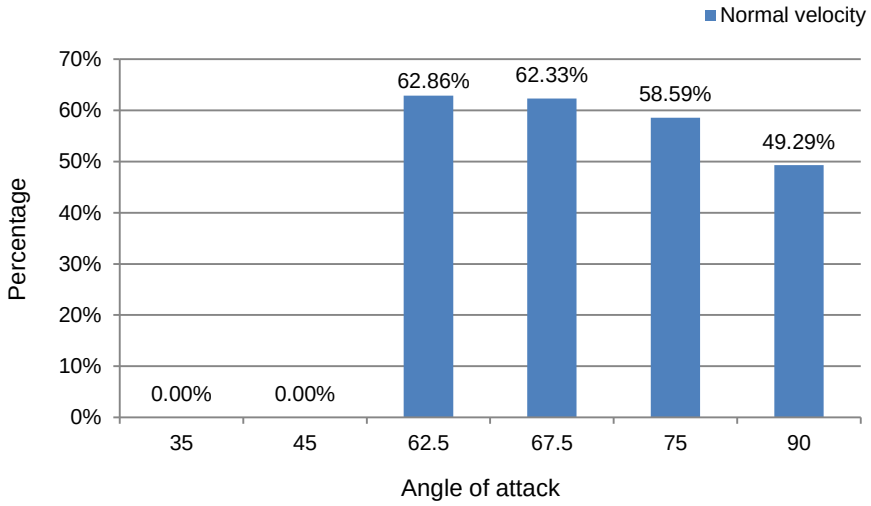

Figure 4.5: Effect of angle of attack on the percentage of particles remaining at normal impact velocity.

4.1.5 Effect of shot diameters

The distribution of impact velocities for differ shot diameters was examined. Specifically, five different shot diameters d_{shot} = 0.4, 0.58, 0.75, 1.0 and 1.5 mm with the process parameters r_m = 9.25 kg/min, V_i = 75 m/s, θ = 62.5° and d = 20 mm were studied. Figure 4.6 shows the number of shots per second delivered from the nozzle for the different shot diameters. For d_{shot} = 0.4 mm a high number of shots (590, 000) are delivered from the nozzle compared to 11, 200 shots for d_{shot} = 1.5 mm. The shot - shot collision decreased almost linearly for d_{shot} = 0.4 mm (18, 057) towards d_{shot} = 1.5 mm (2, 174). Figure 4.7 shows the shot - shot and shot - target interaction numbers for the different shot diameters.

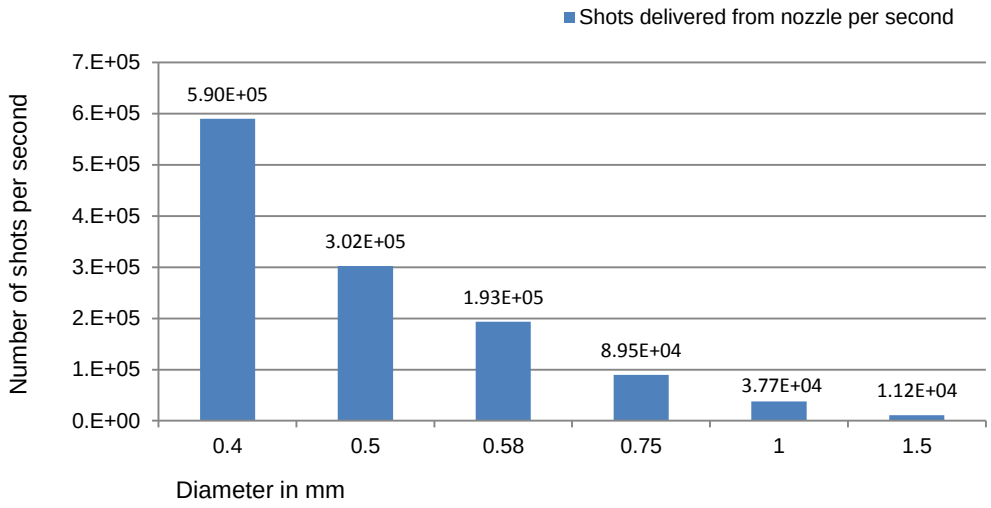

Figure 4.6: Number of shots delivered per second vs. shot diameter.

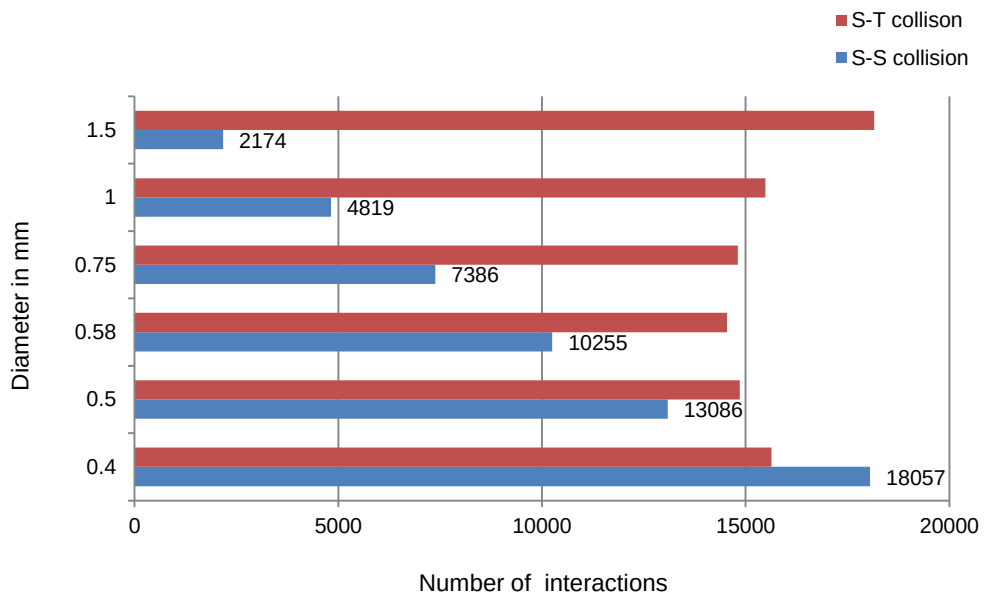

Figure 4.7: Number shot - shot and shot - target interaction for different shot diameters.

4.1.6 Effect of changing the CoR for subsequent impacts

The effect of CoR on shot - shot and shot - target interactions for repeated impacts was investigated. Figure 4.8 shows the energy dissipation for shot - target interactions with a constant CoR and Figure 4.9 show the energy dissipation for shot - target interactions with changing CoR. In the physical shot - target interaction, the indentation size will vary and will depend on the impact angle, impact velocity, shot size etc. Here we have fixed the indentation size at 0.58 mm diameter. When applying the CoR dynamically the energy dissipation decreases with the increasing indentation radius. Table 4.4 shows the results for different indentation radii for 10 000 shots. A target location that is being hit for the first time has a low CoR, resulting in high energy dissipation. The subsequent shot hitting the location that was hit previously and plastically deformed the target surface has a higher CoR, resulting in lower energy dissipation. Subsequent shots hitting the target surface will rebound with a higher velocity and retain more of their kinetic energy. Results show that shot - shot interactions decrease and shot - target interactions increase with the impacting indentation

size. More importantly the average normal velocity at impact increases with the indentation radius, which is important for the generation of CRS.

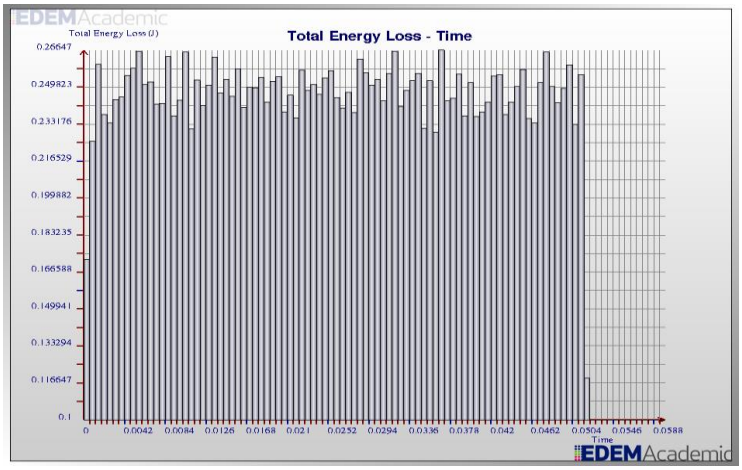

Figure 4.8: Showing the energy dissipation for shot - target interactions with a constant CoR 0.4.

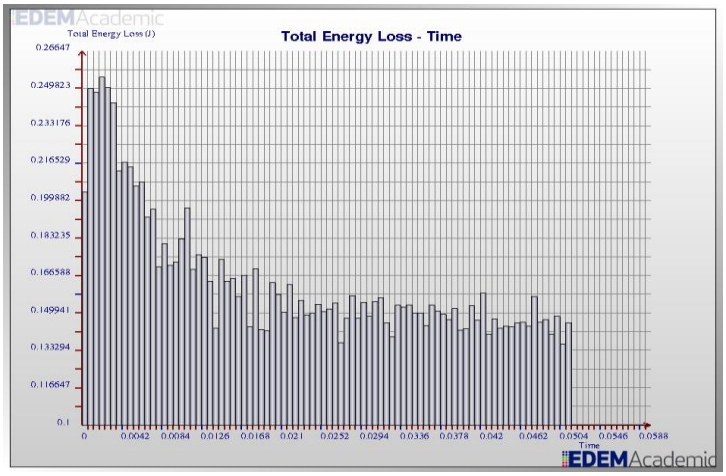

Figure 4.9: Showing the energy dissipation for shot - target interaction with changing the CoR where the indentation radius 0.58 mm.

Table 4.4: Shows the results for different indentation radius.

Indention radius	-	0.5	1	1.5
Shot - Shot collision	6485	5925	5912	5781
Shot - Target collision	13959	15805	15615	15510
Total Energy Loss through Shot - Target collision in J	21.99	14.6865	13.1993	12.9635
Average velocity at impact in m/s	78.29	78.6096	79.3572	79.7216
Average normal velocity at impact in m/s	62.38	63.0097	63.7258	64.3982

4.1.7 Coverage

Coverage is defined as the percentage of a given surface that is saturated by dents or dimples. Coverage beyond 100 % is referred to as full coverage or multiples of time to achieve 100 % coverage. However, in practice, the size of impressions will vary due to the shot size variation, shot velocity, impact angle and peened material properties. The current model only considers the shot size, other relevant parameters can be assigned as a function taking into account a more realistic size of indentation.

The imported target geometries consist of a triangular mesh. The UDL implemented within the DE application counts the number of impacts for every single mesh element, providing a rapid way to analyse the individual peening parameters. Visualizing the impact location in the DE simulation can give a good indication of the peening coverage. Figure 4.10 shows the shot impact location in DEM. Surface location coloured in red indicates a high number of impacts, green a moderate number of impacts and colour blue low/no impacts. The number of impacts for a particular location can be extracted and analysed in more detail. This allows practitioners to analyse more complex peening conditions, such with multiple nozzles and complex geometries.

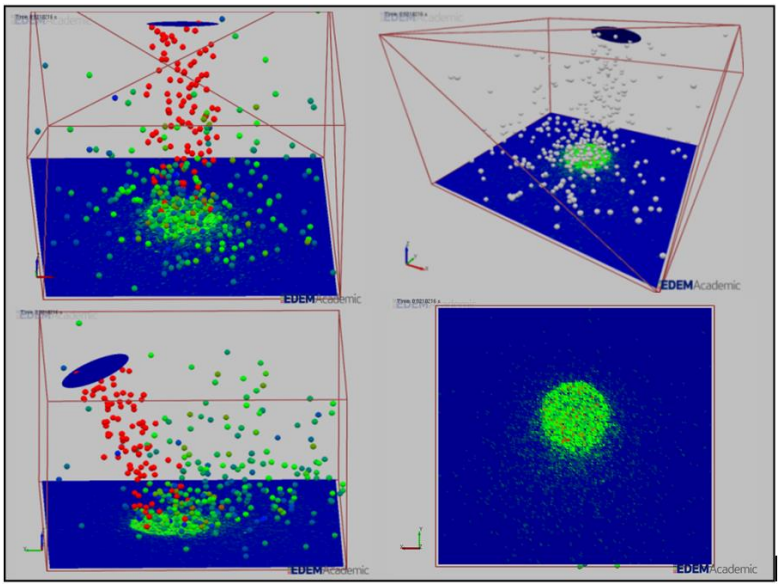

Figure 4.10: Showing three-dimensional discrete element simulation with impact location.

4.2 Finite element simulation

Numerical verification of single shot impact

The three-dimensional FE model was developed to investigate single shot impacts on the circular plate. A comparison was made with the numerical study of Meguid et al. (1999). The circular plate was given the following geometric properties; $R = 4d_{shot}$, height $H = 3d_{shot}$ where d_{shot} is the shot diameter, mass density = 7800 kg/m^3, elastic modulus E = 200 GPa, initial yield stress σ = 600 MPa and linear strain hardening parameter H^1 = 800 MPa as defined in Figure 4.11 was used. The plate was retrained against all displacements and rotations on the bottom end and was modelled using eight-node linear brick elements with reduced integration (C3D8R) with element size $0.05d_{shot}$ x $0.05d_{shot}$ x $0.05d_{shot}$. The shot was modelled as rigid sphere with a mass positioned at its centre. The diameter of the shot was d_{shot} = 1 mm and mass m = 4.085 mg. Additionally, coulomb law with friction μ = 0.25 was applied during the contact.

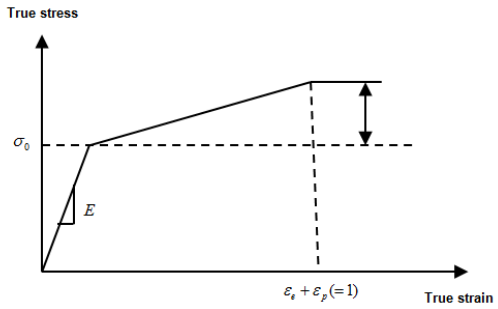

Figure 4.11: Stress- stress behaviour of the linear - strain hardening plastic material.

Two different impact velocities were compared. Figure 4.12 shows the residual stress with depth along the central axis in the component. Comparing the results with (Meguid et al., 1999) showed a close match between the two sets of numerical results.

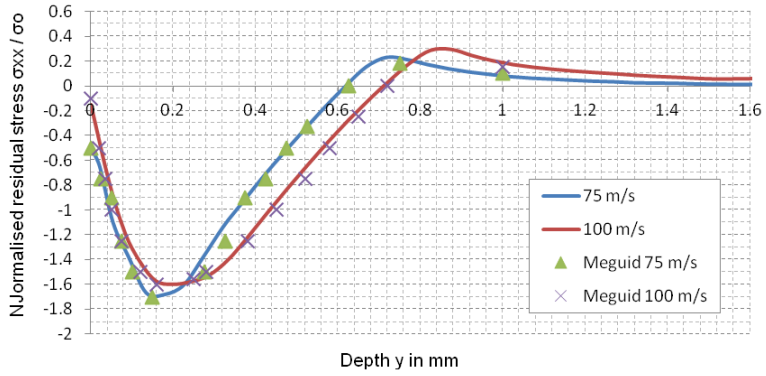

Figure 4.12: Numerical validation of single shot impact with (Meguid et al. 1999) Initial yield stress σ = 600 MPa and linear strain hardening parameter H^1= 800MPa.

Single shot parametric study

In the single shot model, the component is assumed to be elastic-plastic with isotropic hardening material. The reference case of the parameter study uses the identical parameters adopted from Meguid et al. (1999) and initial yield stress σ = 760 MPa and strain hardening parameter H^1 = 500MPa. No friction was considered during contact. The results are plotted in a normalized manner with the residual stress σ_{xx} normalized with σ_o the initial yield stress of the component. The stresses distribution plotted with the normalized deformed depth along the centre line of the component. Figure 4.13 shows the FEM simulation.

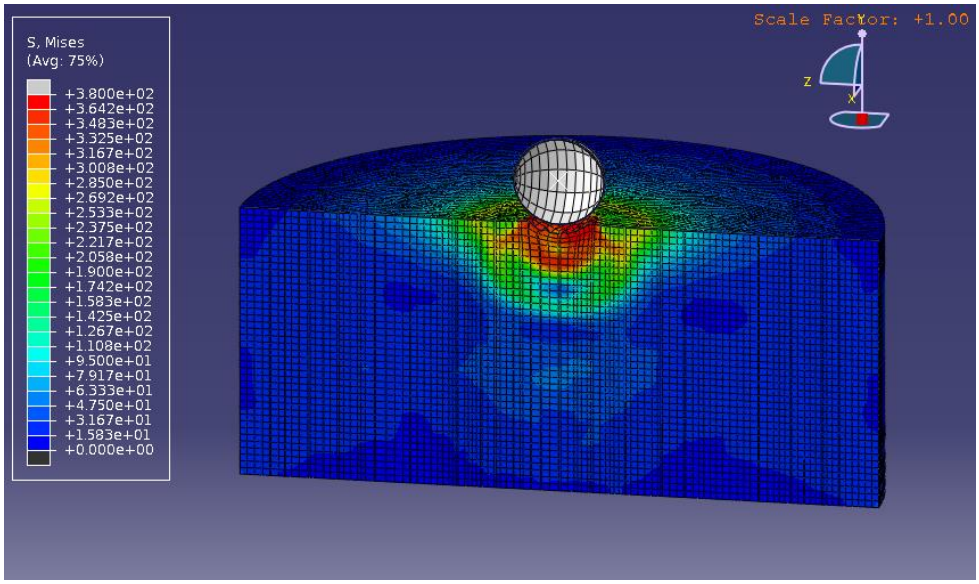

Figure 4.13: The three-dimensional finite element mesh.

4.2.1 Influence of shot velocity

The influence of shot impact velocity on the residual stresses distribution was investigated next. Figure 4.14 shows the residual stress profile for the reference perfect plastic material (H^1 = 0). The results show that the compressive residual stress zone increases with the impact velocity increasing. The impact velocity did not appear to have an effect on the surface and the maximum sub-surface residual stress.

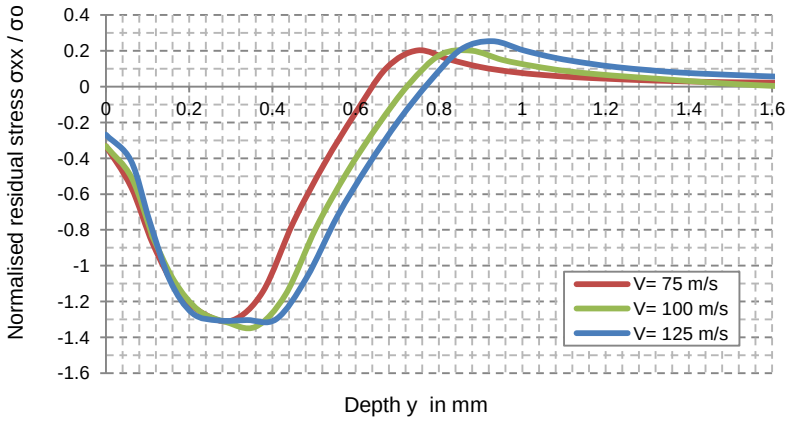

Figure 4.14: Normalised residual stress distribution for H^1 = 0.

4.2.2 Influence of shot diameter

A single shot with velocity V_i = 75 m/s impacting on a target was investigated with three different shot diameters d_{shot} = 0.5, 1, 2 mm and hardening parameter H^1 = 500. The results were normalised with depth *x* in which the *x* is the deformed depth along the centre of the line of the target. Figure 4.15 shows the residual stresses for the different shot diameters. Only a small difference in the subsurface residual stress was observed for the different shot diameters. However, the depth of thecompressive residual stress zone increases almost linearly with the shot diameter increasing.

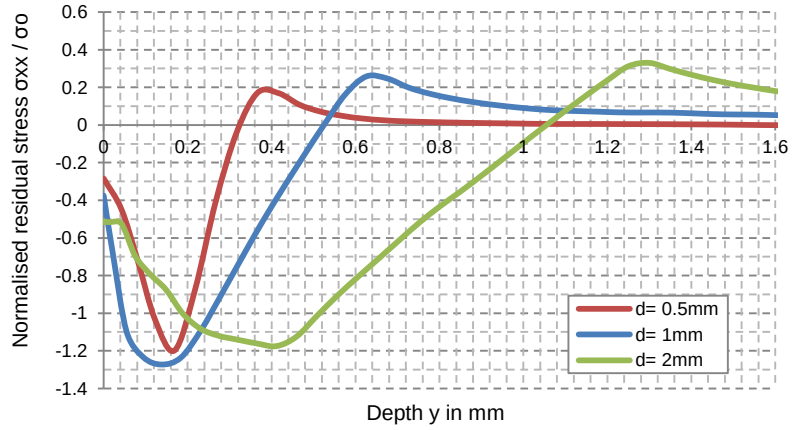

Figure 4.15: Influence of shot diameter.

4.2.3 Influence of shot imparting repeatedly

The effect of repeated impacts at the same location was investigated with impact velocity V_i = 75 m/s. The interaction between incoming shots and rebounding shots was not considered. Figure 4.16 shows the normalised residual stress profile for repeated impacts. Results show that the second shot impact caused a significant change of the residual stress distribution after the first shot. However, it should be noted that the sub-surface residual stress was similar to that of the first impact. Additionally, it can be noted that the change of residual stress distribution between shot 5 and 6 is very small.

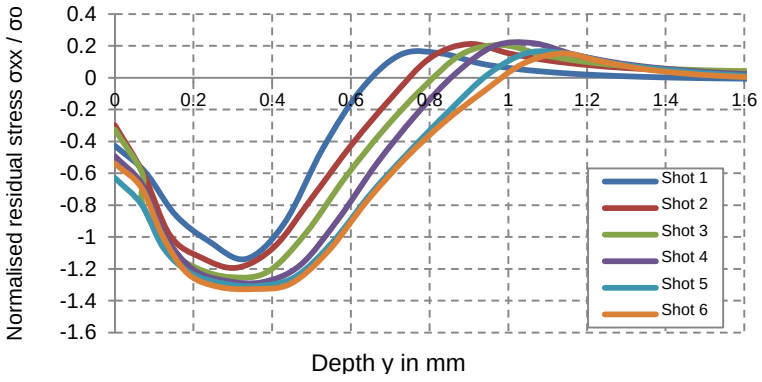

Figure 4.16: Shows the normalised residual stress profile for repeated impacts.

4.2.4 Influence of incident angle

The influence of single shot oblique impacts was investigated. Compared to the residual stress profile created by shots impacted normally, the magnitude and of the residual stress zones for oblique shots were much smaller. It can be concluded that when the incident angle decreases, the magnitude of the compressive surface residual stress and the compressive surface residual stress zone decrease. Figure 4.17 shows the depth of the compressive residual stress zone for different angle of impacts, Figure 4.18 shows the depth of compressive residual stress zone for different angle of impacts and shows the maximum sub-surface residual stress for different angle of impacts.

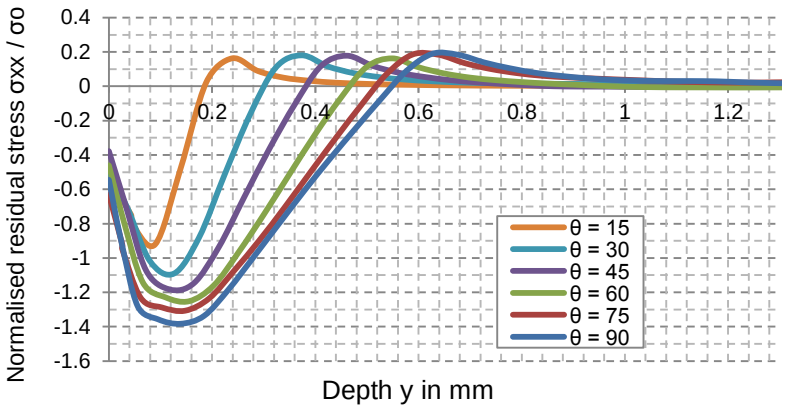

Figure 4.17: Shows the normalised residual stress profile for different angle of attack.

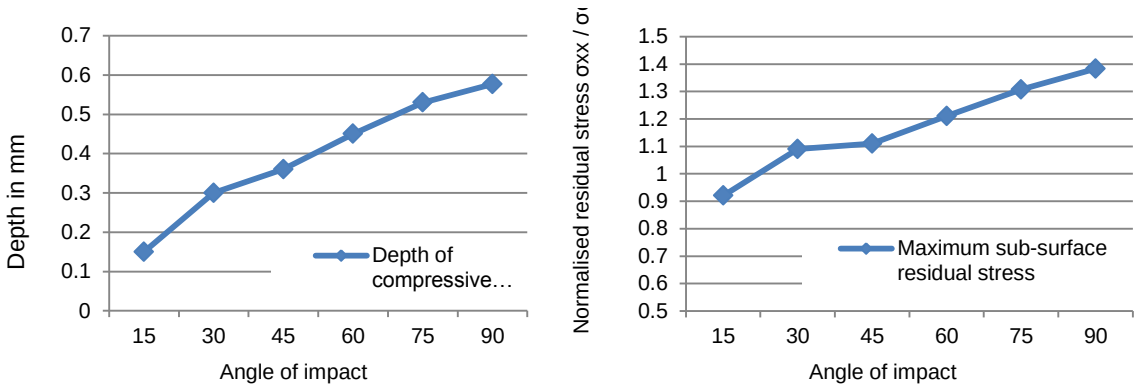

Figure 4.18: Shows the depth of compressive residual stress zone for different angle of impacts and shows the maximum sub-surface residual stress for different angle of impacts.

4.2.5 Influence of strain hardening parameter

As the hardening parameter increases, the depth of compressive residual stress zone and the maximum residual stress increase. Only a small variation in sub-surface residual stresses was encountered.

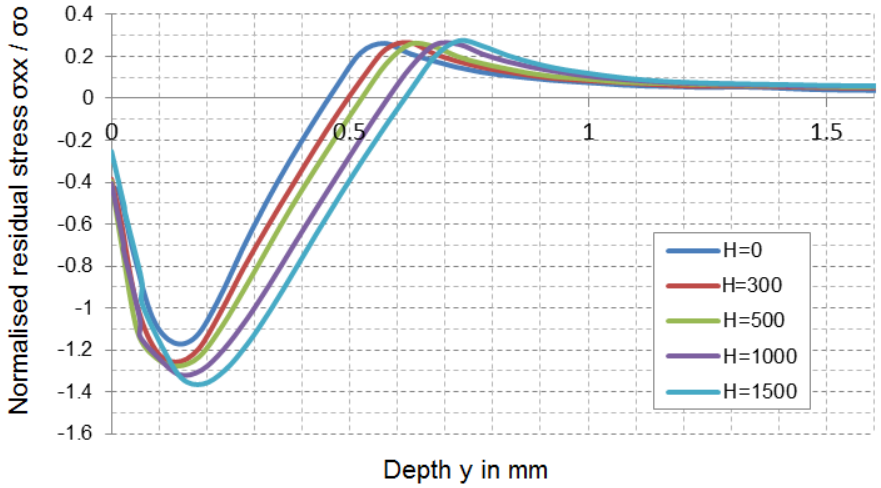

Figure 4.19: Shows the influence of strain hardening parameter on the compressive stress.

4.2.6 Influence of yield stress

Two different set of simulations were performed to investigate the influence of the yield stress. The perfect-plastic case and the strain-hardening plastic case with $H^1 = 500$ were studied. For the perfect-plastic case the different initial yield stresses only has a small effect on the results. It can be concluded that residual stress increase linearly with increasing initial yield stress.

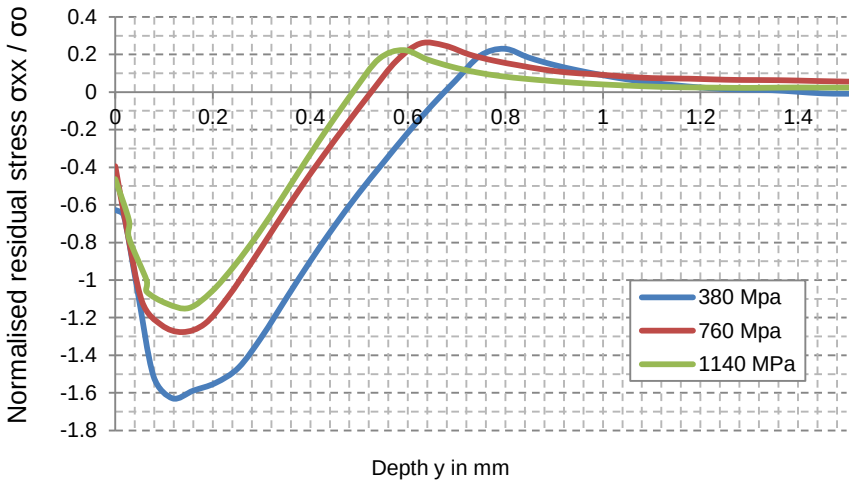

Figure 4.20: Shows the depth of compressive residual stress zone for the case with H^1 = 500.

For the H^1 = 500 case, it can be seen that the magnitude initial yield stress has a much stronger influence on the residual stresses. Comparing the results with the perfect-plastic, the residual stresses were significantly different when σ = 380 MPa. Only a small variation in residual stresses was observed for the highest initial yield stress case. It seems that the hardening parameter has a significant influence on the resulting residual stress when the initial yield stress is small. It can be concluded that when the initial yield stress is very high the impact will not mobilise much of the strain hardening region, which results in only little or no strain hardening effect. The summary of parameters effecting the CRS distribution is show in Figure 4.21.

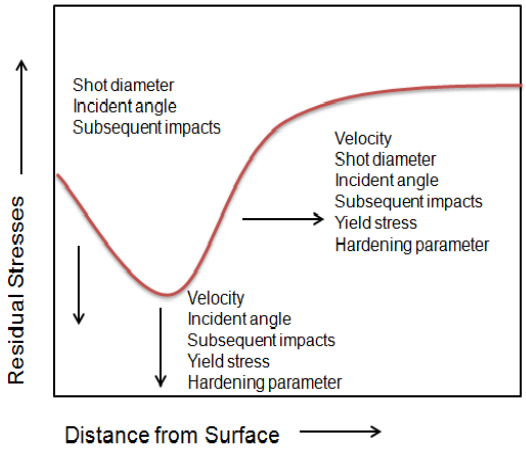

Figure 4.21: The single shot FEM simulations have shown the different parameters affecting the residual stress pattern.

4.3 DEM - FEM linked analysis

A complete SP simulation with the proposed DEM-FEM coupling described in section 3.1.5 was performed with 4000 shots impacting a flat surface. The plate was given the following 5mm x 5mm x 3 mm, mass density = 7800 kg/m^3, elastic modulus E = 200 GPa, initial yield stress σ = 600 MPa and linear strain hardening parameter H^1 = 800 MPa. All displacements and rotations of the plate bottom were restrained. The diameter of the shot was d_{shot} = 1 mm and mass m = 4.085 mg. A friction coefficient of μ = 0.25 was applied during the contact. The CRS distribution over time was measured at the midpoint of the flat surface to evaluate the saturation time. Figure 4.22 shows the impacting surface.

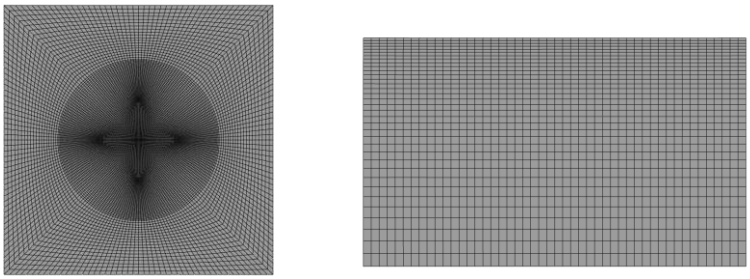

Figure 4.22: Shows the mesh of the impacting surface. (a) The top view and (b) depth view.

Analyses were performed to evaluate the minimum area size required to be modelled to retrieve the true residual stresses. Three different simulations were performed to evaluate the effect of standard, average and variable CoR in DEM on the resulting CRS in FEM. Furthermore, a coupled analysis was performed to access the effect of the peening angle on the resulting CRS and the influence of mass flow rate and velocity on CRS. Figure 4.23 shows the coupled analysis in FEM.

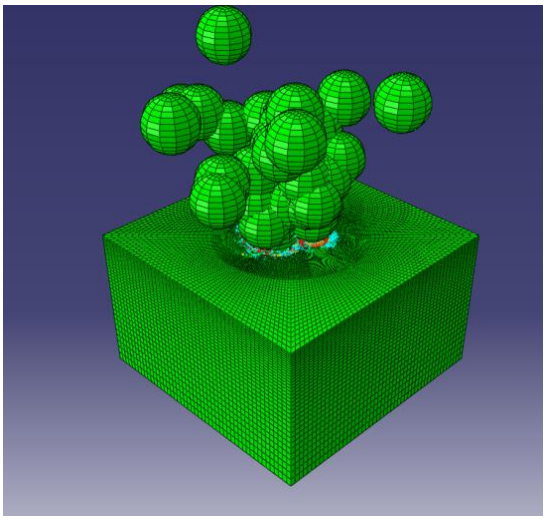

Figure 4.23: The three dimensional finite element numerical simulation model of the multi shot impact in Abaqus.

4.3.1 Minimum simulation domain

Analyses were performed to evaluate the size of the area required to be modelled to retrieve the true residual stresses. The impact area diameter was defined as *1 x R, 2 x R, 3 x R and 4 x R* from the midpoint where *R* is the radius of the shot. Figure 4.24 shows the minimum area 3 x *R*.

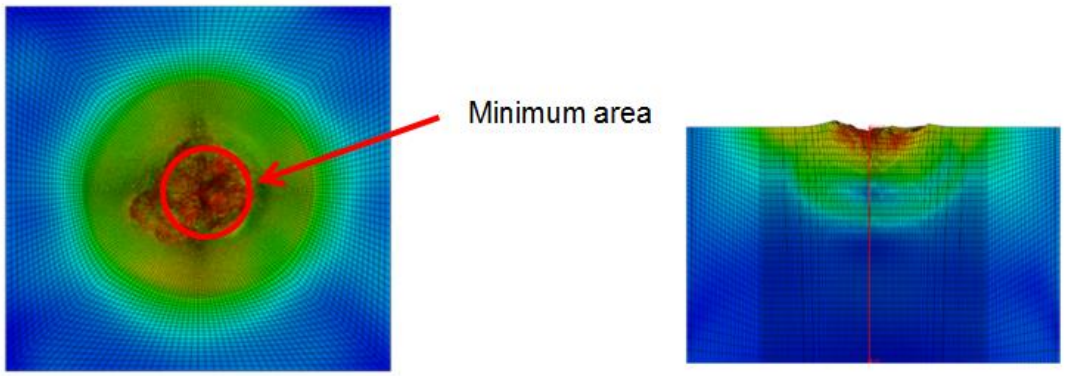

Figure 4.24: Shows the minimum area 3 x *R* and the midpoint at which the CRS is measured.

The CRS is measured at the midpoint and at 3 different points (Midpoint(0,0,0), point 1 (0.1,0,0.1) and point 2 (-0.1,0,-0.1) and point 3 (0.1,0,-0.1)) around the midpoint. The three measurement points lie within the distance of the smallest minimum area *1 X R*. The plastic

strain generated by the high velocity impact varies on the surface layer. Since the surface residual compression progressively relaxed with increased SP coverage, the depth of the CRS layer is consider as the suitable factor to be considered for the different cases. To determine a precise CRS state of the peened material, an average CRS is determined from the four measurements. Table 4.5 shows the CRS for different areas.

Table 4.5: Shows the depth of the CRS zone for different impact area.

Impact Area	1 R	2 R	3 R	4 R
Number of impacts	2	12	35	66
Depth of CRS Zone	0.80mm	0.92mm	0.91mm	0.93mm

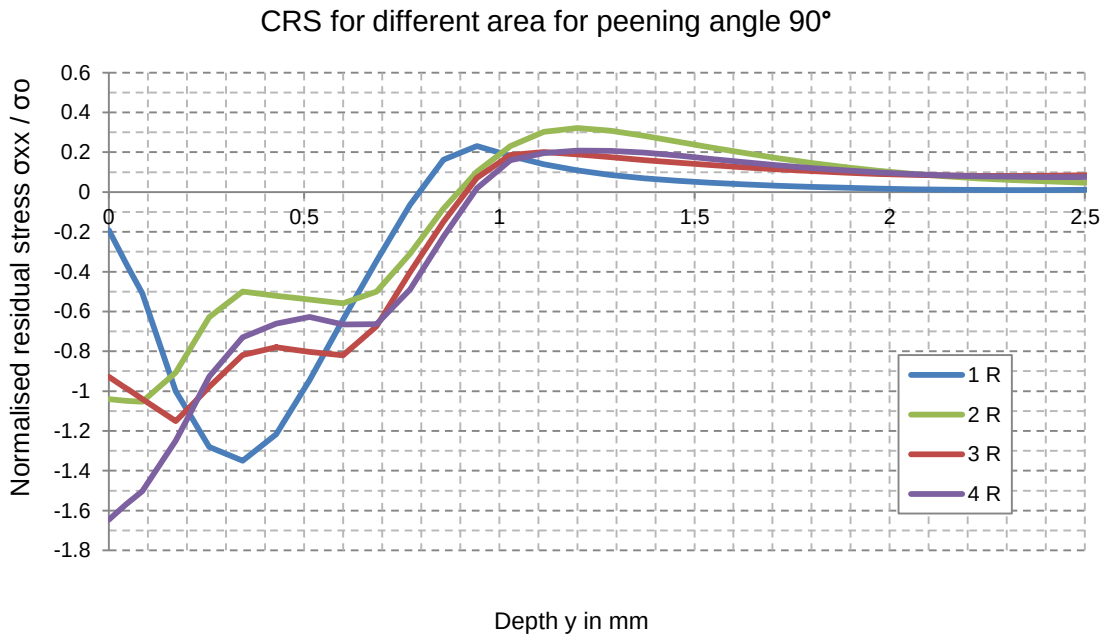

Figure 4.25: Shows the CRS resulting from analysing different area from the same simulation for peening angle θ = 90°.

Evaluating the CRS for different sized areas, it can be noted that the depth of the compressive zone only changes very little when the peening area is greater than 3 x R. The compressive stress at the surface layer varies for the different size areas. Figure 4.25 and Figure 4.26 show the CRS for different area for peening angle $\theta = 90°$ and $\theta = 35°$.

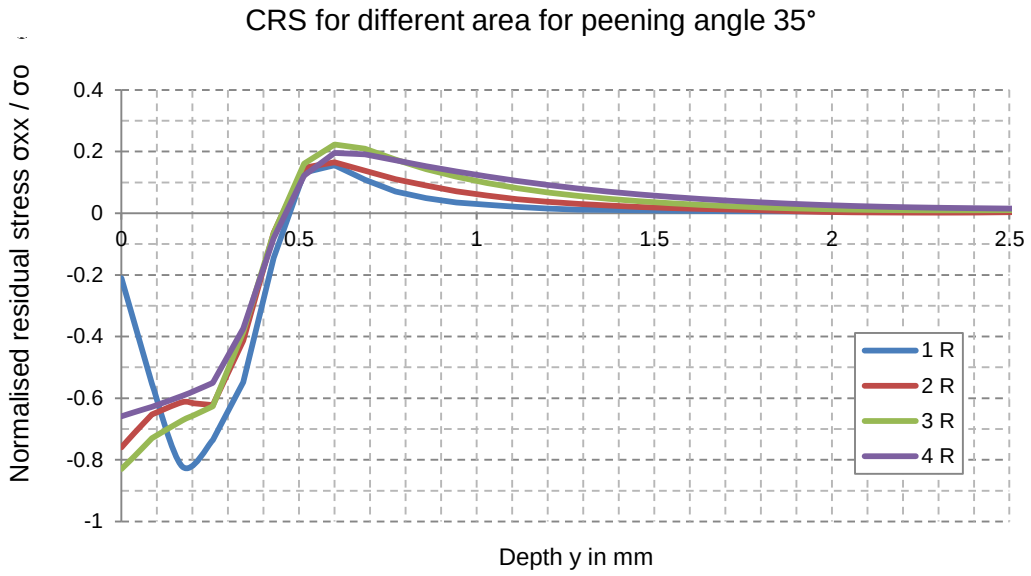

Figure 4.26: Shows the CRS resulting from analysing different area from the same simulation for peening angle 35°.

4.3.2 Effect of COR

Three different simulations were performed to evaluate the effect of standard (0.4), average (0.57) and variable CoR in DEM on the resulting CRS in FEM. Only little variation of the depth of the compressive zone was encountered in the different simulations. Figure 4.27 shows the effect of CoR in DEM on the CRS in FEM.

Table 4.6: the depth of the CRS zone for different CoR in EDEM.

	0.4	**0.57**	**Variable (Table 3.1)**
No. Impacts	35	38	29
Depth of CRS Zone	0.896 mm	0.922 mm	0.882 mm

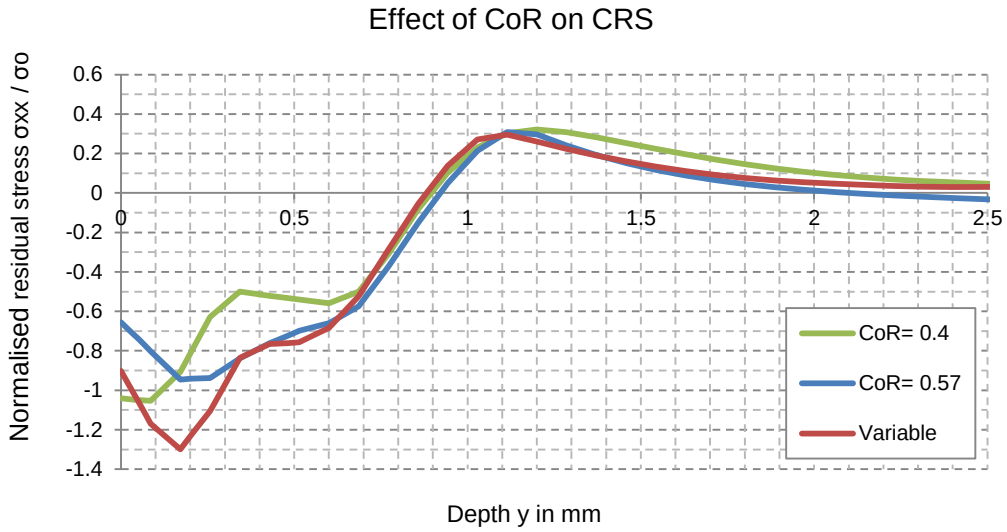

Figure 4.27: Shows the effect of CoR in DEM on the CRS in FEM.

4.3.3 Peening angle

Coupled analyses were performed to investigate the effect of peening angle on CRS. Simulations were performed with the peening angle $\theta = 90°, 75°, 67.5°, 62.5°, 45°$ and $35°$. The peening angle θ has an effect on coverage. A lower penning angle will cover a larger area than peening the component at angle $\theta = 90°$. Figure 4.28 shows the impact location for different peening angles in DEM. CRS results in Figure 4.29 and Table 4.7 show that the CRS zone is large when the angle θ =75° and 90°.

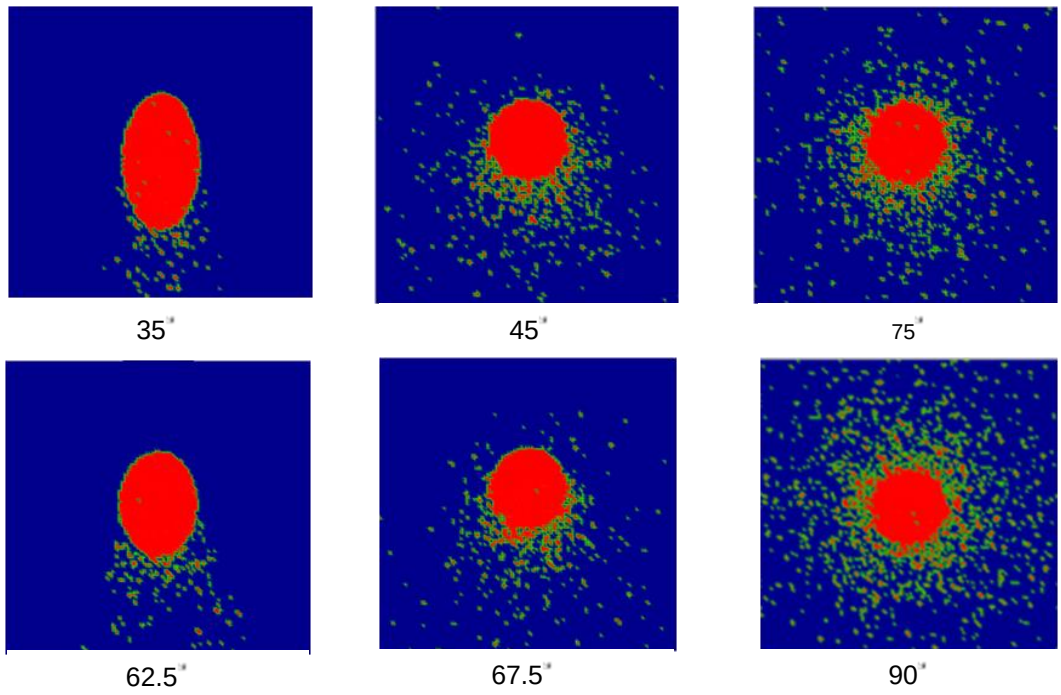

Figure 4.28: Shows the impact location for peening angle in DEM, θ = 35°,45°, 62.5°, 67.5°, 75° and 90°.

Table 4.7: Shows the depth of the CRS zone for different peening angle.

Angle	**35°**	**45°**	**62.5°**	**67.5°**	**75°**	**90°**
No. Impacts	20	30	36	44	40	35
Depth of CRS Zone	0.54 mm	0.59 mm	0.76 mm	0.70 mm	1 mm	90.mm

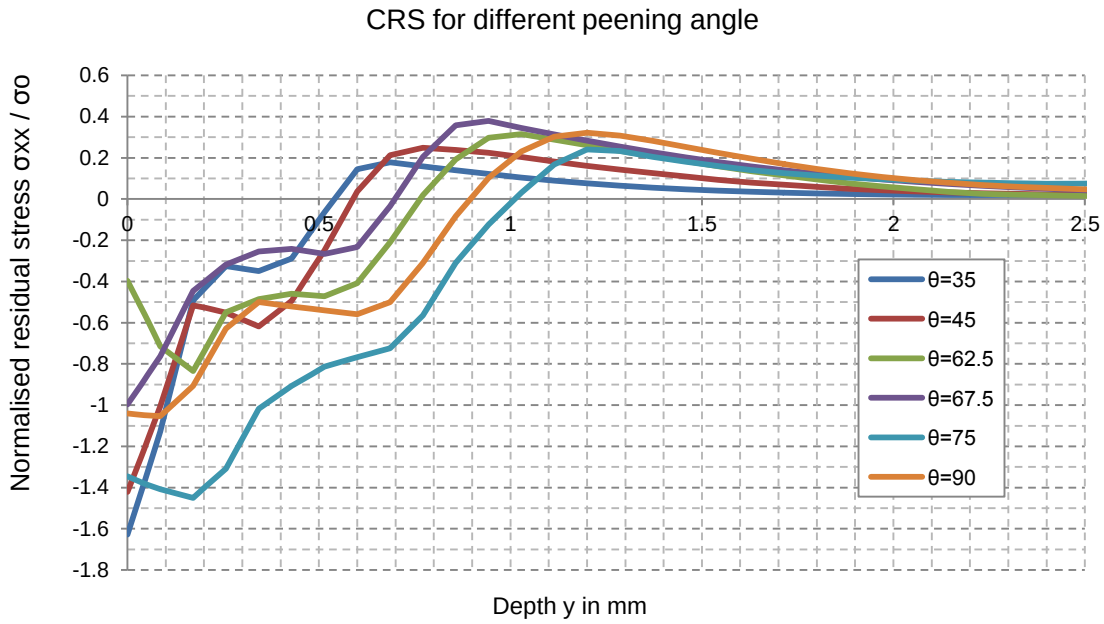

Figure 4.29: Shows the effect of peening angle on the CRS.

4.3.4 Influence of mass flow rate and velocity on CRS

The DEM analyses have shown that for a lower value of ε more shots retain their initial velocity. For the circular area 3 x R, a lower value of γ results in a lower number of shot - target interactions and the number of impacts increases when γ increases. When peening with a lower mass flow rate and lower initial velocity, the shots are delivered more precisely onto the surface. The resulting CRS are analysed for the nine different cases and shown in Figure 4.30. Analysing the resulting CRS graphs for the nine different cases show that for the case where γ is small the CRS zone is large and the CRS zone is small when γ is large. Results also show that when using a higher initial velocity like in cases H4, H7 and H9 the CRS zone is deeper than in cases where a lower initial velocity is applied such as in case H1, H2 and H6.

Table 4.8: Number of impacts for area 3 x *R* for different values of ε adopted from Table 4.1 and corresponding depth of CRS zone.

No	1	2	3	4	5	6	7	8	9
γ g/m	4.333	3.083	2.889	2.167	2.056	1.833	1.542	1.222	0.917
r_m kg/min	13	9.25	13	13	9.25	5.5	9.25	5.5	5.5
V_i m/s	50	50	75	100	75	50	100	75	100
Impacts	48	49	48	37	40	35	31	29	33
Depth of CRS zone in mm	0.54	0.59	1.05	1.14	0.95	0.56	1.05	0.92	1.2

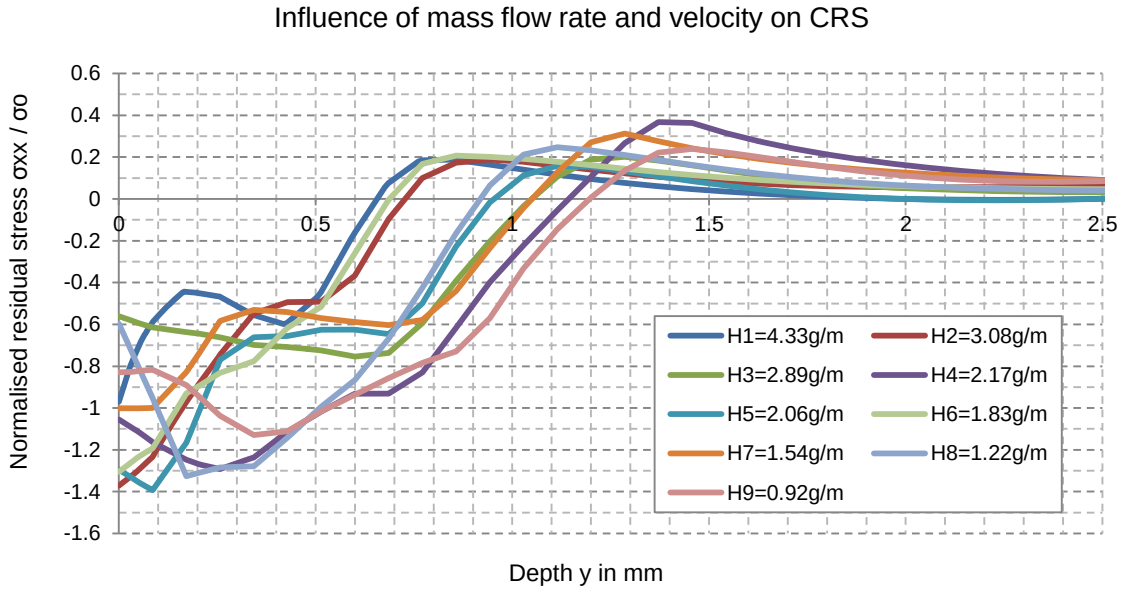

Figure 4.30: Shows the influence of mass flow rate and velocity on CRS.

4.4 Evaluation of alternative methods

Previous work has shown that the Discrete Element Method can increase the fundamental understanding of the SP process, in particular shot -shot collisions and the peening pattern. The Finite Element Method was employed to investigate the resulting Compressive Residual Stresses (CRS). By using the DEM-FEM coupling developed during the first phase of this research and by utilising the commercial codes EDEM and Abaqus, the residual compressive stress profile for any given set of peening parameters and for any given geometry of component can in principle be determined. This method requires the user to provide the geometric surface data in the DEM application and makes a number of simplifying

assumptions, such as the indentation size is equal to the size of the particle. In the previous work, a simulation with 4000 shots impacting a flat surface was performed using the DEM-FEM coupling that took several hours to complete. Furthermore, the current coupling method is computationally very expensive, produces very large output files and requires several operations for the transfer of information between the linked DEM and FEM codes to be carried out manually by the user. Another limitation is due to the fact that users of EDEM and Abaqus have only limited access to source code, because of the commercial nature of both applications.

Hence, having reviewed the capabilities and limitations of the EDEM and Abaqus application, the author concluded that the current software platform has exhausted its scalability and the only way to substantially improve is by exploring other platforms. Several computational aspects for selecting the suitable platform are discussed in the following and areas that generate novelty are proposed.

4.4.1 Selection of software platform

Four different platforms are compared with the aim of choosing the most suitable platform to develop a numerical model for Shot Peening optimisation. The platforms considered are: Abaqus, DEST, EDEM and YADE. Table 4.9 provides a summary of the different applications.

Table 4.9: A summary of the different applications are show below.

Application	Abaqus	DEST	EDEM	YADE
Type	FEM	DEM and FEM	DEM	DEM
Supported Platforms	Windows, Linux	Windows, Linux	Windows, Linux	Mainly Linux
Support	Simulia, widely used		Yes, DEM Simulation	No, but user forum
Programming language support	Fortran	C	C++	C++
Parallel processing	MP and MPI	Shared memory	MPI and MP	MP

Abaqus

Abaqus is a finite element software that could be used on its own to completely model the whole Shot Peening process. However, the simulations have long runtimes, produce very large output files and are therefore not feasible to be run on a single desktop computer. In previous work, researchers have only simulated Shot Peening process involving a handful of shots within a realistic time scales. Abaqus can handle non-spherical particles and allow the implementation of new subroutines (Hibbitt Karlsson and Sorenson 2009). However, these subroutines are limited to constitutive models and creation of user-defined elements.

DEST

DEST is the discrete element method based solver of partial differential equations describing dynamic equilibrium which uses the finite element spatial discretization. It was developed in a flexible integrated programming environment which allows future developments and is very portable, such that it can be run without installation (Petrinic, 1996). Shot Peening modelling in DEST would eliminate repetitive manual steps required to couple the DEM with FEM. However, the performance (speed-up) of the application needs to be evaluated and compared with the coupled DEM-FEM application. The computational aspects of contact detection can be improved and new parallel searching algorithms can be implemented to improve the computational efficiency. In Shot Peening small particles hit the surface at very high velocity often causing the particles to break in several smaller pieces (fragmentation). How a particle breaks depends on the applied impact forces developed during the collisions, the particle size and material properties. Finally, there is an opportunity to develop and parallelise a new hierarchical contact search algorithms which would make it possible to simulate realistic, industrial scale Shot Peening processes within realistic time scales.

EDEM

EDEM is a commercial DEM application. EDEM allows the importation of CAD models of particles and complex geometries. It can handle non-spherical particles and can be coupled directly with CFD (Fluent) software. EDEM also provides data analysis tools and 3D visualisation of particle flow. It comes with an API that allows the user to code and implement their own contact physics, external coupling and particle-generation factories in the form of User Defined Library (UDL).

YADE

YADE is an open-source framework for discrete numerical models, focused on Discrete Element Method (Šmilauer et al., 2010). The application is written in C++ allowing implementation of new algorithm, interfaces with other software packages (e.g. flow simulation), and data import/export routines. Python can be used to create and manipulate the simulation or for post-processing. Table 4.10 summarises the advantages, drawback and opportunities of new developments of the different platforms.

Table 4.10: The table summarises the advantages, drawbacks and opportunities for new developments of the different platforms.

	Abaqus	DEST	EDEM	YADE
Advantages	- Can be used to model non-spherical particles	- Capable of modeling the complete SP process - Portable (can be run without installation)	- Reasonably fast - Can model shot-shot interaction - Parametric analysis - Coupled with CFD and FEM	- Can model shot-shot interaction - New libraries being added by the YADE community. - Supported by community - Python interface
Drawbacks	- Simulating the complete SP is almost impossible - Simulating the complete SP is almost impossible - FEM is very slow and produces large output files		- Can only simulate rigid particle, FEM is required for CRS analysis	- Performance is slow compare to EDEM - Can only simulate rigid particles - Difficult to install, not portable
What developments can be performed?	- Implement new particle shapes, combine rigid and deformable particles - Implement new contact laws - Perform fully coupled	- Implement new contact algorithm for improving accuracy - Implement new contact laws - Implement new particle shapes, combine rigid and deformable particles	- Implement new contact laws - Perform parametric studies - Improve the coupling algorithm - Simulate the shot flow	- Implement new contact laws - Perform parametric studies - Coupling with Abaqus

	analysis with EDEM - Can be used to compare against other software. Singe shot analysis and energy transfer	- Breaking particles - New searching algorithms for improving efficiency - Implement new particles, combined rigid/ deformable particles - Parallelisation algorithms for improving efficiency use of GPUs - Perform parametric studies	using CFD. EDEM can be coupled with FLUENT.	

Having reviewed the different platforms, it can be concluded that DEST is the most suitable platform for creating a tool for Shot Peening optimisation. The main advantages of DEST include the scalability, portability (able to run the application without installation) and the new developments that can be performed. DEST uses open source libraries and can be exported and executed onto another machine using the same operating system. The use of DEST will eliminate any manual pre-processing that is required for the linking/coupling, eliminate the use of two different applications and provide a one off solution for Shot Peening optimisation.

CHAPTER 5 NUMERICAL METHODS - IMPLEMENTATION ASPECTS

The subsequent sections focus on the implementation of the essential tools in DEST required for the enchanced modelling of the Shot Peening process. Firstly, the existing contact search algorithm is evaluated and further improved to incorporate shot insertion and removal. Next, the implementation of essential Shot Peening tools, such as the nozzle, coverage and roughness measurements are discussesed and validated against experimental results published in literature. Finally, an extensive comparison is performed to assess the computational performance of the enhanced contact search algorithm.

5.1 Contact search inprovement

A process that determines whether two or more bodies are in contact is called contact detection or collision detection. Contact detection of moving bodies is an important problem in computational mechanics, particularly in fields such as Discrete Element Method (DEM) and Finite Element Method (FEM). DEM/FEM can be divided into four stages: Object generation, contact detection, calculation of contact tractions and visualization. Figure 5.1 shows the Discrete Element Method and Finite Element application pipeline. The most critical stages of the application process is the contact detection and force calculation, hence it is essential that these stages are processed accurately and efficiently.

Algorithms for contact detection can be grouped into two phases - broad-phase and narrow phase. In the first phase the number of potential contact pairs is reduced with the help of bounding boxes and spatial sorting algorithms. In the second phase a detailed contact check is performed for the resulting potential contact pairs. Performing the contact detection in two phases reduces the computational loads. An overview of contact detection algorithms for both phases of the process is provided by Kockara et al. (2009).

The contact detection algorithm used in this work applies a binary tree structure in combination with a bounding box type search technique with surface facets and is highly optimized for contact detection problems in computational mechanics. It features novel algorithms to insert and remove objects and is well suited for applications such as Shot Peening, grinding mills, fracture and simulations of 3D hopper filling process.

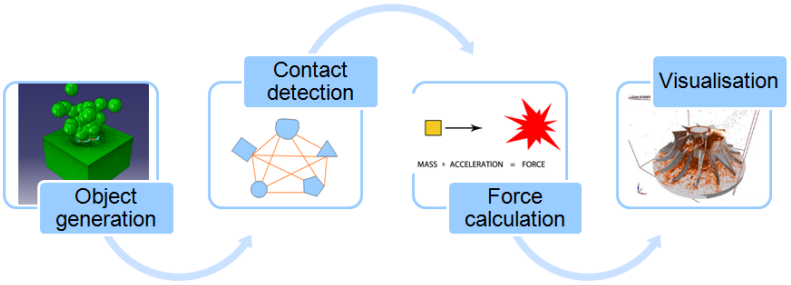

Figure 5.1: Shows the Discrete Element Method and Finite Element application pipeline.

5.1.1 A Multilevel Representation for Contact Resolution

This section reviews existing contact detection approaches and outlines the multilevel contact detection and processing used in this work. The contact interaction process can be divided into four phases: Body location mapping, space bisection, bounding box interaction search and local contact resolution.

Pairs of polyhedral are in contact if their geometrical features such as vertices, edges, or faces are intersecting. The most primitive approach to find the intersection is to check exhaustively for every possible intersection of the geometrical features. Figure 5.4 shows the exhaustive search approach. This approach is well-known to be inefficient and more efficient algorithms have been proposed (Ghaboussi and Barbosa 1990; Eberly 1999; Liu and Lemos 2001). One of the improved methods of reducing the number of intersection computations is to prioritise the check of faces whose normal vectors are pointing toward each other (Keneti et al., 2008). A more efficient way to improve the intersection searching is to create a database in which useful information is stored from the start. Williams and O'Connor (1999)

proposed a method where every facet of an object was defined with a bounding box such that the neighbouring facets potentially in contact can be identified efficiently.

Performing the contact detection in two phases reduces greatly the computational loads (Jiménez et al. 2001; Kockara et al. 2009; Ogarko and Luding 2012). Broad search contact detection can be performed with three different algorithms: all-pair test (exhaustive search Figure 5.4), sweep and prune (coordinate sorting) and hierarchical tables (multi-level grid). The broad phase consist of listing the possible colliding objects and narrow phase inspects the pairs further and determines whether they came in contact and provides more details information such as penetration depth, closest point, etc.

Narrow based algorithm can be grouped into four categories: feature based, simplex-based, volume based, and special data structures (bounding volumes and spatial subdivisions). More advanced types of facet representations are shown in Figure 5.2. Once the facets are defined in some way they need to be spatially sorted before the contact detection can be performed. The next section outlines the different methods of spatial sorting.

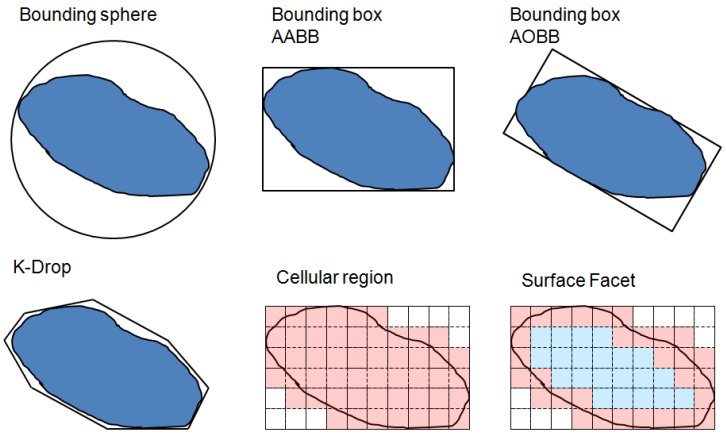

Figure 5.2: Shows the different representation for contact resolution.

Spatial contact detection approaches

Spatial sorting is the identification and sorting of objects that are spatially close to one another at some instant in time. In the first step, the set of objects are spatially ordered using

suitable sorting algorithm. In the next step, the sorted data set is searched for objects situated close to each another. The computational cost of spatial sorting is proportional to the number of objects *n,* and for systems where no assumptions can be made about the location of objects, sorting requires O(*n log n*) operations. The complexity of the determination for contact between two objects can be reduced by using a higher level abstraction for the object geometry, such as bounding spheres or bounding boxes and depends on the way in which the geometry is represented. For lower level abstraction or unstructured boundary representations the complexity is O(n^2). For methods such as Binary Space Partitioning (BSP) trees, the costs can be reduced to O(*n log n*). Figure 5.3 shows the big O complexity for different type of searching and sorting algorithms.

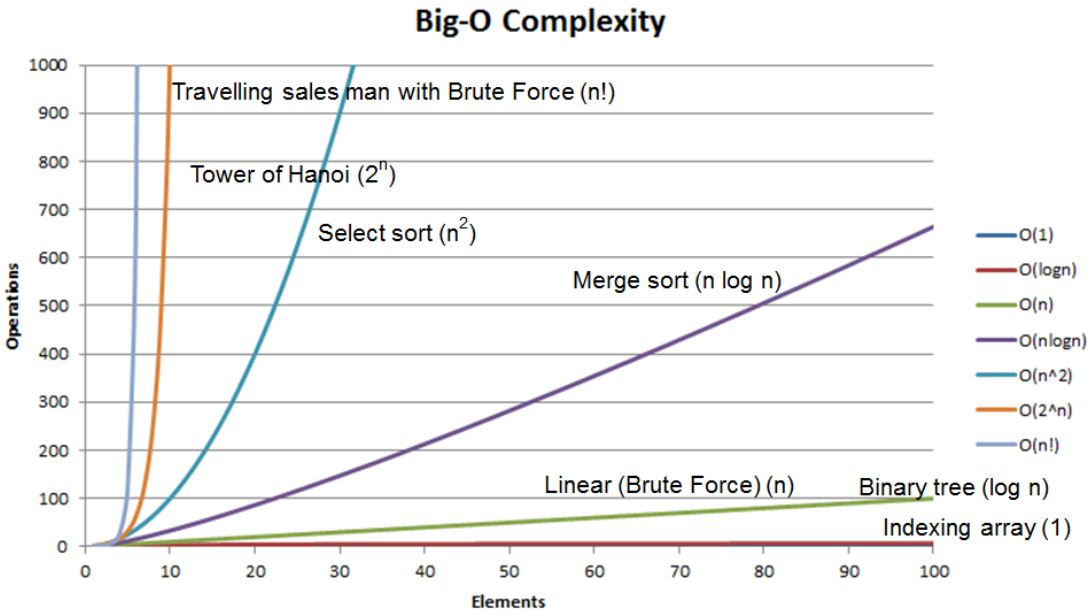

Figure 5.3: Big O complexity for different type of searching algorithms.

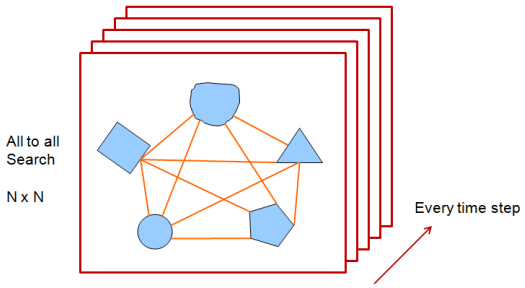

Figure 5.4: Shows the exhaustive inefficient contact detection approach.

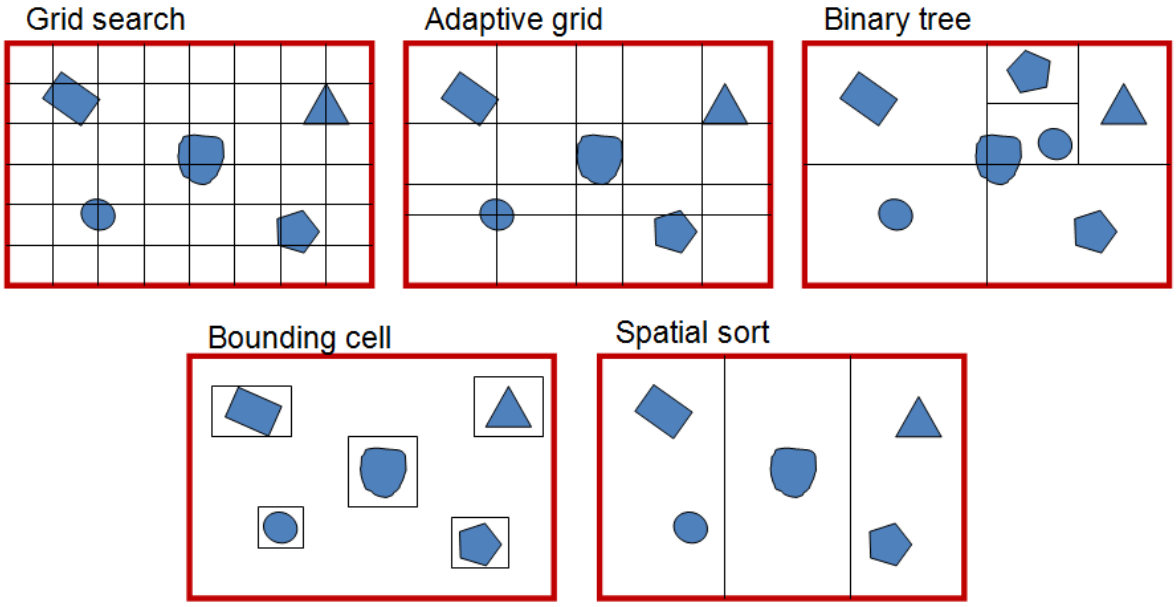

Figure 5.5: Shows the more advanced different broad search contact detection approaches.

Some of the most common and relevant search and sorting methods are outline in the section below.

Grid search method

The grid search method discretizes the simulation volume into rectangular cells. Object in the simulation domain are associated to cells based on their coordinates. For this method it is essential that the object is enclosed by a buffer zone such that the objects close to the cell boundary are encountered. The performance of this method depends purely on the number of object per cell and distribution of objects over the simulation domain. If all objects are in one cell then this method does not provide any advantage.

Adaptive grid methods

In the adaptive grid method, the simulation domain is subdivided into sub-domains by cutting the volume by parallel planes. The advantage of this method is that approximately the same number of objects is on either side of the cutting plane. The disadvantage is that the system needs to manage multiple cell dimensions.

Tree method

A tree-based method uses a tree data structure in which data is stored in some ordered set. The simulation volume is treated as consisting of cells and continuously divided into sub-volumes. Each sub-volume is assigned to one node storing the data of one object. The technique again involves treating the simulation volume as consisting of rectilinear cells, however, in this case only those cells which contain objects are maintained in the tree structure. It should be noted that the search is heavily dependent on how the tree is first constructed. The insertion into the tree should be done in a random fashion, to ensure a relatively uniform distribution of objects, that is, a balanced tree. Minimizing the depth by balancing the branches of the tree can minimise the search. The time to create the tree is of order O($n \log n$) and the time to search this tree is also of order O($n \log n$).

Body based cells

In a body based method the object is bounded by a cell. The centroid of the body is taken to form the bounding cell that can either be a circular, rectilinear or any other type. Objects whose cells overlap are considered potentially in contact and are stored in a list for further computation to establish whether they are in contact.

Spatial sorting

In spatial sorting, the objects are sorted using any other algorithm into cells according to one or more coordinates. Similar to the body based cell method, objects whose cells overlap are considered potentially in contact.

In this work, the BST algorithm is used for the broad search and the detailed body geometry in the narrow search phase to reduce the number of operations that are required to determine the possible contacts in multi body systems.

5.1.2 Binary Search Tree (BST)

In DEST, the BST algorithm is used for the broad search and the bounding volumes in the narrow search phase to reduce the number of operations required determining the possible contacts in multi-body systems (Walizer and Peters 2011; Feng and Owen 2002). Binary trees are one of the most important non-sequential types of data structures. They provide the basis for fast searching algorithms and are widely used for storing a collection of data in various disciplines. Each data item is stored in what is known to be a tree *node* and is extended by addition of two (*left* and *right*) *links* which determine the relation with other data items. This means that from each node of the binary tree it is possible to access at most two other nodes. Furthermore, in order to ensure that every node can be reached, the links are set in such a way that for each node, except for the one known as the *root*, there is one and only one node pointing at it. However, depending on the *root* node, the tree can degenerate where the binary tree holding the structure is unbalanced and thus increasing the average traversal times. Based upon the bounding volume hierarchy (BVH) structures, a BSP tree is generated for each facet group. Then the contact between the facet and the volume holding the facet group is assessed, if there they are not intersecting the search ends. The contact search produces lists for each cell (two facet group pairs) of the upper triangular matrix of potential contacts. Since facets are grouped into facets groups, each cell is one type of contact such as

sphere - sphere or sphere - triangle. Separate potential contact lists, reduce the memory constraints and complexity compared to other methods and can be processed in parallel. In this way the searching process is optimised and searching time is reduced.

Tree generation

Each body in circumscribed with an Axis Aligned Bounding Box (AABB) whose edges are parallel to the global coordinate system axes as shown in Figure 5.6. In 3D a body is represented with two characteristic points' $X_i min$ and $X_i max$.

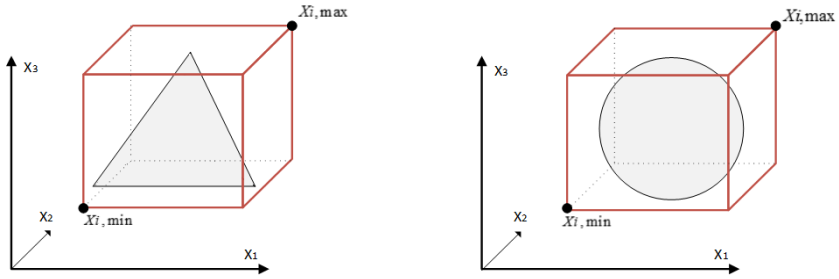

Figure 5.6: Definition of coordinate limits for a body in 3D space.

Having defined the locations of bodies in the R^{2n} space, it is possible to create the data structure to store the information on the bodies' relative spatial position. The data structure created to gather this information should be easy to search through, so that the geometric intersection between bodies can be assessed using as few operations as possible. This paragraph describes the creation of a *binary tree* data structure used to store the information on bodies with respect to their relative position in the R^{2n} space. Figure 5.7 shows the creation of the binary tree space bisection procedure and Algorithm 5.1 describes the BST build process.

Algorithm 5.1: Binary space tree build

```
Loop (over all facets)
{
Set total space bisection coordinates
}

Set first facet as root

Loop (over 1 to N facets)
{
find root facet

        while (search)
        {
        /* Bisect parents space */
        get dimension component
        space = 0.5 * subspace of facet [dimension]

                if (facet coordinates < space)
                {
                        if (left link exits )
                        {
                        get left link
                        }
                        else
                        {
                        set facet as left link
                        set depth of the facet in the tree
                        break
                        }
                }
                else
                {
                        if (right link exits )
                        {
                        get right link
                        }
                        else
                        {
                        set node as right link
                        set depth of the facet in the tree
                        break
                        }
                }
        }
}(all nodes without leafs)
```

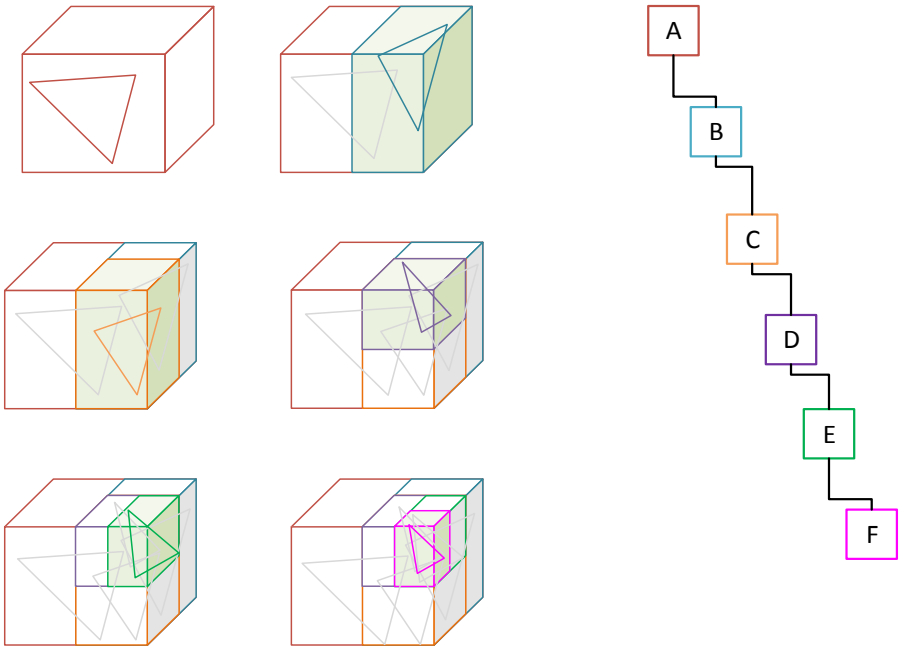

Figure 5.7: Show the creation of the binary tree space bisection procedure.

Each data is stored as a tree node and can have up to two children: left child and right child, and apart from the root node have a parent. Figure 5.8 shows a well-balanced binary tree with tree depth *log(n)/log2*.

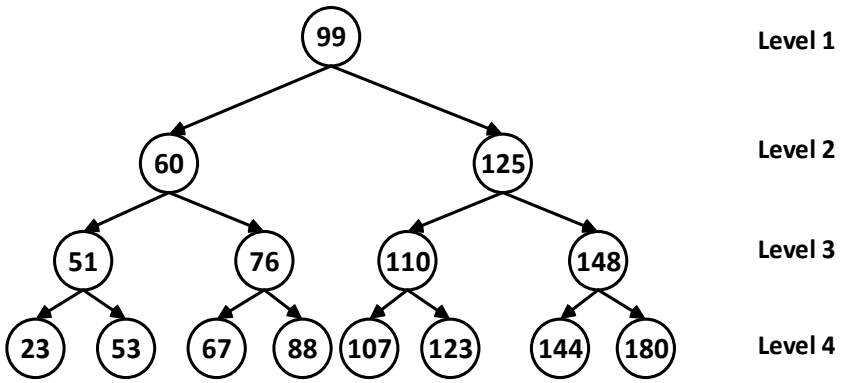

Figure 5.8: Shows a well-balanced binary tree.

In a spatial binary tree, each node is associated with a spatial sub region. The primary operation includes insertion, deletion and the region search. The performance of the operation may depend on the total length/level of the tree.

Bounding box interaction search

The basis for an efficient geometric intersection search algorithm lies in the recursive nature of the space bisection process used to create the binary tree data structure. The data items, stored at tree nodes, contain the information on the bodies' mapped locations in the R^{2n} space as well as the information of the associated bounding sub-regions. The built-in hierarchy of the bounding sub-region provides the key to the fast geometric intersection search algorithm. The bounding sub-region stored at any node of the binary tree supersedes all bounding sub-regions stored at the descending nodes. The following paragraphs illustrate how these features can be effectively used to reduce the computational cost of the geometric intersection search.

A sub-region in (a_i, b_i) in the R^{2n} space, defined as

$$a_i = \left[Y^1_{r,min}, \ldots\ldots, Y^n_{r,min}, X^1_{i,min}, \ldots\ldots, X^n_{i,min}\right]^T$$

$$b_i = \left[X^1_{i,max}, \ldots\ldots, X^n_{i,max}, Y^{n+1}_{r,max}, \ldots\ldots, Y^{2n}_{r,max}\right]^T$$

where the subscript *r* denotes the root node, representing the *search region* associated with the body *i*. In other words, all of the material points inside the bounding box around the body *i* have their location mapping projections inside this region. Furthermore, if the mapped location of a body *k* satisfies the condition

$$a_i^j \leq x_k^j < b_i^j \qquad \text{for } j = 1,2,\ldots\ldots 2n$$

the bounding boxes of bodies *i* and *k* are found to be overlapping. This condition is used while traversing the binary tree in order to generate the short lists of potentially contacting couples for each target body. Here, the body *k* is the *contactor*, while the body *i* is the *target*. For a selected target body, the binary tree traversal always starts from the root node which never plays the role of a contactor. The traversal continues for as long as the target's search

region intersects with the bounding hypercube of the body at the visited node. If this body satisfies the condition, it becomes a contactor to the chosen target body. On the other hand, if the search region does not intersect with the bounding hypercube of the body at a visited node, the whole branch of this body's descendants can be excluded from further search. The number of operations required to accomplish this search is further reduced by comparing only those coordinate components which are associated with the binary tree level at which the traversed node is inserted.

5.1.3 Binary tree balancing

The binary tree is constructed in a random manner and hence does not guarantee that the tree is balanced. Tree balancing can be performed in a number of different ways. Common methods are tree rotation, rebuilding the tree recursively from the median of the in-ordered traversed tree. A well balanced binary tree has the depth $log(n)/log(2)$.

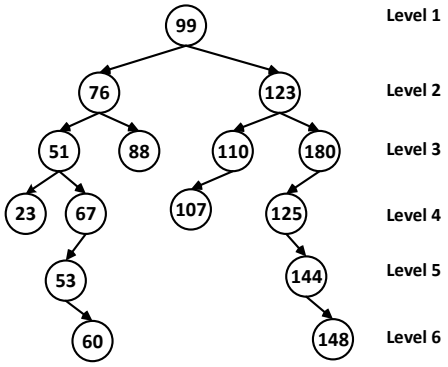

Figure 5.9: Shows an unbalanced binary tree with 6 levels.

Rebuilding from median

Rebuilding the tree from the median requires an in-order traversal of the tree. This can be computationally inefficient as this involves an in-order traversal of costs $O(n)$, and a further $O(log\, n)$ to rebuild the tree, resulting in a total complexity of $O(n\ log\, n)$. Furthermore there is a need to regularly check the length of the tree and rebuild the tree if necessary.

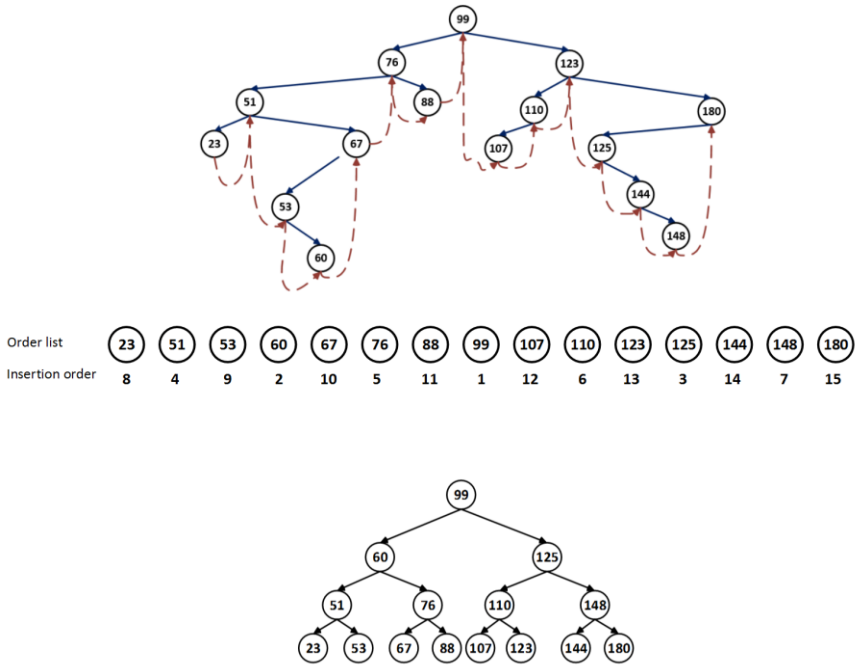

Figure 5.10: Shows the in-order binary tree travel, recursive insertion of the median of the order tree and order binary tree.

Self - balancing

One of the more advanced self-balancing method is AVL (Adelson-Velskii and Landis) (Adelson-Velskii and Landis 1962). In the AVL the height of nodes two child sub-trees can differ by at most one. If they height difference is more than one, rebalancing is performed and the height of nodes is updated. The requirement of rebalancing the sub-tree is determined after and insertion or deletion of a node. There are only four different rotation types, left - right, left - left, right - left and right - right. Insertion and deletion have a complexity $O(log\, n)$. Algorithm 5.2 describes the BST rotation.

Algorithm 5.2: Binary space tree rotation

```
Yfacet = facet
while (Yfacet is not root)
    {
        rotationtype = 0
        balance = depth of left.node - depth of right.node

        If (balance < -1)
        {
```

```
            If (right node of node's left child exists)
            {
            do right-left rotation
            }
            else if (left node of node's left child exists)
            {
            do right rotation
            }
      }
      else if (balance > 1)
      {
            If (right node of node's left child exists)
            {
            do left-right rotation
            }
            else if (left node of node's left child exists)
            {
            do left rotation
            }
      }
}(Yfacet is not root)
```

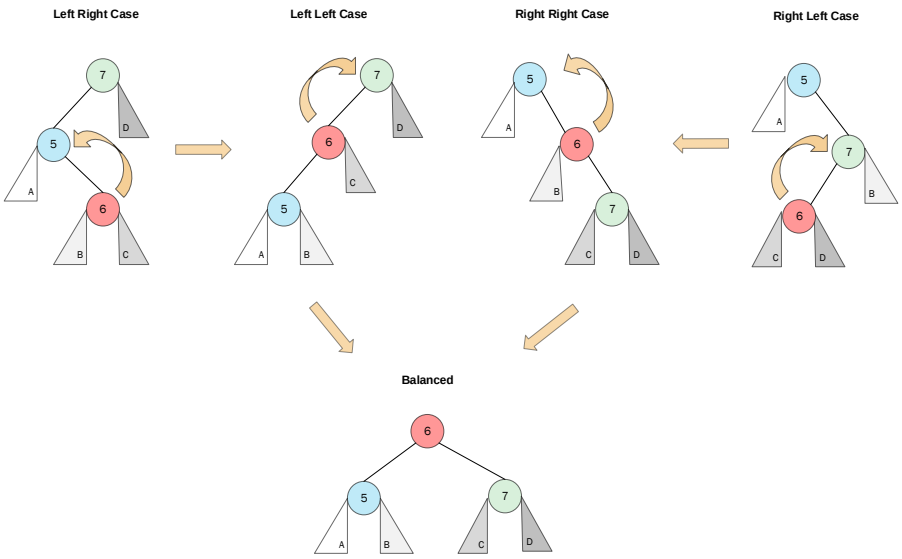

Figure 5.11: Show the different tree rotation methods.

5.1.4 Tightening of associated sub-regions

The bounding box circumscribes the interacting body and is relatively small compared to the simulation domain. Points that are clustered together and not well distributed results in an inefficient balanced tree. These results in poor performance in the tree creation process and in the searching phase. For the leaf note, the associated sub region constrains only the point

stored in the leaf. The associated sub region will be larger than the actual bounding domain of the points stored in the nodes and sub-trees. Tightening of associated sub-regions can reduce the volume of the regions to be searched and reduce the number of possible contacts. A very simple and effective way to tighten the sub-regions is using the bottom-up approach. This algorithm has the complexity $O(n)$. First the nodes that have no left and right children are identified then the dimension of the sub-space of its parent sub-space is expanded to incorporate the child node dimensions and its own facet dimension. This process is repeated until the root facet is reached. This method is very effective and unlike other algorithms can be run in parallel. Figure 5.12 illustrates the tightening of sub regions.

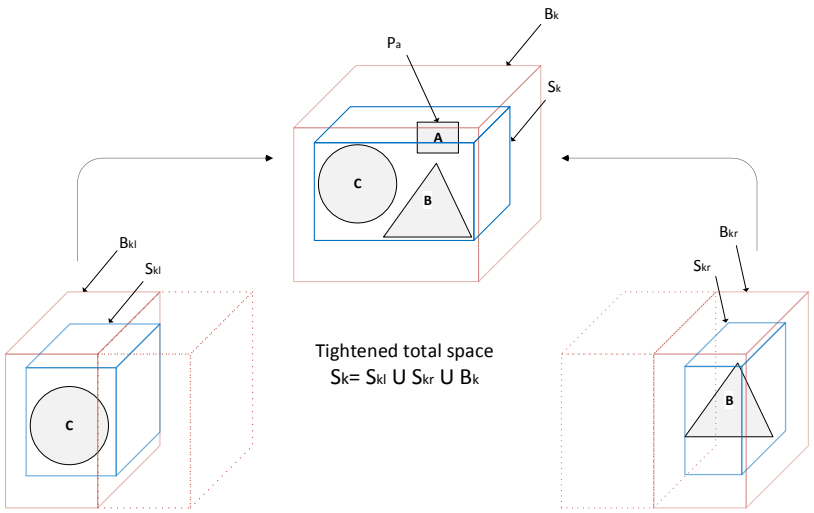

Figure 5.12: Tightening of sub regions.

Algorithm 5.3: Binary tree space tightening

```
for (all nodes without leafs)
{
        While (node==root)
        {
        update node's parent subspace taken into account the subspace of its children
        node = parent node
        }
}(all nodes without leafs)
```

5.1.5 Incremental contact detection

In the combined finite/ discrete element simulation the contact detection is often required to be undertaken very frequently. Creating the binary tree for every single time step can be computationally very expensive. This can be overcome if the subsequent searches after the initial one are performed in an incremental manner. The current search tree structure can be obtained as a modification of the previous structure and some of the search operations can be excluded. Building the entire tree can be avoided by modifying only the sub-trees of the effected nodes. If a particle moves out of its bounding box, the node corresponding to the bounding box can be removed and re-inserted. Deleting a node from the binary tree is a simple process when the node to be deleted is a terminal node. Simply removing the link to its father will render the occupied memory. However if the node to be deleted is an intermediate node, the situation becomes a bit complicated. The unwanted node can be replaced by a terminal node selected from its descendants or by simply modifying the link to suit the new structure of the tree and without moving the memory position. When inserting a new data to the binary tree, a new node must be created and stored in an appropriate memory location. To add a new node, the tree is followed downwards from the root node, until a blank link is found. A link is then set to the memory location of the new node. The insertion and deletion are vital parts of the incremental contact detection algorithm. The removal function is called when the facet has moved out of its subspace and then re-inserted back into the tree and assigned a new sub-space. Figure 5.13 illustrates the process flow of the incremental facet update. The Facet update algorithm, including the insertion and deletion of nodes, is described in Algorithm 5.4.

Algorithm 5.4: Binary space update

for *(no. of facets)*
{
if *(facet has moved out of its subspace)*
{
remove the node using ***Algorithm 5.5***
insert the node using ***Algorithm 5.6***
balance tree as required using ***Algorithm 5.2***
tightening required
}
}

If *(tightening required) tighten subspace using bottom up approach*
{
tighten subspace using ***Algorithm 5.3***
}

Algorithm 5.5: Binary space tree node insertion

Let *node X* be the node with the new value to be added and *node Y* the root node.

Steps performed to add a new node;

1. If *node X* is smaller than *node Y (root) then*
   if *node Y* has a left sub-tree then root's left child becomes the new root *node Y*.
   (Go back to step 1).
   else *node X* becomes root's left child. (Go to step 2).
   else (*node X* is larger than *node Y (root))*
   if *node Y* has a right sub-tree then root's right child becomes the new root *node Y*.
   (Go back to step 1).
   else *node X* becomes root's right child. (Go to step 2).

2. Starting with the *node X's* parent, retrace the path back to the root, adjusting the node balance of it right and left children as needed.

Algorithm 5.6: Binary space tree node deletion

Let *node X* to be node with the values to be deleted, *node Y* the replacement node and *node Z* copy of *node X*.
Steps performed when deleting a node;

3. If *node X* is a leaf node or has only one child, go to step 5. (*node Z* will be new *node X*)
4. Otherwise, find *node Y* by searching the largest node in *node X's* left sub tree (in-order search) or the smallest node in its right sub tree (in-order search).
5. Replace *node X* with the *node Y*. (*node X* is deleted)
6. Select *node Z* to be the *node Y*.
7. If *node Z* has a sub-tree then attach sub-tree to its parent. If has no parent *node Z's* before the root.

8. Delete *node Z*.
9. Starting with the node Z's parent, retrace the path back the root, adjusting the node balance of it right and left children as needed.

As with all binary trees, a node's in-order successor is the left-most child of its right sub-tree, and a node's in-order predecessor is the right-most child of its left sub-tree. In both cases the node will have zero or one children and deleting the node will result in one of the two simpler cases.

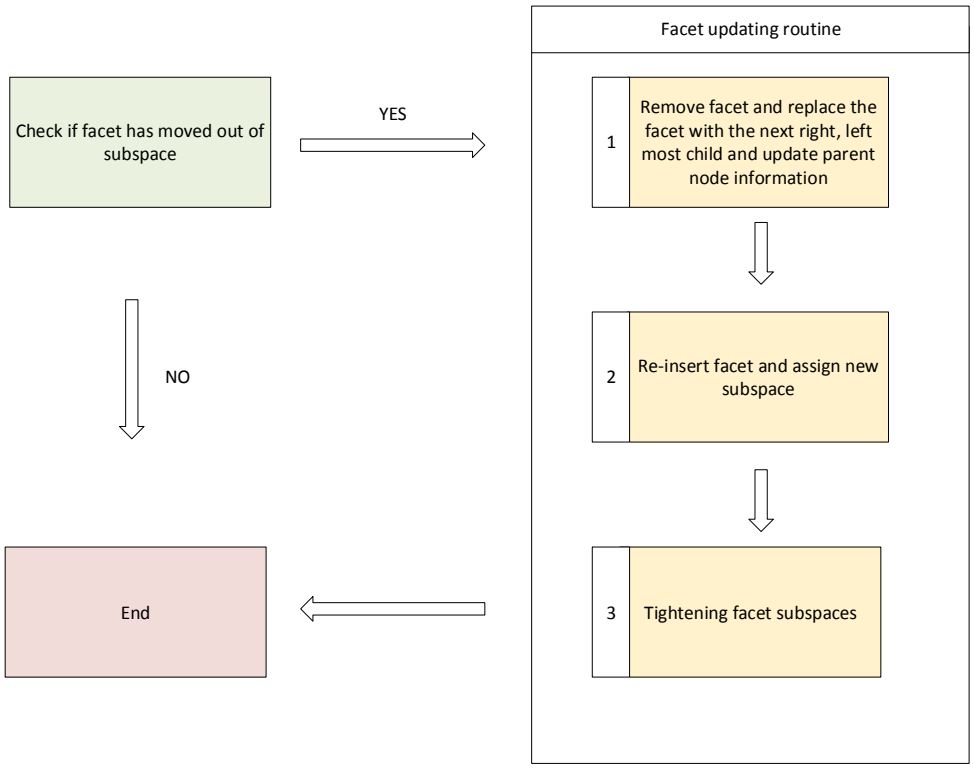

Figure 5.13: Process flow of incremental update of facets.

The validation of the novel binary tree updating is outlined in the section 5.1.6 below and a more extensive performance evaluation is reviewed in section 5.5 Performance comparison.

5.1.6 Validation of improved binary space tree

To validate the improved binary space tree updating algorithm a simple wave propagation problem with seven spheres is assessed. The spheres are placed aligned along the x-axis and a force is applied to the first sphere. The simulations are run with the ordinary and improved algorithms and the binary tree of both versions are accessed. Figure 5.14 illustrates the test case.

Figure 5.14: Illustration of the binary tree assessment test case.

The complexity of the determination of the number of contacts for the case using the bounding box approach can be expressed using the big O notation. A very naive approach has a complexity of $O(n^2 - n)$. For 7 elements this would results in a minimum of 7^2 - 7 = 42 computations in term of node visits. A simple $O\left(\frac{n^2-n}{2}\right)$ would result in a minimum of $\frac{7^2-7}{2}$ = 21 computations. The contact detection using the improved binary tree search for this particular case study is determined in 9 computations. Figure 5.15 illustrates the number of computations required to resolve the contact detection for the test case.

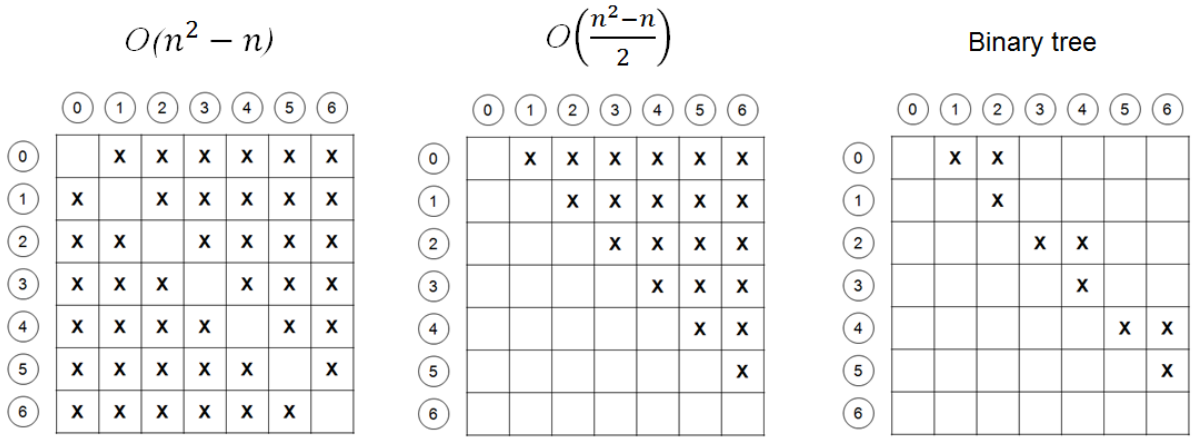

Figure 5.15: Number of computation for different algorithms to resolve the contact detection for the test case.

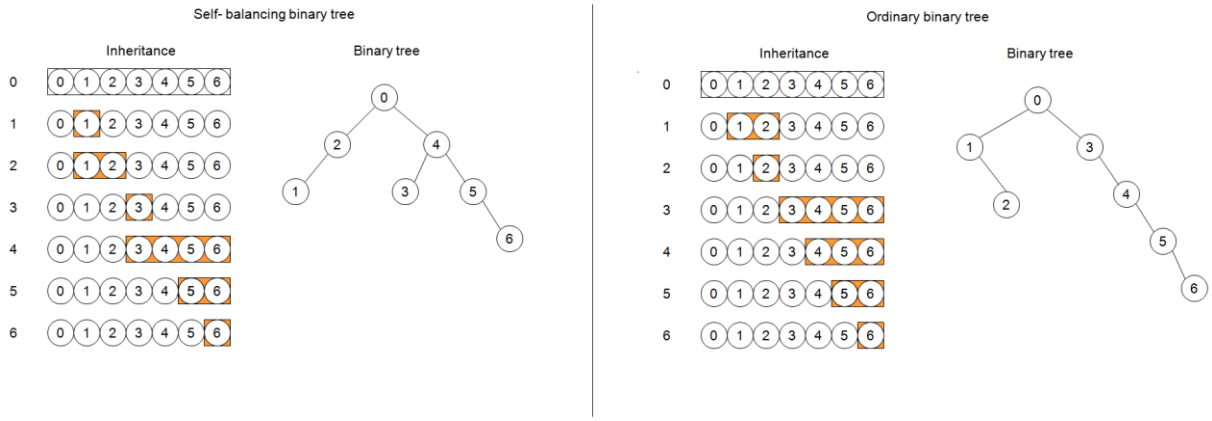

Figure 5.16: Generated binary trees for the test case.

Figure 5.16 shows the self-balanced and ordinary binary tree built for the test case. The orange rectangle boxes indicate the inheritance of the nodes. A better-balanced tree would have a lower number of orange boxes. With the regular binary tree algorithm the whole tree is rebuilt once a single facet has moved out of its buffer zone. With the improved self-balancing algorithm, only the facet which moves out of the buffer zone is removed and re-inserted into the tree. At the same time, the algorithm ensures that the tree is kept balanced. For the particular test case, the self-balancing tree algorithm results in a tree depth of 4 nodes and during the particle interaction phase it is further reduced to a depth of 3, whereas the ordinary algorithm stays constant with a depth of 5 nodes. Figure 5.17 b. illustrates the number of facet updates over the simulation steps for the different algorithms. The number of facet updates is reduced with the improved algorithm as only the facets that are moved outside of the buffer zone are updated.

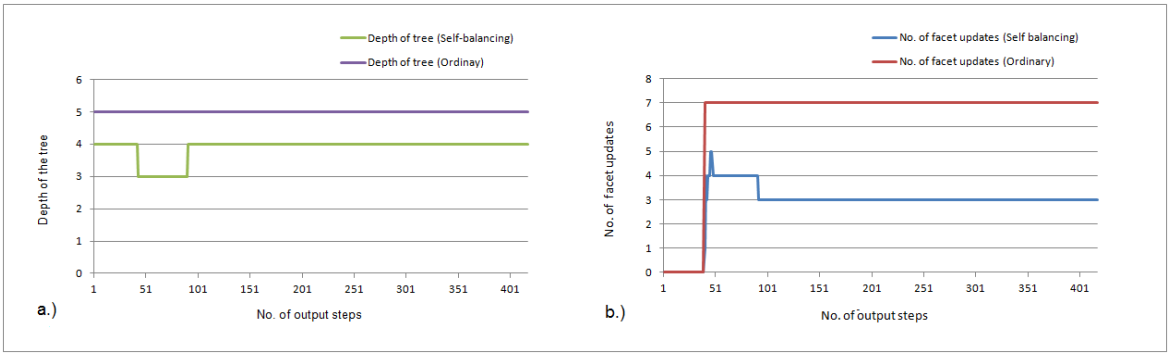

Figure 5.17: Comparison of the ordinary and self-balancing binary tree in terms of depth of the tree and no. of facet updates.

5.2 Local contact interaction

Contact interaction is the final phase of the contact detection procedure. In this phase the actual shape of the interacting bodies is taken into account to determine the surface tractions arising from contacts between the interacting bodies. In the previous phase the improved fast binary search tree and the fast bounding box geometric search technique were applied to generate a shot list of potential contact pairs. To determine if the bodies really intersect a detailed geometric description of the bodies is required. In the finite element method, the surfaces of the bodies are approximated using polygons and polyhedrons in 2D and 3D space respectively. Using the outer facets for contact rather than the whole body simplifies the local contact resolution phase. There are various methods that can be used to define the surface tractions arising from contacts between interacting bodies.

These methods can be divided into two groups according to the way in which the method determines the normal contact tractions. The first group of techniques is based on the Hertz theory which demands that geometric and material properties of the interacting bodies are used to derive the normal contact stiffness (Hertz, 1896). The other group of technique considers the interpenetration to be physically inadmissible and requires an additional force to be applied in order to prevent any overlap between the interacting contacting bodies.

In this work a penalty method based on the Hertz theory is applied. The Herzian method allows for the interacting bodies to penetrate and uses the size and the shape of their fairly small overlap to define the contact tractions.

Buffer zone

The time step increment ensures the stability of the explicit time integration scheme. However in some cases the time step may still be too large to take into account the detection of the contracts during the calculation time step. The velocity of the bodies can be large enough to allow the bodies to fly through each other. To prevent this from happening, the time step needs to be reduced. In order to reduce the time step with respect to the velocities of the bodies, a buffer zone is introduced as illustrated in Figure 5.18.

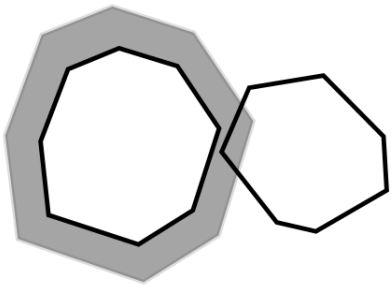

Figure 5.18: Illustration of the buffer zone.

To prevent the bodies from "flying through" one another, the time step increment must be checked to satisfy the following condition

Eq. 5.1

$$\Delta t \leq \frac{d_{bz}}{v_{max}}$$

where d_{bz} is the is the buffer zone thickness and v_{max} is the largest velocity observed

When two bodies intruding each other's buffer zone, a time step reduction is performed to satisfy the condition in Eq.5.1. To keep the accuracy of the numerical solution, the difference

explicit time integration scheme requires an impulse loading to be treated over at least 20 steps. The time step increment should satisfy the following condition.

Eq. 5.2

$$\Delta t \leq \frac{\frac{d^2}{d_{bz}} + d_{cz}\left(1 - \frac{d^2}{d_{bz}^2}\right)}{v_r^n}$$

where d is the current distance between bodies, d_{bz} is the buffer zone thickness, d_{cz} is the contact zone thickness and v_r^n is the relative normal velocity between interacting bodies. The condition above ensures a slow change of the time increment during contact satisfying the condition of the minimum number of time steps over an impulse load and maintaining the accuracy of the solution. In the central difference explicit time stepping scheme, a contract between two discrete elements is detected when these elements are found to be partially overlapping. In DEST the penalty method based on the deformation theories proposed by Hertz (1896) is applied to determine the contact tractions. It is assumed that the size of the overlap of the contact domain is sufficiently small, such that the deformation is represented by the overlap of the elements. The surface tractions are calculated by considering each contacting body to be a semi-infinite deformable solid and are determined by solving the equilibrium and compatibility equations at the interface. A more detailed description of the contact interaction between sphere - sphere and sphere - triangle is given in the next section.

5.2.1 Sphere - Sphere

The contact between two spherical discrete elements is the simplest form of contact. The contact can be evaluated from the Winkler elastic foundation model and can be tuned directly against the well-known Hertz's law. The contact is symmetric and the contract resolution only requires only the material constants, the radii of the spheres and the contact radius.

The Winkler elastic foundation model for two spheres in contact is given by

Eq. 5.3

$$F = \frac{\pi}{4}\left(\frac{kr}{h}\right)\left(\frac{R_1 + R_2}{R_1 R_2}\right)r^3$$

where K is the stiffness of the foundation springs, h is the length of the springs, R_i is the radius of the respective spheres and r is the radius of the circle in the contact plane.

By comparing against the result from Hertz's law, it can be shown that

Eq. 5.4

$$\frac{K}{h} = \frac{16}{3\pi}\frac{E_1 E_2}{E_1(1-v_2^2) + E_1(1-v_1^2)}\frac{1}{r}$$

where E_i and v_i are the Young's modulus and Poisson's ratio of the respective surfaces.

This leads to the force to be applied to the spheres as

Eq. 5.5

$$F = \frac{4}{3}\left(\frac{E_1 E_2}{E_1(1-v_2^2) + E_1(1-v_1^2)}\right)\left(\frac{R_1 + R_2}{R_1 R_2}\right)r^3$$

5.2.2 Sphere - Triangle

The next complexity stage for contact is the contact between spherical discrete elements and triangular facets. The contact can be constructed from finite elements, where a tetrahedral element can be represented with triangular facets. Similarly, a hexahedral element can be represented with quadratic faces. To utilise the same contact algorithm the quadratic faces were split into four triangular facets. The Hertzian law is used to adapt the Winkler elastic foundation model for the contact between the spherical and triangular facets. By considering the limit where one of the radii tends to infinity, (Eq. 5.5) results in

Eq. 5.6

$$F = \frac{4}{3}\left(\frac{E_1 E_2}{E_1(1-v_2^2) + E_1(1-v_1^2)}\right)\left(\frac{r^3}{R_1}\right)$$

where r is the radius of the circle on the plane of intersection with the sphere.

Comparing with a sphere - sphere the sphere - triangle contact is not symmetric and determining the contact forces is complex. In addition to the material constants, overlap distance and radius of the sphere for the sphere - sphere interaction, the intersected volume must be found to resolve the sphere - triangle contact. The equation Eq. 5.6 is valid for facets completely intersecting the sphere and is transformed to the more general equation Eq. 5.7 which allows for facets only partially intersecting the sphere.

Eq. 5.7

$$F = \frac{16}{3\pi}\left(\frac{E_1 E_2}{E_1(1-v_2^2) + E_1(1-v_1^2)}\right)\frac{1}{r}V_{int}$$

where V_{int} is the volume of intersection.

The volume of interest is the portion of the sphere below the area of intersection as described in Figure 5.19.

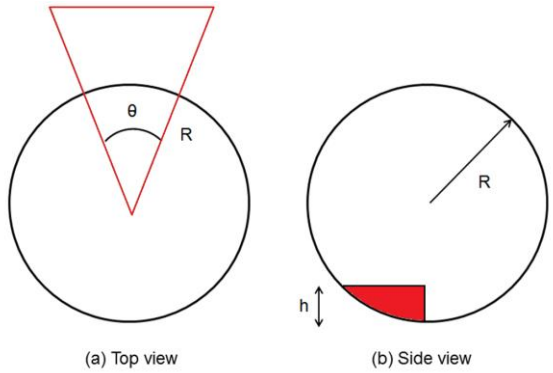

Figure 5.19: Examples of a triangular facet intersecting a sphere with one node along.

From the intersection of the sphere and triangle a number of shapes can arise at the plane of intersection. The volume for the in entire intersection can be easily determined by subdividing the complex shape into circular sectors and triangles.

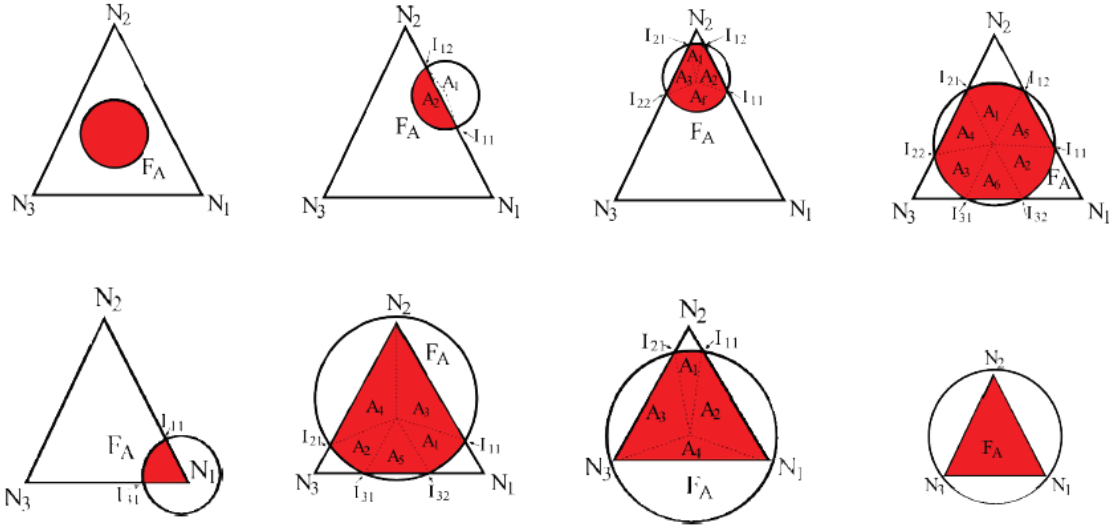

Figure 5.20: Illustrates the 8 different shapes arising from the sphere - triangle intersection after (Schwindt, 2009).

The contact resolution of a sphere and a triangle intersection and a more detailed description of the implemented contact algorithm can be found in (Schwindt, 2009).

5.3 Implementation of Shot Peening features

5.3.1 Nozzle implementation

A nozzle is a type of a particle factory that generates particles and places them on the geometric plane and assigns them a predefined velocity. The proposed implementation should support multiple dynamic particle factories, such that the simulation of multiple dynamic nozzles can be performed. The implementation takes into account a number of input parameters, that control the nozzle such as the mass to be generated, maximum number of particles, particle generation time, initial velocity, material type, particle creation interval and nozzle coordinates and orientation. The input parameters for the nozzle implementation are explained in the Table 5.1 below.

Table 5.1: Nozzle input parameters.

Parameter	Details
Mass to be generated	This creates as many particles as will fit on the chosen geometry section for the time span between the current and previous time until the total mass for the simulation has been reached. If no mass limit is set then the factory should attempt to create particles continuously from the specified start time until the end of the simulation.
Number of particles	Target number - Define the number of particles the simulator will attempt to place in or on the section every second. Target mass - When simulation starts, this rate is converted into mass per-time step. If this is less than the smallest particle mass, the factory does not create a particle but adds the mass to the mass for the next time step. Once there's enough mass, the factory creates a particle. If the mass per-time step is greater than the smallest particle mass, the factory places particles until it reaches the mass per time step.
Start time - end time	Set the time particle creation starts and ends
Max attempts to place particle	The particle factory should attempt to place the particles in a random position on the circular plane. If placing the particle in that position would cause an overlap with any other physical element in the model, the generation algorithm should abandon the position and try to find another valid position. To avoid the generation to end up in an endless loop, only a fixed number of attempts should be carried out.
Velocity	Particles can be given a velocity at the time of creation.
Orientation of plane	The circular factory plane can be given an orientation.
Material type	The material number of the nozzles.
Time step	Time step at which the particles should be generated
Nozzle node	The nozzle node refers to a single node defined in the input file.
Element group	Element group of the particles to be generated.

Particle generation

The number of particles to be generated is defined by the following definition;

Eq. 5.8

$$\text{If } \big((Tc - Tp\,) > Tn\big)$$
$$\text{If } (Tm > Gm)$$
$$Np = Nm \,/\, Pm \,/\, Tn + Op$$

where

Np = No. of particles to be generated
Op = Overflow particles from previous generation
Tp = Time of previous particle generation
Tc = Current time
Tn = Time step for particle generation
Nm = Nozzle mass flow rate
Pm = Particle mass
Gm = Generated mass
Tm = Total mass to be generated

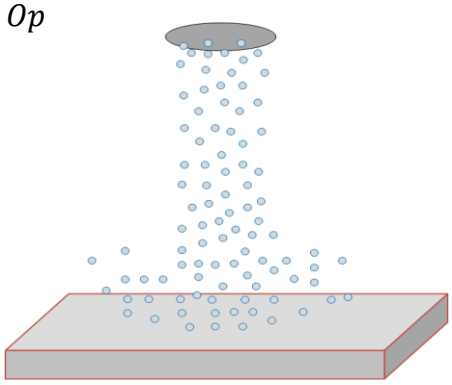

Once the number of particles to be generated is determined, the particles are placed onto the circular nozzle plane in a random manner. First the particles are placed onto a 2D nozzle plane in some random location, where the radius of the nozzle is reduced by the radius of the shot size. In the second step the particle location is rotated according to the defined nozzle angle. In the final step, it is then checked if the new particle causes an overlap with any other physical element in the model. If the new particle overlaps with another object, the generation algorithm abandons the position and tries to find another valid position. To avoid the generation to end up in an endless loop, only a fixed number of attempts should be carried out. This could occur if the mass flow rate is higher than the maximum nozzle output of the nozzle.

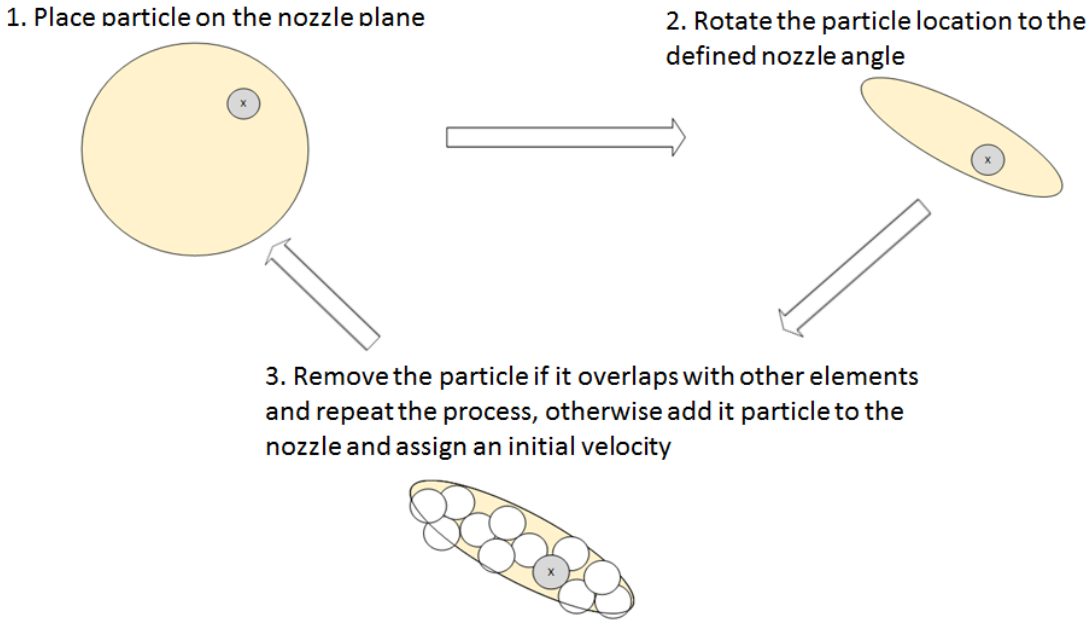

Figure 5.21: Illustration of the particle generation procedure.

Algorithm 5.7: Nozzle (Particle generation)

if (*nozzle is active)*
  if *(nozzle active time is valid)*
    if *((current time - last time particles were generated) > particle generation interval)*
      if *(nozzle maximum number of shots has not been reached)*
        if *(nozzle maximum mass has not been reached)*
          no. new particles = calculate no. of shots to be generated with equation ***Eq. 5.8*** *+*
            over flow particles

          if *(new particles need to be generated)*

```
    if (no. new particles > (maximum number of shots set - no. of shots generated))
      no. new particles = maximum number of shots set - no. of shots generated

   for ( loop over the no. of new particles)

      no. tries to place particle[no new particles] = no tries to place particle
                                                      [no new particles] + 1

      if (no tries to place particle [no new particles] > max. no. of tries to set particle)
           overflow particles = particles generated -1;
       else
            angle1 = random angle (0..360);
            angle2 = random angle (0..360);
            radius =  random(0...nozzle radius);
            new particle coor x [no new particles] = radius * sin(angle1) * PI/180;
            new particle coor y [no new particles] = radius * cos(angle1) *  PI/180;
            new particle coor z [no new particles] = 0;

           /*Transform coordinates of particles to Nozzle coordinates*/
           tempx = new particle coor x [no new particles];
           tempy = new particle coor y [no new particles];
           tempz = new particle coor z [no new particles];

/*Transform coordinates of particles to Nozzle origin (X,Y,Z rotation)*/
if(x rotation is defined)
{
new particle coor y [no new particles] = (tempy * cos(x rotation angle)) - (tempz * sin(x rotation angle));
new particle coor z [no new particles] = (tempy * cos(x rotation angle)) - (tempz * sin(x rotation angle));
tempy = new particle coor y [no new particles];
tempz = new particle coor z [no new particles];
}

if(y rotation is defined)
{
new particle coor x [no new particles] = (tempx * cos(y rotation angle)) - (tempz * sin(y rotation angle));
new particle coor z [no new particles] = (tempx * cos(y rotation angle)) - (tempz * sin(y rotation angle));
tempx = new particle coor x [no new particles];
tempz = new particle coor z [no new particles];
}

if(z rotation is defined)
{
new particle coor x [no new particles] = (tempx * cos(z rotation angle)) - (tempy * sin(z rotation angle));
new particle coor y [no new particles] = (tempx * cos(z rotation angle)) - (tempy * sin(z rotation angle));
tempx = new particle coor x [no new particles];
tempy = new particle coor y [no new particles];
}

/*Check if new particle is in contact with other particles on the nozzle plane*/
new particle coor x [no new particles] = new particle coor x [no new particles] + nozzle coor x;
new particle coor y [no new particles] = new particle coor y [no new particles] + nozzle coor y;
new particle coor z [no new particles] = new particle coor z [no new particles] + nozzle coor z;

material [new particle] = material
velocity [new particle] = velocity

(loop through the new particles generated j is in contact with any other body)
{
xd = new particle coor x[current] - new particle coor x[j];
yd = new particle coor y[current] - new particle coor y[j];
zd = new particle coor z[current] - new particle coor z[j];

distance = square root (xd*xd + yd*yd + zd*zd);
```

```
if (distance <= (new particle radius [current]  + new particle radius[j]))
        {
        j=j-1;
        goto outer loop; /*discard the new coordinates for particle*/
        }
}

for (loop through all element groups)
{
        if (element group is of type sphere)
        {
        inode = db->elgrp[ielgrp].lanods[n][0];
        xd = new particle coor x[inode] - new particle coor x[j];
        yd = new particle coor y[inode] - new particle coor y[j];
        zd = new particle coor z[inode] - new particle coor z[j];

        if (distance <= (new particle radius [inode]  + new particle radius[j]))
        {
        j=j-1;
        goto outer loop; /*discard the new coordinates for particle*/
        }
        }
}(loop through all element groups

outer:; (outer loop exit)

} ( loop over the no. of new particles)

    total particles generated = total particles generated + particles generated
    total mass generated = total mass generated + particles generated * particle mass
    over flow particles = no new particles - particles generated
    last time particle generated = current time

        end if (nozzle maximum mass has not been reached)
       end if (nozzle maximum number)
      end if (check if time step is large enough to generate particles)
end loop
```

Verification

Verification of the nozzle is performed by examining the participle location distribution and monitoring the particle generation mass flow rate over time. For the validation case a simulation of a nozzle generating 1000 particles is assessed. The following simulation parameters were used in the assessment:

Table 5.2: Input parameters nozzle validation.

Nozzle radius	5mm
Particle radius	0.3mm
Nozzle mass flow rate	0.0001 kg/s
Initial velocity of particles	0 -50 0 in m/s
Time step at which particles are generated	0.00001 in seconds

Maximum tries to place particle on nozzle plane	100
Define fixed number of particles to be generated	1000
Define mass to be generated	8 kg

From Figure 5.22 it can be observed that the distribution of particle locations on the nozzle plane is uniform. The nozzle generates a constant and stable rate of mass where the mass generation increases linear over time. Figure 5.23 shows the nozzle mass generation over time.

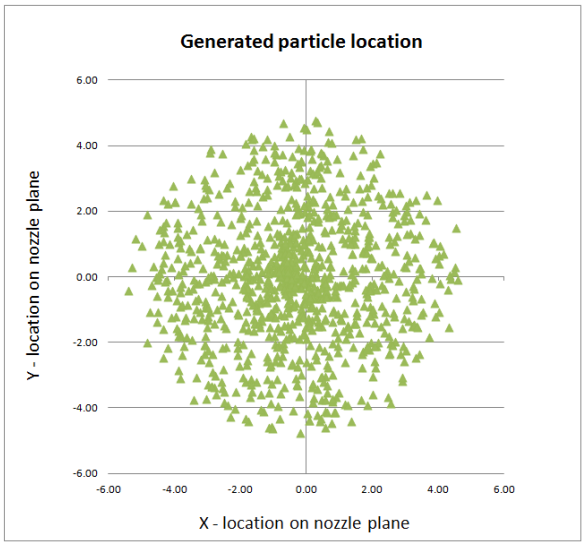

Figure 5.22 : Distribution of particle location on nozzle plane with 1000 data points.

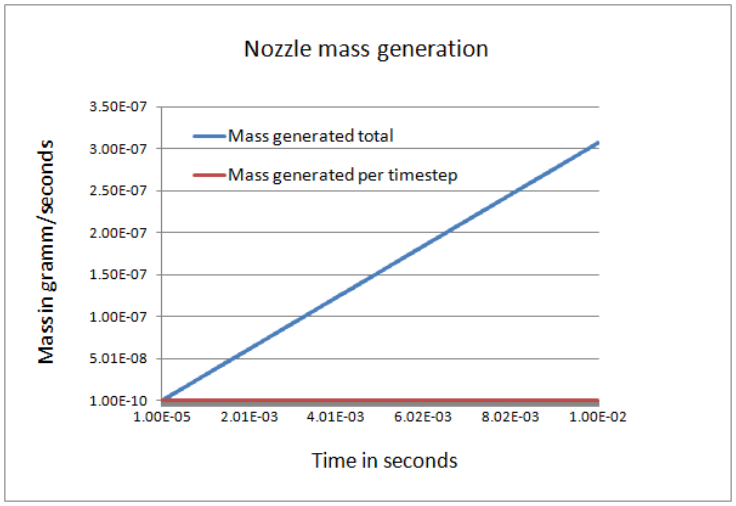

Figure 5.23: Nozzle mass generation over time.

5.3.2 Bounding box (Shot removal)

The bounding box is the volume where the simulation takes place. Particles that move out of the domain during the course of the simulation are permanently removed. Other geometries can move in and out of the bounding box during a simulation. The bounding box has an effect on the overall Shot Peening simulation time - the larger the simulation domain, the more particles will be in the simulation, resulting in longer computation time. The input parameters for the bounding box are presented in Table 5.3. The algorithm for the bounding box is outlined in Algorithm 5.8.

Table 5.3 : Input parameters for bounding box computation (Particle removal).

Parameter	Details
- x	*Lower X boundary*
+ x	*Higher X boundary*
- Y	*Lower Y boundary*
+ Y	*Higher Y boundary*
- Z	*Lower Z boundary*
+ Z	*Higher Z boundary*

Algorithm 5.8: Bounding box

```
for (all active facets groups)
{
    if (facet group == facet type of sphere)
      {
      for (no. of facets)
          {
          if (midpoint of the sphere is outside the bounding box)
              {
              Remove facet from facet group
              Remove element from element group
              Remove facet from binary tree
              }
          } (no. of facets)
      } (facet group == facet type of sphere)
} (over all active facets groups)
```

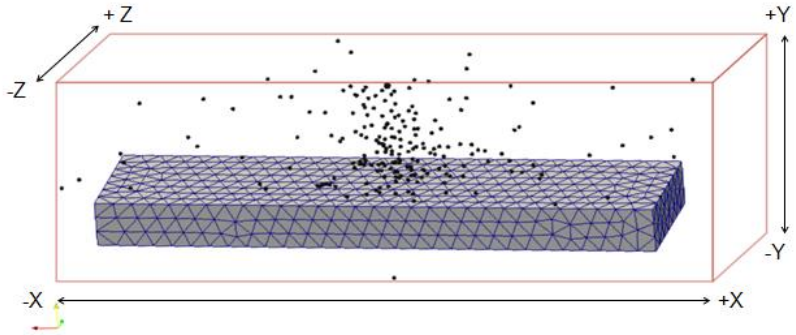

Figure 5.24: The bounding box is used to remove the particles that exceed the required simulation domain.

Verification - Speed up

The implementation has been verified by a simple SP simulation. A simple case was constructed where a flat surface is bombarded with 1000, 2000 and 3000 spherical shots. Two separate simulations were run once with and once without the bounding box for the difference number of shots to evaluate the speed up. The nozzle and bounding box parameter are listed in Table 5.4 below

Table 5.4: Parameters used to verify the implementation of the bounding box.

Nozzle parameters	Details
Nozzle radius	5mm
Particle radius	0.3mm
Nozzle mass flow rate	0.0001 kg/s
Initial velocity of particles	0 -50 0 in m/s
Time step at which particles are generated	0.00001 in seconds
Maximum tries to place particle on nozzle plane	100
Define fixed number of particles to be generated	1000, 2000, 3000
Define mass to be generated	8 kg
Bounding box parameters	**Details**
Lower X boundary	-6
Higher X boundary	-5
Lower Y boundary	-1
Higher Y boundary	6
Lower Z boundary	10
Higher Z boundary	11

By applying the bounding box algorithm the simulation run time decreases on average by 24 %. Over the simulation time, 962 shots are removed for the case with 1000 shots, 1949 for the case with 2000 and 2955 shots for the case with 3000 shots respectively.

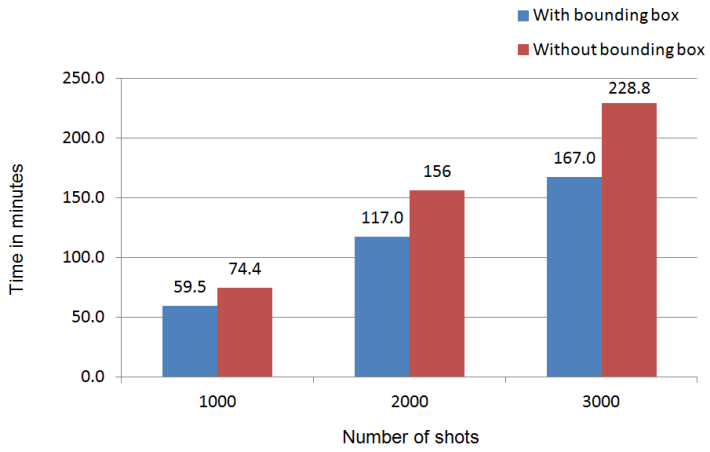

Figure 5.25: Bounding box performance comparison.

5.3.3 Shot Peening Coverage

Coverage is defined as the percentage of the area covered by peening indentations. In practice, the evolution of coverage is performed by visual inspection using a magnifying glass and is purely depended on the perception of the practitioner. In the modelling process, the coverage can be evaluated by inspecting the von Mises equivalent plastic strain on the component surface. Figure 5.26 illustrates the definition of coverage. The accuracy of the results will be mesh size depended but can be numerically better determined.

The input parameters for the coverage model are;

Table 5.5: Input parameters for coverage computation.

Parameter	Details
No. of coverage counter	Defines the number of coverage counter
No. of element group	The element group number is used to access the element state variables from that group.
No. of elements	No. of Elements is used to allocate the memory to access the element.
List of elements	The list of elements is examined for plastic deformation.

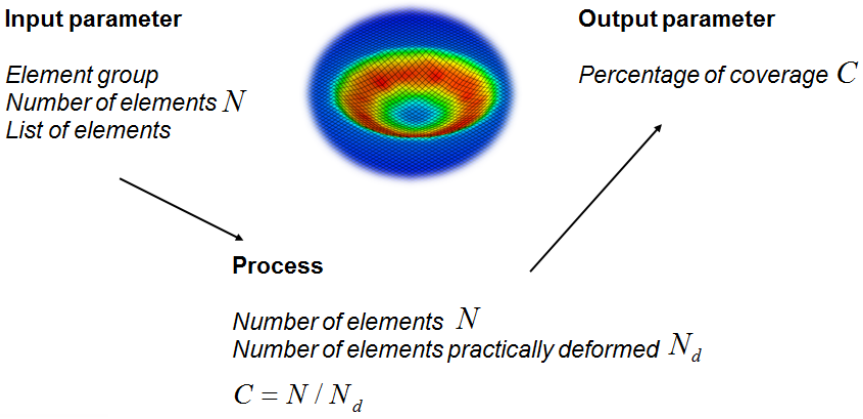

Figure 5.26: Illustrates the definition of coverage.

The percentage of coverage is defined as:

Eq. 5.9

$$C = N/N_d$$

where N = Number of surface elements and N_d is the number of elements plastically deformed.

Algorithm 5.9: Shot Peening Coverage

```
for (all active coverage counters)
{
        if (element group == defined element group)
        {
        Counter=0
                for (no. of elements)
                  {
                  if (element is plastically deformed)
                  Counter = Counter + 1
                  Coverage = Counter / number of elements
                  }
        } (element group = defined element group)
} (all active coverage counters)
```

5.3.4 Shot Peening Intensity

The intensity and saturation is defined by the Almen Strip arc height. During the practical peening process the Almen Strip is fixed with bolts and as the peening takes place, plastification of the component surface produces an induces stress profile in the x-direction σ_x^{ind} . In order to maintain the strip in a flat shape the bolts apply a compressive force F_x and a bending moment M_x Eq. 5.10 and Eq. 5.11. Once the bolts are removed the original flat strip will stretch and bend. In the simulations the strip is retained against all displacements and rotation on the bottom end.

Eq. 5.10

$$\int_0^h \sigma_x^{ind}\, b dz + F_x = 0$$

Eq. 5.11

$$\int_0^h \sigma_x^{ind} \left(\frac{h}{2} - z\right) b dz + M_x = 0$$

The residual stress profile after deformation of the strip can be calculated with

Eq. 5.12

$$\sigma_x^{res} = \sigma_x^{ind} + \sigma_x^s + \sigma_x^b = \sigma_x^{ind} + \frac{F_x}{A} + \frac{M_x \left(\frac{h}{2} - z\right)}{I}$$

where σ_x^{res} is the resulting residual stress, σ_x^s is the stretching stress resulting from force F_x , σ_x^b the bending stress retrieved from the bending moment M_x, h the thickness of the strip.

Eq. 5.13

$$ArcHeight = \frac{3 M_x I^2}{2 E b h^3}$$

where I_m is the reference distance for measuring the Almen intensity, E the young's modulus and b is the width of the strip.

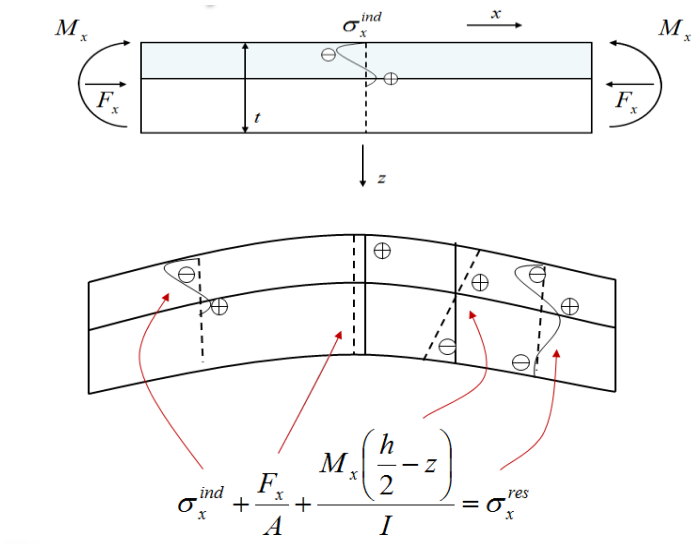

Figure 5.27: Calculation of the residual stresses in the Almen Strip after the bolts are removed.

Finite element simulation of such a strip with a bending moment and a stretching force induced by Shot Peening showed that the influence of the stretching force on the arc height is negligible (H.Y. Miao et al., 2009) and hence not taken into account. The Almen arc is computed during the simulation and can be retrieved at any point during the simulation process. This is a major advantage, as this feature can help the practitioner to analyse the saturation during the simulation without having to stop the simulation to review the data and stop the simulation when saturation point is reached. This will also allow the practitioner to quickly analyse the effect of a set of peening parameters. The input parameters for the intensity model are;

Table 5.6: The input parameters for calculating the peening intensity.

Parameter	Details
Young's modulus	Young's modulus of the target material
Length	Length of the target material
Width	Width of the target material
Thickness	Thickness of the target material
Element group	Element group of the target material
Number of elements	Number of elements to be includes in the computation
List of elements	List of elements to be includes in the computation

Algorithm 5.10: Shot Peening Intensity

```
for (all active measurements)
{
    mx = 0
    for (no. of elements)
    {
    mx = mx + ((height / 2 -  (height / no. of elements * counter )) * stress_component[no. of elements]
    }
   intensity = ( 3 * (mx/counter) * length2) / ( 2 * youngsmod * width * thickness3)
}(all active measuremen
```

5.3.5 Shot Peened Surface Roughness

In practice, the determination of the surface roughness is almost always conducted using Atomic Force Microscopy (AFM). In the modelling process, the coverage can be evaluated by examining the alteration of the surface nodes of the component after Shot Peening. The accuracy of the results will be mesh size depended.

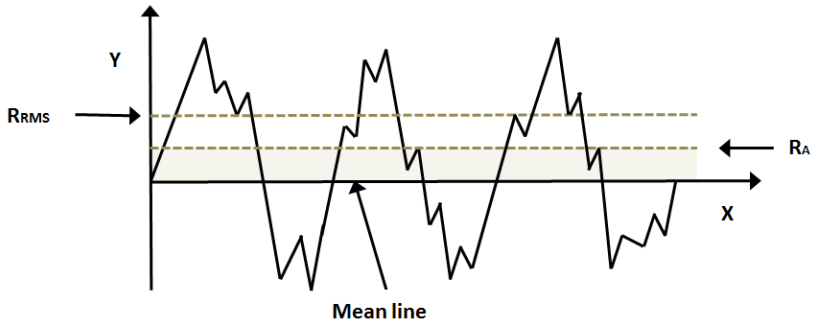

Figure 5.28: Definition of surface roughness of Mean Roughness (RA) and Root Mean Squared (RMS) roughness.

Table 5.7: The input parameters for the roughness.

Parameter	Details
Number of coverage monitor	Number of coverage measurements
Counter for coverage monitor	Coverage counter
Direction of displacement measurement	The direction of the measurement
Number of nodes	Number of elements to be includes in the computation
List of nodes	List of element to be taken into account in the computation

R_a is the Roughness Average is the arithmetic average of the absolute values of the individual measurements taken of the surfaces peaks and valley. It is the most effective surface roughness measures commonly used in general pratice. Roughness Average R_a is defined as

Eq. 5.14

$$R_a = \frac{1}{n}\sum_{i=1}^{n}|y_i|$$

R_{RMS} is the Root Mean Square and is root mean squared average of the individual measurements taken of the surfaces peaks and valley. R_{RMS} is defined as

Eq. 5.15

$$R_{RMS} = \sqrt{\frac{1}{n}\sum_{i=1}^{n}y_i^2}$$

The peak-to-valley roughness parameter R_T is a common roughness parameter used in Shot Peening and is defined as

Eq. 5.16

$$R_T = R_P - R_V$$

where

$$R_P = \max_i y_i$$

and

$$R_V = \min_i y_i$$

Algorithm 5.11: Roughness Average R_a

```
Ra = 0
    for (no. of nodes)
        {
            Ra = Ra + Absolute value (Node [Direction of displacement measurement])
        }
Ra= Ra / no. of nodes
```

R_{RMS}

Algorithm 5.12: Roughness Root Mean Square R_{RMS}

```
R_RMS = 0
d = Get the direction of displacement measurement
        for (no. of nodes)
          {
           R_RMS = R_RMS + (solution node coordinates [d]
                    - initial node coordinates [d] )^2
          }
R_RMS = Square Root( R_RMS / no. of nodes)
```

R_T

Algorithm 5.13: Roughness Peak-to-Valley R_T

```
R_T = 0
    d = Get the direction of displacement measurement
        for (no. of nodes)
            {
                temp= (solution node coordinates [d]
                        - initial node coordinates [d] )
                if (temp > 0)
                 {
                if (temp > maxU)
                            maxU = temp;
                }
                else
                {
                 if (temp < minU)
                            minU = temp;
                }
        } (no. of nodes)
R_T =  maxU - minU
```

5.4 Validation of numerical model

In order to validate the numerical implementation, the results of the study of (H Y. Miao et al., 2009) is compared with the implemented numerical model. In the study a Matlab program combined with ANSYS APDL (ANSYS Program Design Language) was developed to generate the random coordinates of each shot. Explicit solver LS-DYNA was used to simulate the dynamic impingement process. Compared to the target material, the shots were

assumed to be rigid due to their relatively high yield and hardness values. The shots have the same radius (r = 0.5 mm), density (P_s = 7800 kg/m^3), velocity (50 m/s) and an impact angle of 90°. An aluminium plate with dimensions 5 mm x 5 mm x 3 mm was selected as the target component in this Shot Peening model. A Coulomb friction coefficient μ = 0.2 was defined between the shots and the target component. The aluminium is assumed to obey an elasto-plastic behaviour with isotropic hardening and had the following material properties; the elastic modulus E = 71.7 GPa, the Poisson's ratio, v = 0.33, the density P_t = 2810 kg/m^3, the initial yield stress σ = 503 MPa and the linear strain-hardening parameter H^1 = 3.3 GPa. In this study, the potential strain rate sensitivity of the material was not taken into account.

After a convergence study, an impact area of 2 mm x 2mm x 1 mm was discretized into a fine mesh with elements of dimensions 0.05 mm x 0.05 mm x 0.05 mm. In order to study the relationships between intensity, coverage, roughness and the number of shots, the simulations corresponding to 5 different numbers of shot impacts N = {6, 12, 24, 48 and 96} were carried out. To obtain the average induced stress profiles, 9 x 9 = 81 uniformly distributed paths following the depth of the plate in the representative volume were defined by ANSYS General Postprocessor. Stresses in the x-direction (SXX) were interpolated into each of these 81 paths respectively. Then the average values of SXX for constant depths were calculated from these 81 paths to represent σ_x^{ind}. Arc heights can be calculated with Eq. 5.13 using the averaged induced stress profiles.

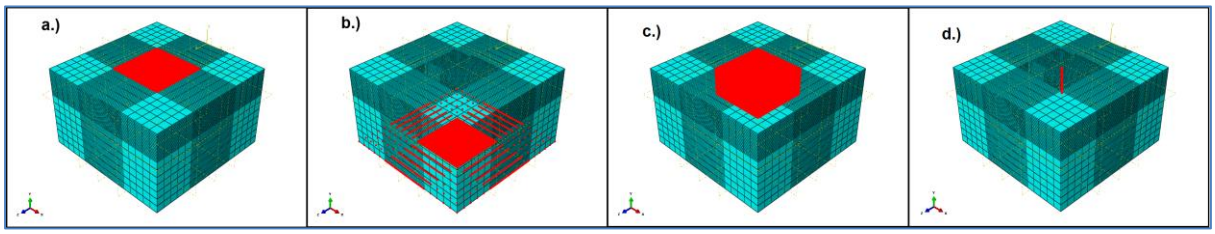

Figure 5.29 : The target mesh refinement; (a) The surface impact area; (b) Component boundary condition; (b) Elements used to calculate the Almen arc; (d) One of the 81 measurement paths.

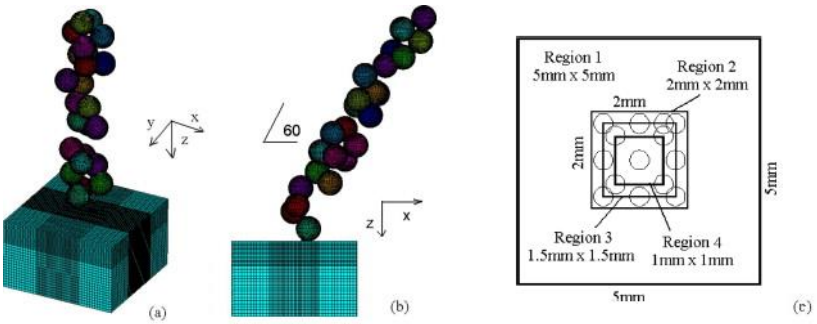

Figure 5.30: 3D random finite element model: (a) multiple shots impinging an aluminium component at normal incidence; (b) multiple shots impinging an aluminium component at 60° angle of incidence; (c) impact area after (H Y. Miao et al., 2009).

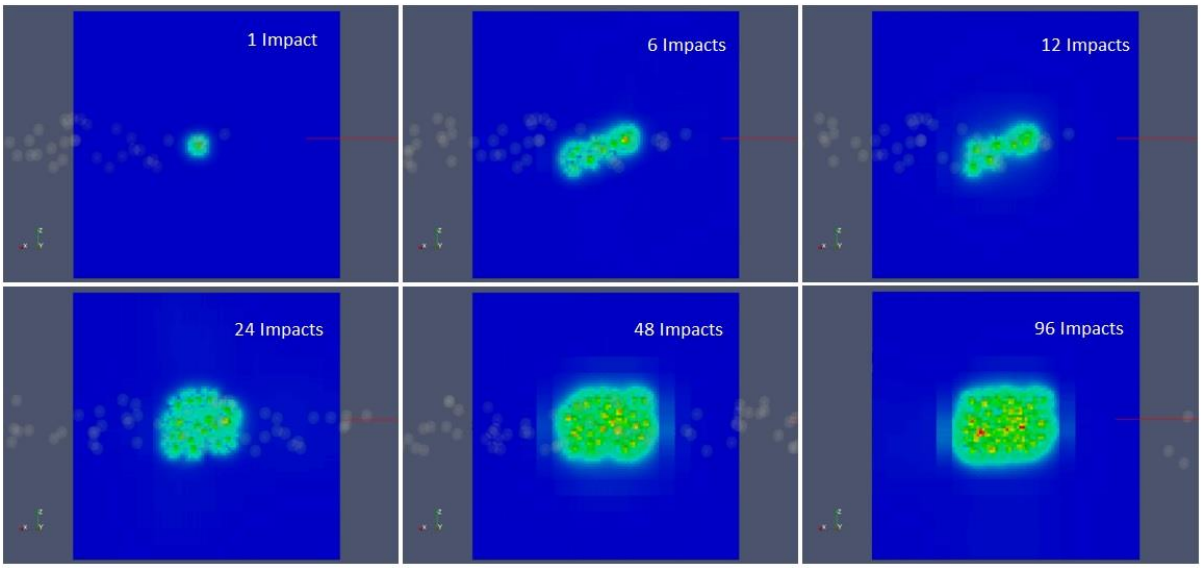

Figure 5.31: Paraview output of the component surface after Shot Peening with 1, 6, 12, 24, 48 and 96 impacts at a peening angle of 60°.

From the 60° multiple impacts in Figure 5.31 it can be seen that the incoming shot-flow from the nozzle is narrow (size of the nozzle), but once several shots have imparted and deformed the surface the rebounding shots rebound at a different angle, resulting in a much wider rebounding shot-flow.

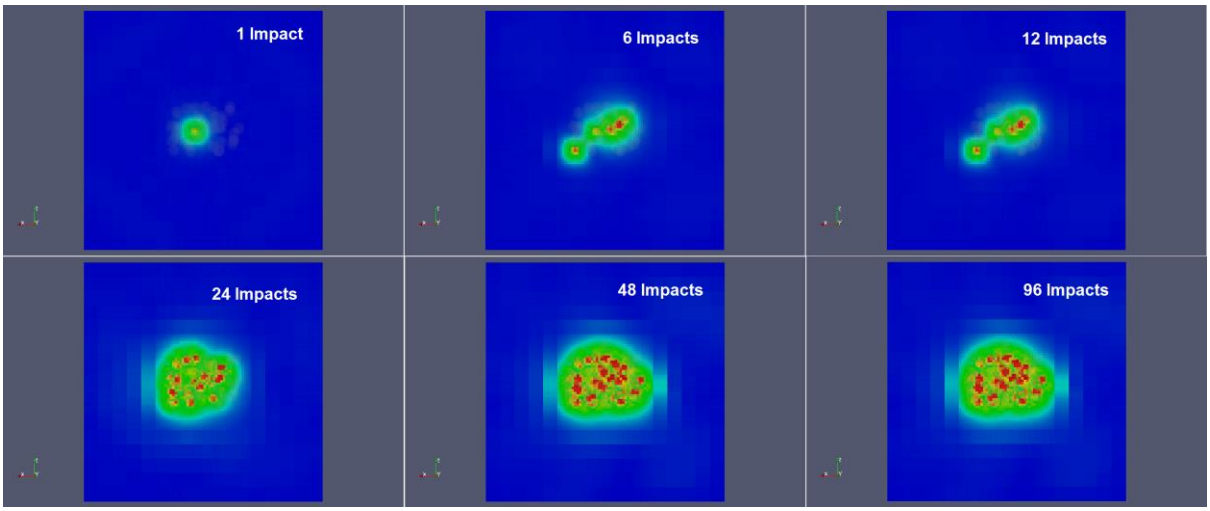

Figure 5.32: Paraview output of the component surface after Shot Peening with 1, 6, 12, 24, 48 and 96 impacts at a peening angle of 90°.

5.4.1 Surface profile after singe impact

Shot Peening coverage is defined in terms of surface plastic indentation. Two simple Shot Peening simulations with one shot were performed in order to compare the plastic indentations produced by one normal impact and one oblique impact with the model developed in this work.

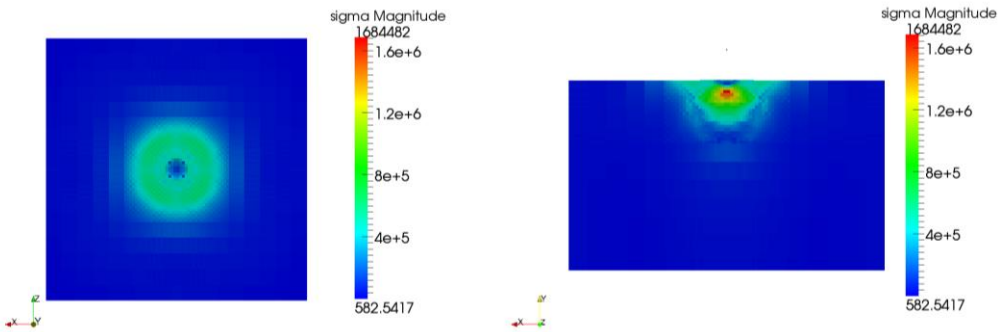

Figure 5.33: Paraview output after one normal single impact.

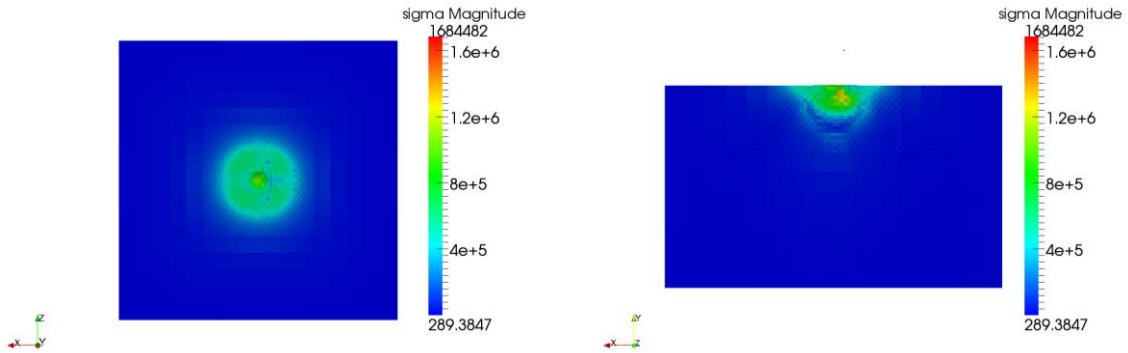

Figure 5.34: Paraview output after one oblique single impact at 60°.

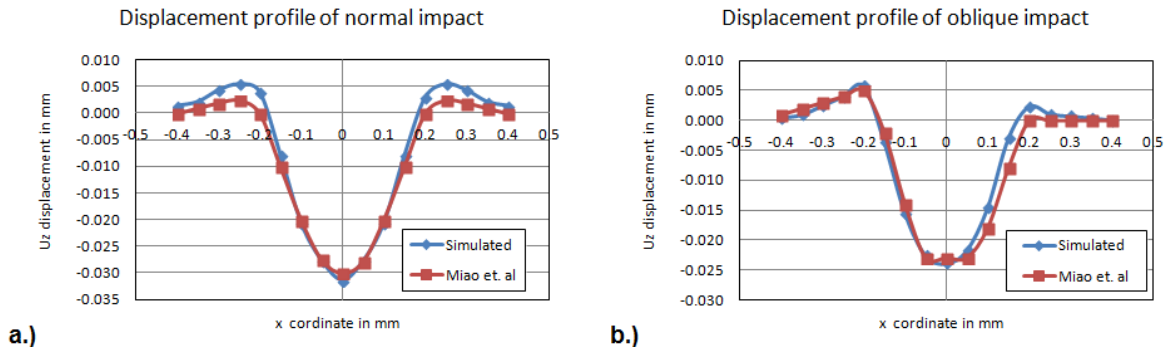

Figure 5.35: a.) Shows the impact profile after a single normal impact. b.) The impact profile after an oblique impact at 60°.

5.4.2 Comparison of the simulated coverage of multi impacts

The impact of multiple shots relating to coverage is evaluated next. The algorithm developed in Algorithm 5.7 is slightly modified such that the particles are generated on a rectangular plane. The algorithm is then used to generate the numerous shots which impact the surface of the component. The peening coverage is related to the indentations on the top layer of the component. The representative component surface is illustrated in Figure 5.29 (a) with 441 nodes. The coverage is obtained throughout the simulation for different number of shots impacts. The Shot Peening coverage was approximated as the ratio of the number of nodes with von Mises plastic strains larger than 0.027. Figure 5.36 presents curves showing the relationship between the surface coverage and the percentage of total peening time. It can be

noted that the surface coverage rate increases quickly at the beginning of the Shot Peening process for the first couple of impacts and decreases with the increase of peening time. The simulated coverage for normal impacts matches well with the results obtained by H Y. Miao et al. (2009).

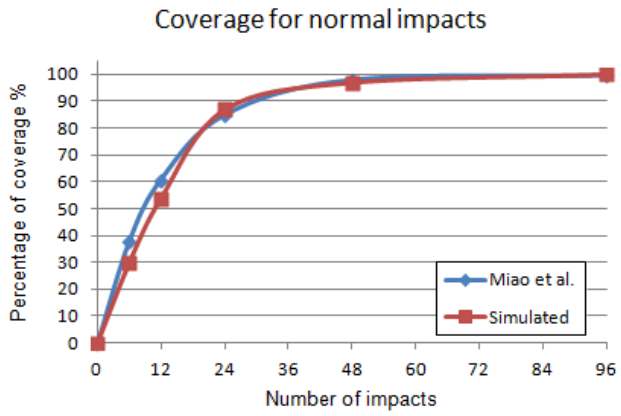

Figure 5.36: Coverage build-up for multiple normal impacts.

5.4.3 Peening induced surface roughness with FEM - normal impacts

One the common roughness parameters used in Shot Peening is the peak-to-valley roughness PV parameter. The PV parameter is defined with Eq. 5.16 and approximated with Algorithm 5.13. Similar to the coverage, the roughness is calculated for every output step and obtained throughout the simulation for different numbers of shot impacts.

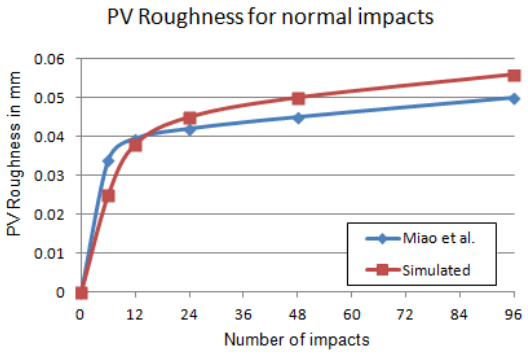

Figure 5.37: PV roughness versus number of shots for normal impacts.

5.4.4 Shot Peening Intensity (Arc height) calculation with induced stress profiles

The Shot Peening Intensity (Arc height) is defined as illustrated in Figure 5.27 and can be approximated with the Eq. 5.13 and the Algorithm 5.10. H Y. Miao et al. (2009) obtained a regression coefficient R^2 = 0.9812 for this case. They found that the arc height reaches saturation for N = 48 and for an intensity of 1.1409 mm. Figure 5.38 shows the comparison of the simulated arc height for the two cases calculated with the results obtained by (H Y. Miao et al., 2009).

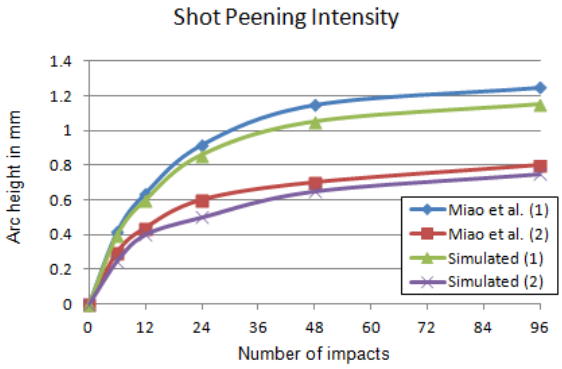

Figure 5.38: Simulated arc height for normal impacts versus the number of shots for the two cases calculated with equation Eq. 5.13 for the normal impact and oblique impact.

5.4.5 Residual stress profiles after multiple impacts

Figure 5.39 compares the residual stress profiles calculated from the induced stress profiles, after 48 normal and oblique impacts with results obtained by H Y. Miao et al. (2009). Normal peening produces higher maximum compressive residual stress and higher surface compressive residual stress compared to the oblique impacts. In addition, normal peening produces higher tensile stress beneath the surface of the strip.

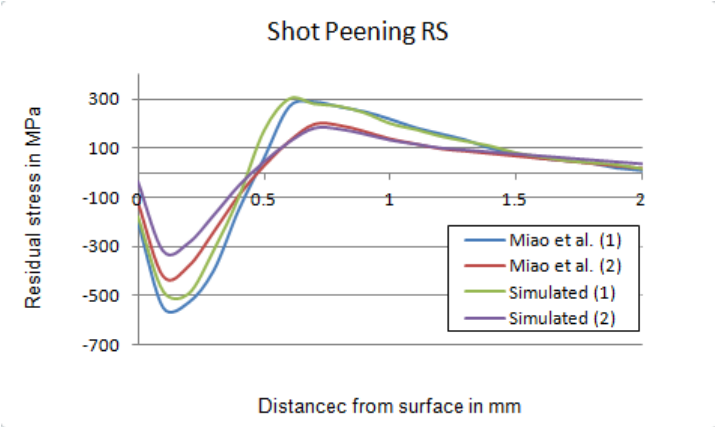

Figure 5.39: Comparison of the residual stress profiles σ_Y^{res}, after normal Shot Peening (case 1) and oblique Shot Peening (case 2) with shot velocity v = 50 m/s and number of shots N = 48.

5.4.6 Discussion and conclusion

The results have shown that the implemented numerical model is capable to capturing the effectiveness of Shot Peening in terms of surface coverage, surface intensity and roughness. The simulated results match well with the results published by H Y. Miao et al. (2009). Their model does not take into account any shot - shot interaction or mass flow rate for shot generation. The developed model takes these parameters into account, but the key advantage of the implementation is that it allows one to assess the effectiveness of the peening at any time during the simulation with no post processing involved and allowing one to terminate the simulation when saturation state is reached. This reduces time and costs in assessing the effectiveness of peening parameters in new components.

5.5 Performance comparison

To measure the performance of the implementation, it is essential to choose the most appropriate and correct technique. It is essential to have the test environment use the identical test parameters for performance testing. Even simple matters such as outputting results to console/terminal can have an effect on the performance. Some shells “sync” the program to

the console output and for instance if your terminal is displaying slowly, the program can be delayed, slowing down the performance of the applications.

In this section, five different computational mechanics problems are presented to assess and evaluate the performance of the proposed implementations. An extensive comparison is performed to assess the performance of the different implementations in terms of number of tree visits, node visits, number of facet updates, depth of the tree, reduction is searching volume, memory usage and most importantly computational time. The test cases are ran on a DELL T7600 workstation using Two Intel Xeon Processors E5-2630 (Six Core, 2.30GHz Turbo, 15MB, 7.2 GT/s) and 64GB (8x8GB) 1600MHz DDR3. To access the performance more accurately, the simulations are executed using one a single thread only.

Example 1: Single shot impact

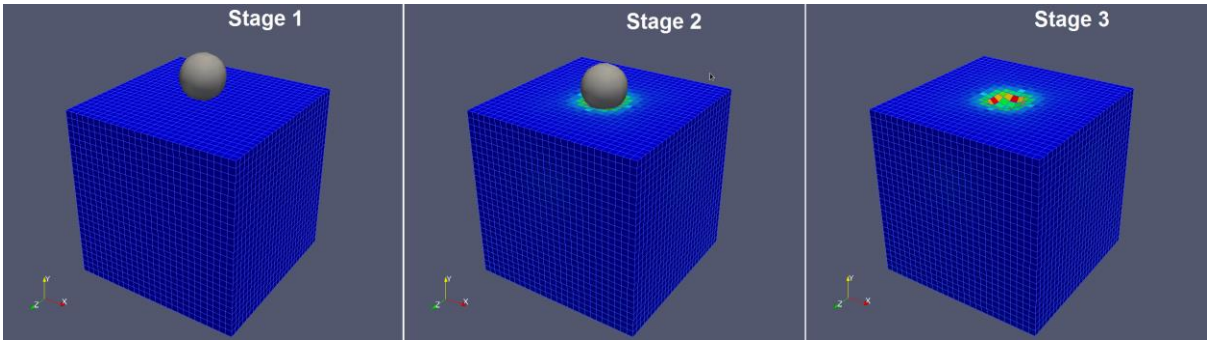

Figure 5.40: Performance test case example 1: Single shot impact.

In the first test case, a single spherical shot is impacted onto a cube. The spherical shot is defined as a single node with a radius of 0.25 mm and the cube is of size 2 x 2 x 2 mm, 19683 8-node hexahedron elments respectivly. An initial velocity of 50m/s is assigned shot and the lenth of the simulation is set to 0.0003 seconds.

Example 2: **Shot Peening with bounding box (Shot removal)**

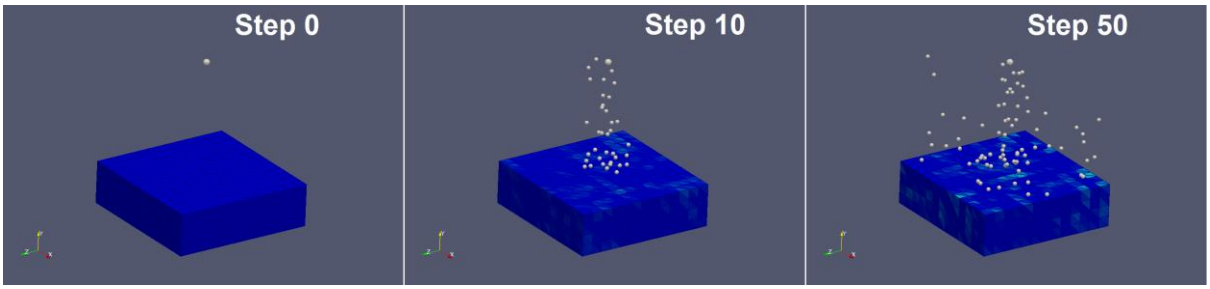

Figure 5.41: Performance test case example 2: Shot Peening simulation.

For the second performance test case a Shot Peening simulation with 1000 shots and a bounding box for shot removal is considered. The nozzle had the following properties: nozzle radius 4.8 mm, mass flow rate of 0.000056 kg/s, shot radius 0.3 mm and shot velocity of 40 m/s. Steel was considered for both the shot and target material. The target has dimensions 30 x 30 x 5 mm with 76076 8-node hexahedron elments and 84630 nodes. Bounding box with coordinates (-x = -15, -y = -10, -z = -15, x = +15, y = +30, z = +15). Total simulation time was set to 0.01 seconds.

Example 3: Settling of sand particles

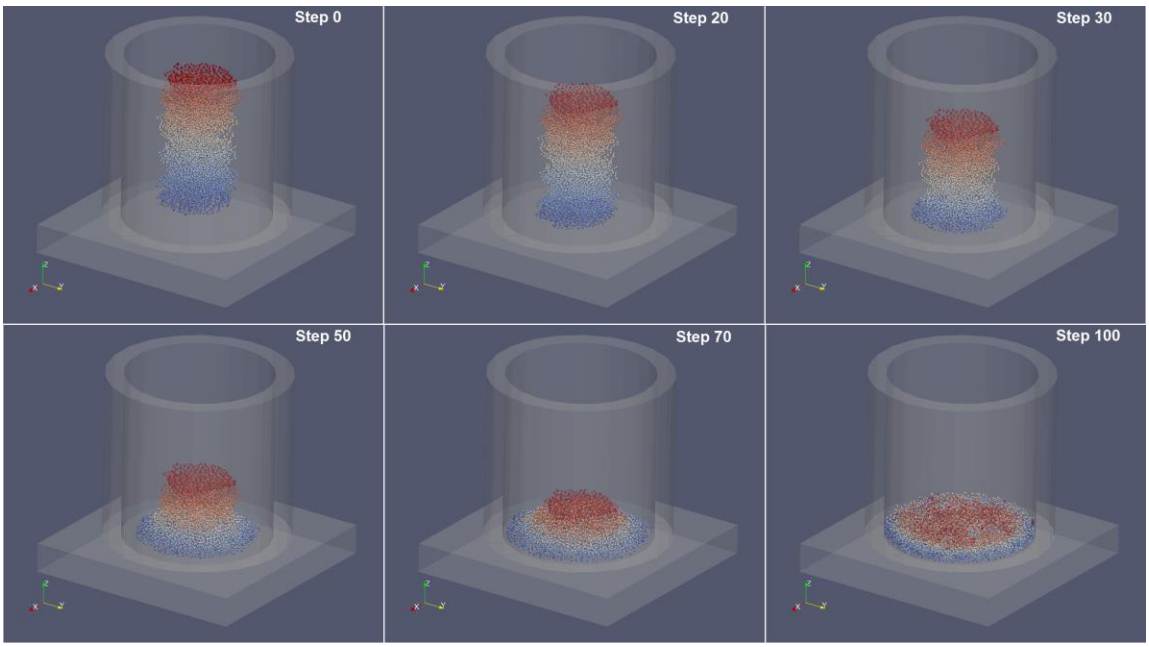

Figure 5.42: Performance test case example 3: Settling of sand particles.

The settling of sand particles in a container was investigated next. 4971 sand particles were generated in a random manner with a radius between 0.175mm and 0.335mm and gravity was applied to the particles (9.81m/s). The tube for the container was made of 23 8-node hexahedron elements and the base with a single hexahedron element. Total simulation time was set to 0.04 seconds.

Example 4: Particle interaction

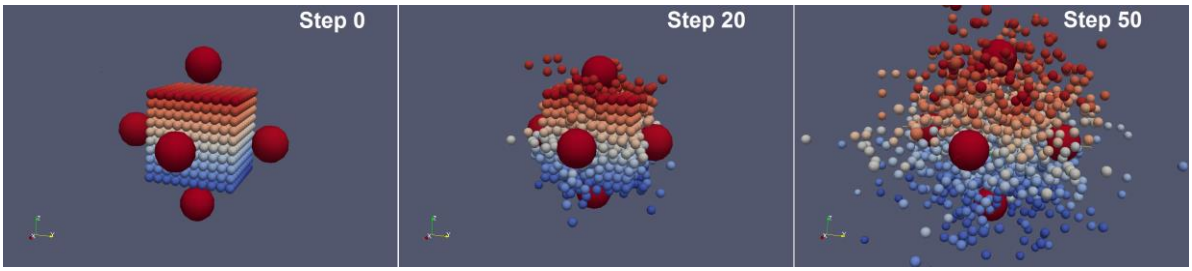

Figure 5.43: Performance test case example 4: Interaction of particles.

In this test case, the performance of the interaction of particles in accessed. 1000 particles with a radius of 0.5 mm are placed in a grid forming a cube as illustrated in Figure 5.43. Additionally, a particle is placed on each side of the cube at a distance of 10mm and an initial velocity of 30 m/s towards the cube is applied. Total simulation time was set to 0.01 seconds.

Example 5: Plate impact

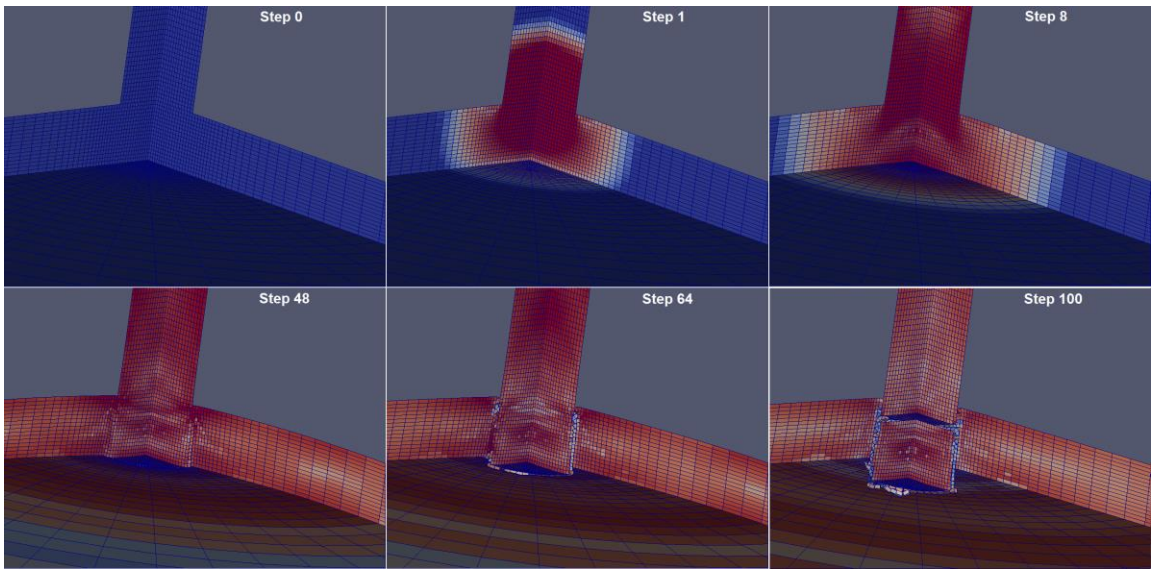

Figure 5.44: Performance test case example 5: Plate impact.

In the final example, a plate impact simulation with element debonding is performed. The plate was made of 8673 and the projectile of 11312 8-node hexahedron elments with a total of 23213 nodes. During the element debonding additional nodes were added to the plate. Initial velocity of 200 m/s was applied to the projectile. The length of the simulation time was 0.00005 seconds.

5.5.1 Depth of the tree - *Tree balancing and update*

The depth of the BST defines the maximum possible number of tree traversals.

Example 1: Single shot impact

In this example there are two element groups. The shot is made of a single facet node with a radius and the target with 19683 8-node hexahedron elments respectivly. The outer facet curl algorithm returned a total number of 4374 facets for the target cube. The tree depth of the ordinary tree is 23 and the depth of the improved algorithm is 14. With the improved balanced tree algorithm the depth of the binary search tree is reduced by 40 %.

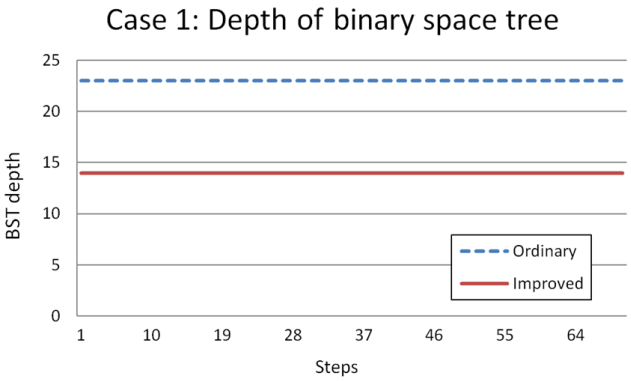

Figure 5.45: Shows the comparison of the depth of the binary space tree for the single shot impact example (case 1).

Example 2: Shot Peening with bounding box (Shot removal)

In the Shot Peening case study, only the depth of the particle binary space tree is considered. As particle are fed into the system the depth of the tree increases, stays at a stable position as

the target mass flow rate is reached and eventually drops when the nozzle terminates. Comparing both algorithms, at the peak of the simulations the depth of the space tree is between 6-8 nodes when the nozzle mass flow rate is stable.

With the improved balanced tree algorithm the depth of the binary search tree is reduced by 16.29 % for this particular example. Figure 5.46 the comparison of the depth of the binary space tree for the Shot Peening case.

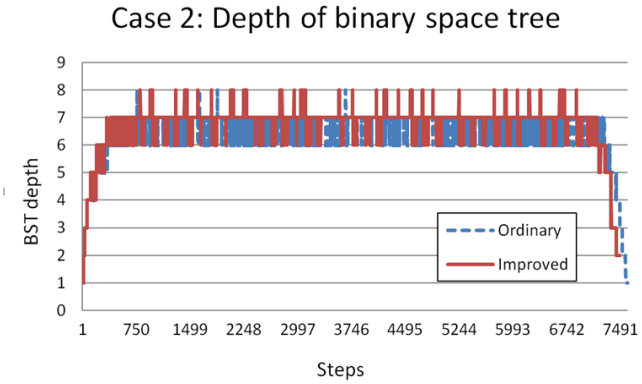

Figure 5.46: Shows the comparison of the depth of the binary space tree for the Shot Peening example (case 2).

Example 3: Settling of sand particles

In the sand particle case study, only the depth of the particle BST is assessed. When the particles are assigned gravity, they all move towards the same direction and since no more particles are added or removed, the binary structure and depth do not change. The depth of the BST using the ordinary algorithm is 27. With the improved balanced tree algorithm the depth of the BST is reduced by 42.65 % and is around 14 - 16 nodes. Figure 5.47 comparison of the depth of the binary space tree for the sand particle interaction case.

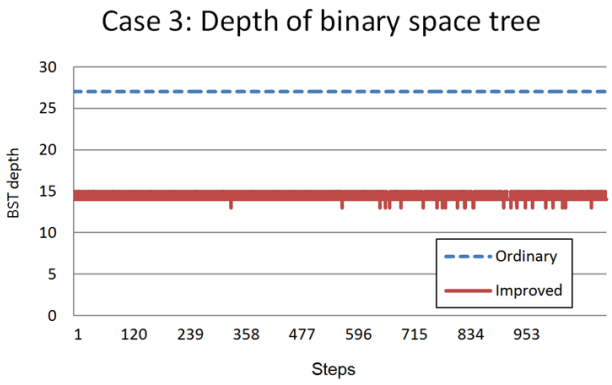

Figure 5.47: Shows the comparison of the depth of the binary space tree for sand example (case 3).

Example 4: Particle interaction

In the particle interaction case study, the depth of the BST using the ordinary algorithm is 14. With the improved balanced tree algorithm the depth of the BST is around 11-12 and is reduced by 18 %. Figure 5.48 illustrates the comparison of the depth of the binary space tree for the particle interaction case.

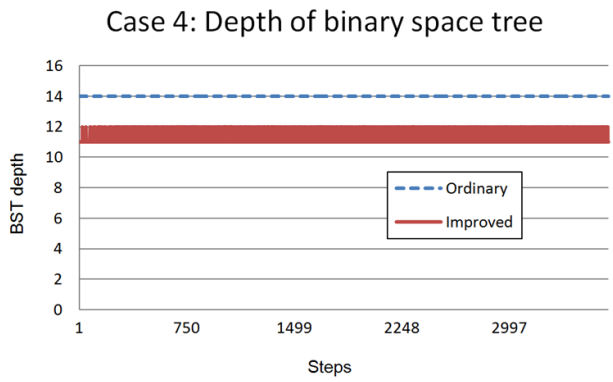

Figure 5.48: Shows the comparison of the depth of the binary space tree for particle interaction example (case 4).

Example 5: Plate impact

In the plate impact case study, only the depth of the plate BST is considered. When the projectile penetrates the plate, elements that are part of the plate deboned and these new elements hold new outer facet that are required to be added to BST. Figure 5.49 illustrates the

depth over time for the two different algorithms. Changes in the depth of the tree indicate the excessive movement of facets. The updating algorithm reduces the depth by 39.93 %.

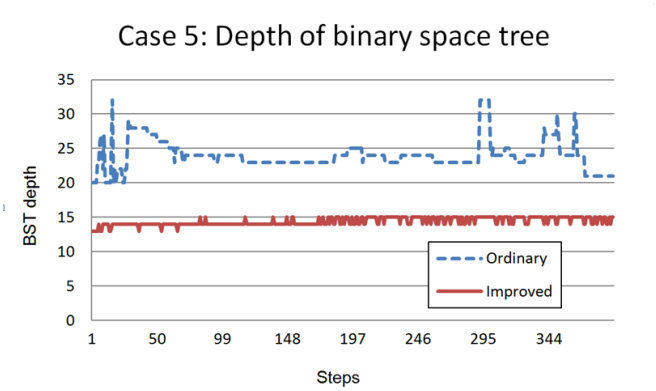

Figure 5.49: Shows the comparison of the depth of the binary space tree for plate impact example (case 5).

5.5.2 Total node and subspace visits

Next, the total node and subspace visits are assessed.

Example 1: Single shot impact

Since the shot is placed on the target surface the initial number of node visits is high. Once the shot rebounds from the target the number of node visits decreases to zero. No difference in the number of node visits was observed when comparing both algorithms. Figure 5.50 shows the comparison of the node visits for the single shot impact case.

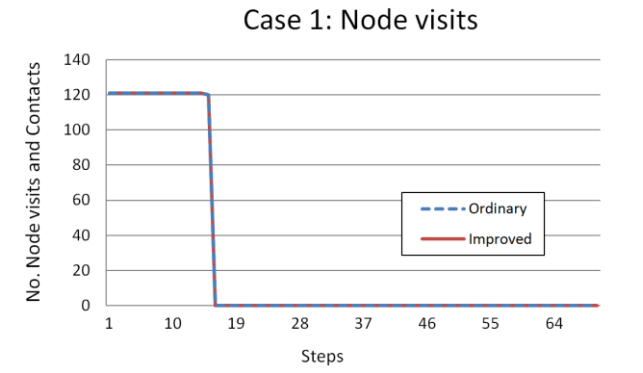

Figure 5.50: Shows the comparison of the node visits for the single shot impact example (case 1).

Example 2: Shot Peening with bounding box (Shot removal)

In this example only the shot - shot intersection is considered. Similar to the depth of the BST, as particles are fed into the system the node visits increase, stays at a stable position as the target mass flow rate is reached. The tree depth eventually drops when the nozzle terminates. On average the node visit is reduced by 44.96 %.

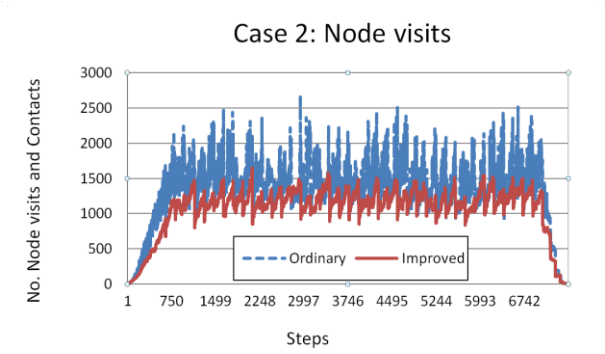

Figure 5.51: Shows the comparison of the node visits for the Shot Peening example (case 2).

Example 3: Settling of sand particles

In this example only the interaction search between the particles is evaluated. When gravity is applied to the particles, they get compacted in space, rebound at the bottom of the closed cylinder and eventually settle. This results in the node visits and contacts increase over time until the particles are fully settled. Figure 5.52 shows the comparison of the node visits for the sand particle case. On average the node visit is reduced by 22.02 %.

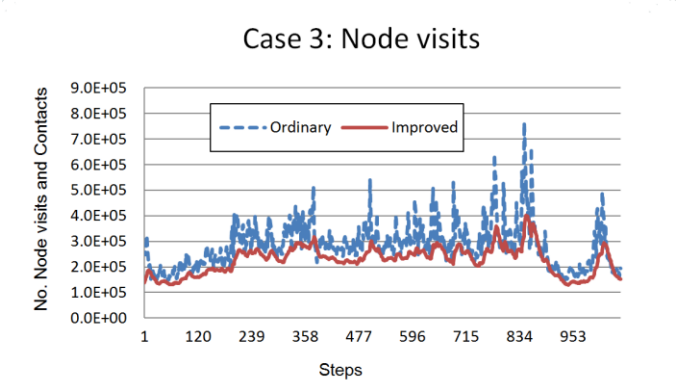

Figure 5.52: Shows the comparison of the node visits for the sand particle example (case 3).

Example 4: Particle interaction

In this example the particles are located in a very small space. Once the larger particles interact with the particles placed in the dense space, the cluster of particles gets distorted and the number of interaction decreases. Figure 5.53 shows the comparison of the node visits for the particle interaction case. On average the node visit is reduced by 11 %.

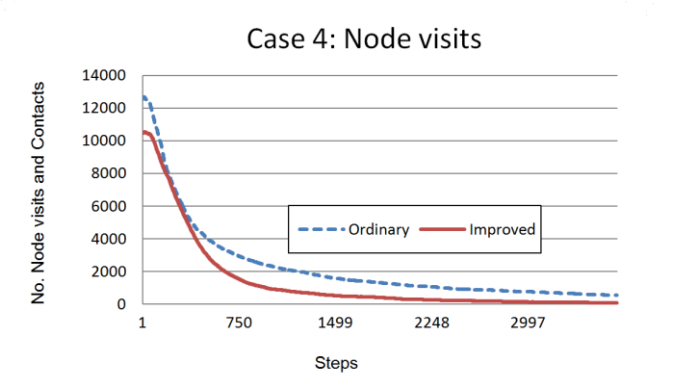

Figure 5.53: Shows the comparison of the node visits for the shot interaction example (case 4).

Example 5: Plate impact

The number of node visits increases while the projectile approaches the plate. The peak of the node visits illustrates the point at which the projectile impacts the plate and debonds the elements. Node visits decrease when the projectile penetrates the plate and seperates the deboned elements from the plate. The improved algorithm reduces the node visits by 7.34 %. Figure 5.53 shows the comparison for the plate impact case.

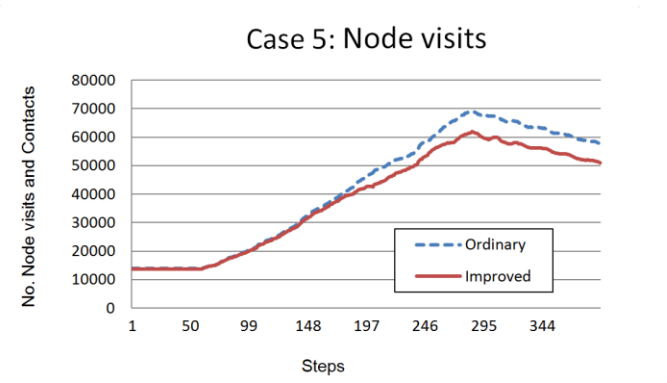

Figure 5.54: Shows the comparison of the node visits for the single shot impact example (case 5).

5.5.3 Reduction in searching volume - *Space tightening*

Next, the BST build and searching volume is assessed. A smaller searching volume could result in a lower number of node and subspace contacts and potential facet - facet contacts.

Example 1: Single shot impact

The improved algorithm reduced the build space by 29.29 %, but no reduction in searched space was observed. Figure 5.55 shows the comparison for the single shot impact case.

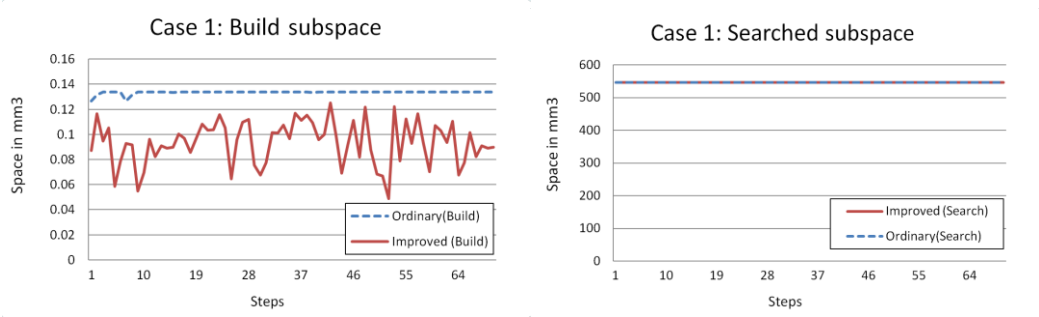

Figure 5.55: Shows the comparison between the build and searched subspace for the single shot impact example (case 1).

Example 2: Shot Peening with bounding box (Shot removal)

In this example only the shot - shot intersection search is evaluated by looking at the reduction in search volume. Both algorithms are executed with an active bounding box, removing the shot exceeding the bounding box space. Once the nozzle has reached a stable mass flow rate, the searching volume remains stable. The build search volume is reduced by 88.14 % and the searched volume is reduced by 29.96 %. Figure 5.56 illustrates the comparison for the Shot Peening case.

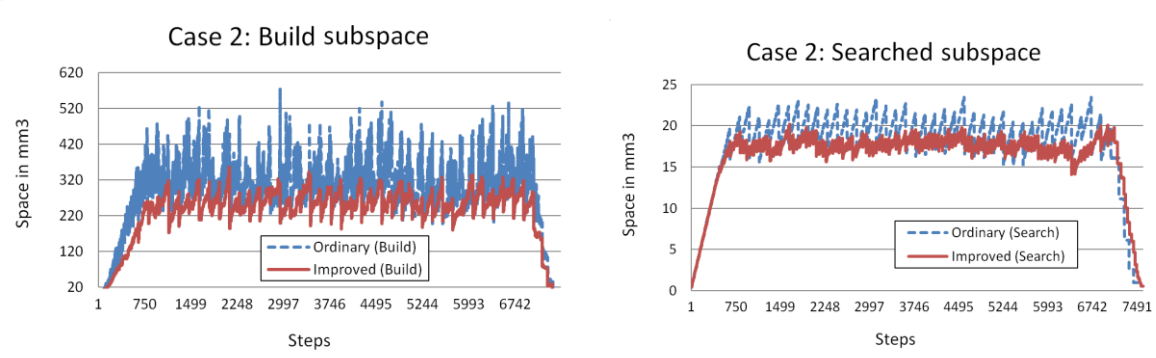

Figure 5.56: Shows the comparison between the build and searched subspace for the Shot Peening example (case 2).

Example 3: Settling of sand particles

In this example the search volume of the sand particle interaction decreases over time until the particles settle. The build search volume is reduced by 93.80 % and the searched volume is reduced by 58.14 %. Figure 5.57 illustrates the comparison for the sand particle interaction case.

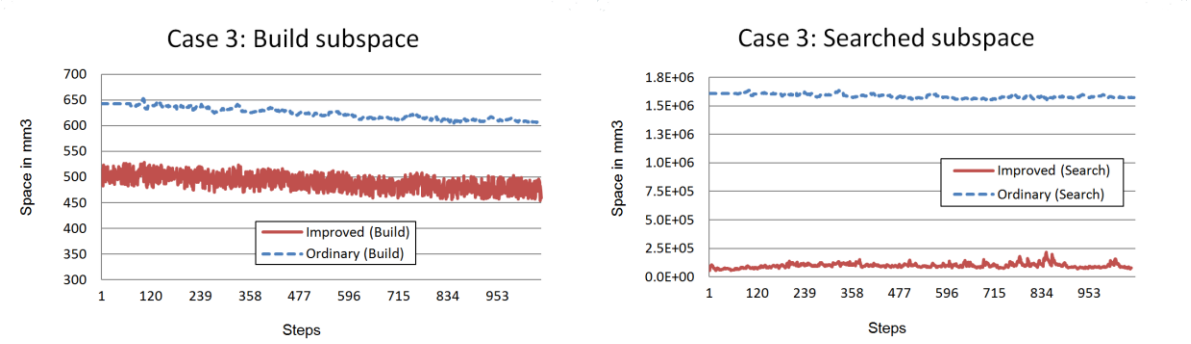

Figure 5.57: Shows the comparison between the build and searched subspace for sand particle interaction example (case 3).

Example 4: Particle interaction

In the particle interaction case the build search volume is reduced by 19.29 % and the searched volume is reduced by 4.99 %. Figure 5.58 illustrates the comparison for the particle interaction case.

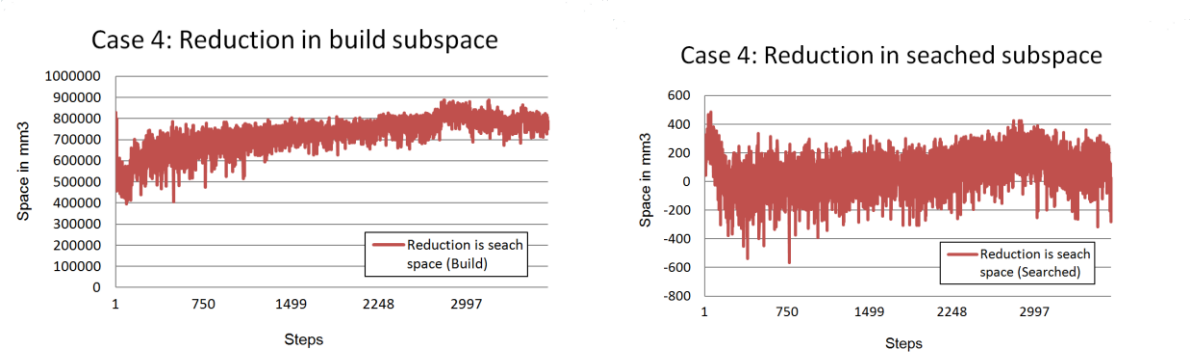

Figure 5.58: Shows the comparison between the build and searched subspace for the particle interaction example (case 4).

Example 5: Plate impact

The searching volume decreases as the projectile approaches the plate, but suddenly peaks at the point of penetration of the projectile, when elements deboned and new facets are introduced. The build search volume is reduced by 7.23 % and the searched volume is reduced by 7.34 %. Figure 5.59 illustrates the comparison for the place impact case.

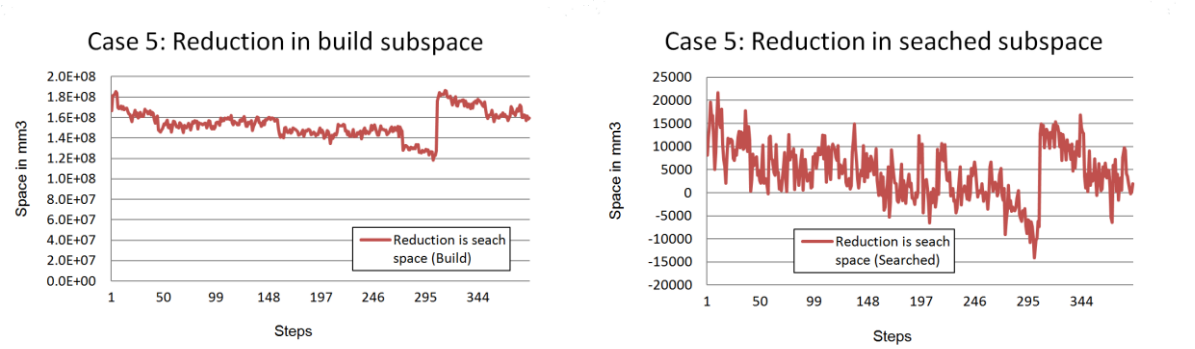

Figure 5.59: Shows the comparison between the build and searched subspace for the place impact example (case 5).

5.5.4 Facet updates vs. rebuilds

One of the advantages of the improved algorithm is that only facets which move out of their own bounding box are updated, whereas the ordinary algorithm rebuilds the tree by updating each facet. This section compares the number of facet rebuilds with the number of facet updates.

Example 1: Single shot impact

In this example the target mesh is made of very fine mesh. As the wave propagate from the single shot impact, the facets move very excessively and facet updates are performed at the length of the simulation. With the improved algorithm, the facet update is reduced by 29.29 %. Figure 5.60 illustrates the facet update vs. rebuild comparison for the single shot impact case.

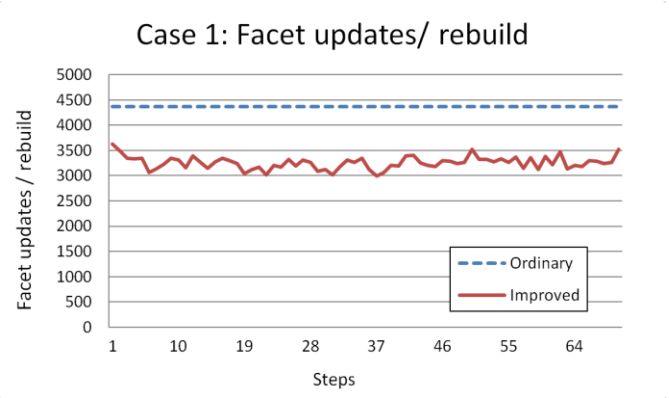

Figure 5.60: Shows the number of facet updates vs. rebuild for the single shot impact example (case 1).

Example 2: Shot Peening with bounding box (Shot removal)

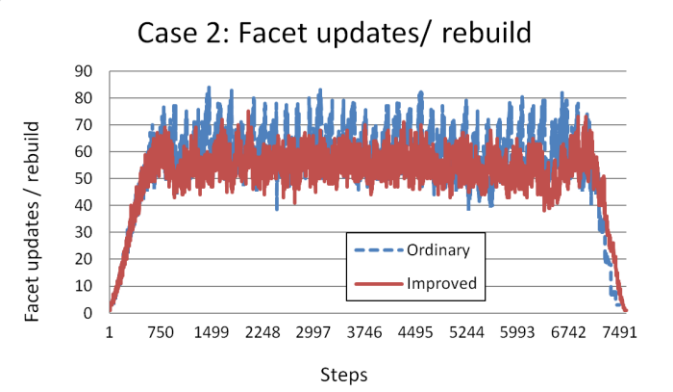

Figure 5.61: Shows the number of facet updates vs. rebuilds for the Shot Peening example (case 2).

In the Shot Peening example the facet update is reduced by 33.22 %. When comparing the general Shot Peening analysis with bounding box with the analysis without the bounding box the facet update is reduced by more than 90 %. Figure 5.61 illustrates the facet update vs. rebuild comparison for the Shot Peening case with the bounding box and shot removal.

Example 3: Settling of sand particles

In this example gravity is assigned to the particle and the particles located near the base of the closed cylinder do not have enough room to move excessively and therefore may not require a facet update, but the particle further away from the base of the cylinder do require frequent

facet updates. The improved algorithm reduces the facet update by 28.72 %. Figure 5.62 illustrates the facet update vs. rebuild comparison for the sand particle interaction case.

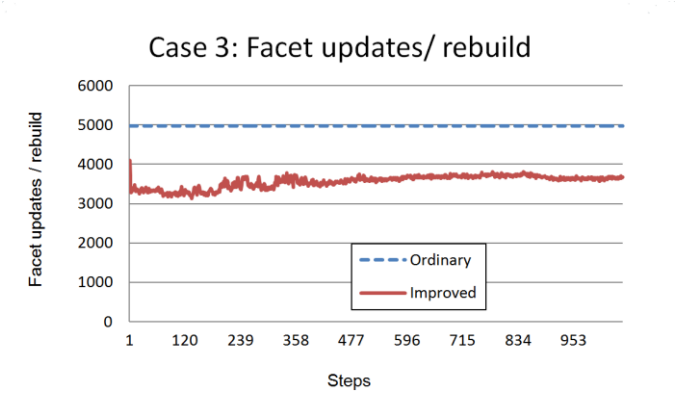

Figure 5.62: Shows the number of facet updates vs. rebuilds for the sand particle interaction example (case 3).

Example 4: Particle interaction

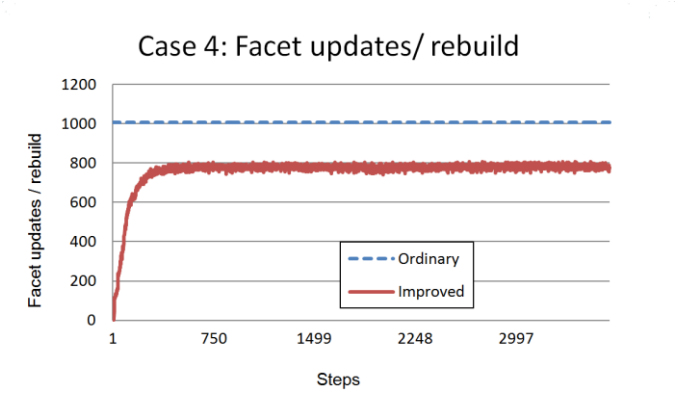

Figure 5.63: Shows the number of facet updates vs. rebuilds for the particle interaction example (case 4).

With the improved algorithm only the facets of the larger particles approaching the grid of particles are updated. Once the particles interact with the grid, the number of facet updates increases to 740 - 800 updates. In the ordinary algorithm all 1006 facets are updated once the larger particles move towards the grid. The facet update is reduced by 24.73 %. Figure 5.63 illustrates the facet update vs. rebuild comparison for the particle interaction case.

Example 5: Plate impact

During the debonding process 2448 new facets are introduced. With the ordinary algorithm the facet update increases from 3366 to 5814 updates. With the improved algorithm the facet update increased from 2448 to 4310. The facet update is reduced by 27.77 %. Figure 5.64 illustrates the facet update vs. rebuild comparison for the Plate impact case.

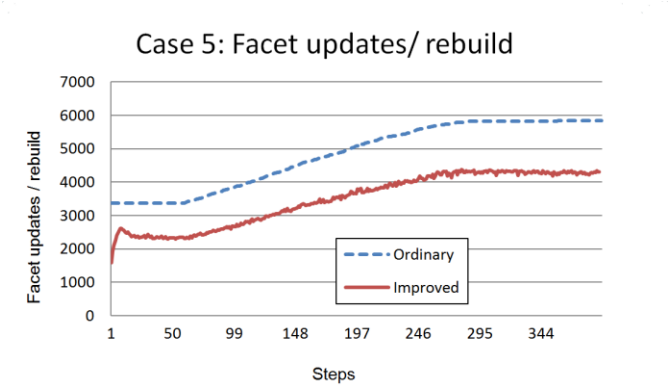

Figure 5.64: Shows the number of facet updates vs. rebuilds for the plate impact example (case 5).

5.5.5 CPU time costs

The computational time is measured as the time taken to complete the analysis. This includes the memory allocation, writing output to file and terminal. Figure 5.65 shows the summary of the computational speedup in time by comparing the ordinary vs. the improved search algorithm. The test results show that the performance increases for test cases were elements are inserted and/or deleted, such as in Shot Peening or Plate Impact with element debonding. The single shot impact and sand particle interaction cases perform poor. This could be due to the high number of sand particles in a small compacted volume. For applications such as Shot Peening the computational speed up increased with the length of the analyses.

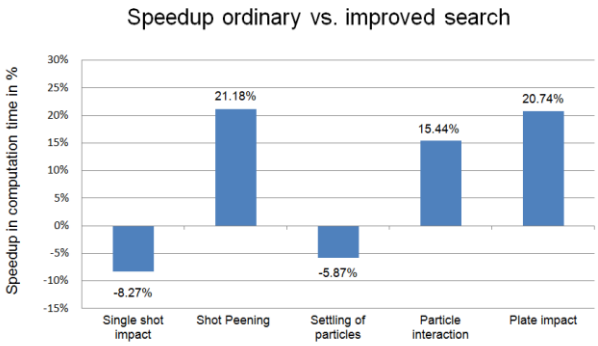

Figure 5.65: Illustrates the computational speedup in time by comparing the ordinary vs. the improved search algorithm.

5.5.6 Conclusion

The choice of binary tree algorithm depends on the problem we are trying to resolve. For instance, when simulating conveyor belts, the majority of the content of the belt will move in one direction. This will result in tree being heavy on one side, therefore requring the balancing routine to be called more frequently. This problem could be resolved with the self-balancing binary tree proposed in this study. Tightening of sub regions reduces the number of node and sub region searches. The performance also heavily depends on the contact zone around the bounding box. A larger contact zone would results in more potential contacts being reported, further increasing the computation time. A smaller contact zone may result in more frequent removal and insertion of the facets into the binary tree. Table 5.8 shows the summary of the ordinary vs. improved algorithm for the different test cases.

Table 5.8: Shows the summary of the ordinary vs. improved algorithm for the different test cases.

	Tree depth	Facet updates	Build space	Searched space	Node visits	Speed up
1. Single Shot	40.00%	25.56%	29.29%	0.00%	0.00%	-8.27%
2. Shot Peening	16.29%	33.22%	88.14%	58.14%	29.96%	31.18%
3. Sandbox	42.65%	28.72%	93.80%	68.40%	22.02%	-5.87%
4.Ball interaction	18.00%	24.73%	19.29%	4.99%	11.00%	15.44%
5. Plate Impact	39.93%	27.77%	7.78%	7.23%	7.34%	20.74%
Average	31.37%	28.00%	47.66%	27.75%	14.06%	10.64%

For problems such as Shot Peening or plate impact with element insertion, deletion or debonding, the proposed method performs better as it eliminates the need to rebuild the whole binary search tree. Deletion and insertion allows reusing of the allocated memory space, allowing one to investigate complex peening processes with very high number of particles and multiple nozzles. The length of the SP peening simulation is no longer limited by the available computer memory and is only limited by the size of peening part and the maximum number of shots present in the analyses at a time step over the whole simulation time.

CHAPTER 6 SINGLE SHOT IMPACT ANALYSIS

One of the major challenges is to understand and the material response due to repeated impingements of small particles over a wide range of impact conditions such as particle size, velocity and incidence angle. Due to the wide range of preening conditions and the difficulty conducting tests with extremely small particle sizes, no efforts have been made to experimentally investigate and model single shot impacts relevant to Shot Peening conditions. Assumptions made by other studies included spherical shots, spherical impact dimple, quasistatic impact and homogeneous material response. Single particle impact tests were conducted over a range of conditions aligned with industrial Shot Peening parameters. By looking at the single shot impact it is possible to obtain information about initial mass, intial velocity, recoil angle, resulting dimple dimensions, and micro structural changes surrounding the impact site. This information can also be used to calculate the coefficient of restitution, *e*, which is the ratio of kinetic energy before and after impact. This is a measure of the dissipation, and provides some characterization data for the material response.

The main objective of the single particle impact test is to gain a better understanding of what happens to the material under impact conditions similar to those seen in production peening. Changes in material response were of particular interest.

Goal of the experiments

The goal of the experimental investigation is to link the impact parameters with the material state after impacts, which could then be used to understand the effect of specific Shot Peening condition. A small gas gun is used to perform single shot impacts test onto Ti-6Al-4V targets. Shots sizes of 0.29 mm to 3 mm in diameter are fired at velocities ranging from 44 - 72 m/s. The material response is assessed by looking at the dimple size (depth, diameter and shape). The CoR is determined using a high speed camera. The changes in microstructure before and

after impact are investigated using optical 3D microscopy, scanning electron microscope (SEM) and Electron Backscatter Diffraction Analysis (EBSD).

Titanium Material

Titanium has a high strength of weight ratio, and good corrosion resistance. It is a naturally occurring element and can be alloyed with multiple different elements such as molybdenum, iron, aluminium and vanadium to enhance and desirable properties of a specific alloy. Titanium has the strength comparable of that of steel but with around half the density. It is denser than aluminium but about twice as strong.

Ti-6Al-4V is a titanium based alloy which consists of various alloying elements, primarily aluminium (6 % weight) and vanadium (about 4 % weight). It is also a two phase alpha - beta alloy. Ti-6Al-4V obtains its alpha stabilization from aluminium and beta stabilization from the vanadium alloy. Ti-6Al-4V accounts for about half of all industrial applications today and is used in the aerospace industry in both propulsion systems and airframes. It is used widely in the medical industry and in the automotive industry and can be found in various component requiring high strength and low weight materials with good corrosion resistance. In the production of the commercially available titanium alloys, the most economical and advantageous manufactured products are flat rolled titanium in strip form. These strips may be continuously annealed, pickled and cold rolled. Titanium based alloys are highly susceptible to the directional effects and show considerable physical anisotropy. The anisotropy is primary evident as differences in mechanical properties such as the elastic moduli when measured parallel (longitudinal) and perpendicular (transverse) to the rolling direction. Even when directionality appears to have been minimized by conventional annealing and cold rolling practices, the mechanical properties are inconsistent in that they vary with the direction in which they are measured. Such directional properties are highly undesirable in flat rolled metal products. The difficulties created by unidirectional rolling of

titanium can be overcome by cross rolling sheets during hot rolling. Cross rolling titanium and titanium alloy sheets reduces the amount of anisotropic effects. The material was originally manufactured as a cross rolled plate. For the purpose of this study, the plates were further annealed to relieve any existing residual stresses induced during the manufacturing and cutting processes. The tests compare shot velocity (40 to 80 m/s) against shot size (0.29 STD peening media to 3 mm) in an experimental characterisation matrix presented below.

6.1 Experimental setup

6.1.1 Gas gun

A gas gun was employed to investigate the dynamic indentation of shots on Ti-6Al-4V targets. The setup is capable of estimating the force applied to the target and the force transmitted to the back support of the system. During the experiments, the velocity of the projectile prior to the impact, and the strain produced on the backing bar behind the target and the moment of the impact are recorded using a using a high-speed camera. The impact velocity can be controlled sufficiently to replicate a single shot impact of the Shot Peening media. The velocity can be accurately controlled by the amount of compressed Nitrogen gas that is released from the pressure vessel using a ball valve release system. Once the actuator is released the projectile accelerates down the barrel. The compressed Nitrogen gas chamber has a maximum pressure capacity of 80 bars. The barrel connected to the pressure vessel is made of steel, coated with zinc and of length 2400 mm with internal and external diameters 12 mm and 20 mm respectively. The barrel is held in place with supports to avoid moving perpendicularly to its length, and to resist recoil momentum when firing.

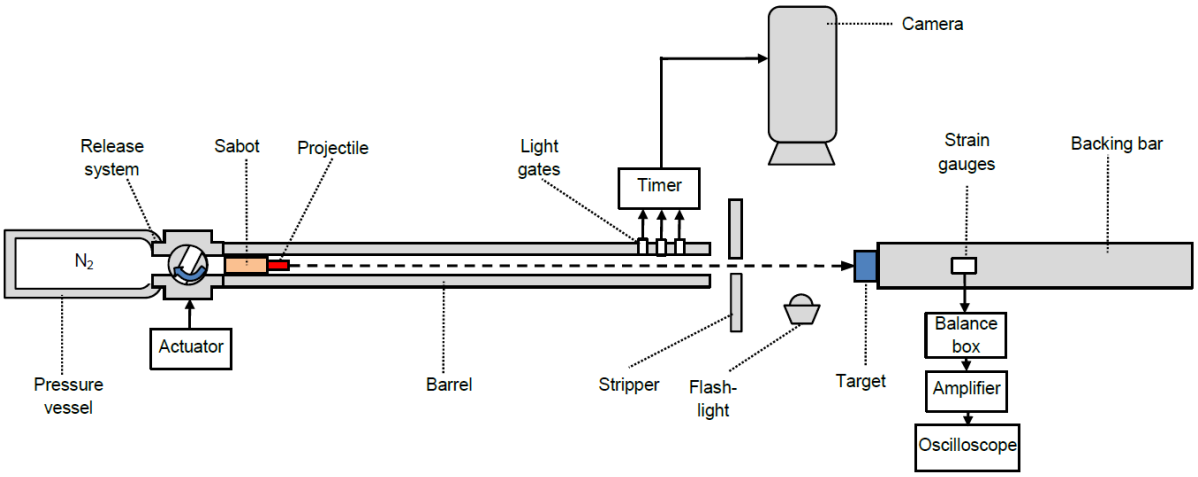

Figure 6.1: Illustration of the gas gun after (Spawton, 2011).

Before firing, each projectile is attached to the centre of a nylon sabot using double-sided tape. The sabot has roughly a diameter of 12mm to ensure the correct positioning of the sabot into the barrel. The sabot is of a length of 25 mm and weights approximately 4.1 g. The low weight minimises frictional force inside the barrel. The velocity of the subot before the impact is measured using three light gates that are placed sequentially at 25mm apart at the exit end of the barrel. The light gates trigger the high-speed camera and flash light to record the impact. A set of strain gauges located on the backing bar, as shown on Figure 6.2, measure the voltage which is converted into transmitted strain during impact. A safety compartment is fitted around the end of the barred to retain the sabot, projectile and target after impact. Before using the gun to populate the test matrix, a number of sample shots are fired to calibrate the set up and verify repeatability and consistency of the data obtained.

6.1.2 Camera

The impact of the projectile was recorded using a Phantom 7.1 High Speed Video Camera (Vision Research, USA) recording at a frame-rate of 66,667 frames per second, with 2μs exposure time, 13μs inter-frame time. The camera was mounted perpendicular to the

projectile flight path and parallel to the projectile surface. The velocity of the projectile was then measured using three light curtains.

6.1.3 Backing Bar

The target was mounted with a small quantity of vacuum grease on a 5mm diameter, 300mm length titanium bar. The bar was instrumented with 4 strain gauges as show in Figure 6.2 where pairs of strain gauges were placed on opposite sides of the bar

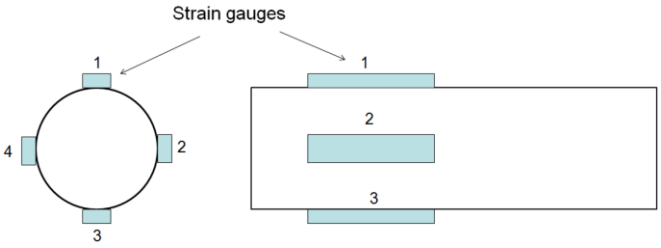

Figure 6.2: Wiring diagram and strain gauge placement for backing bar.

This set-up measures axial strain whilst isolating the influence of any bending strains imposed on the bar. The excitation voltage was measured at 5.05 Volt, and the output voltage was fed through a pre-amplifier with a gain of 1000 x. The amplified voltage was logged by a PXI data logger with a sample rate of 0.2 μs. As the projectile impacts the target, the strain pulse generated by the impact is measurement by the bridge as a pulse of voltage against time. The strain in the rod for a given voltage is given by the standard equation:

$$\varepsilon = \left(\frac{V_{out}}{a}\right)\frac{2}{GF \cdot V_{in}} \qquad \text{Eq. 6.1}$$

where ε is the strain, V_{out} is the logged voltage (V), a is the gain (1000), GF is the gauge factor of the strain gauge (2.16), V_{in} is the input voltage (5.05V).The corresponding force required to generate that strain is given by:

Eq. 6.2

$$F = \varepsilon EA$$

F is the force (N), E is the Young's modulus of Ti-6Al-4V (108 GPa), A is the cross-sectional area of the bar ($2.5^2\pi$ x10^{-4} m²). If we assume that the wave propagating through the bar has a constant velocity, the time and position of the wave are proportional the total momentum transferred to the backing bar is given by:

Eq. 6.3

$$Q = \int_0^T F\, dt = \int_0^T \varepsilon EA\, dt = \int_0^X \frac{AE}{c} \cdot \varepsilon\, dx$$

Using the trapezium rule to approximate the integral, the final equation used is:

Eq. 6.4

$$Q = \frac{AE}{c}\int_0^X \varepsilon\, dx \approx \frac{AE}{c}\sum_{x=0}^{X} \varepsilon\, \Delta x$$

Where Q is the total momentum, T is the time period of the wave, F is the force applied to the backing bar, t is the time elapsed, E is the Young's modulus, c is the speed of sound in the material, X is the length of the wave, x is the position along the bar, ε is the strain in bar.

6.1.4 Preparation of the target

Two different sample sets of Titanium Ti-6Al-4V specimens are used in the study.

Samples: Set-1

Titanium Ti-6Al-4V rods with length of 300 mm and diameter of 5 mm are cut into cylinder sections with a length of 5 mm using a Linear Precision Saw (Buehler, USA) with a Diamond Wafering Blade (Series 15 LC) (Buehler, USA).

An optical 3D micro coordinate system *Infinite Focus* (Alicona, Austria) was used to measure the profile form and roughness of the sample surfaces under 20 x and 50 x objective lens. The root-mean-square roughness (R_{RMS}) for each target is recorded, which is a standard measure

of profile roughness and is calculated by image analysis software *Alicona IFM 3.5* (Alicona, Austria), with the standard equation:

Eq. 6.5

$$R_{RMS} = \sqrt{\frac{1}{n}\sum(x_i - \bar{x})^2}$$

where n is the number of equally spaced points along the trace x_i, and $\bar{x}$ are the vertical distances to the i^{th} data point and to the mean line respectively. The average surface profiles measurements of the 3 different specimens are shown in Table 6.1.

Table 6.1: Average surface profile measurements.

Description	Name	Value	Unit
Average roughness of profile	Ra	405.625	µm
Root-Mean-Square roughness of profile	Rq	521.485	µm
Maximum peak to valley height of roughness profile	Rt	3.14665	µm
Mean peak to valley height of roughness profile	Rz	2.369175	µm
Maximum peak to valley height of roughness profile within a sampling length	Rmax	2.9736	µm
Maximum peak height of roughness profile	Rp	1.600075	µm
Maximum valley height of roughness profile	Rv	1.5466	µm

Samples: Set-2

A separate set of Titanium Ti-6Al-4V specimens were created using a cross rolled plate. The specimens were cut into 7 x 6 x 5 mm (T1), 6 x 5 x 4 mm (T2) and 7 x 5 x 4 mm (T3) blocks using a Linear Precision Saw (Buehler, USA) with a Diamond Wafering Blade (Series 15 LC) (Buehler, USA). To distinguish the different specimens, and maximise produced specimens with the available material, unique dimensions were used for the type of specimens with different surface orientation as shown in Figure 6.3.

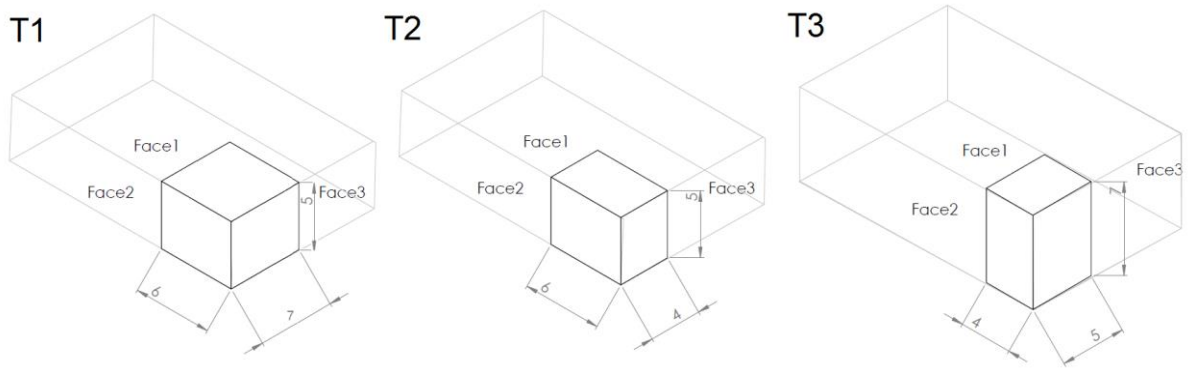

Figure 6.3: Specimen used in the second experiments.

The specimens were first grinded with the EcoMet 300 Grinder (Buehler, USA) and then polished with fluid silica (50 nm particle size) under the pressure of 10 N in a FORCIMAT specimen mover. A polishing fixture was produced, to allow four specimens to be polished at a time and to minimize the abrasion of the edges of the specimen.

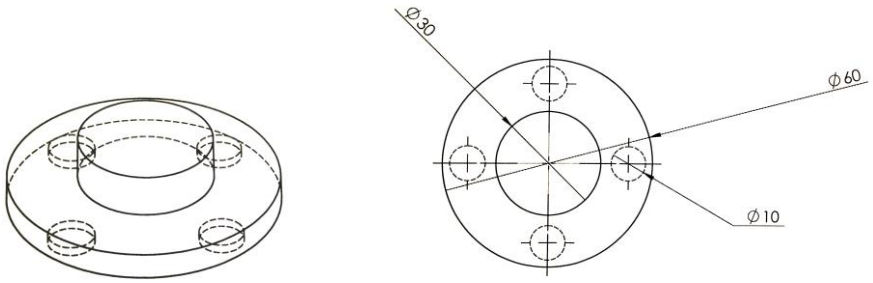

Figure 6.4: Fixture used for the polishing procedure, minimize the abrasion of the edges of the specimen.

After the polishing procedure the surface profile was examined with Alicona. The average surface profiles measurements of the 3 different specimens are given in Table 6.2.

Table 6.2: Surface profile data obtained by Alicona analysis.

Description	**Name**	**Value**	**Unit**
Average roughness of profile	Ra	0.8662	µm
Root-Mean-Square roughness of profile	Rq	1.0578	µm
Maximum peak to valley height of roughness profile	Rt	5.7827	µm
Mean peak to valley height of roughness profile	Rz	4.0925	µm
Maximum peak to valley height of roughness profile within a sampling length	Rmax	4.8496	µm
Maximum peak height of roughness profile	Rp	2.7548	µm
Maximum valley height of roughness profile	Rv	3.0279	µm

The Alicona analysis revealed that the average roughness profile of the polished set-2 speciments were 500 times lower than that of the unpolished set-1 speciemens.

6.2 Experimental results

6.2.1 Camera footage of impacts

The footage obtained during the shot impact from the Phantom camera for different shot sizes are show below.

		Shot diameter 0.29 mm Ø Pressure 4 PSI Velocity 44m/s
		Shot diameter 1 mm Ø Pressure 4 PSI Velocity 45m/s
		Shot diameter 2 mm Ø Pressure 4 PSI Velocity 45m/s
		Shot diameter 3 mm Ø Pressure 4 PSI Velocity 45m/s

The velocity of the shot before and after impact was examined through image analysis. The Phantom image camera control application, 'Phantom Camera Control Version: 8.1.607.0-C PhCon:607', was used to track the velocity of the shots and compared with the results obtained from the simulation. Although the three light curtains attached to the end of the bar measure the velocity of the sabot, they do not measure the velocity of the shot. Image

analysis provides an additional method to approximate the shot velocity at impact. The accuracy of the results however, depends of the resolution of the image and number of frames per second at which images are recorded. With a single camera, the flying path of the shot can only be analysed in two dimensional space and can therefore only be approximated. The results show that the velocity obtained at impact, from the image analyses, varies from 2 to 6 %. It can also be concluded that in both the experiments and simulations the CoR decreases with the increase of shot size and increase of impact velocity. The results are summarised in Table 6.3.

Table 6.3: Comparison of impact and rebounding velocity of single shot impacts (experiments vs. simulation).

Shot diameter in mm	Impact velocity (experiment) in m/s	Rebounding velocity (experiment) in m/s	CoR Experimental	Impact velocity (simulation) in m/s	Rebounding velocity (simulation) in m/s	CoR Simulation
0.29	45.26	34.53	0.7629	44	23.558	0.5354
0.29	58.43	38.36	0.6565	56.5	27.92	0.4942
0.29	68.59	39.73	0.5793	70	32.569	0.4653
1	46.56	28.75	0.6176	45	21.891	0.4865
1	54.42	29.61	0.5442	57	26.0717	0.4574
1	75.15	31.19	0.4150	71	30.977	0.4363
2	46.06	23.53	0.5109	45	17.54	0.3898
2	58.96	23.86	0.4047	57	21.74	0.3814
2	72.27	25.58	0.3540	71.5	27.57	0.3856
3	42.78	14.83	0.3468	44	10.37	0.2357
3	54.55	17.06	0.3128	58	10.19	0.1757
3	64.26	20.84	0.3244	66.5	9.99	0.1502
3	70.01	19.64	0.2806	71	10.01	0.1410

6.2.2 Target characterisation after impact

Microscopic examination specimen: Set-1

Firstly, an optical 3D micro coordinate system, the Infinite Focus (Alicona, Austria), was used to measure the indentation size and depth of the impacted samples of under a 20 x and 50 x objective lens.

0.29mm shot ø Pressure 4 PSI Impact velocity 44 m/s Indentation depth -0.00150 mm Indentation width -110 µm	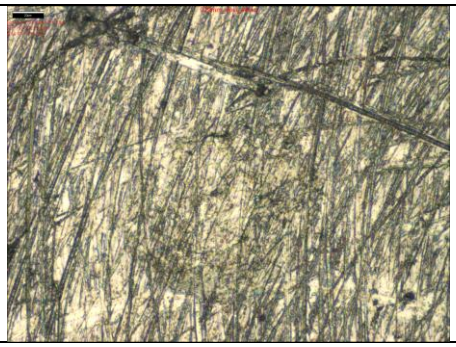	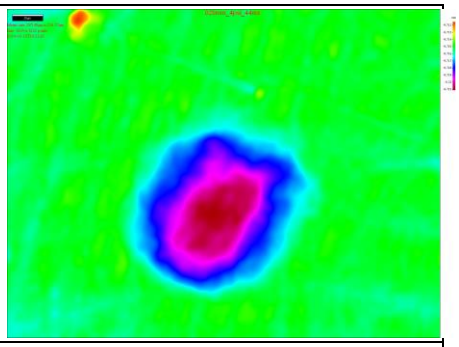
	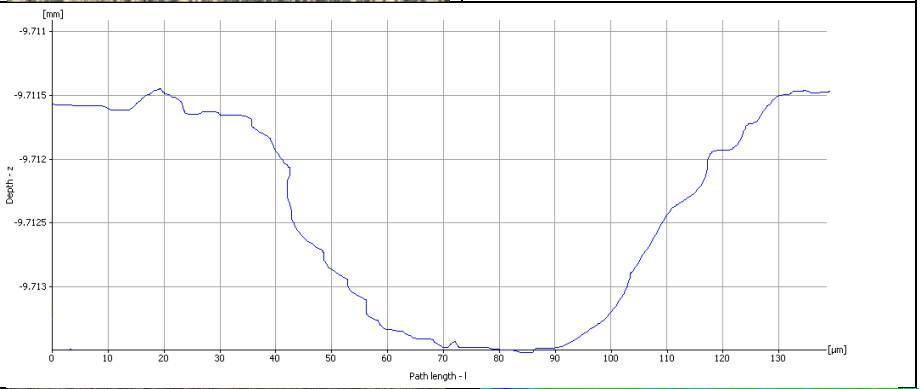	
0.29mm shot ø Pressure 6 PSI Impact velocity 56.5 m/s Indentation depth -0.00510 mm Indentation width -135 µm	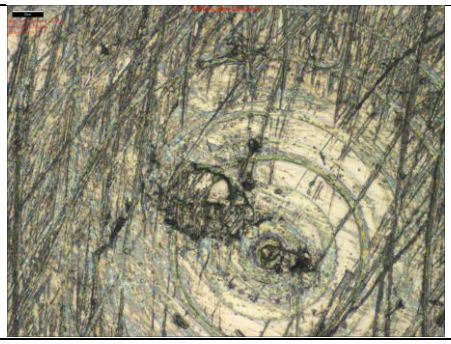	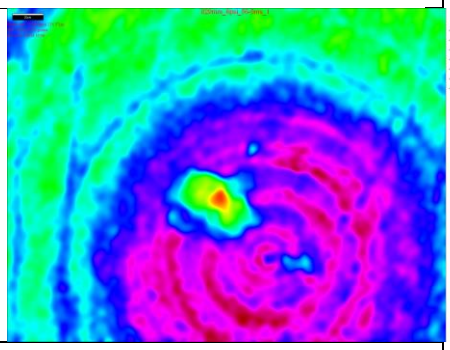
	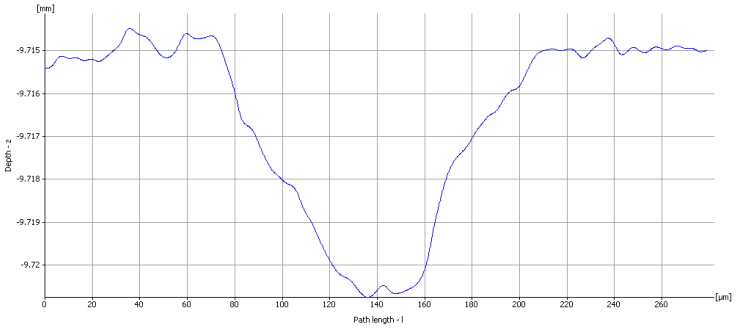	
0.29mm shot ø Pressure 9 PSI Impact velocity 70 m/s Indentation depth -0.00780 mm Indentation width -166 µm	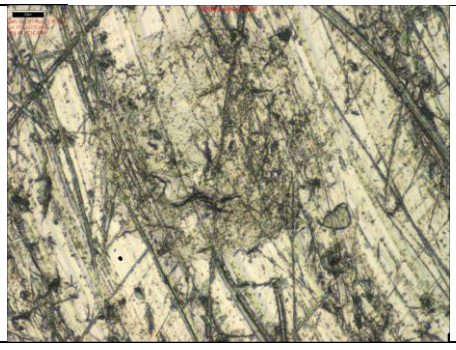	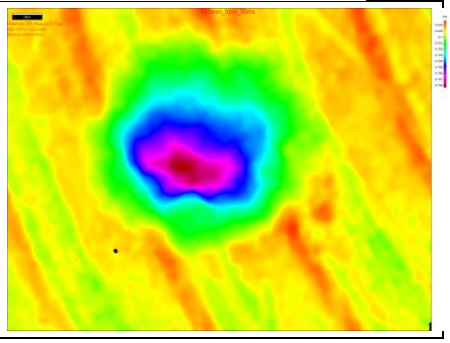

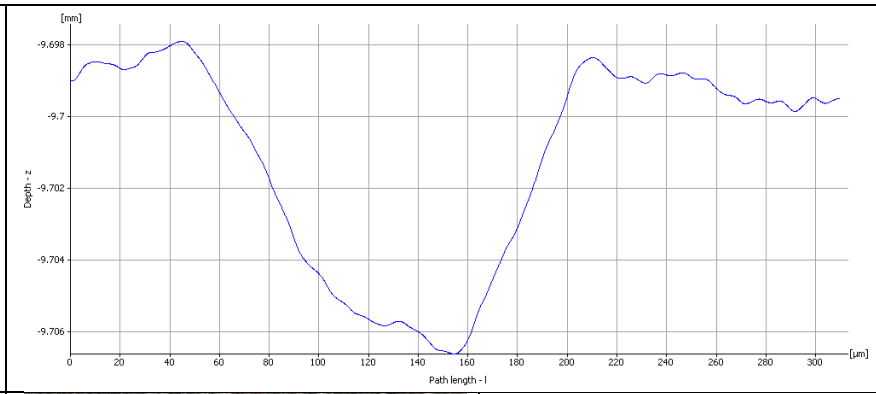

1 mm shot ø
Pressure 4 PSI
Impact velocity
45 m/s
Indentation
depth
-0.01220 mm
Indentation
width
-340 µm

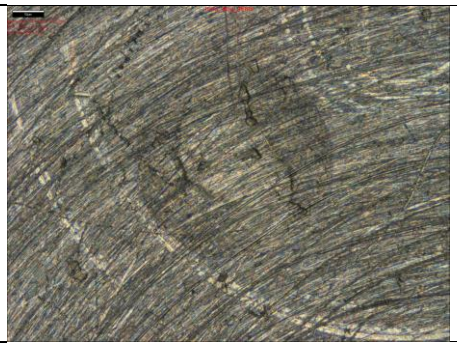

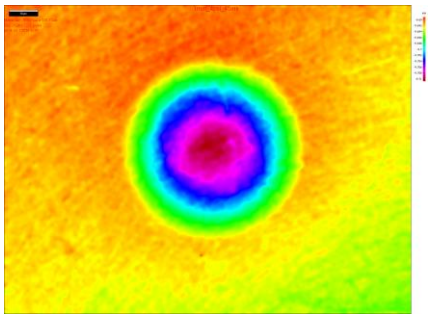

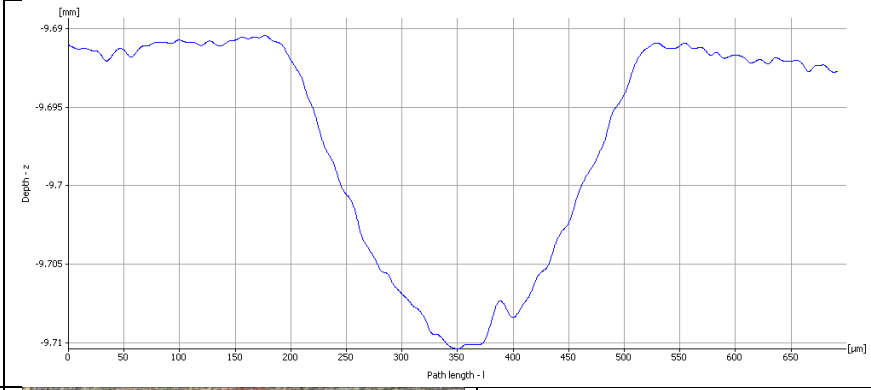

1 mm shot ø
Pressure 6 PSI
Impact velocity
57 m/s
Indentation
depth
-0.02850 mm
Indentation
width
-380 µm

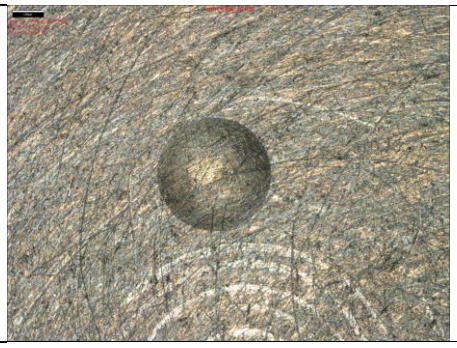

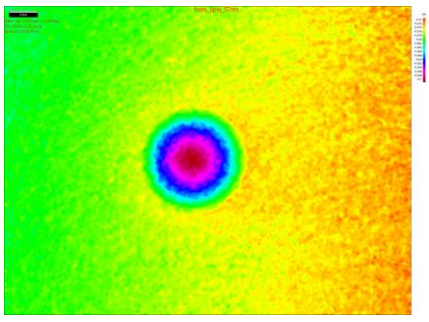

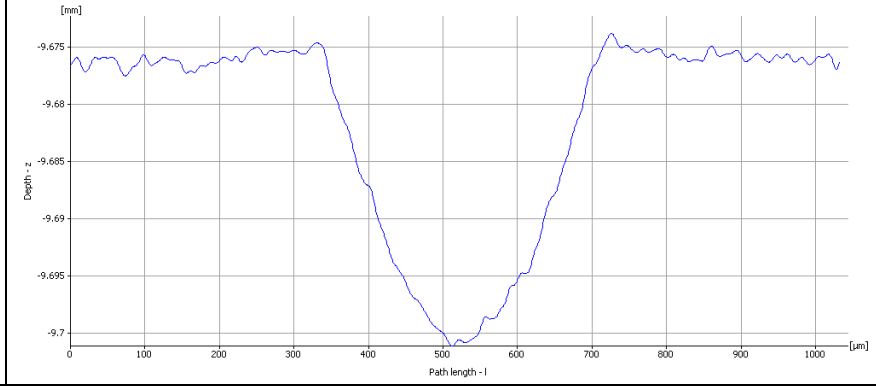

1 mm shot ø Pressure 9 PSI Impact velocity 71 m/s Indentation depth -0.03100 mm Indentation width -425 µm	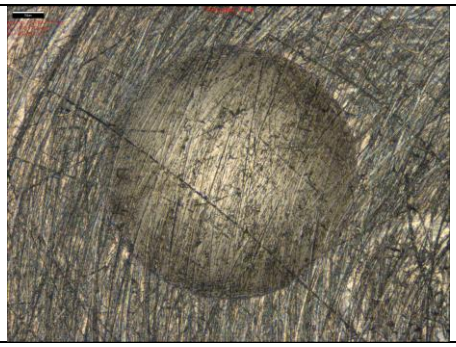 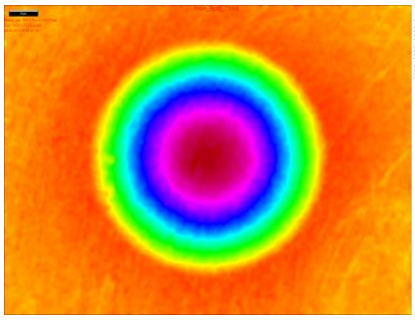 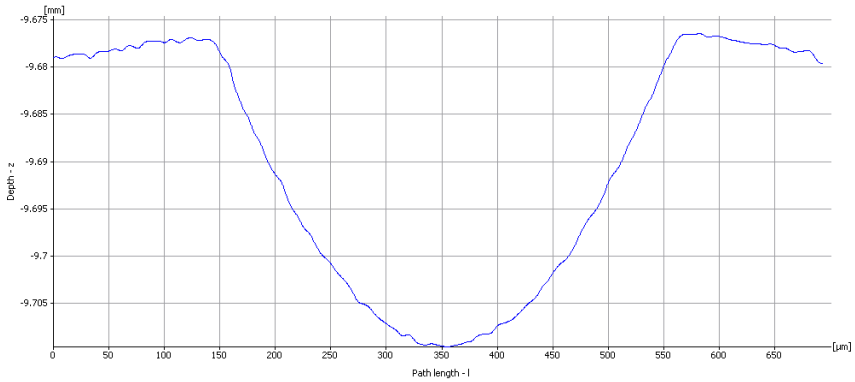
2 mm shot ø Pressure 4 PSI Impact velocity 45 m/s Indentation depth -0.03 mm Indentation width -620 µm	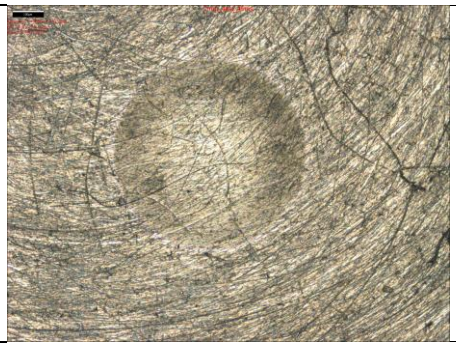 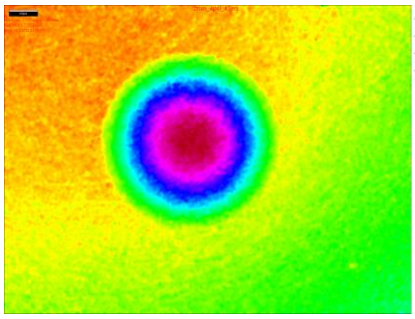 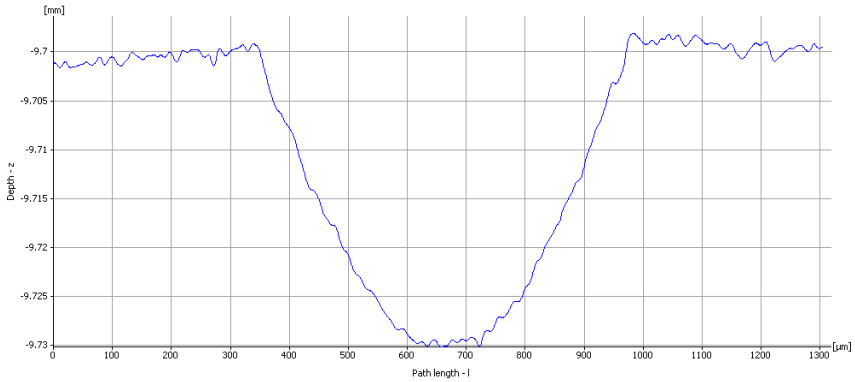
2 mm shot ø Pressure 6 PSI Impact velocity 57 m/s Indentation depth -0.04 mm Indentation width -700 µm	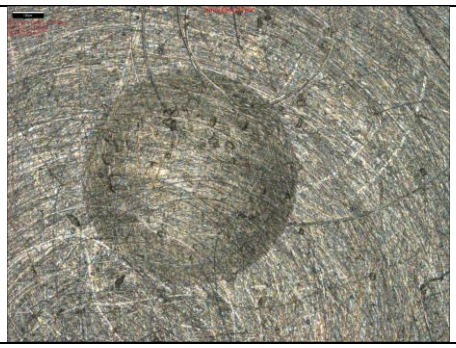 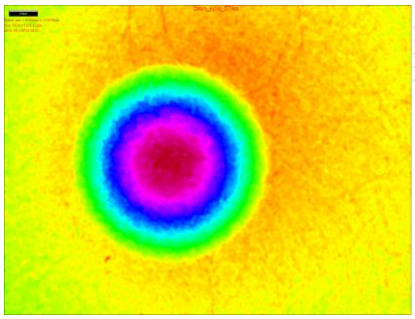

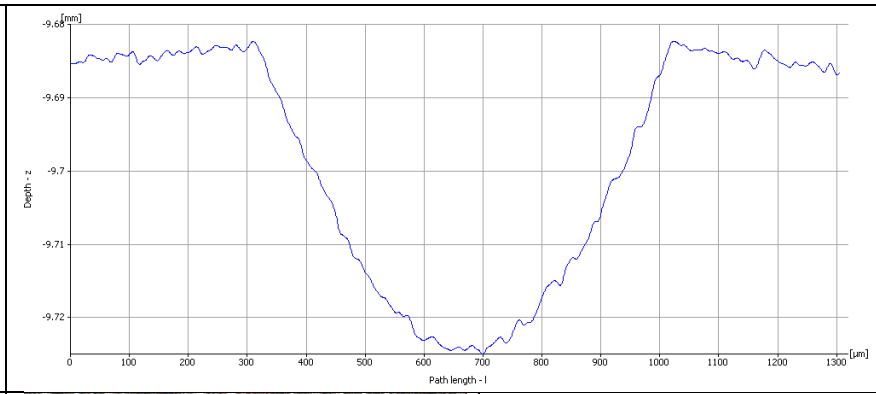

2 mm shot ø
Pressure 9 PSI
Impact velocity
71.5 m/s
Indentation
depth
-0.07 mm
Indentation
width
-800 µm

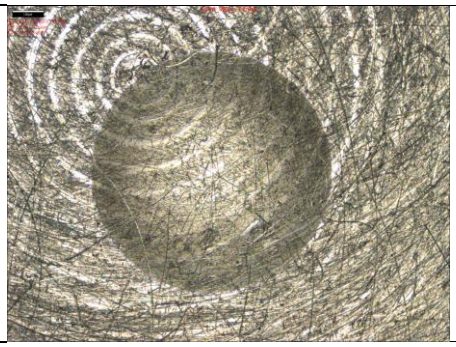

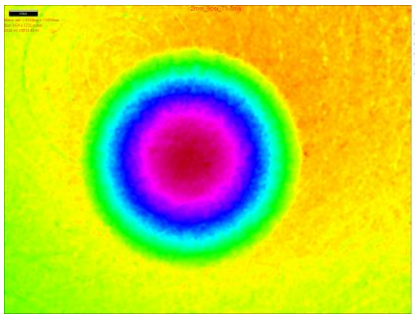

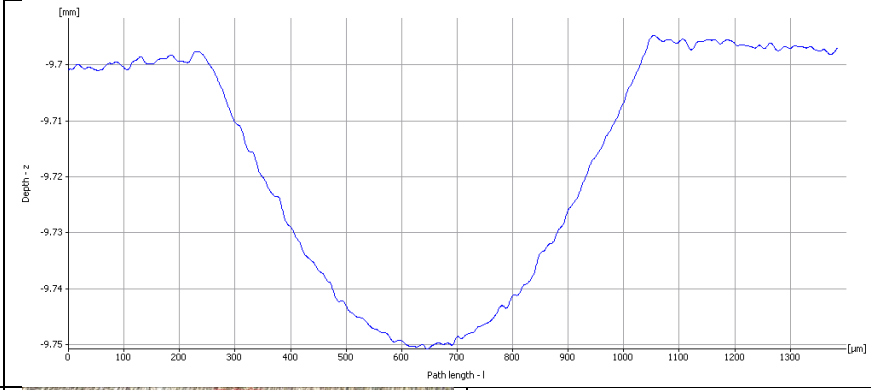

3 mm shot ø
Pressure 3 PSI
Impact velocity
17 m/s
Indentation
depth
-0.0125 mm
Indentation
width
-550 µm

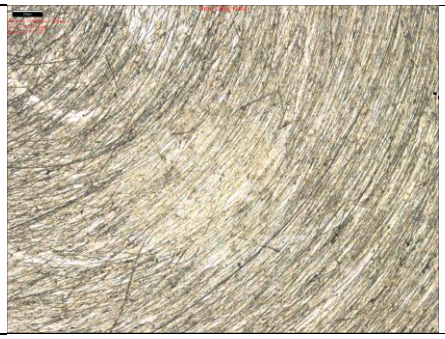

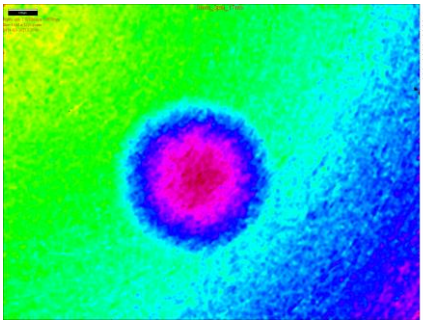

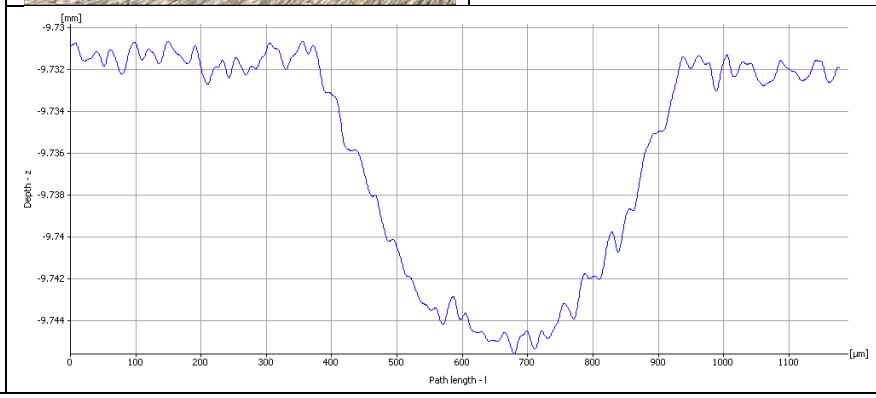

3 mm shot ø Pressure 4 PSI Impact velocity 44 m/s Indentation depth -0.049 mm Indentation width -900 µm	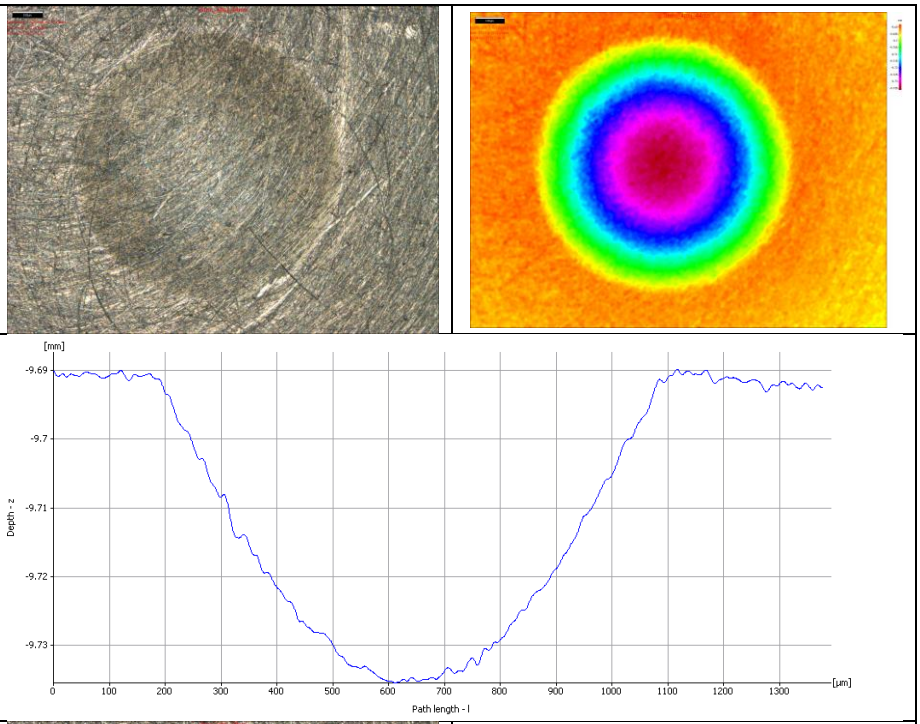
3 mm shot ø Pressure 6 PSI Impact velocity 58 m/s Indentation depth -0.064 mm Indentation width -990 µm	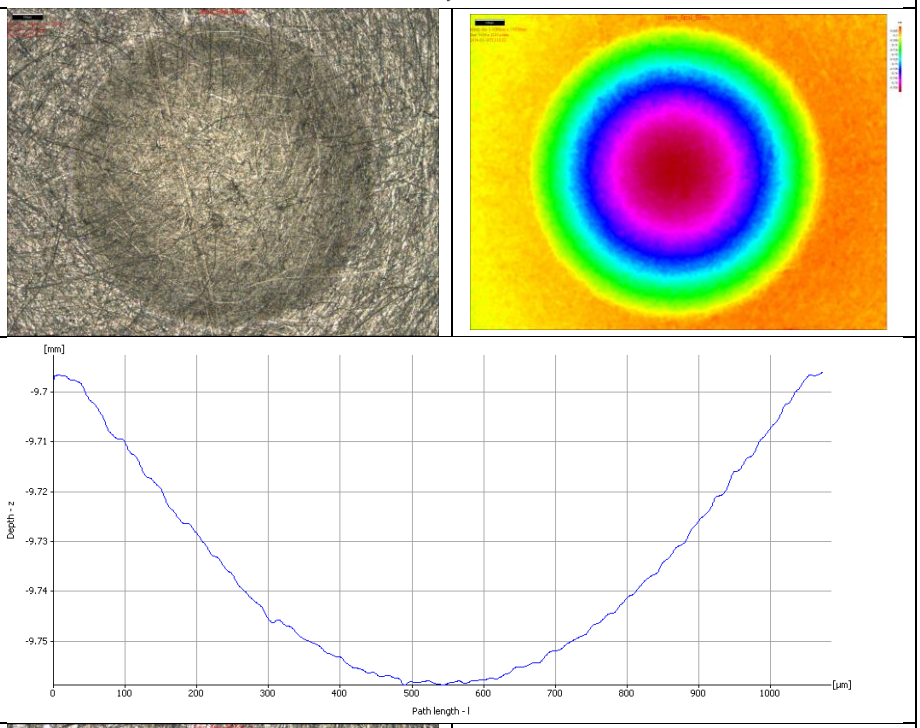
3 mm shot ø Pressure 8 PSI Impact velocity 66.5 m/s Indentation depth -0.078 mm Indentation width -1070 µm	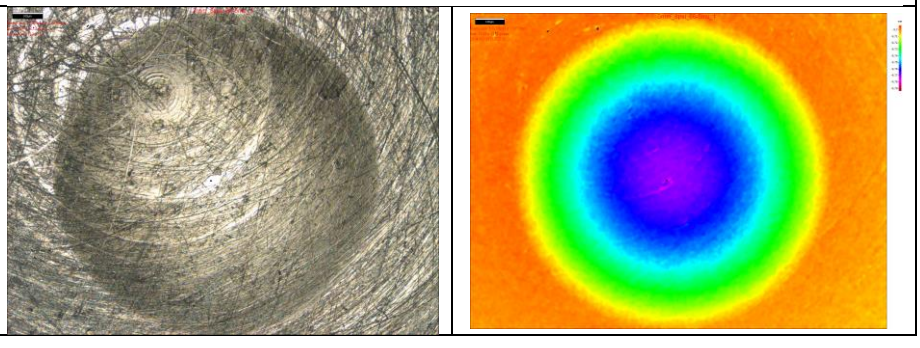

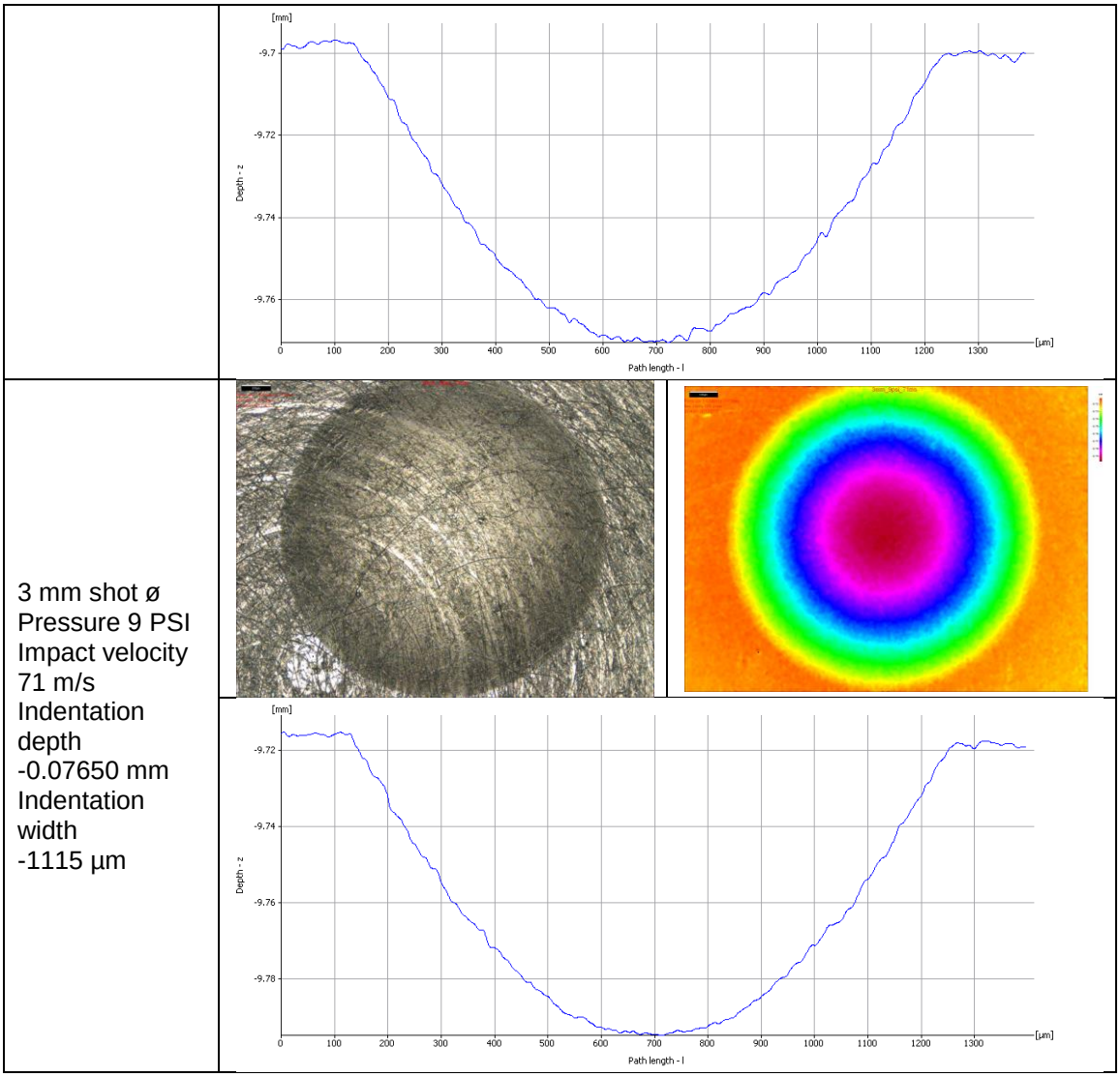

Due to the small indent size and rough target surface it was difficult to obtain an accurate indentation profile for the shot size with diameter 0.29 mm. Table 6.4 shows the summary of the indentation depth and width for different shot diameters and impact velocities.

Table 6.4: Table summarises the indentation depth and width for different shot diameters and impact velocities.

Shot diameter in mm	Impact velocity in m/s	Indentation depth in mm	Indentation width in µm
0.29	44	-0.00150	-110
0.29	56.5	-0.00510	-135
0.29	70	-0.00780	-166
1	45	-0.01220	-340
1	57	-0.02850	-380

1	71	-0.03100	-425
2	45	-0.03000	-620
2	57	-0.04000	-700
2	71.5	-0.07000	-880
3	17	-0.01250	-550
3	44	-0.04900	-900
3	58	-0.06400	-990
3	66.5	-0.07800	-1070
3	71	-0.07650	-1115

Scanning Electron Microscopes: Set-2

The polishing of the second set of specimens made the surface finish glossy and very difficult to be examined with the ALICONA. Instead, the surface indentations were analysed using SEM. A Zeiss Merlin Gemini II Scanning Electron Microscopes (SEM) was used to characterize the surface after the impact.

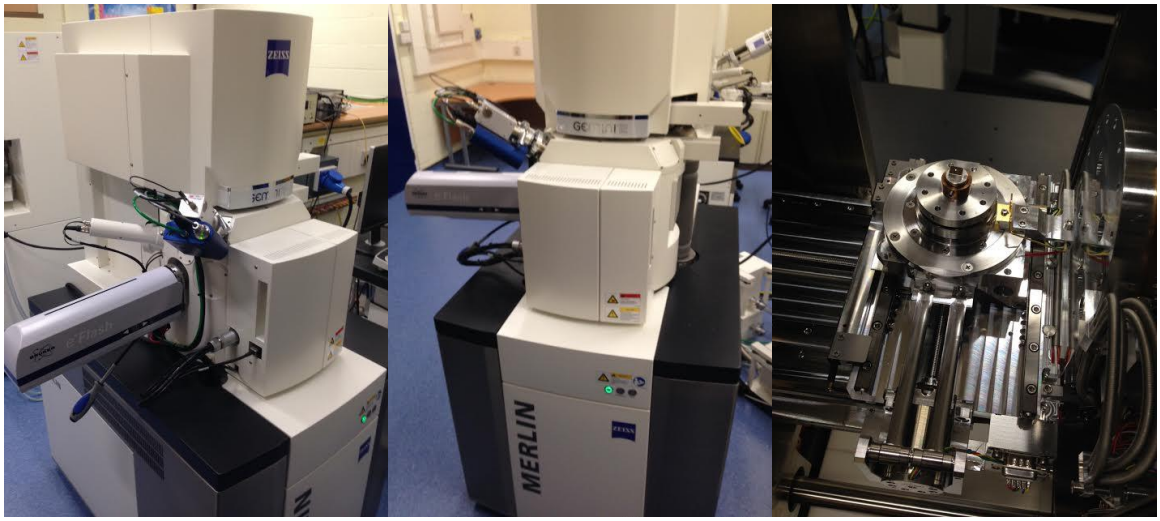

Figure 6.5: Illustration of the Zeiss Merlin Gemini II Scanning Electron Microscopes used in the study.

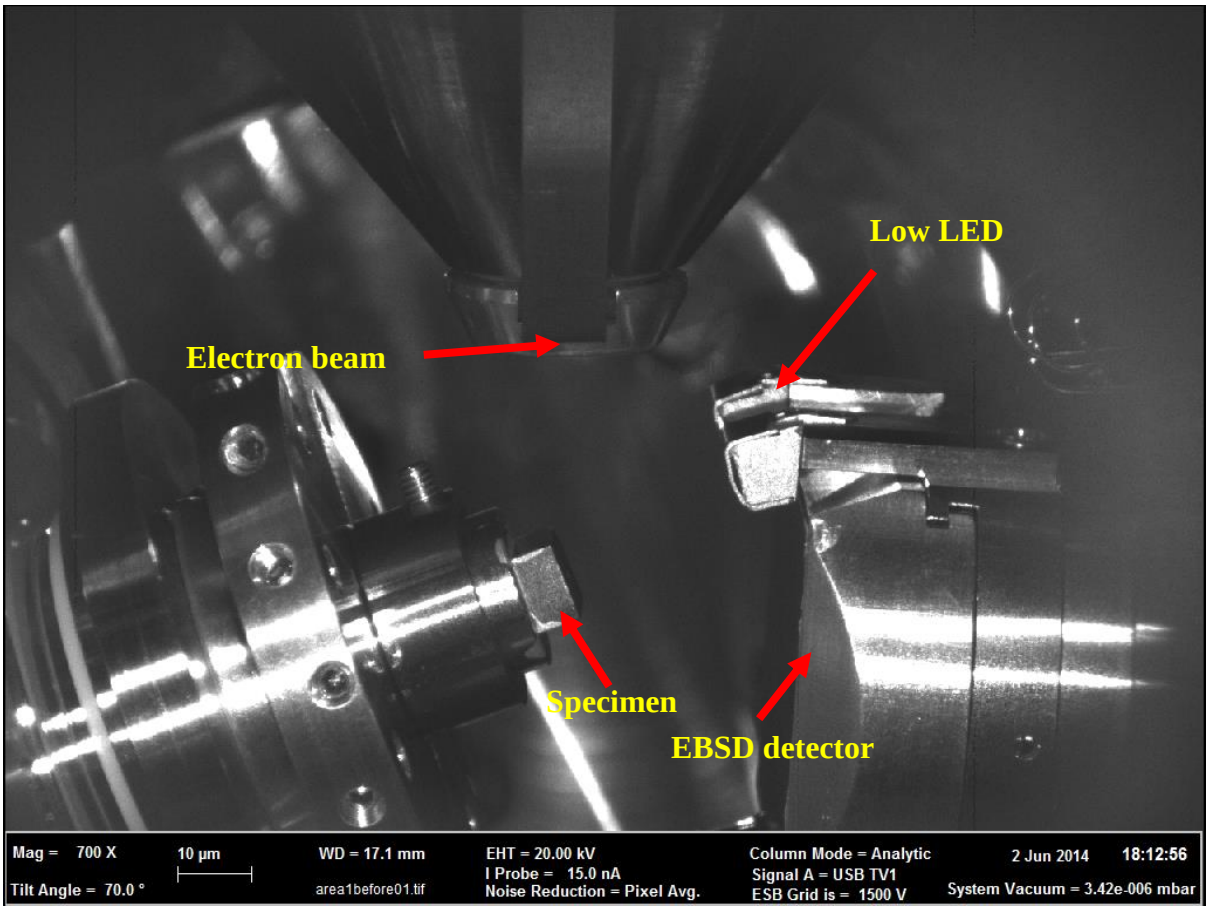

Figure 6.6: Shows the specimen in the microscope with the EBSD sensor, with a working distance of 17.1 mm, at a tilted angle of 70° and 700 X magnification.

Electron backscatter diffraction

Electron backscatter diffraction (EBSD), is a microstructural-crystallographic technique that is applied to examine the crystallographic orientation of materials. This method is used to study the texture or orientation of crystalline or polycrystalline material, perform defect, grain boundary and morphology studies or micro strain mapping.

In practice EBSD is performed using a Scanning Electron Microscope (SEM) with an EBSD detector containing a phosphor screen, compact lens and low light CCD camera. During the measurement process a polished titanium specimen is placed in the SEM compartment. To increase the contrast in the electron backscatter diffraction pattern, the specimen is positioned at a highly tilted angle (~70° from horizontal) towards the diffraction camera, under a 700x

magnification with a distance of 17.1mm from the lens. An ETH of 20kV and probe 15nA under a vacuum of 3.7e-006 mbar were also used. Figure 6.6 shows the measurement procedure. The phosphor screen within the specimen chamber of the SEM is linked to a compact lens. The contact lense focuses the image from the phosphor screen onto the CCD camera. Some of the electrons enter the sample backscatter and escape at the Bragg condition relate to the spacing of the periodic atom planes of the crystalline structure and diffract. Some of the diffracted electrons escape the material and collide and stimulate the phosphor causing it to fluoresce.

The diffraction of different planes on different electrons form Kikuchi bands resulting in an electron backscatter diffraction pattern (EBSP). The Kikuchi bands can be related to the underlying crystal phase and orientation of the material. Scanning the electron beams in a prescribed manner results in many maps; these maps can describe the crystal orientation of the material being investigated and can also be used to examine micro texture and morphology. These maps can also describe grain orientation and grain boundary. Statistical tools can then be used to quantify the average miss orientation, grain size, and crystallographic texture of the material. From the orientation data, a great set of information can be formulated that can be of benefit in the understanding of a components microstructure and the manufacturing/processing history of the material. Figure 6.7, Figure 6.8 and Figure 6.9 show the SEM mapping of the different orientation types. T1 type mapping shows an average grain size of 7 - 10 μm, T2 and T3 specimens show elongated grains of average length 12 - 15 μm and width of 7 - 10 μm.

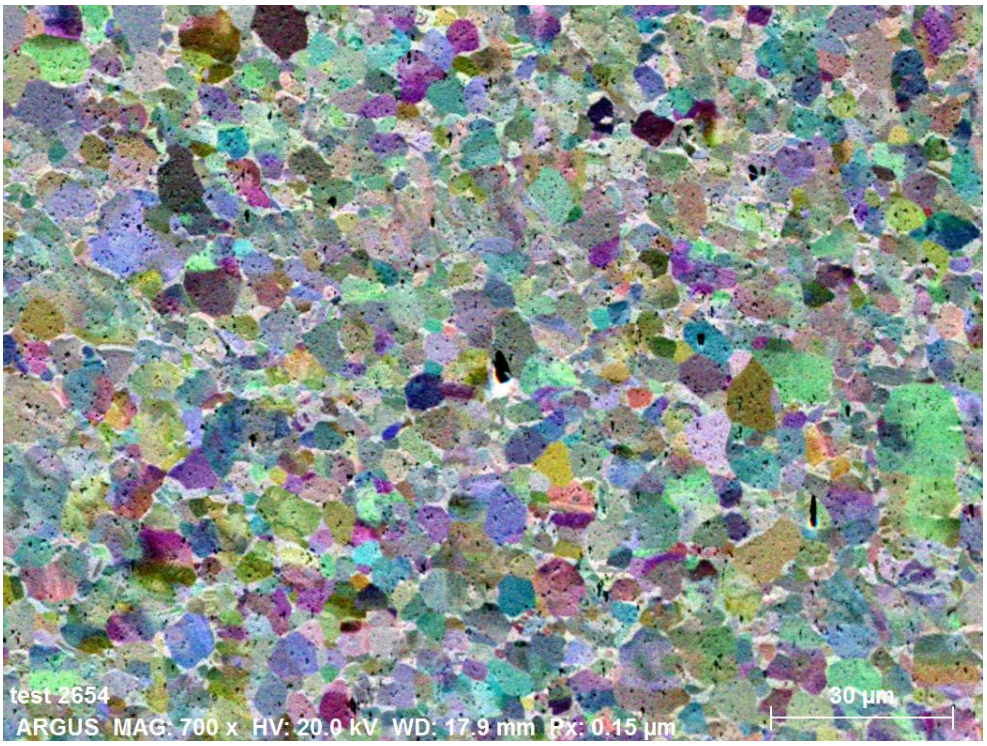

Figure 6.7: SEM image of the polished specimen before the impact of type T1.

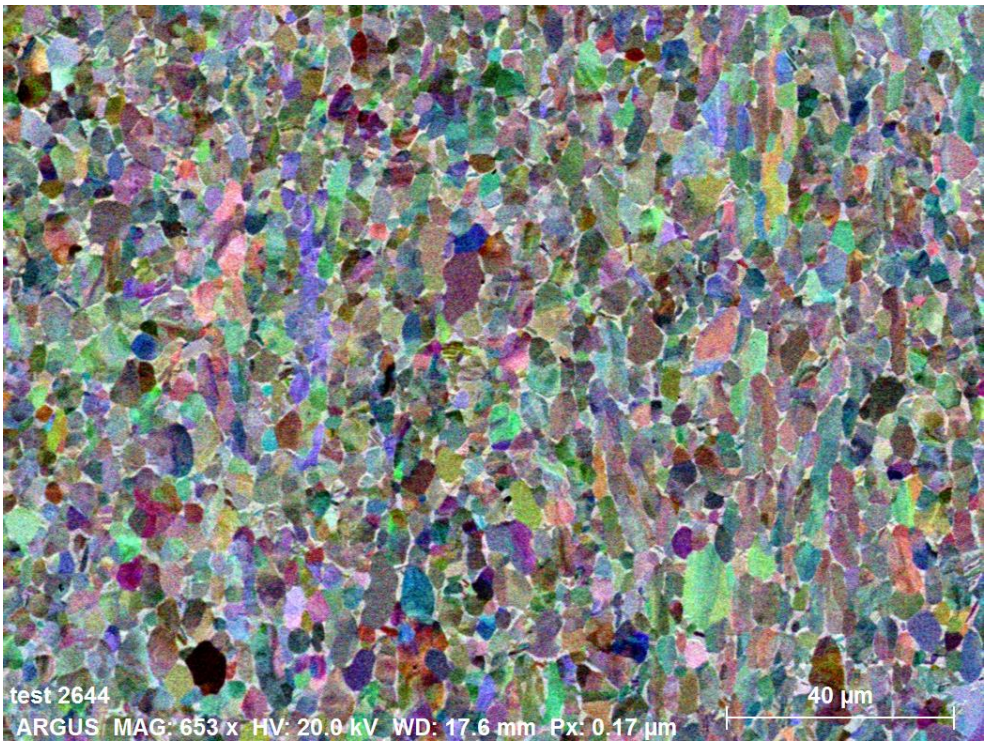

Figure 6.8: SEM image of the polished specimen before the impact of type T2.

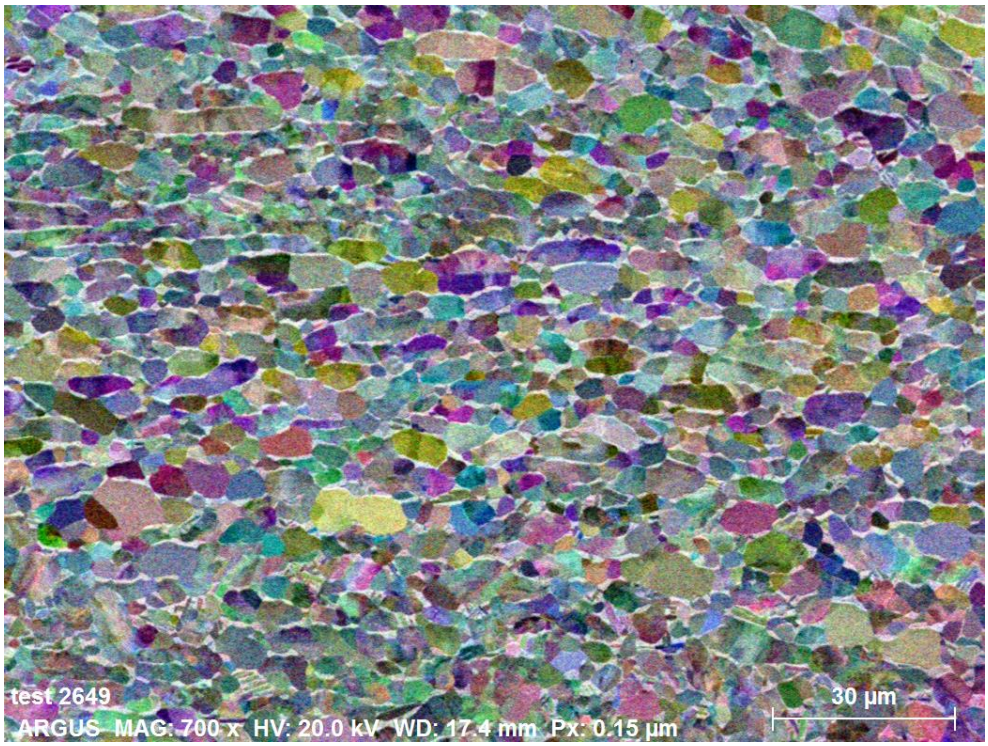

Figure 6.9: SEM image of the polished specimen before the impact of type T3.

Since the second set of specimens were pre-treatment and polishing the surface was too glossy to be examined with the ALICONA. Instead, the surface indentations were analysed using SEM.

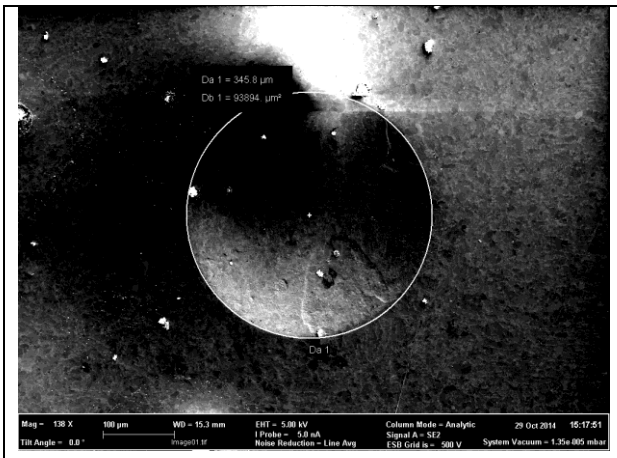

T1: 2mm at 46m/s, diameter 345.8 µm

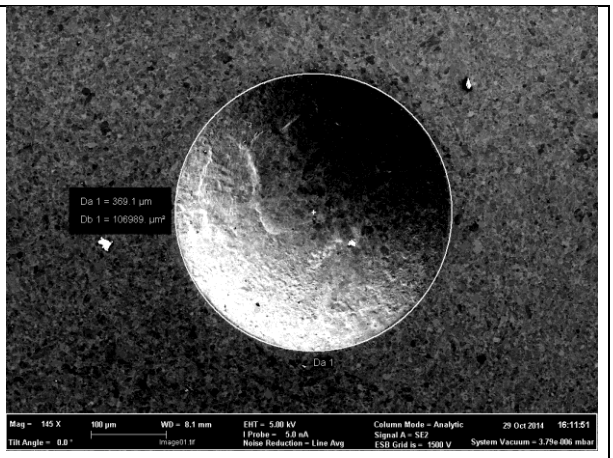

T1: 2mm at 58m/s, diameter 369.1 µm

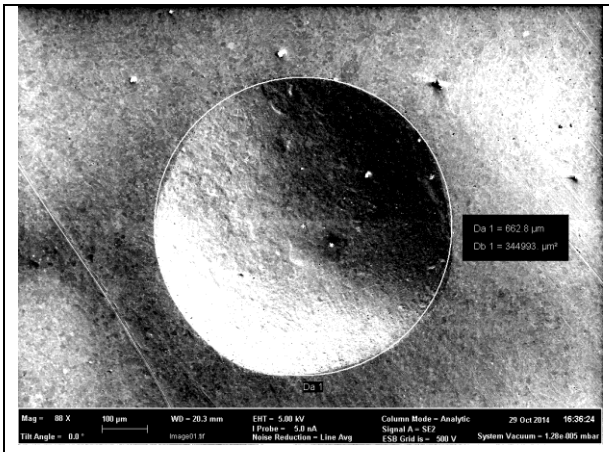

T1: 3mm at 46m/s, diameter 662.8 µm

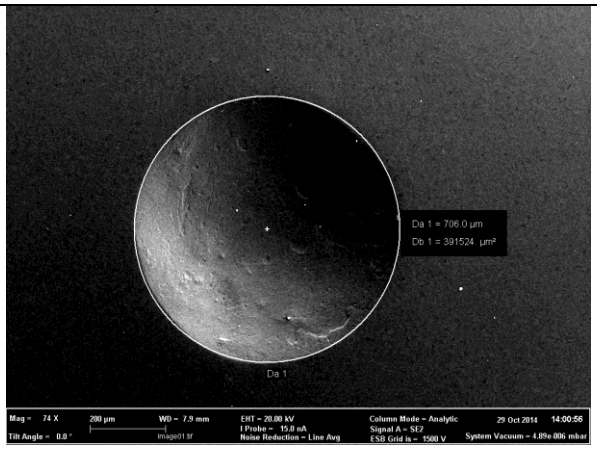

T1: 3mm at 58m/s, diameter 706 µm

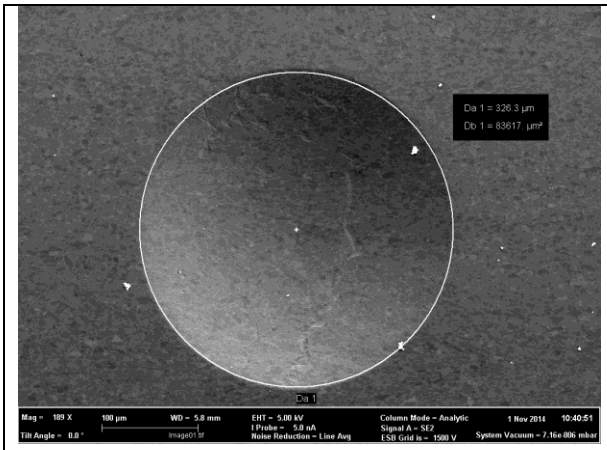

T2: 2mm at 46m/s, diameter 326.3 µm

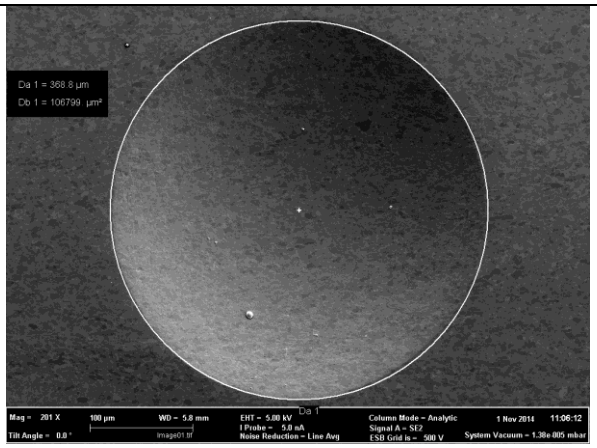

T2: 2mm at 58m/s, diameter 368.8 µm

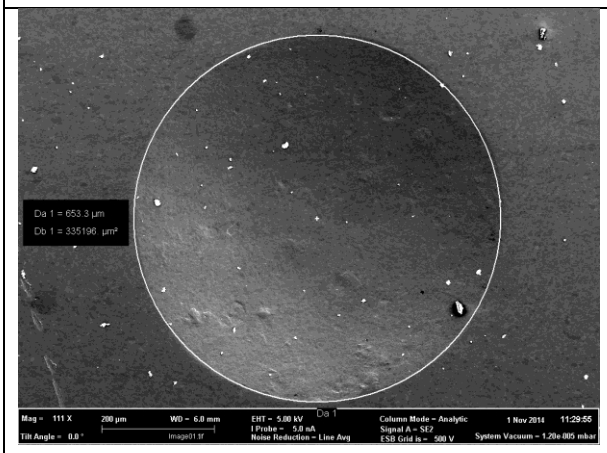

T2: 3mm at 46m/s, diameter 653.3 µm

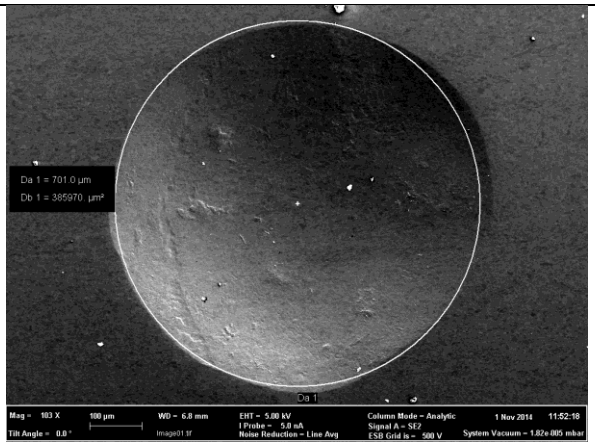

T2: 3mm at 58m/s, diameter 701 µm

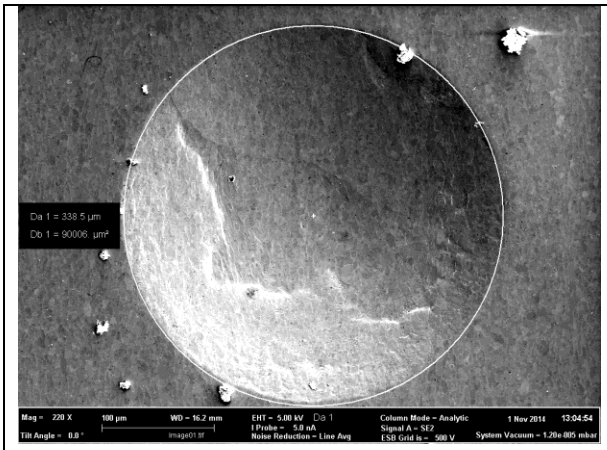

T3: 2mm at 46m/s, diameter 338.5 µm

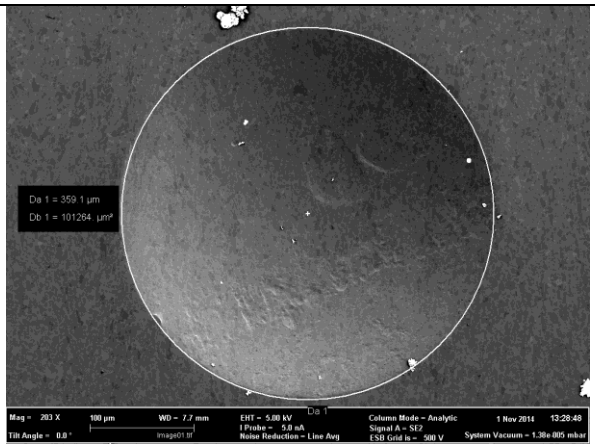

T3: 2mm at 58m/s, diameter 359.1 µm

T3: 3mm at 46m/s, diameter 649.5 µm

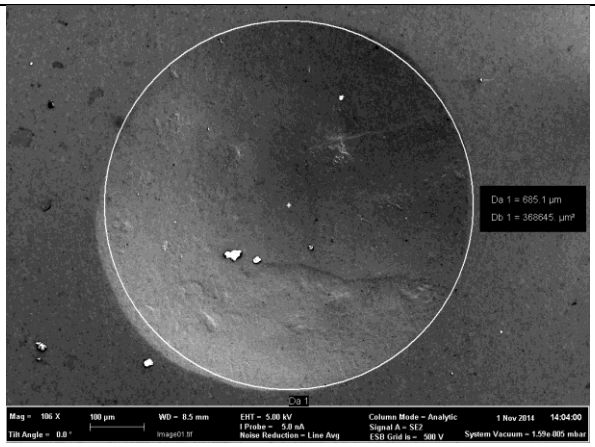

T3: 3mm at 58m/s, diameter 685.1 µm

6.2.3 Plastic zone

The size of the plastic zone of the impacted surface can be determined by examining the zones of slip band formations. The formation of slip bands are primarily depended on the microscopic and macroscopic geometries of the material, such as grain size and structure. Each specimen is examined as shown in Figure 6.10 and the plastic zone is recorded.

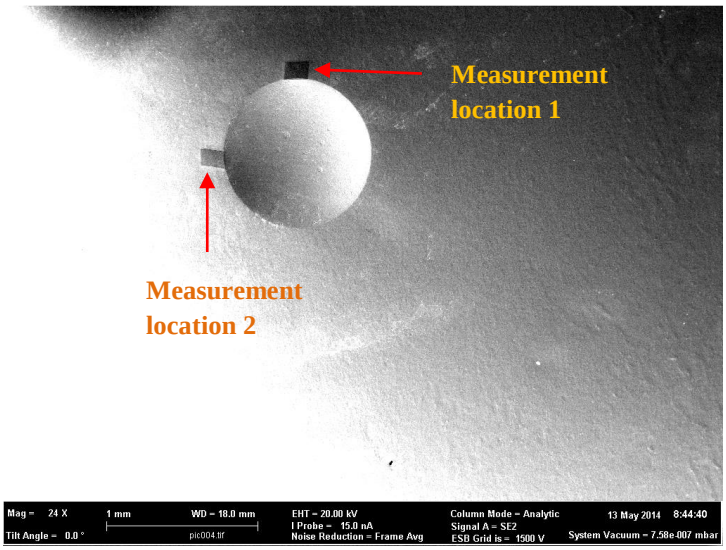

Figure 6.10: Shows the specimen with impact location and two measurement points.

Plastic zone of T1 specimens

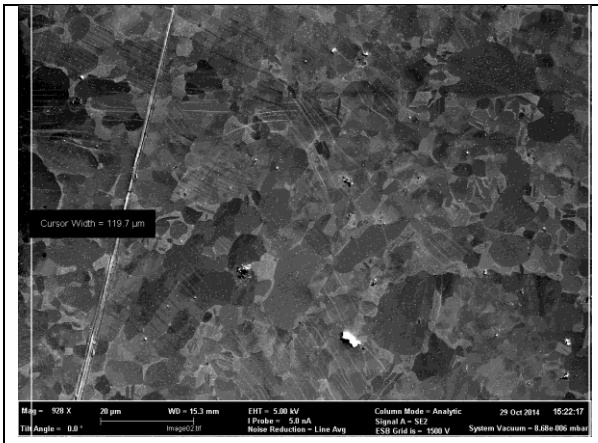	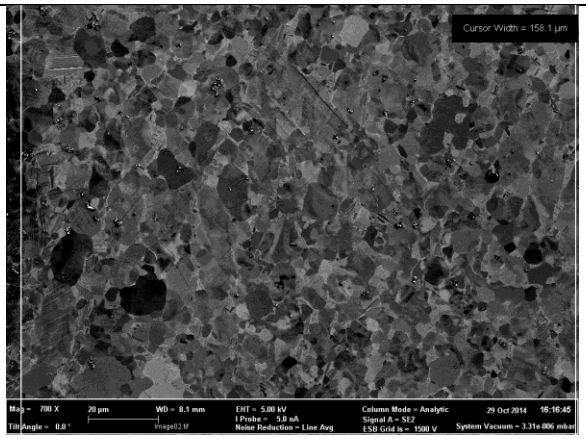
T1: 2mm at 46m/s, plastic zone of 119.7 µm	T1: 2mm at 58m/s, plastic zone of 158.1 µm
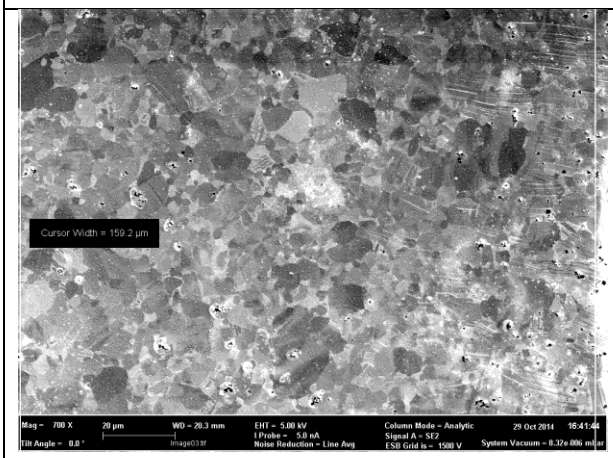	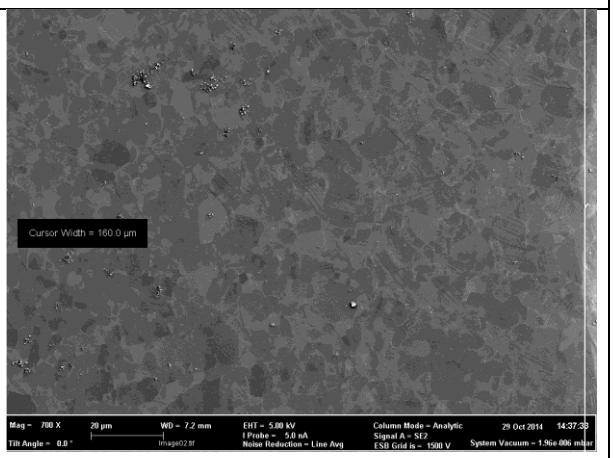
T1: 3mm at 46m/s, plastic zone of 159.2 µm	T1: 3mm at 58m/s, plastic zone of 160.0 µm

Plastic zone of T2 specimens

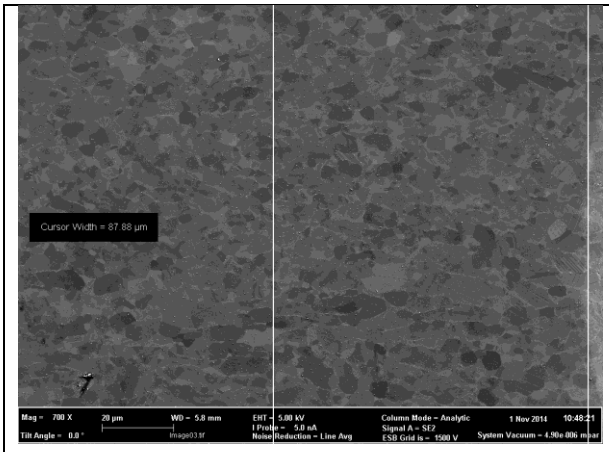

T2: 2mm at 46m/s, plastic zone of 87.88 µm

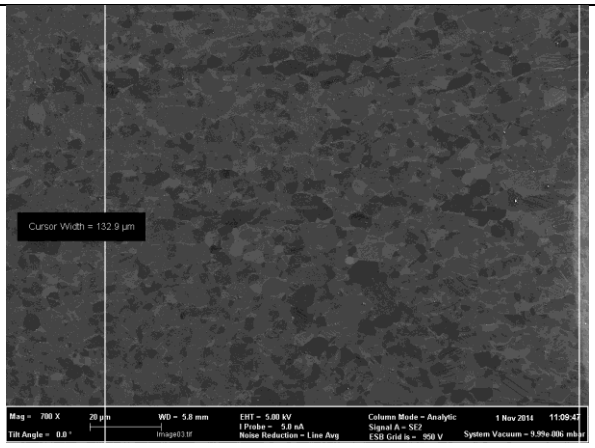

T2: 2mm at 58m/s, plastic zone of 132.9 µm

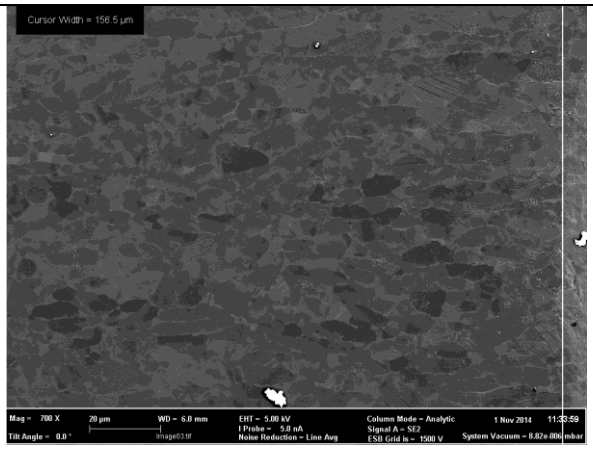

T2: 3mm at 46m/s, plastic zone of 156.5 µm

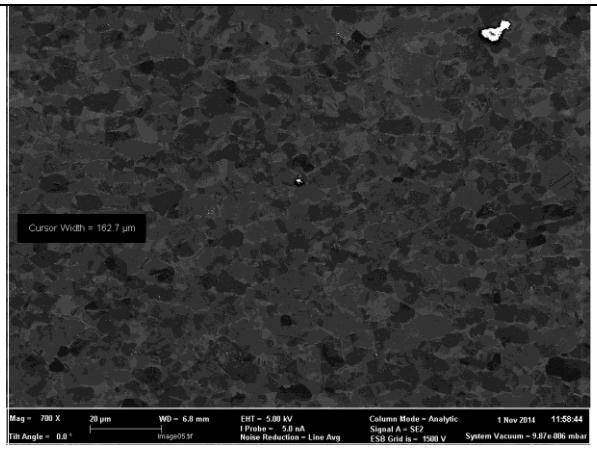

T2: 3mm at 58m/s, plastic zone of 162.7 µm

Plastic zone of T3 specimens

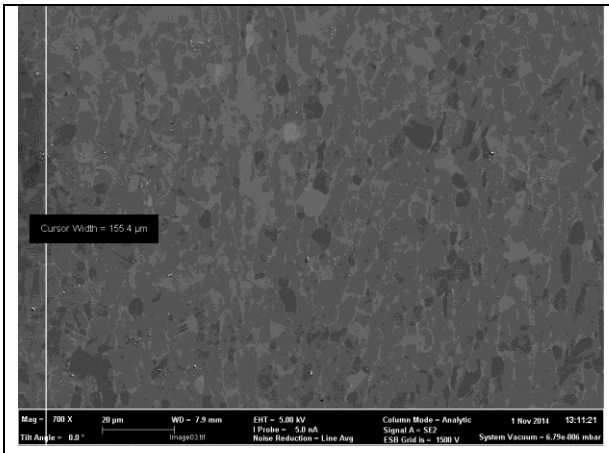

T3: 2mm at 46m/s, plastic zone of 155.4 µm

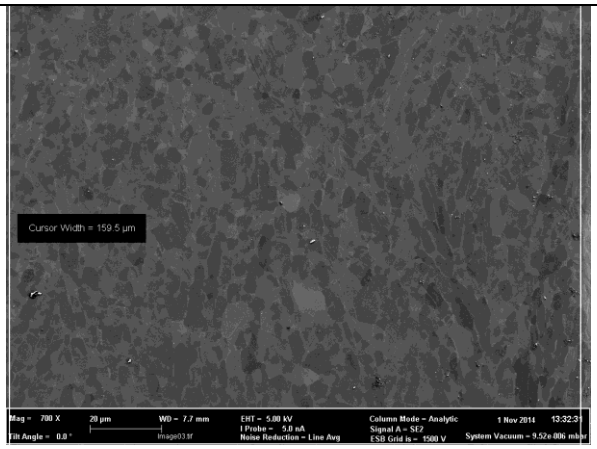

T3: 2mm at 58m/s, plastic zone of 159.5 µm

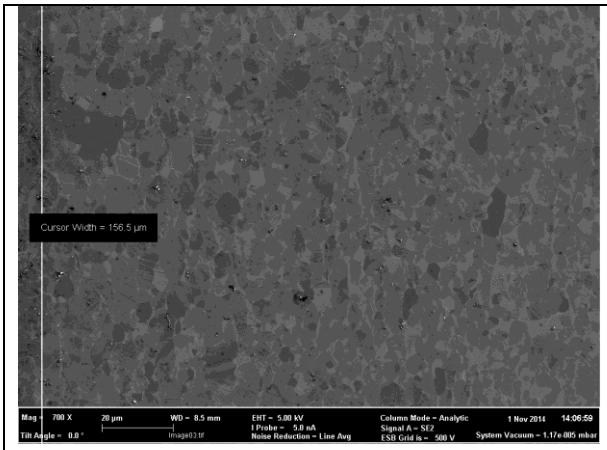

T3: 3mm at 46m/s, plastic zone of 156.5 µm

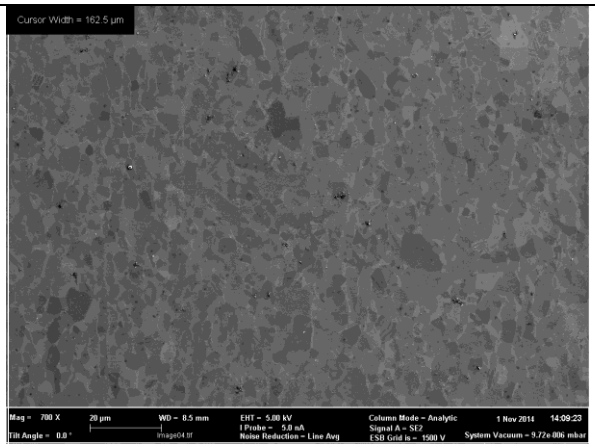

T3: 3mm at 58m/s, plastic zone of 162.5 µm

6.3 Modelling of single shot impact

Numerical models based on the executed experiments were developed in DEST. Each model consists of three parts as shown in Figure 6.11; projectile (blue), titanium target (red), and backing bar (grey). The material models and the constitutive constants used for each part are shown in section 6.3.1, Table 6.5 and Table 6.6. The contact was enabled for shot - target and target - bar part. Units used in these models are consistent in kg, mm, ms and GPa for the mass, length, time and stress respectively.

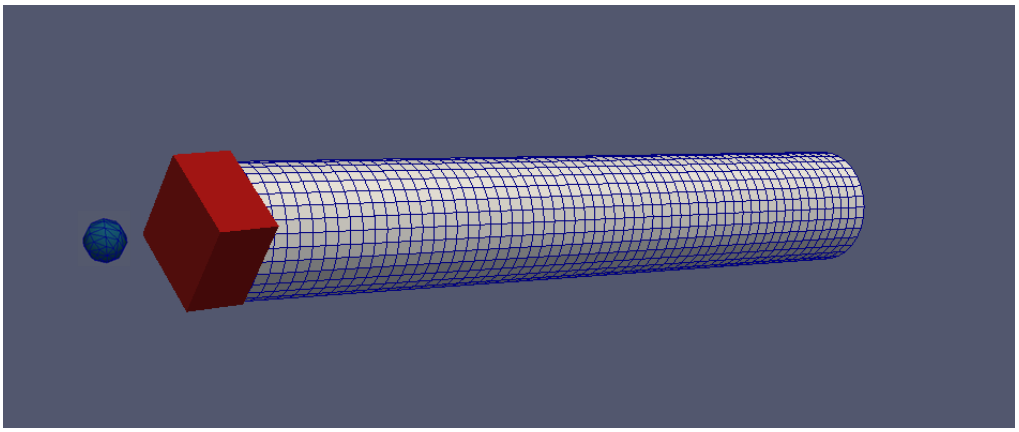

Figure 6.11: Simulation of single shot impact in DEST.

Table 6.5: Physical material parameters Ti-6Al-4V.

Common Properties	**Units**	**Values**
Density	kg/m^3	4430
Young's modulus	GPa	108.3
Poisson ratio		0.3

Table 6.6: Physical material parameters - Steel.

Common Properties	**Units**	**Values**
Density	kg/m^3	7800
Young's modulus	GPa	200
Poisson ratio		0.3

6.3.1 Material model

The baseline constitutive model used during this study is a physically based, internal state variable (ISV) model with void growth and shear damage laws. Since the flow stress is dependent on the strain paths, an enhanced modelling method of simulating competing dilatational and distortional failure mechanism and stress - strain localisations are used. This approach attempts to enhance the commercial material, based on the work of Bammann and Aifantis (1987) by improving the shear failure mechanisms, this is critical for torsional and compressive loading conditions. Shear failure in dynamic events creates the formation of adiabatic shear bands as the primary failure mechanism and is therefore an important development for impact simulations. Aspects of the enhanced constitutive model and the relevant calculation steps are illustrated in Figure 6.12.

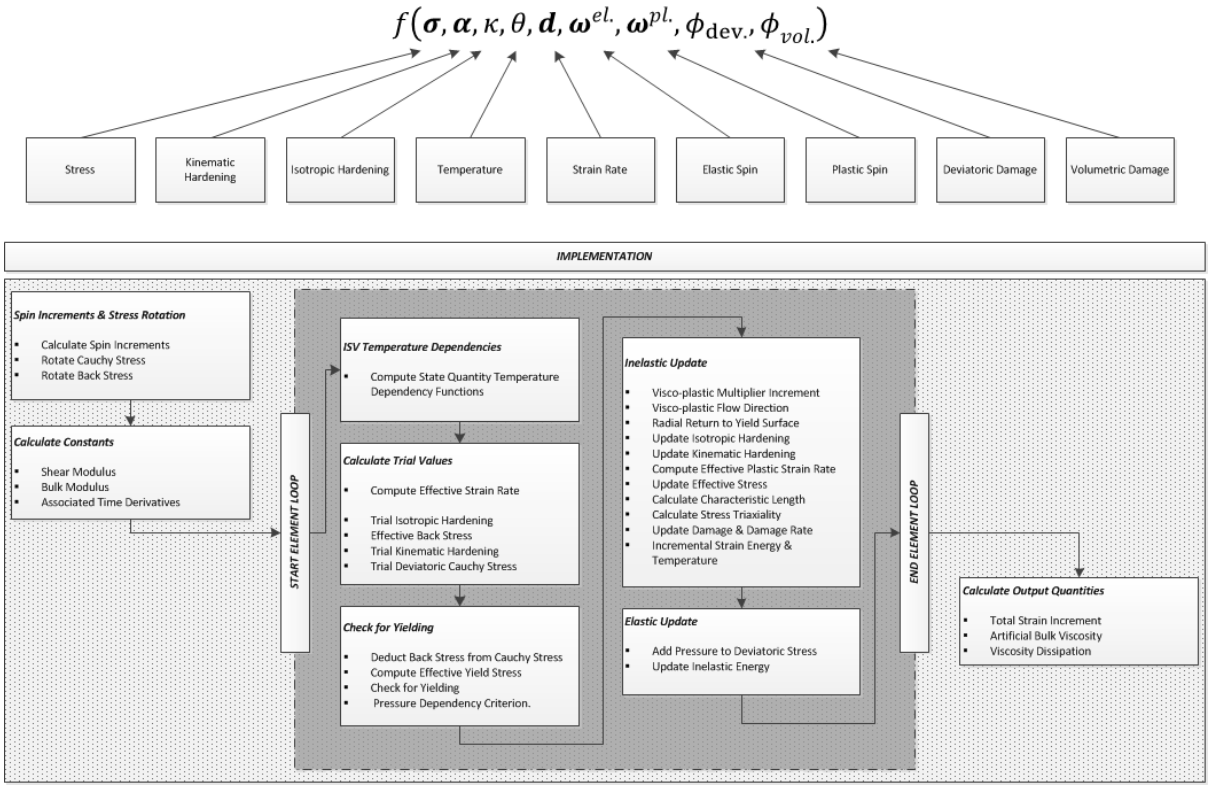

Figure 6.12: Simplified constitutive modelling process flow diagram after (Cousins et al., 2012).

The baseline model is based on the Sandia isotopic hypo-elastic visco-plastic model, originally developed by (Bammann and Aifantis 1987; Bammann 1984; Bammann and Chies 1993). The modified model distortional damage factor ˙ is based on Lemaitre's continuous damage model for ductile failures (Lemaitre and Desmorat 2005). The implemented baseline model in DEST has been shown to closely approximate the commercial LS-DYNA equivalent in terms of flow stress and rate sensitivity and validated using experimental datasets (Cousins et al., 2012).

Material model parameters

The Bammann model introduces a series of non-physical parameters which can be difficult to determine accurately (Guo et al., 2005). For the purpose of this work materials parameters identified via combined experimental and an inverse identification numerical approach developed by (Elliott 2007a), details of which are shown in Table 6.7 and Table 6.8.

Specimens were taken from a cross-rolled plate with a Young's modulus of 108 GPa, true fracture stress ~1300 MPa and true fracture strain ~ 40% for QS room temperature loading conditions (Elliott 2007b).

Table 6.7: Physical material model parameters Ti-6Al-4V.

Common Properties	**Units**	**Values**
Density	kg/m^3	4430
Young's modulus	GPa	108.3
Poisson ratio		0.3
Linear Bulk Viscosity		1.0
Quadratic Bulk Viscosity		5.0
Rayleigh's damping factor		0.0
Initial Temperature	K	293.0
Initial damage (porosity)		0.0032

Table 6.8: Baseline material model parameter Ti-6Al-4V.

Parameter Description	**Values**
Heat generation coefficient	0.331
Yield Function	
Rate-independent yield stress, $Y(\theta)$	952.0
Rate dependent transition, $V(\theta)$	21.6
Rate dependency of yielding, $f(\theta)$	0.54
Kinematic Hardening Variables	
Dynamic recovery of kinematic hardening $r_d(\theta)$	0.2
Kinematic hardening modulus $h(\theta)$	1000
Thermal recovery of kinematic hardening $r_s(\theta)$	1.74e-05
Isotropic Hardening Variables	
Dynamic recovery of isotropic hardening $R_d(\theta)$	0.01
Isotropic hardening modulus $H(\theta)$	1600
Thermal recovery of isotropic hardening $R_s(\theta)$	0
Damage parameters	
Void growth constant, m	2.56
Shear location constant, So	
Mesh regularization	7.0055

6.3.2 Simulated results

Specimens: Set -1

The indentation depth and width of set-1 specimens across different shot sizes and velocities are compared in Figure 6.13 and Figure 6.14. A summary of the results are provided in Table 6.9.

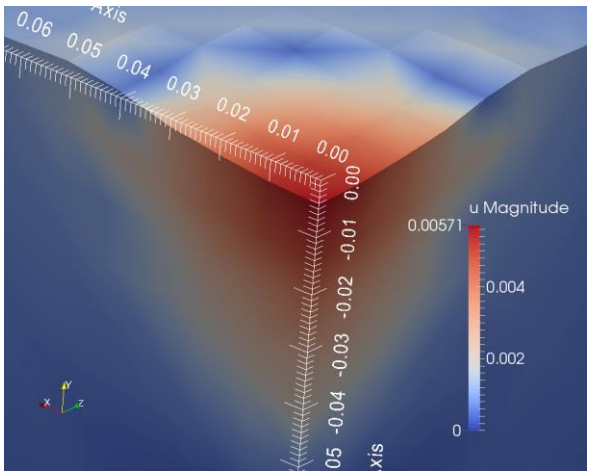	Shot diameter 0.29 mm Impact velocity 44 m/s Indentation depth -0.004 mm Indentation width 106 µm

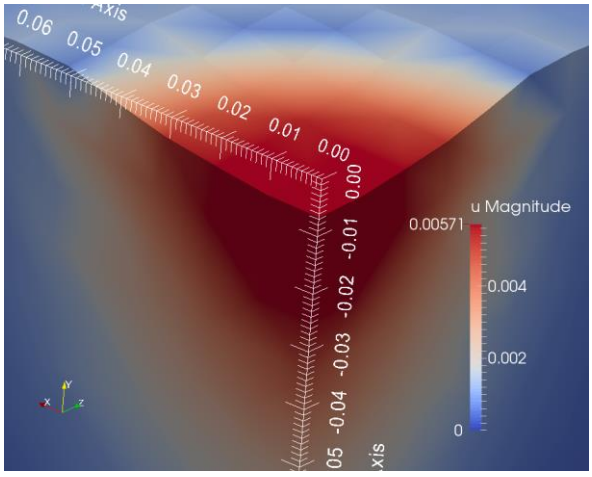	Shot diameter 0.29 mm Impact velocity 56.5 m/s Indentation depth -0.0065mm Indentation width 108 µm

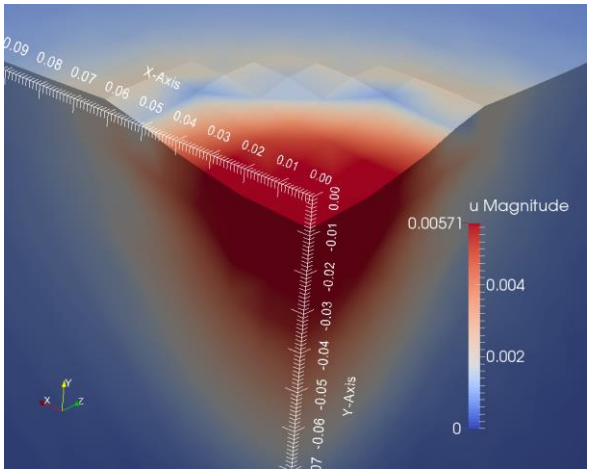	Shot diameter 0.29 mm Impact velocity 70 m/s Indentation depth -0.008 mm Indentation width 130 µm
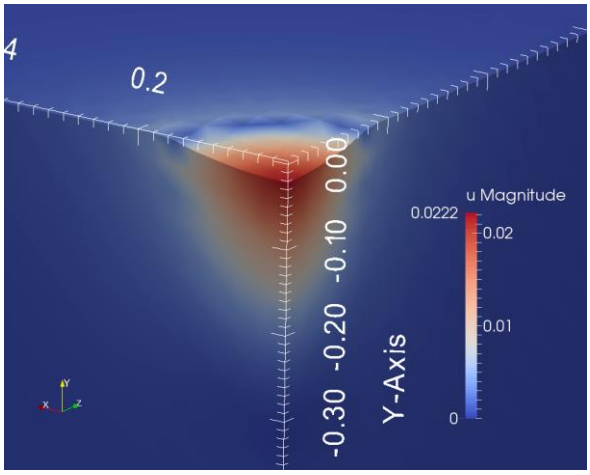	Shot diameter 1 mm Impact velocity 45 m/s Indentation depth -0.02 mm Indentation width 350 µm
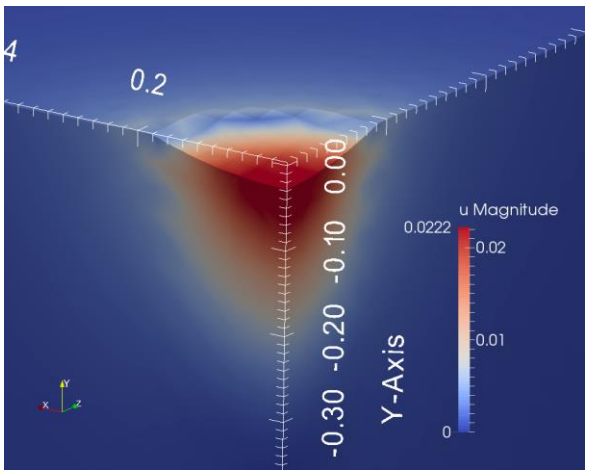	Shot diameter 1 mm Impact velocity 57 m/s Indentation depth -0.025 mm Indentation width 400 µm

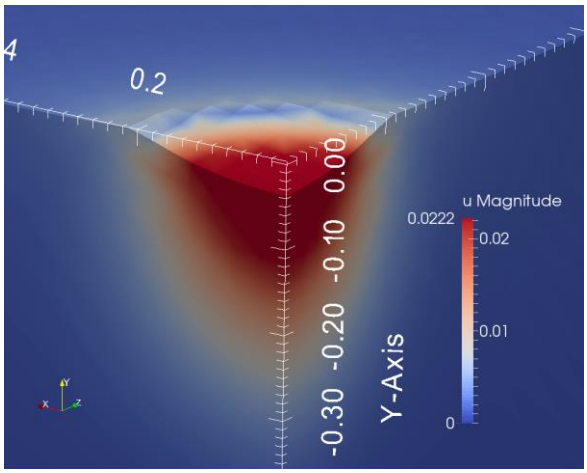	Shot diameter 1 mm Impact velocity 71 m/s Indentation depth -0.035 mm Indentation width 410 µm
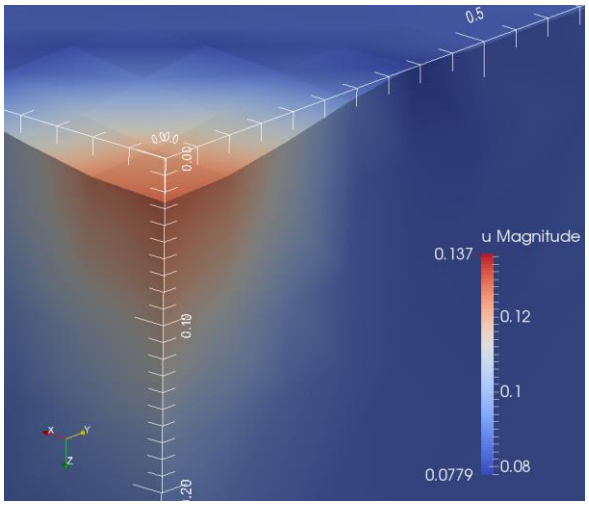	Shot diameter 2 mm Impact velocity 45 m/s Indentation depth -0.027 mm Indentation width 700 µm
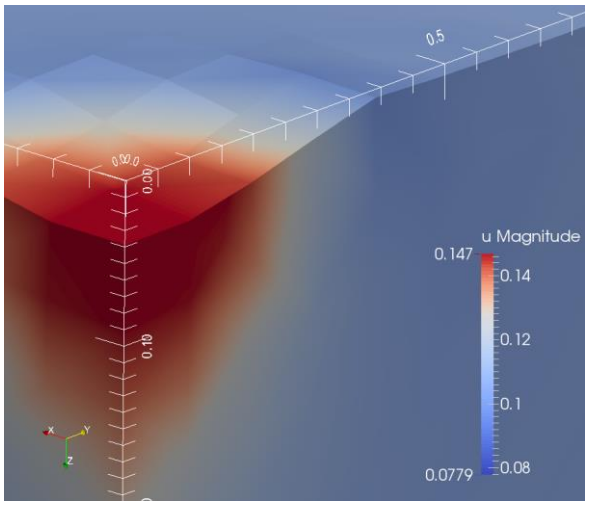	Shot diameter 2 mm Impact velocity 57 m/s Indentation depth -0.04 mm Indentation width 760 µm

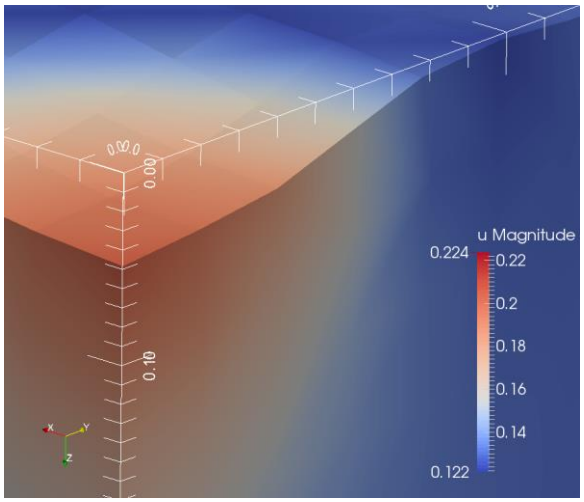	Shot diameter 2 mm Impact velocity 71.5 m/s Indentation depth -0.06 mm Indentation width 800 µm
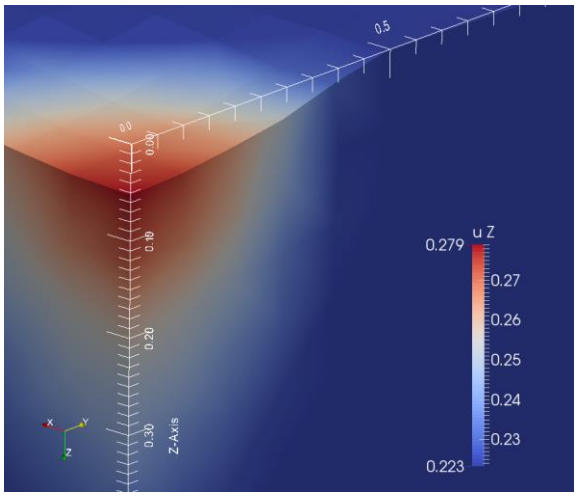	Shot diameter 3 mm Impact velocity 44 m/s Indentation depth -0.05 mm Indentation width 960 µm
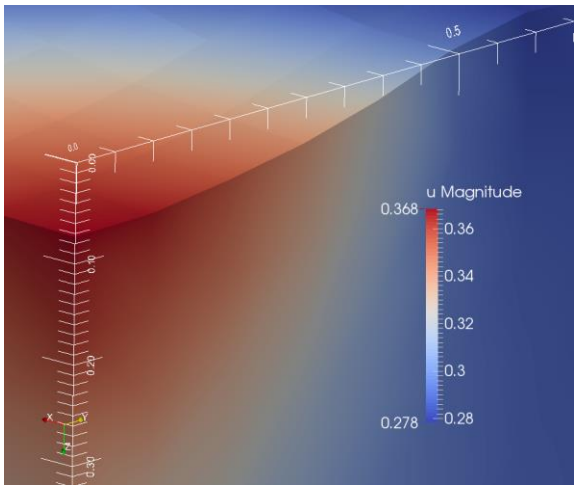	Shot diameter 3 mm Impact velocity 58 m/s Indentation depth -0.07 mm Indentation width -1000 µm

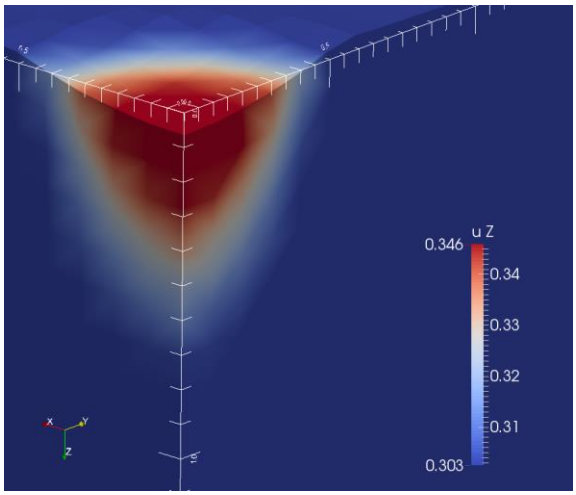	Shot diameter 3 mm Impact velocity 66.5 m/s Indentation depth -0.08 mm Indentation width -1160 µm
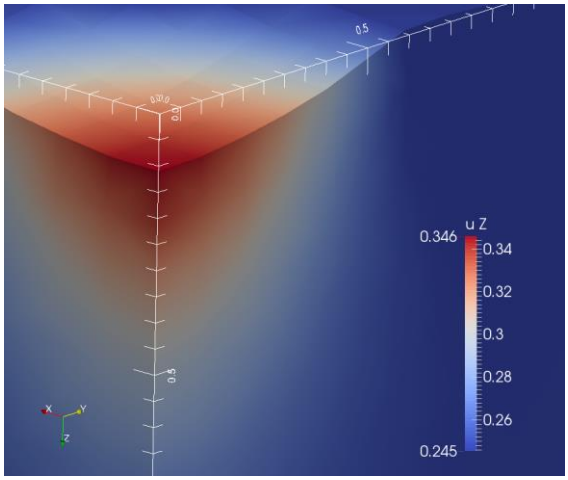	Shot diameter 3 mm Impact velocity 71 m/s Indentation depth -0.08 mm Indentation width -1200 µm

Table 6.9: Simulations compared with the results obtained from the set-1 specimens.

		Experiment		Simulation	
Shot diameter in mm	Impact velocity in m/s	Indentation depth in mm	Indentation width in µm	Indentation depth in mm	Indentation width in µm
0.29	44	-0.0015	110	-0.004	106
0.29	56.5	-0.0051	135	-0.0065	108
0.29	70	-0.0078	166	-0.008	130
1	45	-0.0122	340	-0.02	350
1	57	-0.0285	380	-0.025	400
1	71	-0.031	425	-0.035	410
2	45	-0.03	620	-0.027	700
2	57	-0.04	700	-0.04	760
2	71.5	-0.07	880	-0.06	800
3	44	-0.049	900	-0.05	960
3	58	-0.064	990	-0.07	1000
3	66.5	-0.078	1070	-0.08	1160
3	71	-0.0765	1115	-0.09	1200

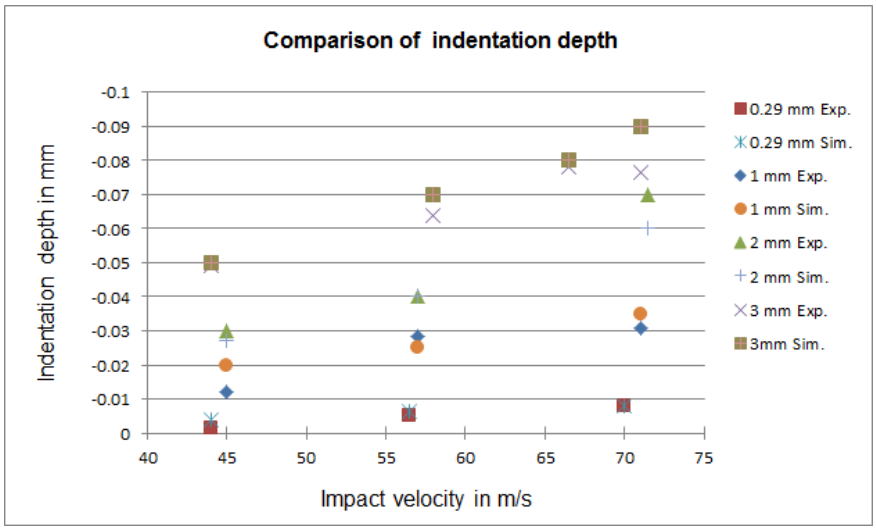

Figure 6.13: Comparison of simulated vs. experimental indentation depth for set-1 specimens.

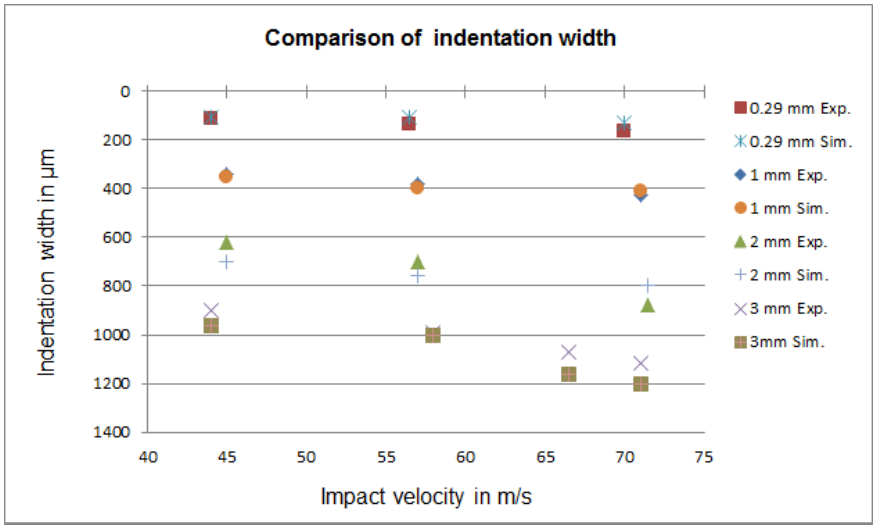

Figure 6.14: Comparison of simulated vs. experimental indentation width for set-1 specimens.

Specimens: Set -2

The indentation width and plastic zone of set-2 specimens across the different shot sizes and velocities are compared in Figure 6.19 and Figure 6.20.

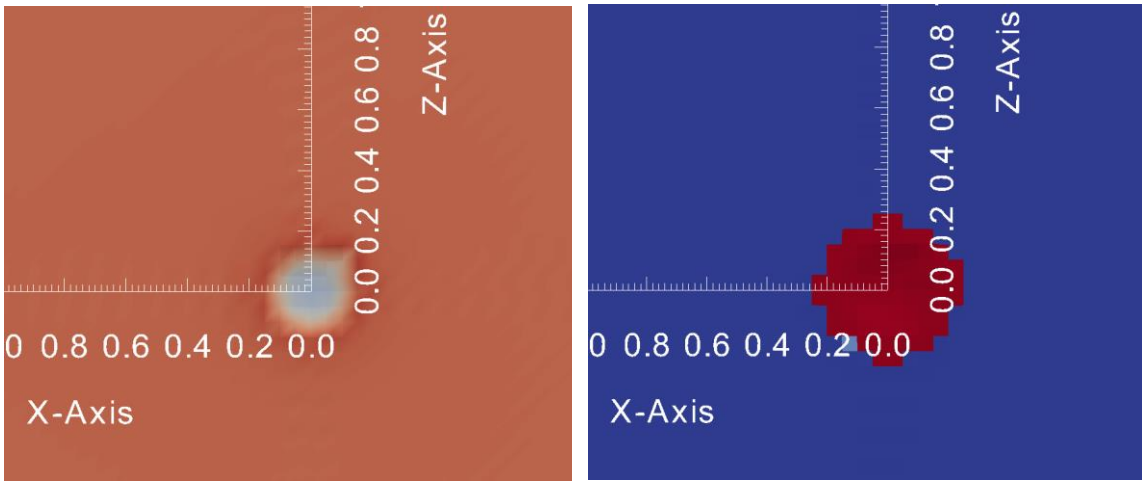

Figure 6.15: Illustration of indentation size (left) and plastic zone (right) for shot size 2 mm and impact velocity 45 m/s.

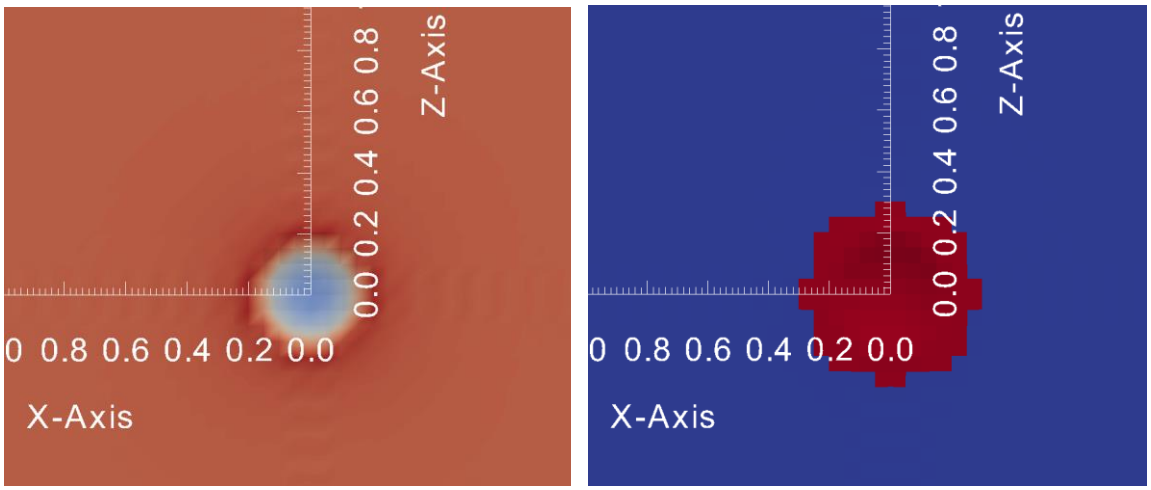

Figure 6.16: Illustration of indentation size (left) and plastic zone (right) for shot size 2 mm and impact velocity 58 m/s.

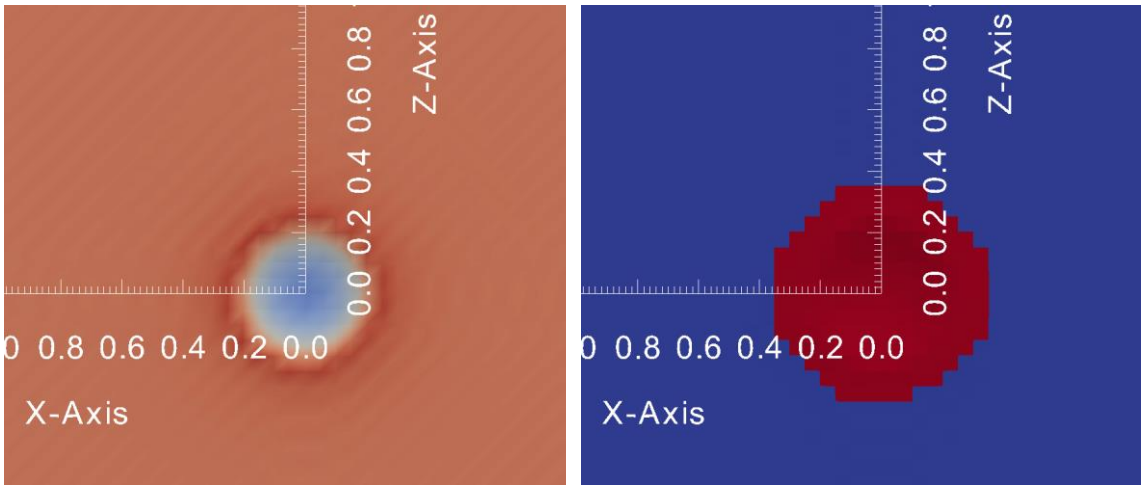

Figure 6.17: Illustration of indentation size (left) and plastic zone (right) for shot size 3 mm and impact velocity 45 m/s.

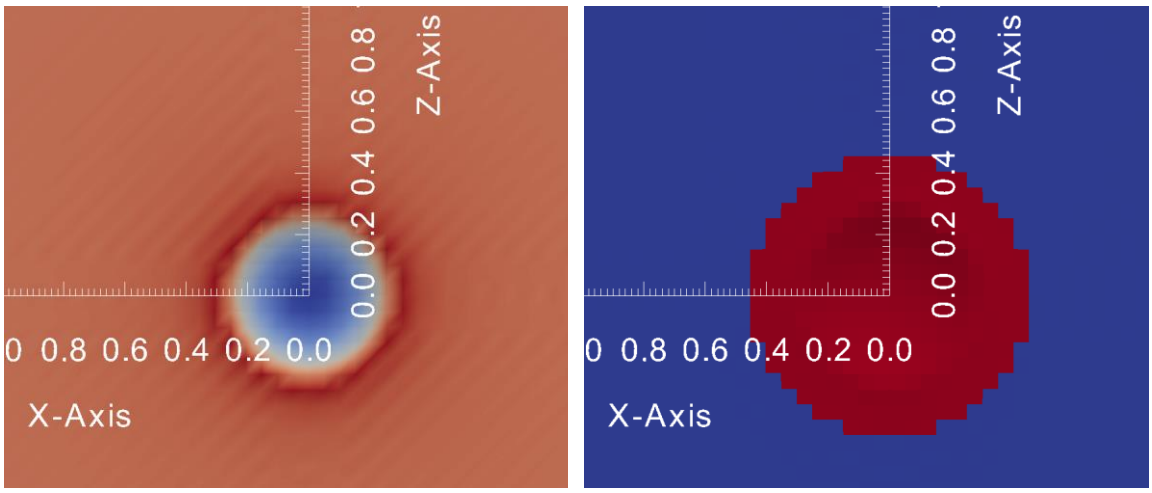

Figure 6.18: Illustration of indentation size (left) and plastic zone (right) for shot size 3 mm and impact velocity 58 m/s.

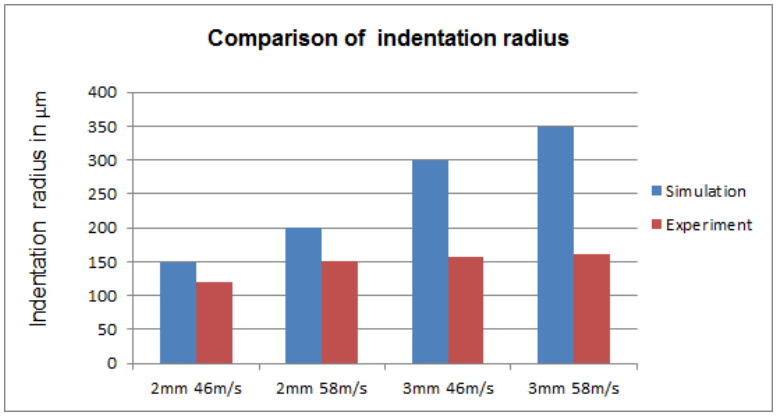

Figure 6.19: Comparison of simulated vs. experimental indentation radius for set-2 specimen.

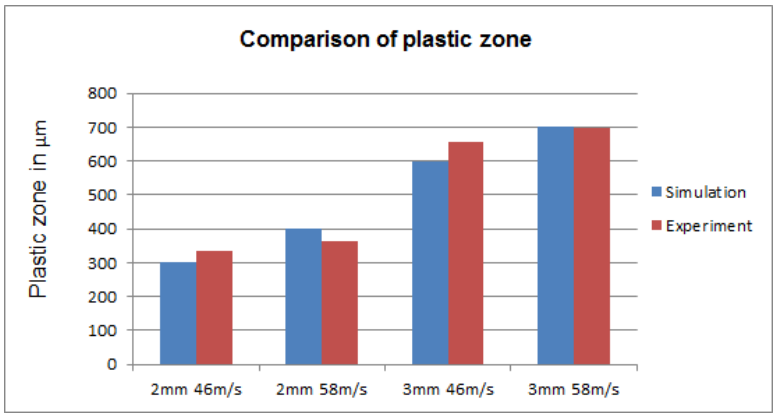

Figure 6.20: Comparison of simulated vs. experimental indentation radius for set-2 specimen.

6.4 Conclusion

A gas gun was employed to investigate the dynamic indentation of shots on Ti-6Al-4V targets with the aim to gain a better understanding of what happens to the material under impact conditions similar to those seen in production peening. Several shot sizes and velocities were compared in a matrix, including peening media MR110 (0.29 mm diameter steel shots). The constitutive model used in the study has been shown to demonstrate the ability to predict the indentation sizes for the set-1 specimens. For the set-1 specimens the material model could describe the indentation depth and width seen in the experiments very well. However, for set-2 specimens the indentation widths were overestimated by approximately 35 % and the variance increases with velocity and shot size.

Finally, the depth of the indentation could not be accurately measured for set-2 material due to the measurement techniques' (ALICONA - Infinite Focus) inability to perform reliably on highly reflective surfaces. Without this information, the only other option available would be much more time consuming and involve determining the sub-surface residual stress. In addition to the identification of appropriate material parameters, the mesh density also needs to be an appropriate scale. Whilst the material model has the ability to reduce the influence of mesh size, through characteristic element length calculations which influence the damage accumulation rate, larger elements will reduce the accuracy of the

indentation profile.Furthermore, when combined with the inherent anisotropic nature of the set-2 material, which is well known in titanium alloys due to the polycrystalline structure, may have also influenced the accuracy of the indentation profile, as the current material model formulation is isotropic.

CHAPTER 7 SHOT PEENING OF Ti-6Al-4V TEST BLOCKS

Automated robotic peening systems typically use one or more nozzles at different incident angles per operation. They are capable of following the contours of the component and maintaining the same incident angle during the peening process such that the same Shot Peening conditions, across the component surface, can be achieved at all times.

However, conventional peening machines that are capable of peening components using multiple nozzle set-ups are set at different angles to peen different parts of the component during the same peening operation. As a result of component rotation and nozzle movement, there are areas of a component that may experience over spray, and thus creating coverage at different intensities in certain areas. The coverage produced from conventional peening compared with multi-incident angle nozzles on Almen Strips and during component validation will affect the final saturation curves requiring consideration of component set-ups prior to peening components during manufacture.

Case studies were performed to compare the coverage, intensity and residual stress data when peening with single and when peening with multiple nozzles at different angles of impingement. These tests were conducted to determine if the saturation curves are affected by the use of peening with multiple incident angle nozzles compared to single nozzle at a set incident angles. The trials were conducted by only changing one peening parameter, the incident angle or coverage rates. The aim was to determine if these parameters influence the resultant residual stress profile achieved in the material, even though the intensity seen on the saturation curve would remain the same. This is to ensure that when data cards are being created, the initial validation captures the true intensity point for the peening process. This

ensures that the generated saturation curves equates to the accurate compressive stress throughout the depth of the material set by the engineering definition.

7.1 Test block case study

7.1.1 Testing strategy

The peening trials were conducted at Metal Improvement Company (MIC) Ascot Drive, Derby. The peening was performed using a gravity feed peening machine, which is traditionally used for peening Rolls Royce Aerospace components. The peening was performed such that the coverage on the samples build up slowly, allowing one to accurately monitor the development of the coverage and saturation curves. A feed pipe restrictor was fitted at the exit pipe from the gravity feed hopper to control the peening process. Conditioned regular hardness 110R cast shot media, controlled in accordance with RPS428 were used for all eight trials. Two test pieces were peened per trial and were subjected to two residual stress tests. The measurements were performed at Stresscraft LTD using the target strain gauge/-centre hole drilling method.

7.1.2 Preparation of specimen

The test piece material used for the trials was supplied from Barnoldswick Laboratory. The material was MSRR8672 Ti-6Al-4V (Plate 6.5 mm thick). This material available was determined to be acceptable for use in these trials to evaluate the differences in intensity for Ti-6Al-4V between the distinct peening methods. The plate was water jet cut out to a dimension of 19 mm x 77 mm to replicate an Almen Strip; this was subsequently polished with silicon carbide paper (180-600 grit and water) to remove any scratches and to create a uniform surface finish between each test piece prior to peening. The test pieces were cleaned and heat-treated at 1hr for 700°C to ensure that they receive a full stress relieve. The test pieces were then descaled to ensure there were no contaminants on the surface prior to peening. Figure 7.1 shows the peened test piece.

Figure 7.1: Example of the peened test piece after (S.Kennerell, 2012).

7.1.3 Outline of the experiments

Eight different peening trials were conducted to show the effect of single nozzle and multiple nozzle peening operations. The correlation of saturation curve and compressive residual stress were compared during these trials. The trials were carried out at the minimum requirements of 6 Almen, but trials 1 and 8 will set the datum range for the Ti-6Al-4V alloy at 6-8 Almen (0.006-0.008" Almen). The trial conditions for the eight trials including their data card are described below.

Trial 1: Parameters shall be deloped to allow slow coverage build-up on the test piece up to 100 % coverage. This baseline test shall consist of one nozzle hitting the surface at 90° at a recorded saturation point of 6 Almen. The shot flow must be controlled such that the titanium strip does not achieve full coverage after 1 pass and coverage build up can be assessed. This was done using a 3mm restrictor, which is inserted inside the hopper outlet. The shot flow results when fitted for the trial were 98 grams per minute. Saturation curve will be developed for the process to compare it against the residual stress profile of the test piece.

SUBJECT AREA: Shot peen sample with 1 nozzle set at 90° to vertical. (0° to horizontal).		
SPECIFICATION	RPS428	
INTENSITY	6 – 6.5A	
MEDIA	MI 110R	
COVERAGE	Build up to 100%	
Air Pressure	55 psi ± 5psi	
Nozzle Size	3/8"	
Air Jet Size/ Position	1/4"HI	+1/2"
No Nozzles	1	
Orifice	N/A	
Nozzles from Part	5"± 1"	
Rotation Rpm	20 rpm ± 3 rpm	
Oscillation distance	4 ½"	
Oscillation speed	30"/min ±2"/min	
Counts (1count=2passes)	20 counts/40 passes	
Time cycle/total	-	
MACHINE	2214-3	
ALMEN STRIPS: Position	x x x	
1 off on Almen strip fixture made for trial.		
QTY: 1 Osc: 4 ½" Time: 14 counts		

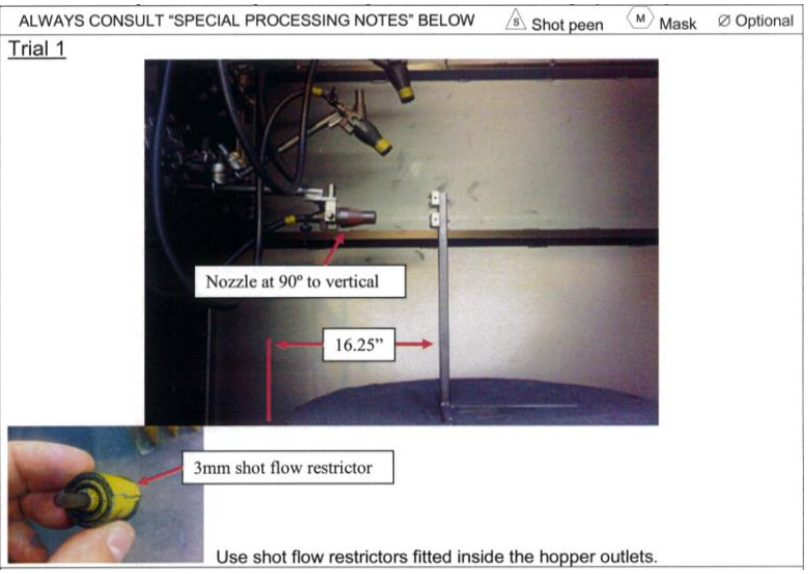

Figure 7.2: Illustrates the data card for trial 1 after (Metal Improvement Company, 2012).

Trial 2: Test was performed with one nozzle peening the surface at 45° using the same parameters as trial 1. This is to demonstrate the drop off in intensity and residual stress from 90° to 45°. Coverage achieved shall allow the study of slow coverage build-up on the test piece up to 100 % coverage. Saturation curves were developed for the process of comparing it against the residual stress profile of the test piece

SUBJECT AREA: Shot peen sample with 1 nozzle set at 45° to vertical.		
SPECIFICATION	RPS428	
INTENSITY	4-4.5A	
MEDIA	MI 110R	
COVERAGE	Build up to 100%	
Air Pressure	55 psi ± 5psi	
Nozzle Size	3/8"	
Air Jet Size/ Position	1/4"HI	+1/2"
No Nozzles	1	
Orifice	N/A	
Nozzles from Part	5"± 1"	
Rotation Rpm	20 rpm ± 3 rpm	
Oscillation distance	4 ½"	
Oscillation speed	30"/min ±2"/min	
Counts (1count=2passes)	20 counts/40 passes	
Time cycle/total	-	
MACHINE	2214-3	
ALMEN STRIPS: Position	x x x	
1 off on Almen strip fixture made for trial.		
QTY: 1 Osc: 4 ½" Time: 15 counts		

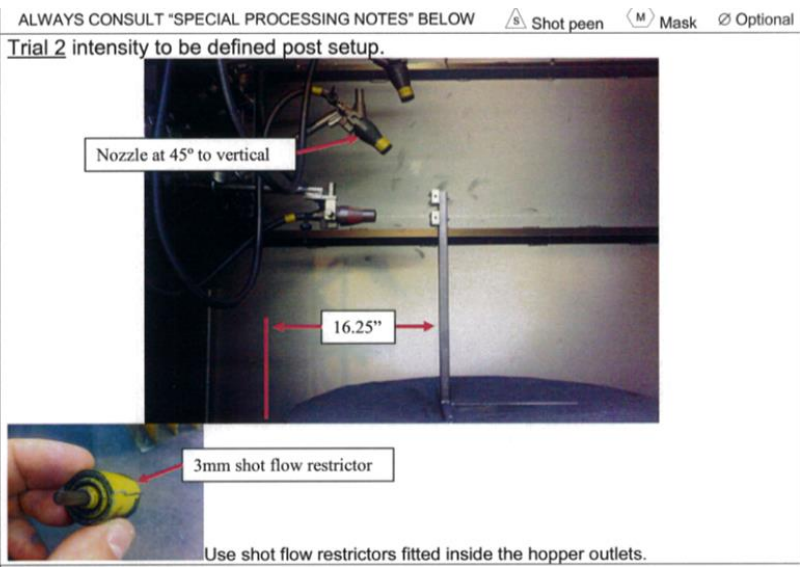

Figure 7.3: Illustrates the data card for trial 2 after (Metal Improvement Company, 2012).

Trial 3: This test consists of one nozzle hitting the surface at 20° with the same parameters from trial 1 to show the drop off in intensity and residual stress from 90° to 20°. Coverage achieved shall allow the study of slow coverage build-up on the test piece up to 100 % coverage. Saturation curves were developed for the process of comparing it against the residual stress profile of the test piece.

SUBJECT AREA: Shot peen sample with nozzle set at 20° to vertical. (70° to horizontal).		
SPECIFICATION	RPS428	
INTENSITY	3-3.5A	
MEDIA	MI 110R	
COVERAGE	Build up to 100%	
Air Pressure	55 psi ± 5psi	
Nozzle Size	3/8"	
Air Jet Size/ Position	1/4"HI	+1/2"
No Nozzles	1	
Orifice	N/A	
Nozzles from Part	5"± 1"	
Rotation Rpm	20 rpm ± 3 rpm	
Oscillation distance	4 ½"	
Oscillation speed	30"/min ±2"/min	
Counts (1count=2passes)	42 counts/84 passes	
Time cycle/total	-	
MACHINE	2214-3	
ALMEN STRIPS: Position	x x x	
1 off on Almen strip fixture made for trial.		
QTY: 1 Osc: 4 ½"	Time: 39 counts	

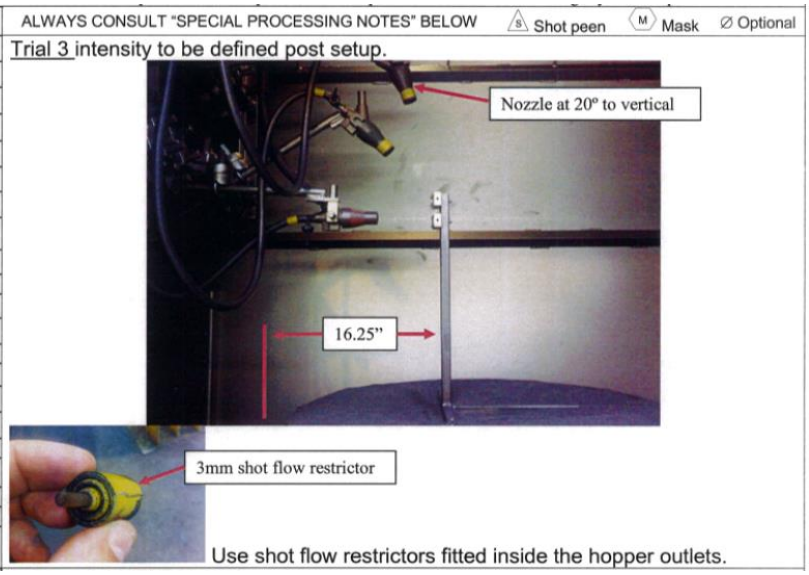

Figure 7.4: Illustrates the data card for trial 3 after (Metal Improvement Company, 2012).

Trial 4: Test with all 3 nozzles hitting the surface at 90º, 45º and 20º with the same parameters from trial 1 including peening time to ensure the 90° nozzle achieves 100 % coverage on its own. This is to determine if the residual stress profile changes with all the nozzles peening the test piece, coverage on the test piece will be greater than 100 %. Saturation curve will be developed for the process to compare it against the residual stress profile of the test piece.

Trial 5: Test with all 3 nozzles hitting the surface at 90º, 45º and 20º with the same parameters from trial 1 excluding peening time. Coverage on the test piece developed to allow slow coverage build-up on the test piece to 100 % coverage. This will determine the

residual stress profile when the 90° Nozzle will not achieve 100 % coverage on the test piece. Therefore 100 % coverage is made up of all 3 nozzles angles 90º, 45º and 20°. (Note trials 6, 7, 8 will show the individual coverage produced by each nozzle). No saturation curve is required as it will be the same as trial 4 as the peening parameters are the same on test piece peening time is affected, this is independent of intensity shown for the process parameters.

Trial 6: Test was performed with one nozzle peening the surface at 90° using the same parameters as in trial 1 but at the test piece processing time from trial 5. No saturation curve is required as it will be the same as trial 1.

Trial 7: Test was performed with one nozzle peening the surface at 45° using the same parameters as trial 2 but at the test-piece process time from trial 5. No saturation curve is required as it will be the same as trial 2.

Trial 8: Test was performed with one nozzle peening the surface at 20° using the same parameters as trial 3 but at the test-piece process time from trial 5. No saturation curve is required as it will be the same as trial 3.

Figure 7.5: Multiple nozzles setup for trials 4 and 5 after (Metal Improvement Company, 2012).

Figure 7.5 of the multiple nozzles set up does not accurately reflect the set up that was used for the trials. The top nozzle at 20° had to be off set as it was noted it affected the shot stream of the 90° and 45° nozzle set up. The results of trails 1 and 2 were not affected.

Table 7.1: Summary of the trials.

	Nozzle angle	Ti-6Al-4V test pieces 75 x 19"x 6mm	Test piece coverage	Saturation curve required	Experiment
Trial 1	90°	2	100%	Yes	Base Line saturation curve and residual stress profiles
Trial 2	45°	2	100%	Yes	Base Line saturation curve and residual stress profiles
Trial 3	20°	2	100%	Yes	Base Line saturation curve and residual stress profiles
Trial 4	90°,45°, 20°	2	All nozzles on at the process time for trial 1	Yes	Simulates 3 nozzles individually hitting the area with 100% coverage of the 90° nozzle
Trial 5	90°,45°, 20°	2	100% with all nozzles on	No	Simulates only achieving a 3rd of the coverage at intensity with the 90° nozzle but with all the nozzles on
Trial 6	90°	2	As per time for trial 5, coverage to be accessed	No	Simulates the residual stress achieved from the coverage achieved from the individual nozzle @ low coverage
Trial 7	45°	2	As per time for trial 5, coverage to be accessed	No	Simulates the residual stress achieved from the coverage achieved from the individual nozzle @ low coverage
Trial 8	20°	2	As per time for trial 5, coverage to be accessed	No	Simulates the residual stress achieved from the coverage achieved from the individual nozzle @ low coverage

Preparation of saturation curve

The saturation curve is obtained by plotting Almen Strip arc height versus exposure time for a given set of conditions. The saturation curve is obtained as per the requirements of SAE J443 standard (Kirk 2012). The Saturation Curve Solver program SCS2 (2PF STANDARD vers.09) was used to create the saturation curves from (Kirk, 2005). A best-fit curve is generated through the arc height points. Saturation is defined as the earliest position on the best fit curve where doubling the exposure time produces no more than a 10 % increase in arc height on the best fit curve, this is known as T1 and T2 time respectively. The saturation

point (T1) is also known as the peening intensity. The saturation curve shall consist of a minimum of 4 points, other than zero, for each Intensity determination location. It is accepted that saturation and 100 % coverage are achieved on an Almen Strip at approximately the same time and must be inspected for uniformed coverage to ensure the test has been carried out correctly.

Residual stress measurement

Stresses have been determined using the target strain gauge / centre hole drilling method to a maximum depth of 320 μm. The test blocks, typical strain gauge installations (two gauges per block) and the arrangement for incremental drilling are shown in Figure 7.7. Pairs of gauges were offset longitudinally by ±10 mm from the centre, remote from any masking effects caused by the retaining fastener heads; the target centre of each gauge was positioned at the centre of 19 mm width. Gauges at the two positions were identified as 'A' and 'B'. Residual stresses were recorded at depths 8 μm, 40 μm, 80 μm and 256 μm from the test blocks. These directions of the measurement refer to stresses σ1 and σ3 in the subsequent results sheets. Typical gauge installations are shown in Figure 7.7.

The incremental orbital hole drilling procedure was carried out at each gauge recording the changes in relaxed strains at 12 drill depth increments of 4 x 16 μm + 4 x 32 μm + 4 x 64 μm to give a completed hole depth of 448 μm. Residual stresses were calculated from relaxed strains using the Integral Method. This method provides a separate residual stress analysis at every hole drilling depth increment.

The relevant material properties used for strain-to-stress data reduction (Ti-6Al-4V) were:

Young's modulus (E) 115.0 GPa

Poisson's ratio (μ) 0.32

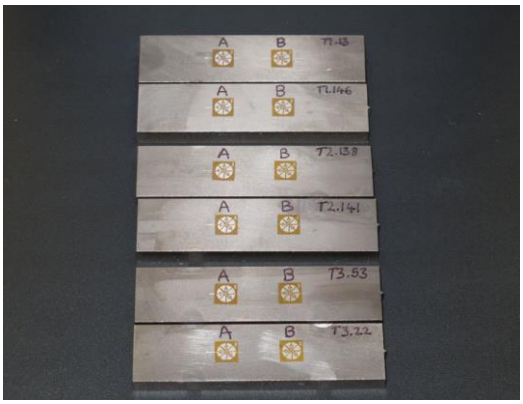

Figure 7.6: Shot peened Titanium blocks pairs after (Whitehead and Lodge 2012).

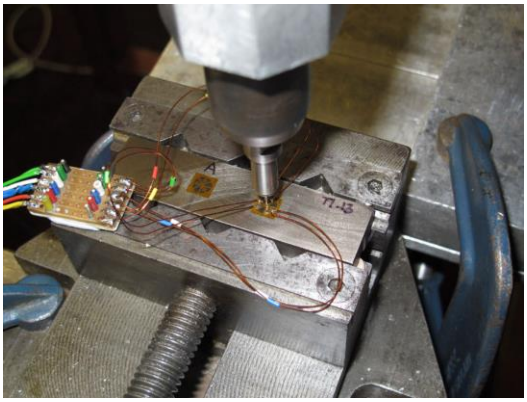

Figure 7.7: The test blocks with strain gauge installations (two gauges per block) for incremental drilling after (Whitehead and Lodge 2012).

7.1.4 Experimental results

The coverage and saturation curves for trials according to Table 7.1 are provided below.

Coverage and Saturation

Trial 1

The test strip was peening with a single nozzle set up using regular 110 cast steel shots at 90°. A saturation curve was produced between 6-6.5 A. The coverage was observed using a x10 magnification. The ensure that the test strip is not fully covered after one pass, a 3 mm restrictor was inserted inside the hopper outlet. The shot flow results, when fitted for the trial were 98.4 grams per minute**.** 100 % coverage was achieved after 20 peening counts. Almen saturation point was determined at T = 13.32.

Table 7.2: Coverage increments in counts for trial 1.

Counts	0	2	4	6	8	10	12	14	16	18	20
Coverage	0%	10%	30%	50%	60%	70%	80%	85%	90%	95%	100%

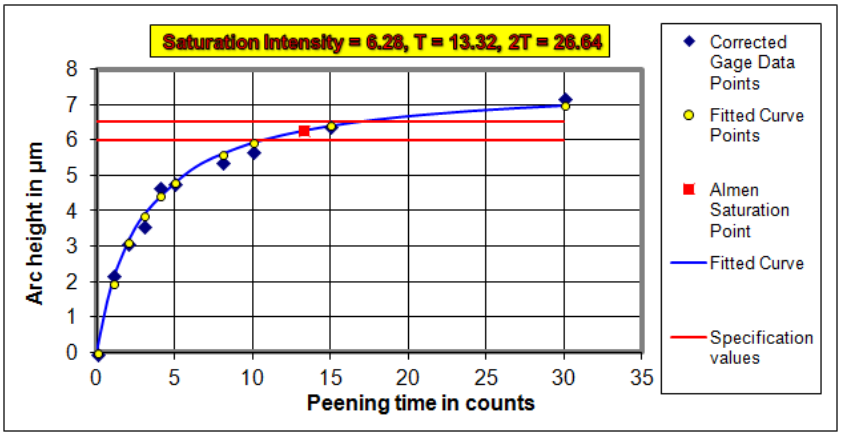

Figure 7.8: Saturation curve for trial 1.

Trial 2

The same process parameters were used as in trial 1, expect a 45° peening angle was applied for the same amount of passes. The Almen Strip readings are taken and inserted into a saturation curve solver. A 3 mm restrictor was fitted and the shot flow results were 99.5 grams per minute. 100 % coverage was achieved after 20 peening counts. Almen saturation point was determined at T = 14.31.

Table 7.3: Coverage increments in counts for trial 2.

Counts	0	2	4	6	8	10	12	14	16	18	20
Coverage	0%	20%	40%	50%	60%	70%	80%	90%	95%	98%	100%

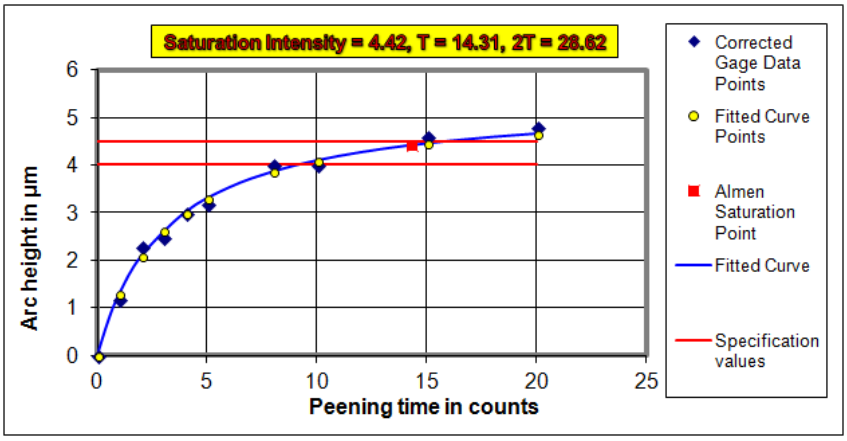

Figure 7.9: Saturation curve for trial 2.

Trial 3

The same process parameters as in trial 1 were used, expect a 20° peening angle was applied for the same amount of passes. The Almen Strip readings were taken and inserted into a saturation curve solver (PROGRAM SCS2 2PF STANDARD vers.09). A 3 mm restrictor was fitted and the shot flow results were 91.4 grams per minute. 100 % coverage was achieved after 42 peening counts. Almen saturation point was determined at T = 38.88.

Table 7.4: Coverage increments in counts for trial 3.

Counts	0	2	4	6	8	10	12	14	16	18	20
Coverage	0%	10%	20%	35%	45%	55%	60%	75%	80%	85%	90%
Counts	22	24	26	28	30	32	34	36	38	40	42
Coverage	92%	94%	95%	96%	97%	98%	99%	99%	99%	99%	100%

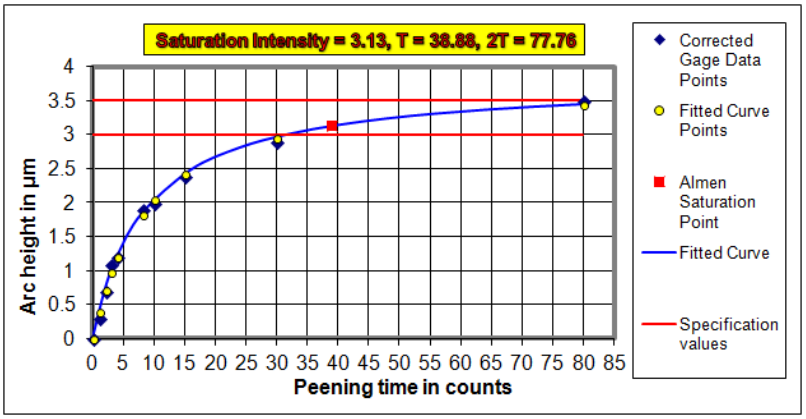

Figure 7.10: Saturation curve for trial 3.

Trial 4

In trial 4, the test block is peened with 90°, 45° and 20° nozzles individually for the same peening time as in trial 1. The achieved converged is higher than 100 %. This is to determine if the RS changes when using multiple nozzles. Almen saturation point was determined at T=6.71.

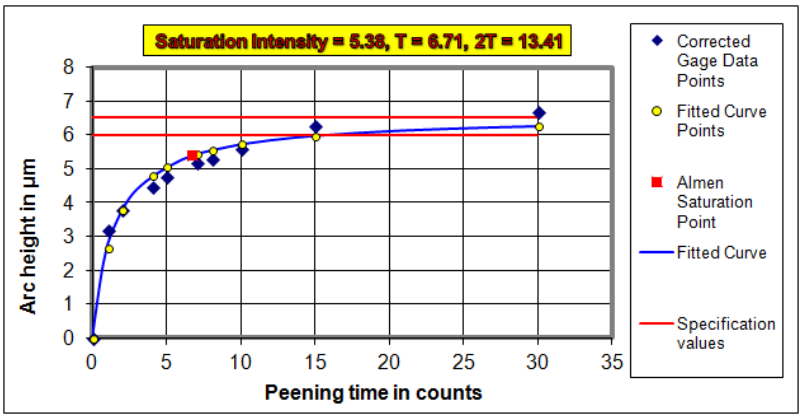

Figure 7.11: Saturation curve for trial 4.

Trial 5

For trial 5 the test block was peened with all 3 nozzles, 90°, 45° and 20° using the same parameters as trial 1. The test block was fully peened until 100 % coverage was achieved. Here 100 % coverage is made up of all 3 nozzles and full coverage was reached after 12 counts. Table 7.5 illustrates the coverage build-up for trial 5.

Table 7.5: Coverage increments in counts for trial 5.

Counts	0	1	2	4	6	8	10	12
Coverage	0%	10%	30%	45%	65%	85%	98%	100%

Trial 6

In trial 6 the test block was peened with only the 90° nozzle using the same process parameters as trial 1 but using the peening time of trial 5.

Trial 7

Similar to trial 6, in trial 7 only the 45° nozzle was active using the same parameters as trial 2 and using the peening time of trial 5.

Trial 8

Only the 20° nozzle was active using the same parameters as trial 3 and using the peening time of trial 5.

Table 7.6: Summary of Coverage build-up for different trials.

		Percentage of Coverage built up in counts																						
Trial	Saturation point (T1)	1	2	4	6	8	10	12	14	16	18	20	22	24	26	28	30	32	34	36	38	40	42
Trial 1 (T1)	6.27A @13.33C	x	10	30	50	60	70	80	85	90	95	100	x	x	x	x	x	x	x	x	x	x	x
Trial 2 (T2)	4.42A @ 14.30C	x	20	40	50	60	70	80	90	95	98	100	x	x	x	x	x	x	x	x	x	x	x
Trial 3 (T3)	3.12A @ 38.87C	x	10	20	35	45	55	60	75	80	85	90	92	94	95	96	97	98	99	99	99	99	100
Trial 4 (T4)	5.39A @6.72C	Coverage rate as per T1 but with the additional coverage achieved T2 and T3 at 20 Counts (290%)																					
Trial 5 (T5)	As per Trial 4	10	30	45	65	85	98	100	x	x	x	x	x	x	x	x	x	x	x	x	x	x	x
Trial 6 (T6)	As per Trial 1	Coverage rate as per T1 but at only 12 counts as per T5 (80%)																					
Trial 7 (T7)	As per Trial 2	Coverage rate as per T2 but at only 12 counts as per T5 (80%)																					
Trial 8 (T8)	As per Trial 3	Coverage rate as per T3 but at only 12 counts as per T5 (60%)																					

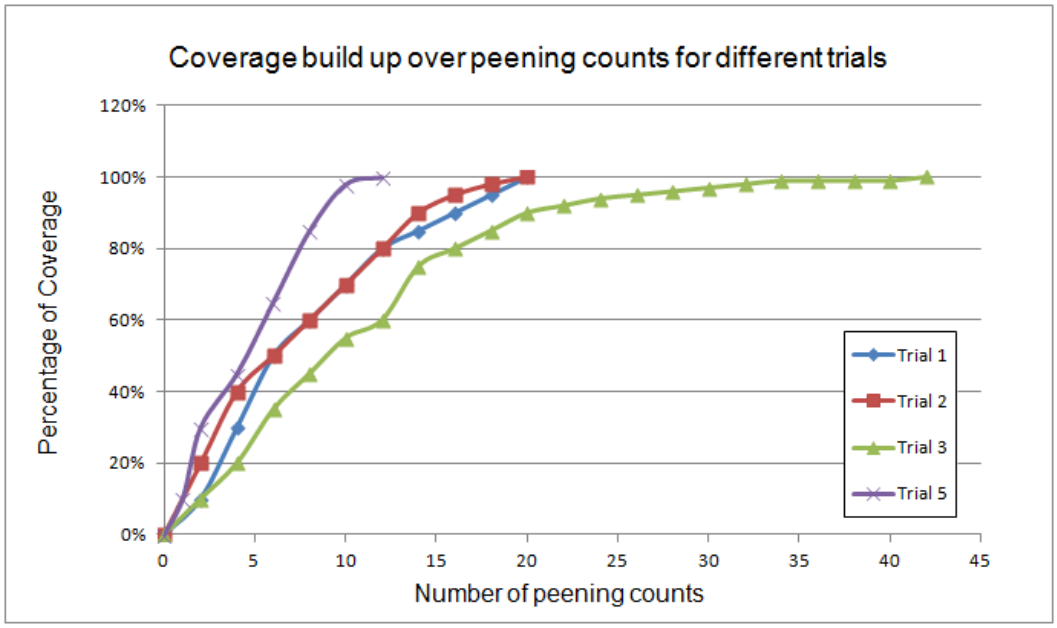

Figure 7.12: Summary of Coverage build-up for different trials.

Stress measurement

An overall summary of results containing average stress distributions from all trials is presented in Table 7.7. Residual stresses at depths of 8 µm, 40 µm, 80 µm and 256 µm from the test blocks (tabulated as the average from 4 gauges in each of 8 trials) were as follow:

Table 7.7: Shows the residual stresses at depths 8 µm, 40 µm, 80 µm and 256 µm from the test blocks**.**

Trial	Average Longitudinal Stress σ1 Mpa				Average Transverse Stress σ3 Mpa			
	8 µm	*40 µm*	*80 µm*	*256 µm*	*8 µm*	*40 µm*	*80 µm*	*256 µm*
1	-617	-673	-487	33	-673	-724	-526	26
2	-594	-590	-270	29	-550	-601	-287	29
3	-615	-463	-44	15	-594	-519	-67	13
4	-656	-663	-450	37	-673	-746	-517	35
5	-748	-696	-383	30	-759	-748	-409	29
6	-562	-629	-413	26	-637	-667	-423	26
7	-626	-576	-206	28	-569	-590	-221	26
8	-562	-242	0	23	-570	-259	-6	21

The greatest penetration of compressive stresses was detected in trial 4 test blocks while the smallest penetration was detected in trial 8 test blocks.

7.2 Test block Simulation

7.2.1 Mesh sensitivity

In a 3D SP simulation model with multiple shots interactions, the most significant limitation in the computation is the solution time. In an explicit finite element application the overall solution time is determined by the minimum element size. Hence, it is essential to choose an appropriate mesh size for the resolution and accuracy of the results. After performing a mesh sensitivity study the central mesh size of 0.01 mm was found to be sufficient to provide satisfactory results. Figure 7.13 shows the simplified mesh model with refined mesh toward the centre.

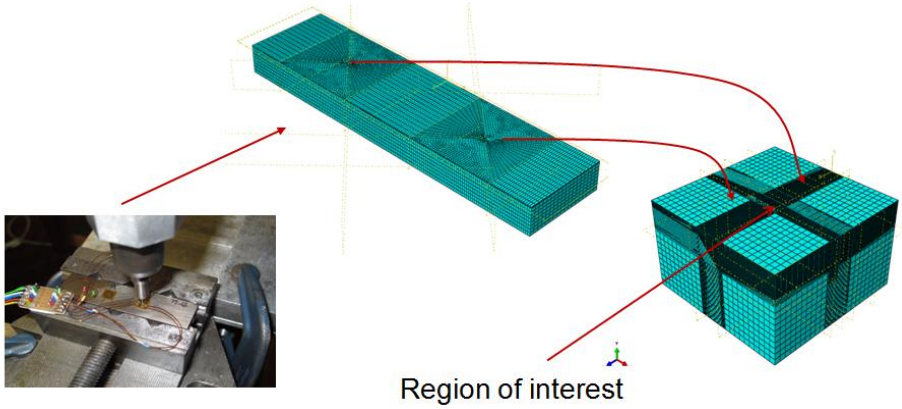

Figure 7.13: A small refined patch is used to simulate the SP process. The results are later superimposed onto the test block. The mesh is defined as being biased toward to the centre of the patch with mesh size of 0.01 of global size in mm.

7.2.2 Model simplification

Simulating only the essential time when the nozzle is directly above of the patch to be studied can greatly reduce the solution time. To speed up computation, only a small patch (1/4th) of the strip is modelled. After performing mesh senility studies the minimum area of 1 mm x 1 mm x 2 mm was discretized into a fine mesh defined as being biased toward to the centre of the patch with mesh size of 0.01 of global size in mm. The constitutive material model used in this study is outlined in section 6.3.1. The physical material model parameters in Table 6.7 and the material model parameter in Table 6.8 are applied.

The shots were modelled as spheres with diameter d_{shot} = 0.29 mm, density ρ = 7800 kg/m^3, elastic modulus E = 200 GPa and Poisson's ratio v = 0.3. The nozzle was modelled as a single circle with inner diameter d_n = 9.525 mm; Initial velocity V_{in} = 44 m/s; Mass flow rate r_m = 98 g/min and nozzle distance d = 20 mm.

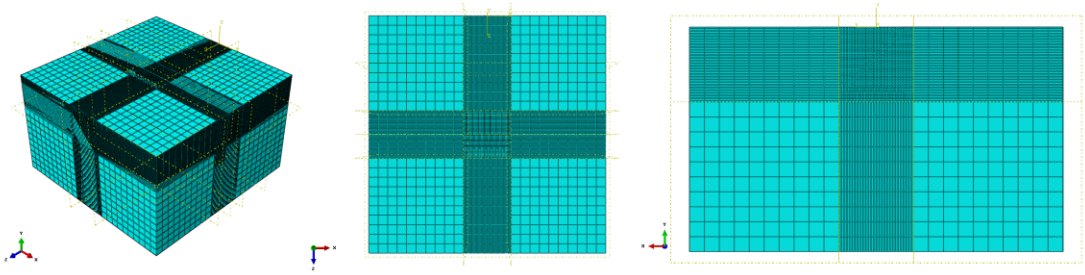

Figure 7.14: Figure shows the mesh used for the study.

Instead of moving the nozzle across the specimen for each count, the exposure time of the nozzle at the specimen was evaluated and later applied as an overall peening time. A bounding box was employed to remove particle that are generated outside of the zone of interest (component surface area). Outputs were extracted at each time step corresponding to each peening count. During the simulation, the coverage, residual stress and intensity were evaluated. The simulation was terminated once the number of required peening counts was reached.

Coverage

The peening coverage is determined by examining the surface elements of the penned component. The coverage is determined using Eq. 5.9 and Algorithm 5.9. For the ease of analysis, the area of interest is clipped and shown in Figure 7.15. In addition the final stress state is measured at depths 8 µm, 40 µm, 80 µm and 256 µm from the test blocks as illustrated in Figure 7.16.

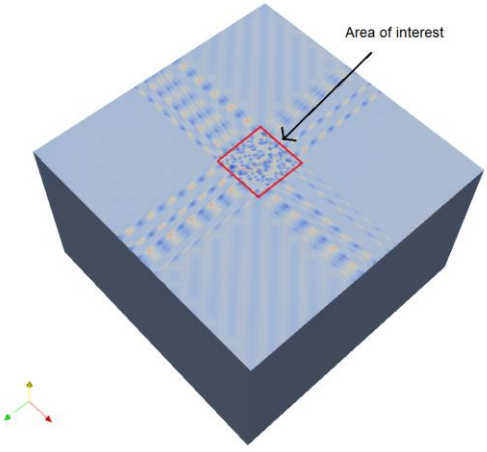

Figure 7.15: Illustration of the area of interested for post processing.

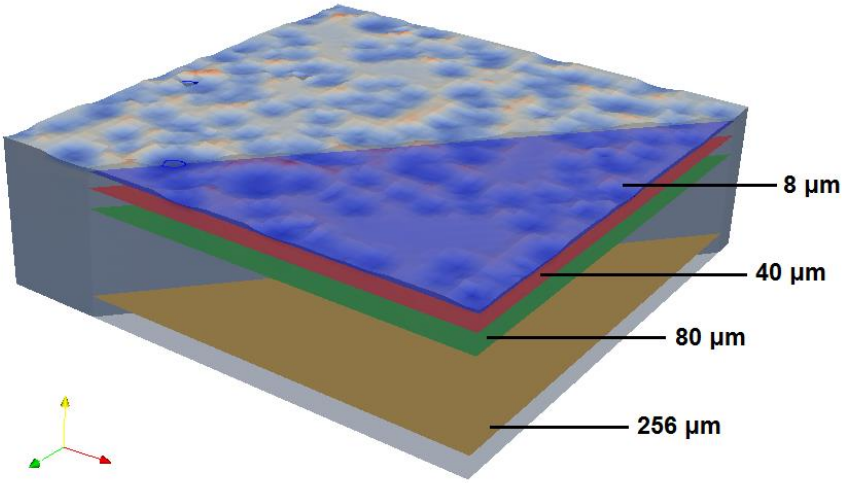

Figure 7.16: Stresses measurements at depths 8 µm, 40 µm, 80 µm and 256 µm from the centre of the test block.

7.2.3 Simulated results

Single nozzle

This section presents the numerical results obtained from single nozzle trails 1 - 3 and 6 - 8. The coverage build-up, saturation and intensity over the number of peening counts are assessed and compared.

Trial 1

Full coverage was reached after 22 peening counts.

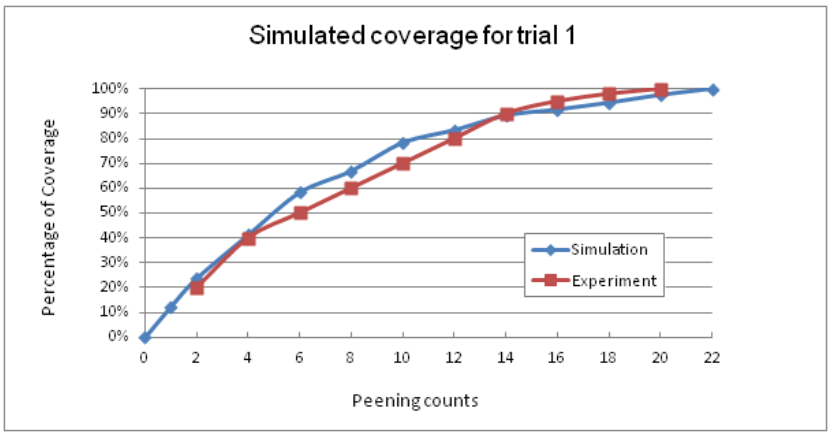

Figure 7.17: Comparison of simulated vs. experimental peening coverage for trial 1.

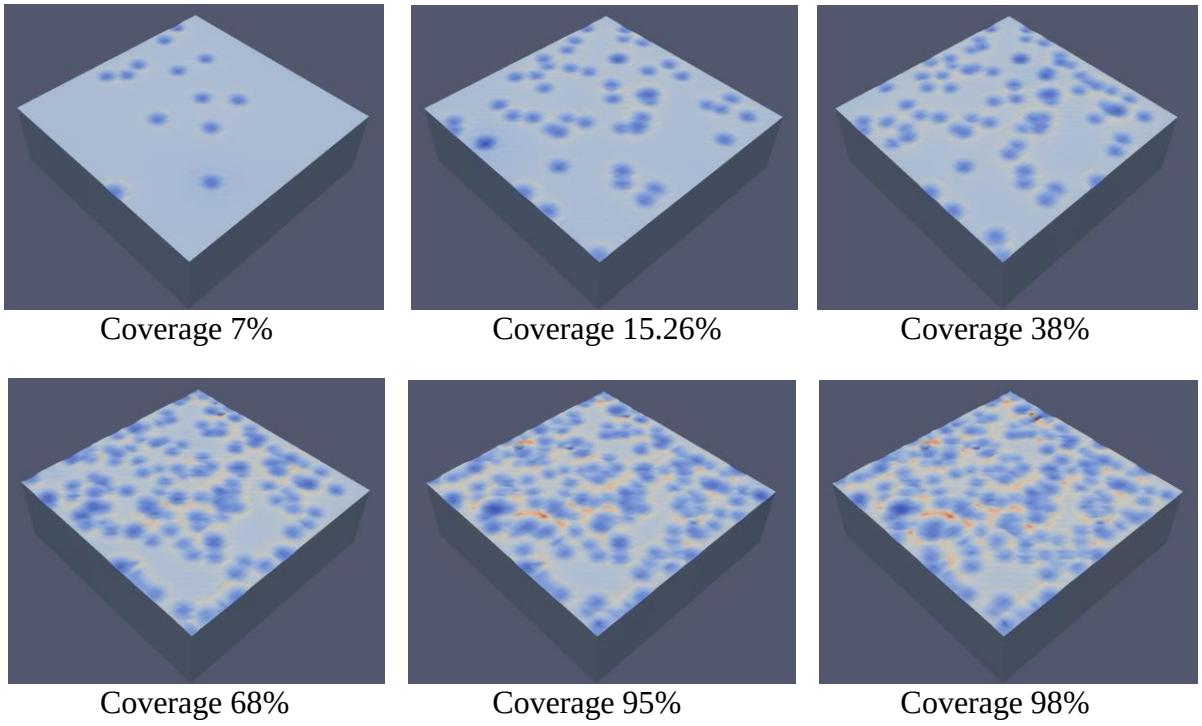

Figure 7.18: Illustration of simulated coverage build-up for trial 1.

Trial 2

Full coverage was reached after 20 peening counts, matching well with the experimental results.

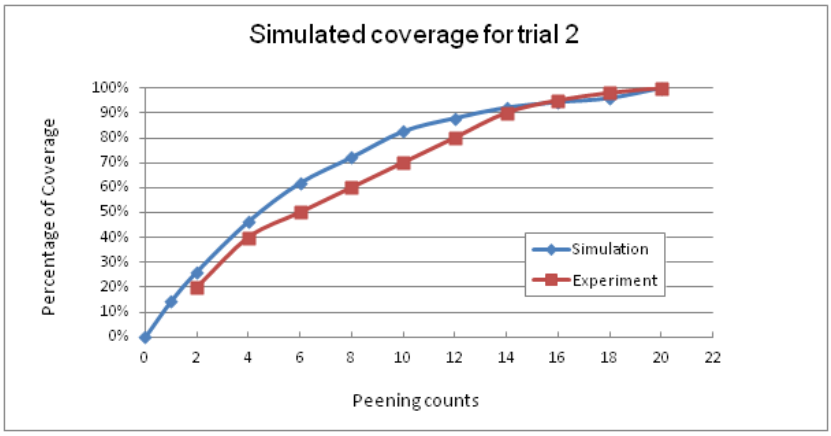

Figure 7.19: Comparison of simulated vs. experimental peening coverage for trial 2.

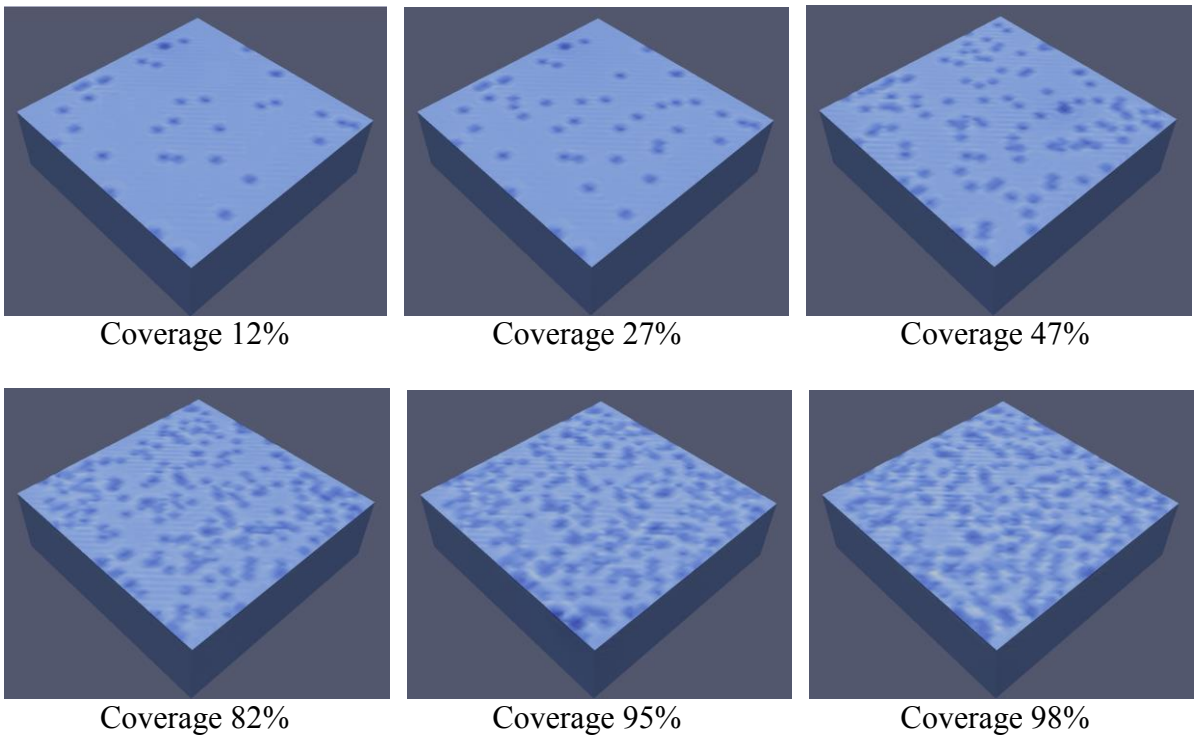

Figure 7.20: Illustration of simulated coverage build-up for trial 2.

Trial 3

Full coverage was reached after 50 peening counts compared to the 42 peening counts measured in the experiment.

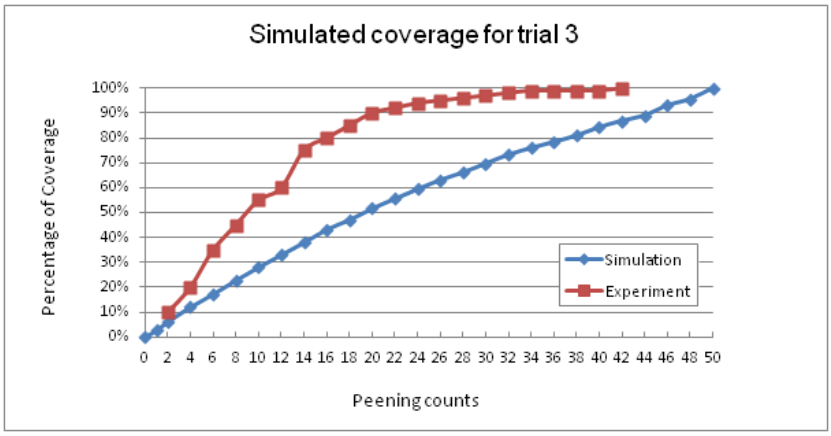

Figure 7.21: Comparison of simulated vs. experimental peening coverage for trial 3.

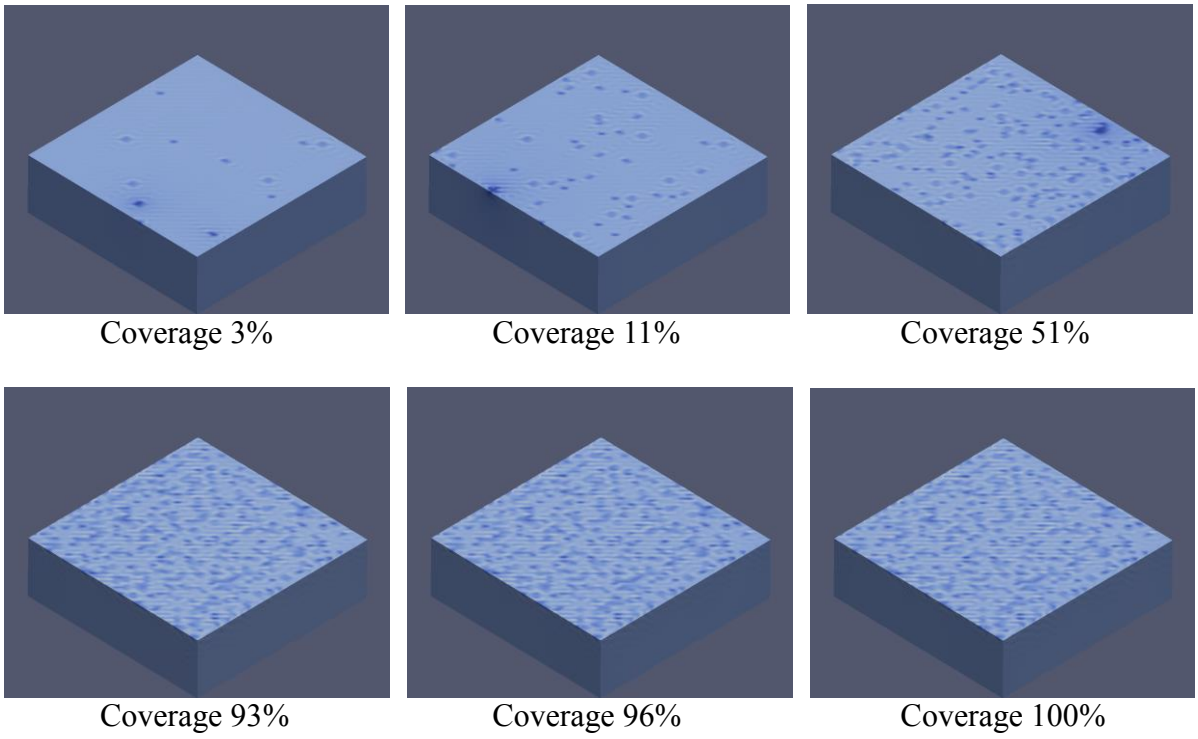

Figure 7.22: Illustration of simulated coverage build-up for trial 3.

Trial 6

Coverage as per trial 1 but only 14 counts as per trial 5 (89.28 %)

Trial 7

Coverage as per trial 2 but only 14 counts as per trial 5 (92.12 %)

Trial 8

Coverage as per trial 3 but only 14 counts as per trial 5 (38.03 %)

Multiple nozzles

This section presents the numerical results obtained from the multi nozzle trails 4 and 5. The coverage build-up, saturation and intensity for both cases are assessed.

Trial 4

Simulation with three nozzles was performed for 22 peening counts (peening time of trial 1). The coverage was made out of three nozzles, trial 1 100 % coverage, trial 2 100 % coverage and trial 3 56 %, reaching a total coverage of 256 %.

Trial 5

100 % coverage was reached with three nozzles after 14 peening counts compared to the 12 peening counts in the experiment.

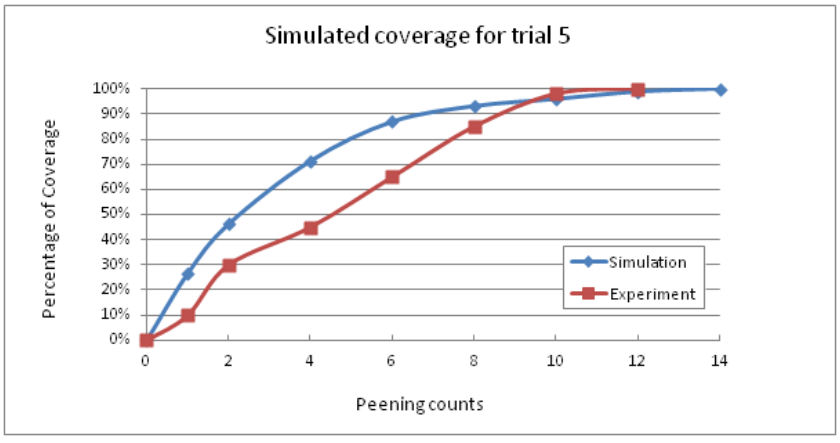

Figure 7.23: Comparison of simulated vs. experimental peening coverage for trial 5.

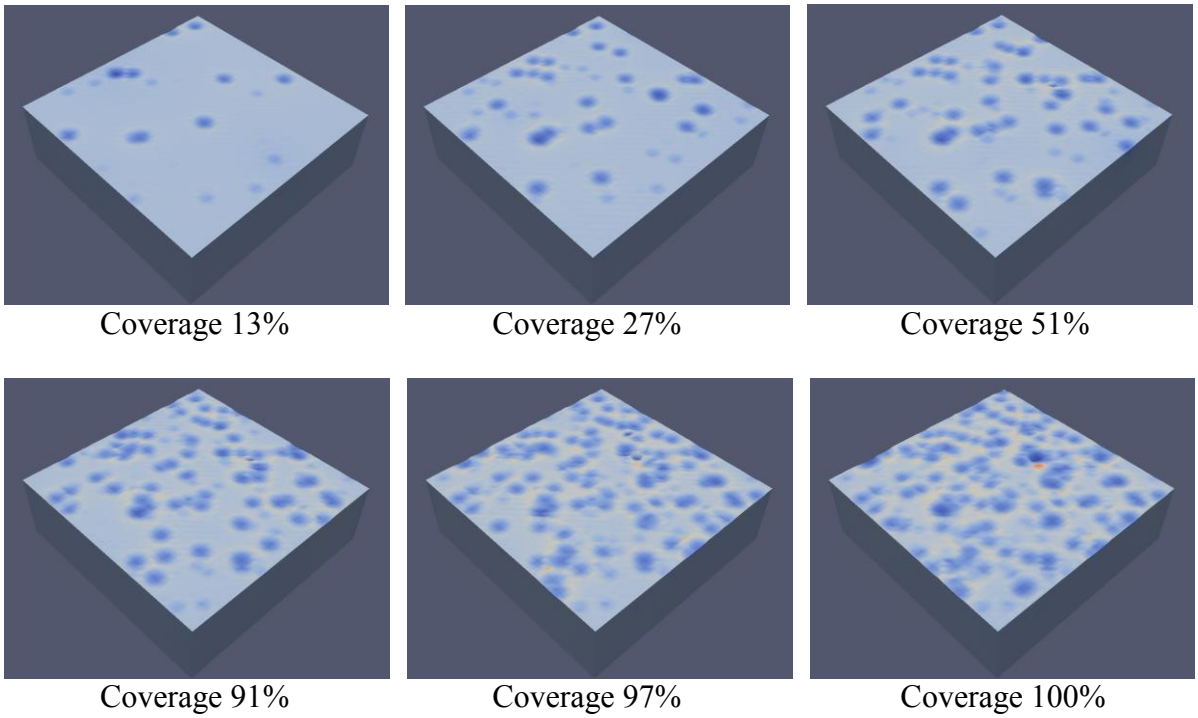

Figure 7.24: Illustration of simulated coverage build-up for trial 5.

Measured residual stresses

Table 7.8: Average simulated stresses for different trials.

Trial	Average simulated stress in Mpa			
	8 µm	*40 µm*	*80 µm*	*256 µm*
1	-573.05	-677.03	-438.82	32.76
2	-384.82	-592.5	-125.28	36.48
3	-307.32	-226.3	-112.5	12.16
4	-608.3	-612.72	-440.44	49.2
5	-813.6	-544	-2.22	33.2
6	-382.69	-414.73	-311.26	70.68
7	-568.8	-415.8	-168.96	19.32
8	-486.35	-202.16	3.4	19.09

7.3 Concluding remarks

The numerical algorithms proposed in this thesis were used to model the peening operations with single and multiple nozzles at different incident angles. The peening coverage, saturation curve and residual stresses were examined, showing that the numerical tools are versatile and can be used to examine various peening parameters.

The simulated coverage for the single nozzle trials (trial 1 and trial 2) had a good agreement with the experiments. For trial 3, 50 counts were required to reach full coverage vs. 42 counts observed in the experiments. In the simulation, 100 % coverage was reached with all three nozzles after 14 peening counts compared to the 12 peening counts seen in the experiment. The simulated results showed a very steady build-up of peening coverage, whereas an irregular coverage build-up was seen in the experimental results. This could be related the inconsistent feeding of the Shot Peening media or the errors occurred approximating the coverage by the practitioner. The depth of the final stress state observed in the simulations corresponds well with the depth of the residual stress observed in the experiments. It was found that, when peening operations are performed with multiple nozzles at different incident angles, the saturation curves do not correlate with the residual stress profiles observed from baseline tests using a single nozzle setup. The results show that, altering the peening coverage rates has an impact on the residual stress profile. It has also been demonstrated that the residual stress is reduced if the dominant nozzle does not achieve 100 % coverage on the peened surface even if the total coverage is in excess of 100 % coverage when all nozzles are combined. Saturation curves only correlate to the residual stress profile if the same incident angle is tested for the saturation curve and component. It should be noted that multiple nozzles of the same incident angle will also correlate. The investigation has determined that unless the dominant nozzle from a multi nozzle setup achieves 100 % coverage, the maximum component residual stress will not be achieved.

To summarise, it can be concluded that without knowing the individual nozzle intensity from an individual saturation curve the true intensity for that peening process cannot be calculated for a multi nozzle setup and to be consistent in achieving a repeatable condition for the part and existing data, setups with single or multi nozzle setups with the same incident angles should be used.

CHAPTER 8 CONCLUSION

In this thesis, novel numerical tools for Shot Peening simulations have been proposed. The main conclusions of this thesis are summarised.

8.1 Summary of thesis contribution and conclusion

A number of contributions in the fields of numerical modelling related and experimental characterisation to Shot Peening have been made and are summarised below.

8.1.1 Parametric study using DEM and FEM (Chapter 4)

The literature review in Chapter 2 indicated that SP parameters are customarily chosen on the basis of either empirical laws or past practice and that experimental studies can require high costs to optimize a new set of peening parameters. Numerical simulations can help to understand the influence of the individual peening parameters on the field of residual stresses. However, literature review has shown that, modelling SP processes is very complex since it involves the interaction of a metallic surface with an enourmous number of shots. To address these challenges, a numerical model has been developed with the capabilities to optimize the peening process and material response. The combined DEM/FEM approach can simulate the Shot Peening process and assist in the understanding of the relationship between SP parameter and the residual stress distribution generated in the peened material (Section 4.3). The Discrete Element Method applied in Section 4.1 can increase the fundamental understanding of the SP process, in particular shot - shot collisions and the peening pattern. The DE model provides a rapid method to investigate the individual peening parameters. Visualizing the shot impacts in DEM can help to comprehend the coverage when peening a component with a complex geometry with very little computational effort. The model can be used to analyse the shot flow in more details and assist to improve and develop new nozzle design.

The simulations have shown that for the parameters used in the study in 4.1.1, the shot flow reached steady state at 4000 impacts. The air pressure of the nozzle (V_o) was found to be the most important factor, followed by the mass flow rate r_m and the duration of the peening process. Investigating the mass flow rate and initial velocity, in section 4.1.3, it was found that a low mass flow rate is useful for maintaining the energy at impact, since the incoming stream is very lean (hence minimising the number of shot - shot collisions). For a higher mass flow rate and lower initial velocity, less shot retain their initial velocity at impact but the number of impact is greater than for the case where a higher velocity and lower mass flow rate is used. These findings are significant because they can assist practitioners to identify set peening parameters for new components.

8.1.2 Linking DEM and FEM (Chapter 4)

A novel DEM-FEM linking procedure was implemented that provides a convenient way of linking DEM with FEM (EDEM and Abaqus), without the need of external coupling tools. The minimum size of the area required to be modelled to retrieve the true residual stresses was found to be 3 x *R* where the *R* is the radius of the shot and a number of coupled analysis were performed. Investigating the angle of attack and the normal impact velocity, it emerged that the normal impact velocity can be large and in some cases up to 60 %. With the parameters investigated in the study, the optimal angle of attack in DEM was found to be $\theta = 62.5°$. However, analysing the peening angle in the combined analysis showed that the depth of the CRS zone is largest when $\theta = 70°$ followed by $\theta = 90°$.

A novel algorithm was implemented to change the CoR for repeated impacts, reasonably taking into account the work hardening and the impact area. Results showed that changing the CoR decreases the number of shot - shot collisions and increases the shot - target collisions. The average impact velocity increases compared to the conventional method. Only a very small variation in CRS was encountered for the different cases. A higher

number of impacts resulted in a deeper CRS zone. Results of the coupled analysis showed that the initial velocity is more important than the mass flow rate. In cases where the initial velocity is high (100 m/s), the CRS depth zone was deeper than in the cases where a lower velocity was used.

The DEM-FEM linking proposed in this chapter requires the user to provide the geometric surface data in the DEM application and makes a number of simplifying assumptions, such as the indentation size is equal to the size of the particle. Furthermore, the current coupling method is computationally very expensive, produces very large output files and requires several operations for the transfer of information between the linked DEM and FEM codes. A fully coupled simulation was found to be necessary. The findings have been reported in a more abbreviated form in Murugaratnam et al. (2015).

8.1.3 Advanced contact search algorithm (Chapter 5)

This chapter presented a novel and more efficient binary spatial tree (BST) algorithm for the contact detection phase of contact mechanics simulations. A BST in Section 5.1.2 is used to create the data structure to store the information on the bodies' relative spatial position, such that the geometric intersection between bodies can be assessed using as few operations as possible. This, together with the node updating (insertion and removal) (Section 5.1.5), sub-space tightening (Section 5.1.4) and BST self-balancing algorithm (Section 5.1.3), enables the reduction in the number of node visits, the amount of searching volume and computation costs. Several examples of DEM/ FEM examples are presented to examine the robustness of the algorithms and provide an assessment of the performance of the improved BST method (Section 5.5). The case studies have shown that tightening of sub regions reduces the number of node and sub region searches. The performance of the algorithm also depends on the contact zone around the bounding box. A larger contact zone would result in more potential

contacts being reported, further increasing the computation time. A smaller contact zone may result in more frequent removal and insertion of the facet into the binary tree.

For problems such as Shot Peening or plate impact with element insertion, deletion or debonding, the proposed method performs better as it eliminates the need to rebuild the whole binary search tree. Deletion and insertion allows reusing the allocated memory space, enabling one to investigate complex peening processes with very high number of particles and multiple nozzles. The length of the SP peening simulation is no longer limited by the available computer memory. Instead, it is only limited by the size of peening part and the maximum number of shots present in the analyses at a time step over the whole simulation time.

8.1.4 Implementation of Shot Peening features (Chapter 5)

In chapter 5, the proposed Shot Peening algorithms have been shown to be capable of capturing the Shot Peening features. A nozzle factory was implemented and validated by examining the particle location distribution and monitoring the particle generation mass flow rate over time. The nozzle generates a constant and stable rate of mass where the mass generation increases linear over time. Numerical models have been implemented to measure Shot Peening effects during the simulation. The results have shown that the implemented numerical model is capable of capturing the effectiveness of Shot Peening in terms of surface coverage, surface intensity and roughness. The results match well with the results published by H Y. Miao et al. (2009). Their model does not take into account any shot - shot interaction or mass flow rate for shot generation. The developed model takes these parameters into account, but the key advantage of the implementation is that it allows one to assess the effectiveness of the peening at any time during the simulation with no post processing involved and terminate the simulation when saturation state is reached. This reduces time and costs in assessing the effectiveness of peening parameters in new components.

8.1.5 Experimental study of single shot impact analysis of Ti-6Al-4V (Chapter 6)

Experimental study and simulations of single shot impact analysis of Ti-6Al-4V were demonstrated in Chapter 6. Several shot sizes and velocities were compared in a matrix, including peening media MR110 (0.29 mm diameter steel shots). The constitutive model used in the study (Section 6.3.1) has been shown to demonstrate the ability to predict the indentation sizes for the set-1 specimens. For set-2 specimens the predicted plastic zone matched well with that obtained in the experiments. However, the indentation widths were overestimated by about 35 % and variance increases with velocity and shot size.

The material model, in its current calibration state, appears to over predict softening and is therefore predicting a larger indentation size than the experiments for set-2 material. Experimental data from the single shot impacts have exhibited a larger plastic zone when impact velocities increase. In order to fully validate the material model uniaxial tension, compression and torsion data is required at differing strain-rates over a range of temperatures. The non-physical material parameters required numerical methods, such as inverse modelling approaches, to determine the remaining parameters. Sub-surface damage within the indented specimens may also yield information as to the prevailing damage mechanisms and the extent of their influence and depth of interaction. This data would inform the material model as to the degree of localisation and rate of growth required to accurately predict the material response in set-2 tests.

In addition to the identification of appropriate material parameters, the mesh density also needs to be an appropriate scale. Whilst the material model has the ability to reduce the influence of mesh size, through characteristic element length calculations which influence the damage accumulation rate, larger elements will reduce the accuracy of the indentation profile. Furthermore, when combined with the inherent anisotropic nature of the set-2 material, which is well known in titanium alloys due to the polycrystalline structure, may have also

influenced the accuracy of the indentation profile, as the current material model formulation is isotropic.

Finally, the depth of the indentation could not be accurately measured for set-2 material due to the measurement techniques' (ALICONA - Infinite Focus) inability to perform reliably on highly reflective surfaces. Without this information, the only other option available would be much more time consuming and involve determining the sub-surface residual stress. Therefore, the accuracy of the bulk deformation and corresponding residual stress could also be used as a validation criterion.

8.1.6 Case study of Shot Peening of Ti-6Al-4V test blocks (Chapter 7)

The thesis concludes by modelling an experimental study using the proposed numerical tools, with the purpose to demonstrate that the numerical tools are capable of capturing specific Shot Peening effects. The experimental study has shown that for peening operations with multiple nozzles at different incident angles, the saturation curves do not correlate with the residual stress profiles observed from baseline tests using a single nozzle setup. It can be concluded that altering the peening coverage rate affects the final residual stress profile. The residual stress is reduced if dominant nozzle does not achieve 100 % coverage on the peened area, even if the total coverage is in excess of 100 % coverage when all nozzles are combined. Saturation curves only correlate to the residual stress profile if the same incident angle is tested for the saturation curve and component. It should be noted that multiple nozzles of the same incident angle would also correlate.

The study has determined that unless the dominant nozzle from a multi nozzle setup achieves 100 % coverage, the maximum component residual stress will not be achieved. It can be concluded that without knowing the individual nozzle intensity, the individual saturation curve cannot be calculated for the multi nozzle setup.

8.2 Summary

An efficient numerical tool has been proposed in this thesis to model and optimise the Shot Peening process. The robustness has been tested extensively through numerical verification exercises and by comparing the numerical model with experimental data. The work demonstrates that the numerical Shot Peening model can help study the effects of process parameters on the peening quality. It is also capable of capturing details of the case study and provides valuable insight through the sensitivity analyses.

CHAPTER 9 FUTURE WORK

A number of contributions in each of these topics were made, further increasing the understanding of the process and parameters of Shot Peening. However, opportunities for further research remains very challenging and possible future opportunities directly related to this work are presented in the following.

9.1 Experimental Methods

9.1.1 Further single shot impact tests

The single shot impact, although extensively analysed in the literature, is still worth investigating. The foundations were laid out during this study and useful knowledge was gained. The often-used Shot Peening media is not perfectly spherical and hence indentation size and RS may vary when comparing results with spherical shot impact under the same condition. The shots are usually metallic, i.e., relatively hard steel, but ceramic or glass shots are also used. A wide range of materials with different ratios of yield stress and elastic properties, shot sizes; impact velocities and angle of impacts could be investigated. Overlapping shots and their effect on the residual stresses can be examined using the gas gun used in Chapter 6. Hong (2005a) investigated overlapping shots and found that two overlapping shots will result in reducing the residual stress level at the central axis of the first impact. This is in agreement with the results published by Guagliano (2001) and Meguid et al. (1999, 2001). The indented specimens can be then used to determine the macroscopic and microscopic subsurface residual stress distributions using X-ray diffraction.

9.1.2 Material model

The material model used in this project is certainly incomplete and could to be further improved. An extensive material characterization process involving at least asymmetric uniaxial testing up to higher strain-rates can be conducted to assess the cyclic behaviour and

strain-rate sensitivity. Considering the possible influence of increased temperatures during Shot Peening arising during repeated impacts, both in terms of thermal expansion and mechanical properties, it would also be useful to perform high-temperature testing. In addition, pressure-dependent yield criteria could also be investigated. The experimental data could then be used to choose and construct an appropriate material constitutive theory and determine material parameters for each individual material. Another important modelling aspect is the microstructure. The development of crystal plasticity laws including cyclic, high strain-rate and thermal behaviour would lead to a more fundamental understanding. The effects of grain size and crystallographic texture on the resulting material state could also be investigated. Furthermore, single shot impact experiments at different angles on single crystals with different crystallographic orientations could be performed to investigate the deformation mechanisms with EBSD or SEM.

9.1.3 Peening of more complex geometries

Manufactures are interested in obtaining a uniform peening depth for complex geometries and optimisation of Shot Peening parameters. Existing studies on Shot Peening optimisation only investigate flat surfaces and none of the review articles investigate complex geometries such as geometries with curvatures and edges. Most peening systems will also have dynamic nozzles that will be in constant motion during the peening process. The shot stream of a static nozzle will be significantly different from that of a dynamic nozzle that is in motion. Due to the shot interaction during peening, shots impact surfaces that are not directly exposed to the nozzle. The amount of shots and energy transfer of these indirect shot impacts can be easily assessed with the developed tool described herein. This also has an effect on the peening intensity, coverage and the overall peening quality.

9.1.4 Fatigue tests

Compressive residual stresses produced by Shot Peening have a beneficial effect on the improvement of the fatigue life. However, the surface roughness generated by Shot Peening may have an unfavourable effect on the component performance. Studies could be performed with optimised peening parameters, resulting residual stress profiles and surface roughness to study their effects on fatigue life prediction.

9.1.5 Requirement to clearly establish cost the parameter by taking into account peening time and mass flow versus costs.

Minimising the processing time during the peening application is an important aspect. Reducing the time during the peening applications would result in higher productivity rates. The peening application costs include treatment cycle time, consumption of beads, energy, compressed air and peening technique (treatment of component without having to dismantle parts or integration in the production line). Depending on the type of shot and the intensity, the amount of shot that is damaged in a single peening cycle can range from ~1 % to 10 % or more. The cost of shot media is one of the major expenses in Shot Peening and reclaiming the shot is a valuable and effective measure to reduce Shot Peening costs. Some advanced peening machines have the capability of reclaiming a large amount of used shots. As the total cost depends on several factors, it is difficult to establish a guideline to reduce production costs and investigation of individual cases is required.

9.2 Numerical Methods

9.2.1 Parallel processing, CPU and GPU

Increasing the clock frequency was the primary method of improving processor performance, however the maximum clock speeds have been pushed to their limits and the performance increase can only be achieved using parallelism. Currently, DEST only supports single thread execution. Implementing the parallelisation of the DEM/FEM code in either MP (Multi-

Processing), MPI (Message Passing Interface) or OpenGL (GPU Parallelisation) would massively increase the computational power. MP is a method of parallel implementation, where the master thread initiates several slave "threads", which execute the allocated task in parallel. The threads are allocated to different processors and take advantage of the globally shared memory.The MPI is employed within and across several nodes and uses a programming model to communicate with other processes by calling library routines. In this model the user has complete control over data distribution and process synchronization. However the disadvantage is that existing applications require a significant restructuring.

The performance improvement gained by using parallel processing depends on the implemented software algorithms which are, again, limited by the fraction of the software that can be run in parallel simultaneously expressed as Amdahl's law. The CPU that has a fast cache is therefore suitable for data reuse and can result in improved performance when processing different task or Threads. CPUs are generally well suited for task parallelism whereas GPU's can be very effective when computing a large number of results for which the same computations are executed. Compared to CPUs, GPUS are designed to run parallel tasks such as rendering and can process fragments and independent vertices. They provide fast access with the on-board memory and have a large memory bandwidth with a high number of maths units. Every year GPUs performance accelerates by around 1.7 -2.3 times whereas the computation power of a CPU increases by 1.4 times every year. A GPU can process a number of applications such as large matrix/vector operations, Sorting/Searching, Physical Simulations, Molecular Dynamics and many more and is therefore suited for running DEM/FEM applications such as DEST, but would requires major redesign of the existing algorithm.

9.2.2 Dynamic bounding box

A simulation domain can be defined where the simulation takes place. Particles moving out of the domain during the simulation time are removed from simulation. The size of the domain has an effect on the simulation time. A larger domain will contain more particles and simulation time would be longer than when a smaller domain is used. A bounding box has been introduced in this work to remove particles that have moved outside of the box. Since, the surface layer state is the consequence of the local plastic deformation, a dynamic bounding box can be implemented to follow the nozzle movement. This approach could be further improved by generating a bounding box around each shot and only compute the elements of the component that are within the bounding box.

9.2.3 Peen forming

Peen forming is a manufacturing method commonly used in the aerospace industry to shape large, relatively thin parts to complex contours. This process is a derivative of Shot Peening and uses peening-induced compressive stresses to produce thin components with complex shapes, involving double curvatures, such as wing skins**.** Stress peen forming studies could be carried out with the implemented model to study the forming of small size components with simple shapes such as rectangle or square strips. Further studies could focus on larger and more complex components such as real wing skins. The results from experimental and numerical studies could then be used to create a tool to predict the peening forming parameters according to the required geometric shape.

9.2.4 Improve the intensity model

The intensity model used in this study, assumes that the induced average stress profile calculated from a representative volume of the component is uniformly distributed throughout whole target component. The average stress profile was used to calculate the

deformation of the strip. In practice the stress profile across the component may vary and the implemented method may not reflect the true intensity. A more advanced method could be implemented that takes into account the induced stress profile of the strip at different locations and map them onto a FEM model to calculate the intensity of the strip.

REFERENCES

Adelson-Velskii, G.M. & Landis, E.M., 1962. An information organization algorithm (in Russian). *Doklady Akademia Nauk SSSR*, 146, pp.236–266.

Ajovalasit, A., Petrucci, G. & Zuccarello, B., 1996. Determination of non-uniform residual stresses using the ring-core method. *J Mater Process Technol*, 118(2), pp.224–228.

Al-Hassani S.T.S., 1981. Mechanical aspects of residual stress development in SP. In *International Conference on Shot Peening - 1*. Paris, pp. 14–17.

Al-Hassani, S.T.S., 1982. The shot peening of metals–mechanics and structures. *Shot Peening for Advanced Aerospace Design*, p.2.

Al-Hassani, S.T.S., Kormi, K. & Webb, D.C., 1999. Numerical simulation of multiple shot impact. In *International Conference on Shot Peening-7*. Warsaw, pp. 217–227.

Almen, J.O. & Black, P.H., 1963. *Residual Stresses and Fatigue in Metals*, New York: McGraw-Hill.

Altenberger, I. et al., 2001. Characterization of Fatigue Crack Formation in Mechanically Surface Treated Austenitic Stainless Steel. In *Advances in Fracture Research- Proc. Int. Conf. on Fatigue 10*. Honolulu.

Altenberger, I. et al., 1999. Cyclic deformation and near surface microstructures of shot peened or deep rolled austenitic stainless steel AISI 304. *Materials Science and Engineering: A*, pp.1–16.

Bammann, D. & Aifantis, E., 1987a. A model for finite-deformation plasticity. *Acta Mechanica*, 69(1), pp.97–117.

Bammann, D. & Aifantis, E., 1987b. A model for finite-deformation plasticity. *Acta Mechanica*, 69(1), pp.97–117.

Bammann, D.., 1984. An internal variable model of viscoplasticity. *International Journal of Engineering Science*, 22(8-10), pp.1041–1053.

Bammann, D.J. & Chies, M.F., 1993. Failure in ductile materials using finite element simulations. In *The 3rd International Symposium on Structural Crashworthiness and Failure*. Liverpool: Elsevier Applied Science.

Baughman, D.., 1981. of Centrifugal Wheel SP in Aerospace Industry and Recent Applications. In *International Conference on Shot Peening -1*. Paris, pp. 101–108.

Bhuvaraghan, B. et al., 2008. SP modeling by combining DEM and FEM. In *International Conference on Shot Peening -10*. Tokyo, pp. 131–142.

Burck, L.H., Sullivan, C.P. & Wells., C.H., 1970. Fatigue of a glass bead blasted Nickelbase superalloy. *Met. Transactions*, 1, pp.1595–1600.

Cao, W., Fathallar, R. & Castex, L., 1995. Correlation of Almen arc height with residual stresses in shot peening process. *Materials Science and Technology*, 2, pp.967–973.

Christ, H.-J. & Mughrabi., H., 1992. Microstructure and Fatigue. In *Low Cycle Fatigue and Elasto-Plastic Behavior of Materials-3*. New York: Elsevier Applied Science, pp. 56–69.

Clausen, R. & Stangenberg, J., 1999. Roughness of shot-peened surfaces – definition and measurement. In *International Conference on Shot Peening -7*. Warsaw, pp. 69–77.

Cousins, B., Thomas, M. & Petrinic, N., 2012. *An enhanced explicit constitutive material model for Ti-6Al-4V with competing dilatational and distortional damage models*, Oxford.

Cundall, P.A. & Strack, O.D.L., 1979. A discrete numerical model for granular assemblies. *Geotechnique*, (29), pp.47–65.

Deslaef, D., Emmanuelle, R. & Rasouli, Y.S., 2000. 3D Finite Element models of shot peening process. *Journal of Materials Science Forum*.

Eberly, D., 1999. Distance between point and triangle in 3D. *Magic Software, http://www.magic- …*, pp.1–6. Available at: http://continuous-collision-detection.googlecode.com/svn/trunk/Docs/Bounding_Volume_Hierarchies/ElementalTests/DistancePoint3Triangle3.pdf [Accessed December 4, 2013].

Edberg, J., Lindgren, L.-E. & Mori, K.-L., 1995. Shot peening simulated by two different finite element formulations. In *Shen S, Dawson E, editors. Simulation of materials processing*. Rotterdam, pp. 425–430.

EDEM, 2013. EDEM 2.5 User guide.

Elliott, B., 2007a. *Inverse Identification of Constitutive Parameters for Simulation of Impact on Rate-Dependent Media*. University of Oxford.

Elliott, B., 2007b. *Inverse Identification of Constitutive Parameters for Simulation of Impact on Rate-Dependent Media*. University of Oxford.

Feng, Y.T. & Owen, D.R.J., 2002. An augmented spatial digital tree algorithm for contact detection in computational mechanics. *International Journal for Numerical Methods in Engineering*, 55(2), pp.159–176.

Finnie, I., Stevick, G.R. & Ridgely, J.R., 1992. The influence of impingement angle on the erosion of ductile metals by angular abrasive particles. *Wear*, 152(1), pp.91–98.

Fisher, J.W., Statnikov, E.S. & Tehini, L., 2001. Fatigue Strength Enhancement by Means of Weld Design Change and the Application of Ultrasonic Impact treatment. In *Proc. of Intl. Symp. On Steel Bridges*. Chicago.

Gariépy, A., 2012. *Finite Element Modelling of Shot Peening and Peen Forming processes and characterisation of penned AA2024-T351 Aluminium alloy*. Département de génie mécanique de l'École Polytechnique de Montréal.

Ghaboussi, J. & Barbosa, R., 1990. Three-dimensional discrete element method for granular materials. *International Journal for Numerical and Analytical Methods in Geomechanics*, 14(7), pp.451–472.

Gillespie & K., L., 2009. Hit it again, harder. *Cutting Tool Engineering Plus*. Available at: http://www.ctemag.com/aa_pages/2009/0908_PartsFinishing.html.

Guagliano, M., 2001. Relating Almen intensity to residual stresses induced by shot peening: a numerical approach. *Journal of Materials Processing Technology*, 110(3), pp.277–286.

Guagliano, M. & Vergani, L., 2001. An approach for prediction of fatigue strength of shot peened components. *Int. Journal of Engineering Fracture Mechanics*, 71, pp.501–512.

Guo, Y.B., Wen, Q. & Horstemeyer, M.F., 2005. An internal state variable plasticity-based approach to determine dynamic loading history effects on material property in manufacturing processes. *International Journal of Mechanical Sciences*, 47(9), pp.1423–1441.

Hammond, D.W. & Meguid, S.A., 1990. Crack propagation in the presence of shot-peening residual stresses. *Engineering Fracture Mechanics*, 37(2), pp.373–387.

Han, K. et al., 2000. A combined finite/discrete element simulation of shot peening processes - Part II: 3D interaction laws. *Engineering Computations*, 17, pp.680–702(23).

Hertz, H., 1896. Über die berührung fester elastischer Körper (On the contact of rigid elastic solids). *J. reine und angewandte Mathematik 92*, p.156.

Hibbitt Karlsson & Sorenson, 2009. ABAQUS User Manual Version 6.9.

Higounenc, O., 2005. Correlation of SP parameters to surface characteristic. In *International Conference on Shot Peening - 9*. Paris, pp. 28–35.

Holdgate, N.M.D., 1993. *Peen Mechanics in the shot peening process*. University of Cambridge.

Holzapfel, H. et al., 1998. Einfulss der Kugelstrahlparameter auf die Randschichteigenschaften von 42 CrMo 4,. In *Harterei-Techn. Mitt.* pp. 155–163.

Homer, S.E. & VanLuchene, R.D., 1991. Aircraft Wing Skin Contouring by Shot Peening. *Journal of Materials Shaping Technology*, 9(2), pp.89–101.

Hong, T. et al., 2005. A numerical simulation to relate the shot peening process parameters to the induced residual stresses. In *International Conference on Shot Peening - 9*. Paris, pp. 100–106.

Hong, T., Ooi, J.Y. & Shaw, B.A., 2008. A numerical study of the residual stress pattern from single shot impacting on a metallic component. *Adv. Eng. Softw.*, 39(9), pp.743–756.

Hutchings, I.M., Winter, R.E. & Field, J.E., 1976. Solid Particle Erosion of Metals: The Removal of Surface Material by Spherical Projectiles. *Proceedings of the Royal Society of London. Series A, Mathematical and Physical Sciences*, 348(1654), pp. 379–392.

Iain, F., Wolak, J. & Kabil, Y., 1967. Erosion of Metals by Solid Particles. In *J. Mater*. pp. 682–700.

Jain, A., Nadkarni, V.S. & Mahesh C. Sharma, 2002. Effect of Shot Peening on Erosion and Fatigue in Combined Bending and Torsion of the Magnesium Alloy AZ80. In *International Conference on Shot Peening - 8*. Munich, pp. 137–141.

Jiménez, P., Thomas, F. & Torras, C., 2001. 3D collision detection: a survey. *Computers & Graphics*, 25.

Johnson, K.L., 1985. *Contact Mechanics*, Cambridge University Press.

Keneti, A.R., Jafari, A. & Wu, J.-H., 2008. A new algorithm to identify contact patterns between convex blocks for three-dimensional discontinuous deformation analysis. *Computers and Geotechnics*, 35(5), pp.746–759.

Kiel, S., 1992. Experimental determination of residual stresses with the ring-core method and an on-line measuring system. *Exp Tech*, 16(5), pp.17–24.

Kim, T. et al., 2012. A 3D {FE} model with plastic shot for evaluation of equi-biaxial peening residual stress due to multi-impacts. *Surface and Coatings Technology*, 206(13), pp.3125–3136. Available at: http://www.sciencedirect.com/science/article/pii/S0257897211012618.

Kirk, D., 2005. Almen Saturation Curve Solver Program. Available at: http://www.shotpeener.com/learning/solver.php [Accessed September 10, 2013].

Kirk, D., 2012a. J443 An Evolutionary Guide to Shot Peening Intensity Measurement. *The Shot Peener*, pp.24–32.

Kirk, D., 2012b. J443 An Evolutionary Guide to Shot Peening Intensity Measurement. *The Shot Peener*, pp.24–32.

Kirk, D. & Abyaneh, M.Y., 1993. Theoretical Basis of Shot Peening Coverage Control. In *International Conference on Shot Peening -5*. Oxford, pp. 9–14.

Klemenz, M. et al., 2005. Similarity rules for Shot Peening process based on Finite Element simulations. In *International Conference on Shot Peening - 9*. pp. 94–99.

Kloos, K.H. & Macherauch, E., 1987. Development of Mechanical Surface Strengthening Processes from the beginning until Today. In *International Conference on Shot Peening -*. Garmisch-Partenkirchen.

Kockara, S., Halic, T. & Bayrak, C., 2009. Contact detection algorithms. *Journal of …*, 4(10), pp.1053–1063.

Komotori, J. & Shimizu, M., 1992. Microstructural Effect Controlling Exhaustion of Ductility in Extremely Low Cycle Fatigue. In *Low Cycle Fatigue and Elasto-Plastic Behaviour of Materials—3*. pp. 136–141.

König G., 2002. Life Enhancement of Aero Engine Components by SP: Opportunities and Risks. In *International Conference on Shot Peening - 8*. Garmisch-Partenkirchen, pp. 13–22.

Kopp, R. & Schulz, J., 2002. Optimising the double-sided simultaneous shot peen forming. In *International Conference on Shot Peening - 8*. Garmisch-Partenkirchen, pp. 227–233.

Koster, W.P., Gatto, L.R. & Cammett, J.T., 1981. Influence of shot peening on surface integrity of some machined aerospace materials. In *International Conference on Shot Peening -1*. San Francisco, pp. 287–293.

Lemaitre, J. & Desmorat, R., 2005. *Engineering Damage Mechanics*, Springer.

Lieurade, H.P., 2005. Fatigue improvement of welded components by SP. In *International Conference on Shot Peening - 9*. pp. 16–27.

Liu, X.L. & Lemos, J.V., 2001. Procedure for contact detection in discrete element analysis. *Advances in Engineering Software*, 32(5), pp.409–415.

Lukáš˘, P., 1996. Fatigue crack nucleation and microstructure. In *Fatigue and Fracture*. Ohio, pp. 96–109.

Majzoobi, G.H., Azizi, R. & Alavi Nia, A., 2005. A three-dimensional simulation of shot peening process using multiple shot impacts. *Journal of Materials Processing Technology*, 164-165, pp.1226–1234.

Meguid, S.A. et al., 1999. Three-dimensional dynamic finite element analysis of shot-peening induced residual stresses. *Finite Elements in Analysis and Design*, 31(3), pp.179–191.

Metal Improvement Company, 2012. *Shot Peening Trials*, Derby.

Miao, H.Y. et al., 2009. Advances in Engineering Software : On the potential applications of a 3D random finite element model for the simulation of shot peening. *Advances in Engineering Software*, 40, pp.1023–1038.

Miao, H.Y. et al., 2010. An analytical approach to relate shot peening parameters to Almen intensity. *Surface and Coatings Technology*, In Press,, pp.2055-2066.

Miao, H.Y. et al., 2009. On the potential applications of a 3D random finite element model for the simulation of shot peening. *Adv. Eng. Softw.*, 40(10), pp.1023–1038.

Milbradt, K., 1951. Ring-method determination of residual stresses. In *Proc SESA*. pp. 63–74.

Mindlin, R., 1949. Compliance of elastic bodies in contact. *Journal of Applied Mechanics*, pp.256–268.

Misra, A. & Finnie, I., 1981. On the size effect in abrasive and erosive wear. *Wear*, 65, pp.359–373.

Murugaratnam, K., Utili, S. & Petrinic, N., 2015. A combined DEM–FEM numerical method for Shot Peening parameter optimisation. *Advances in Engineering Software*, 79, pp.13–26.

Ogarko, V. & Luding, S., 2012. A fast multilevel algorithm for contact detection of arbitrarily polydisperse objects. *Computer Physics Communications*, 183(4), pp.931–936.

Peige, S. et al., 1996. Qualitative Analysis about Effect of SP on Fatigue Limit of 300M Steel under the Rotating Bending Condition. In *International Conference on Shot Peening -6*. San Francisco, pp. 290–295.

Petrinic, N., 1996. *Aspects of Discrete Element Modelling involving Facet-to-Facet Contact Detection and interaction*. University of Wales.

Peyrac, C. & Flavenot, J. f., 2005. Optimisation of carburising SP in order to improve both bending and contact fatigue behaviour for gear applications. In *International Conference on Shot Peening -9*. Paris, pp. 214–220.

Rossini, N.S. et al., 2012. Methods of measuring residual stresses in components. *Materials & Design*, 35(0), pp.572–588.

Rouquette, S. & Rouhaud, E., 2005. Thermo-elasto-plastic model for shot peening: A numerical and experimental approach. *International Conference on Shot Peening-9*, pp.113–118.

Ru, J., Wang, R. & Li, X., 1996. Investigation on shot peening strengthening of René 95 powder alloy. In *International Conference on Shot Peening - 6*. San Francisco, pp. 338–347.

S.Kennerell, 2012. *Comparison of saturation curves versus residual stress measurements when comparing peening with multiple Nozzles at different incident angles to single nozzle single angle peening methods.Rolls Royce Plc*.

Schulze, V., 2002. Characteristics of Surface Layers Produced by Shot Peening. In *International Conference on Shot Peening -8*. Munich, pp. 147–160.

Schwindt, S., 2009. Methodologies for Simulating Soft-Body Impacts and Development of an Improved Artificial Bird.

Sharma, M.C. et al., 2002. Virtues & Limitations of Almen Round. In L. Wagner, ed. *International Conference on Shot Peening - 8*. Munich, pp. 83–88.

Sharp, P.K., Clayton, J.Q. & Clark, G., 1994. The fatigue resistance of peened 7050-T7451 aluminum alloy: Sharp. P.K., Clayton, J.Q. and Clark, G. Fatigue Fract. Eng. Mater.

Struct. (Mar. 1994) 17 (3), 243–252. *International Journal of Fatigue*, 17(5), pp.243–252.

Šmilauer, V. et al., 2010. Yade Documentation.

Spawton, J., 2011. *Ceramic Armour*, Oxford.

Tange, A. & Okada, H., 2002. Shot peening and coverage. *Shot Peening (L. Wagner, ed.) Wiley-VCH (…*. Available at: http://www.shotpeener.com/library/pdf/2002067.pdf [Accessed December 3, 2013].

Tatton R.J.D., 1987. Shot Peen Forming -An Economical Solution. In *International Conference on Shot Peening - 3*. Garmisch- Partenkirchen, pp. 309–318.

Thornton, C. & Yin, K.K., 1991. Impact of elastic spheres with and without adhesion. *Powder Technology*, 65(1-3), pp.153–166.

Timothy, S.P. & Hutchings, I.M., 1981. Microstructural features associated with ballistic impact in Ti6Al4V. In *7th International Conference on High Energy Rate Fabrication*. pp. 19–28.

Tsuji, Y., Tanaka, T. & T.Ishida, 1992. Lagrangian numerical simulation of plug flow of cohesionless particle in a horizontal pipe. *Powder Technology*, 71, pp.239–250.

Wagner, L. & Luetjering, G., 1981. Influence of shot-peening on the fatigue behavior of titanium alloys. In *International Conference on Shot Peening-1*. Paris, pp. 453–460.

Walizer, L.E. & Peters, J.F., 2011. A bounding box search algorithm for DEM simulation. *Computer Physics Communications*, 182(2), pp.281–288.

Watanabe, Y. & Hasegawa, N., 1995. Simulation of residual stress distribution on SP. In *International Conference on Shot Peening-6*. San Francisco, pp. 967–973.

Whitehead, J.S. & Lodge, P.S., 2012. *Shot peened trial coupons in Ti6/4*,

Williams, J. & O'Connor, R., 1999. Discrete element simulation and the contact problem. *Archives of Computational Methods in …*, 6(June 1996), pp.279–304.

Wu, C.-Y., Thornton, C. & Li, L.-Y., 2009. A semi-analytical model for oblique impacts of elastoplastic spheres. *Proceedings of the Royal Society A: Mathematical, Physical and Engineering Science*, 465(2103), pp.937–960.

Zhao, F. et al., 2010. Environmental assessment of laser assisted manufacturing: case studies on laser shock peening and laser assisted turning. *Journal of Cleaner Production*, 18(13), pp.1311–1319.